Elevation change and mass balance of Svalbard glaciers from geodetic data

by

Geir Moholdt

PhD thesis

Oslo 2010

Department of Geosciences

Faculty of Mathematics and Natural Sciences

University of Oslo

Series of dissertations submitted to the
Faculty of Mathematics and Natural Sciences, University of Oslo
No. 1035

ISSN 1501-7710

Cover: Inger Sandved Anfinsen.
Printed in Norway: AIT Oslo AS.

Produced in co-operation with Unipub.
The thesis is produced by Unipub merely in connection with the
thesis defence. Kindly direct all inquiries regarding the thesis to the copyright
holder or the unit which grants the doctorate.

Abstract

The Arctic region is more affected by recent climate change than the lower latitudes. Glaciers and ice caps are sensitive indicators of climate change, and there is a high demand for more accurate quantifications of glacier changes in the Arctic. This thesis uses ground-based, airborne and spaceborne elevation measurements to estimate elevation change and mass balance of glaciers and ice caps on the Svalbard archipelago in the Norwegian Arctic. Previous assessments of the overall glacier mass balance of Svalbard have been based on in-situ measurements of surface mass balance from a limited number of sites, mainly in western Svalbard. Little has been known about the mass balance of eastern Svalbard glaciers, among those the Austfonna ice cap which covers more than 20% of the total glaciated area of 34600 km^2 on Svalbard. Annual field campaigns at Austfonna were initiated in 2004, providing in-situ data on surface mass balance and elevation change which are used to validate remote sensing data. A new and more accurate DEM of Austfonna is constructed by combining satellite SAR interferometry with ICESat laser altimetry. The precision of the DEM is sufficient to correct ICESat near repeat-tracks for the cross-track topography such that multitemporal elevation profiles can be compared along each reference track. The calculated elevation changes along ICESat repeat-tracks agree well with more accurate elevation change data from airborne laser scanning and GNSS surface profiling. The average mass balance of Austfonna between 2002 and 2008 is estimated to -1.3 ± 0.5 Gt y^{-1}, corresponding to an area-averaged water equivalent elevation change of -0.16 ± 0.06 m w.e. y^{-1}. The entire net loss is due to a retreat of the tidewater fronts. In-situ measurements indicate a slightly positive surface mass balance of 0.05-0.12 m w.e. y^{-1} between 2004 and 2008. Earlier time periods are difficult to assess due limitations in the amount and quality of previous elevation data sets. Other Svalbard regions have been precisely mapped by aerial photogrammetry, so the 2003-2008 ICESat profiles can be compared with existing topographic maps and DEMs from 1965-1990. The mass balance for this period is estimated to -9.7 ± 0.6 Gt y^{-1} (or -0.36 ± 0.02 m w.e. y^{-1}), excluding Austfonna and Kvitøya. Repeat-track ICESat data is also processed for the entire Svalbard yielding an average 2003-2008 mass balance of -4.3 ± 1.4 Gt y^{-1} (or -0.12 ± 0.04 m w.e. y^{-1}) when tidewater front retreat is not accounted for. The most accurate elevation change estimates are obtained using all available ICESat data in a joint analysis where surface slope and elevation change are estimated for rectangular planes that are fitted to the data along each track. The good performance of the plane method implies that it can also be used in other Arctic regions of similar characteristics where accurate DEMs typically are not available.

Acknowledgements

This work would not have been possible without the help and inspiration from colleagues at the Section of Physical Geography, Department of Geosciences. I am especially thankful to my supervisors; Jon Ove Hagen, Andreas Kääb and Trond Eiken. Jon Ove had the idea of the project and has been of great support and encouragement throughout the years. He even gave me some salary now and then when I was running overtime! Andi has build up a good research group in remote sensing and is always knowledgeable and helpful. Trond is the "know-how" in the field and makes me feel safer at Austfonna than in downtown Oslo. He is also a great resource for all kinds of geodetic problems. The rest of the Austfonna crew, in particular Thomas V. Schuler and Thorben Dunse, is highly acknowledged for many good Austfonna discussions and invaluable help with data collection, processing and paper writing. Bernd Etzelmüller distracted me with a lot of teaching responsibility which was a very good experience after all (thanks!). Last but not least, Chris Nuth deserves a big thank you for making me expand the ICESat work to the remainder of Svalbard. Chris is always critical (in a positive way!) and it was fun to constantly dig into new problems and solve them together.

I am grateful for having been given the opportunity to travel abroad for inspiring summer schools, interesting conferences (including skiing!) and a half year visit to the University of Alberta in Canada. Martin Sharp was a welcoming host, and I learned a lot from working with his group on the mighty Canadian glaciers. The research stay was possible thanks to a grant from the Leiv Eriksson mobility programme of the Research Council of Norway. Other important sources of funding relevant to my research have been the Arktisstipend grant from the Svalbard Science Forum, the ESA CryoSat Calibration and Validation Experiment (CryoVEX), the GLACIODYN project of the International Polar Year (IPY) and the ice2sea programme of the European Union 7th Framework Programme. I am also thankful to the numerous data contributors (NPI, ESA, SPIRIT-IPY, NASA/NSIDC etc.), especially the ICESat science team who basically saved my PhD project after the failure of CryoSat. It has been a pleasure to work with freely accessible data of such a high quality.

Lastly, I want to thank family and friends for encouraging me to finish this work and for pulling me away from it when needed!

Blindern,
20 October, 2010 Geir Moholdt

Contents

PART II – Papers

The thesis is based on four papers which are referred to by Roman numbers. The papers are ordered according to thematic considerations.

Paper I:

Moholdt, G., and Kääb, A. (In prep.). A new DEM of the Austfonna ice cap by combining differential SAR interferometry with ICESat laser altimetry. *Manuscript for submission*.

Paper II:

Moholdt, G., Hagen, J. O., Eiken, T., and Schuler, T. V. (2010). Geometric changes and mass balance of the Austfonna ice cap, Svalbard. *The Cryosphere, 4*, 1-14, www.the-cryosphere.net/4/21/2010/, doi:10.5194/tc-4-21-2010.

Paper III:

Nuth, C., Moholdt, G., Kohler, J., Hagen, J. O. and Kääb A. (2010). Svalbard glacier elevation changes and contribution to sea level rise. *Journal of Geophysical Research - Earth Surface, 115,* F01008, doi:10.1029/2008JF001223.

Paper IV:

Moholdt, G., Nuth, C., Hagen, J. O. and Kohler J. (2010). Recent elevation changes of Svalbard glaciers derived from ICESat laser altimetry. *Remote Sensing of Environment, 114,* 2756-2767, doi:10.1016/j.rse.2010.06.008.

Part I

Overview

1. Introduction

1.1. Motivation

The climate in the Arctic is changing more rapidly than in other regions of the world. The cryosphere (glaciers, sea ice and permafrost) plays a key role in the climate and the ecosystem of the Arctic, and there is a need for more and better data on cryospheric changes. Remote sensing is especially important in this context due to the limited amount of ground data from this inhospitable environment. This thesis focuses on quantification of glacier mass changes on the Svalbard archipelago in the Norwegian Arctic. Svalbard glaciers and ice caps cover a total area of 34600 km^2 which is about 6% of the worldwide glacier coverage outside of Greenland and Antarctica. Until recently, mass balance assessments of Svalbard glaciers have been based on extrapolation of a few surface mass balance records to the entire archipelago. There are however large regional variations in surface mass balance and the iceberg calving flux is not well known. Satellite remote sensing does not measure glacier mass balance directly, but it provides related data with a semi-continuous coverage at a regular time interval. If glacier mass balance can be derived from such data, there will be a large potential for regular mass balance monitoring over vast areas. In-situ measurements are still needed in order to validate remote sensing techniques.

Annual field campaigns were initiated at the Austfonna ice cap in spring 2004 as a part of the CryoSat calibration and validation experiment (CryoVEX). Unfortunately, CryoSat was lost in a launch failure in 2005, and the replacement satellite (CryoSat-2) was not launched until April 2010. An alternative satellite system is the ICESat laser altimeter which has been in operation between 2003 and 2009. It provides accurate elevations along reference profiles that are repeated several times each year. ICESat altimetry has been frequently used to quantify elevation changes over the Greenland and Antarctic ice sheets, but the usage over Arctic glaciers and ice caps has so far been limited. Compared to image stereo photogrammetry, ICESat has the advantage of a better vertical accuracy and a higher temporal resolution, while photogrammetry benefits from a continuous spatial coverage in cloud-free conditions. Photogrammetric techniques are though difficult to apply to extensive and featureless terrain like Austfonna due to poor image contrast.

Elevation changes can be spatially extrapolated to entire glacier basins in order to calculate volume change. Volume change can further be converted into mass balance if the

glacier density variation is known. This is typically not the case, so mass balance estimates from elevation change measurements are typically assuming a constant density distribution.

1.2. Objectives

The objectives of this thesis are two-fold. First, it aims to quantify the overall mass balance of Svalbard glaciers and ice caps over the last few decades. Second, the goal is to develop data processing techniques that can be used to monitor glacier volume change and mass balance over the entire Arctic using remote sensing data. Satellite altimetry was chosen as the preferred technique since it provides accurate surface elevation data at regular time intervals. After the failure of CryoSat-1 in 2005, ICESat was the only operational satellite altimeter which could potentially provide precise elevation data in sloping terrain like on Svalbard. We wanted to figure out if ICESat could be used to determine long-term elevation changes with respect to existing elevation data sets (Paper III) and short-term elevation changes within the 2003-2009 ICESat period (Paper IV). Ultimately, the goal was to extrapolate these elevation changes to estimate regional volume change and mass balance.

Papers I and II concern the Austfonna ice cap which is the main target glacier for this thesis and the place where annual spring field campaigns have been carried out since 2004. Austfonna contains 30-40 % of all ice masses on Svalbard and differs from most other Svalbard glaciers and ice caps in terms of geometry, climate and dynamics. A better understanding of glacier changes at Austfonna is needed in order to assess the overall mass budget of the archipelago. Austfonna is also an ideal test site for satellite altimetry due to its gentle slopes and large extent (7800 km^2). We wanted to validate elevation change estimates from ICESat with more precise elevation change dat from airborne laser scanning and GNSS surface profiling during the same period. In situ measurements of surface mass balance provide an additional control. After having validated the methods on Austfonna (Paper II), the ambition was to apply the same methods to the remaining Svalbard glaciers (Paper IV). The next step will then be to do similar studies in the Canadian and Russian Arctic.

1.3. Outline

This thesis is divided into two parts. Part I provides an overview of different topics that are relevant to the research. After this introductory chapter, the climate and glaciology of Svalbard is described in Chapter 2. It focuses most on how the overall mass balance can be

determined from measurements or modelling of surface mass balance and iceberg calving. Examples from existing research on Svalbard are given. Chapter 3 provides an overview of different measurement techniques for glacier topography, while Chapter 4 describes relevant methods for calculating elevation change and mass balance. These two chapters aim to give a general methodological overview that applies to all kinds of glacier environments, but the techniques are always discussed in the context of Svalbard in order to make it easier for the reader to understand why certain techniques were prioritized in the work. Emphasis is put on SAR interferometry and ICESat laser altimetry since they are the main measurement techniques in the scientific papers. A summary of the research in Papers I-IV is provided in Chapter 5 along with some relevant auxiliary material that was not included in the published papers. The main implications from the thesis are briefly summarized in Chapter 6.

Part II consists of four scientific papers which are the main outcome of this thesis. Papers II-IV are peer-reviewed and published in scientific journals, while Paper I is a manuscript for submission to a journal. I am the second author of Paper III and the first author of Papers I and III-IV. The numbering of the papers follows the chronological and thematic order of the work although the sequence of publication has been different.

2. Svalbard – Climate, glaciers and mass balance

Svalbard is a 61000 km^2 archipelago in the Norwegian high Arctic located at 74-81˚ N latitude and 10-35˚ E longitude. Spitsbergen is the largest island, followed by Nordaustlandet, Edgeøya, Barentsøya and Kvitøya (Fig. 1). About 60 % of the archipelago is covered by glaciers and ice caps (Hagen et al., 1993). Most glaciological research has been carried out in the vicinity of the main settlement Longyearbyen and the two research stations in Ny-Ålesund and Hornsund. Other important field sites are Lomonosovfonna, Vestfonna and Austfonna. This chapter provides an overview of existing data and research that are relevant for the geodetic mass balance estimates in Papers II-IV. It starts with a general description of Svalbard's climate (Sect. 2.1) and glaciers (Sect. 2.2), and finishes off with a more thorough discussion on how the overall glacier mass balance of Svalbard (Sect. 2.5) can be determined from independent estimates of surface mass balance (Sect. 2.3) and calving (Sect. 2.4).

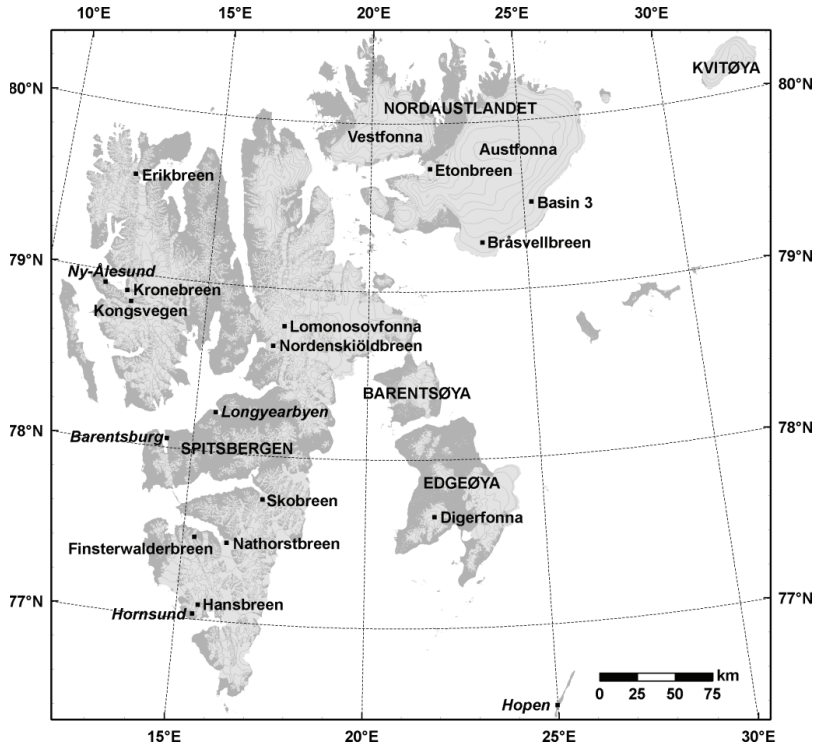

Fig. 1. Map of the Svalbard archipelago showing glaciers in light grey. Names of islands (uppercase), settlements (italics) and glaciers (plain) are provided for places mentioned in the text. Austre Brøggerbreen and Midtre Lovenbreen are located close to Ny-Ålesund.

2.1. Climate conditions and trends

The Svalbard climate is relatively mild for its latitude due to the northward Atlantic currents which bring warm water to the west coast of Spitsbergen (Fig. 2). This keeps the surrounding waters to the west ice-free for most of the year, while sea-ice dominates in the north and east during winter. The mild and humid sea winds from the southwest are often met by cold and dry polar winds from the north and east, making Svalbard's weather very variable both temporally and spatially. Rainfall or snowfall can happen at any time of the year, and the temperature fluctuations are large, especially during winter (Fig. 3). Large year-to-year variations in seasonal temperatures (Fig. 4) and precipitation (Fig. 5) imply that climate trends need to be strong or averaged over long time series in order to be statistically significant (Førland and Hanssen-Bauer, 2003).

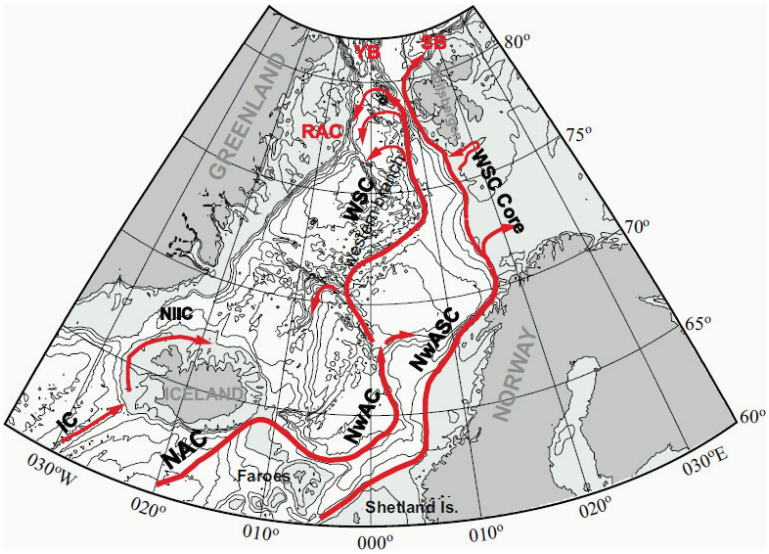

Fig. 2. The main pathways of Atlantic water in the Nordic Seas (from Piechura and Walczowski, 2009). The most notable currents around Svalbard are the West Spitsbergen Current (WSC), the Svalbard Branch (SB) and the Return Atlantic Current (RAC).

2.1.1. Temperature

Ice core proxies suggest that the 20th century was the warmest period during the past 600 years on Svalbard (Isaksson et al., 2003). Instrumental records of temperature are scattered and limited to the last hundred years. A homogenized long-term time series has been established for the Svalbard Airport in Longyearbyen based on statistical analyses of several

time series from different meteorological stations (Nordli and Kohler, 2004). It shows a remarkable warming around the 1920s, followed by more stable conditions and a pronounced cooling around 1960 (Fig. 4). Since then, there has been a gradual warming with an apparent stronger trend during the last few decades. The temperature trends are much more pronounced for the winter seasons (December-February) than for the summer seasons (June-August). This seasonality in climate change has been observed over most of the Arctic (Polyakov et al., 2003) and is believed to be amplified by variations in sea-ice thickness and extent (Manabe and Stouffer, 1980; Serreze et al., 2009).

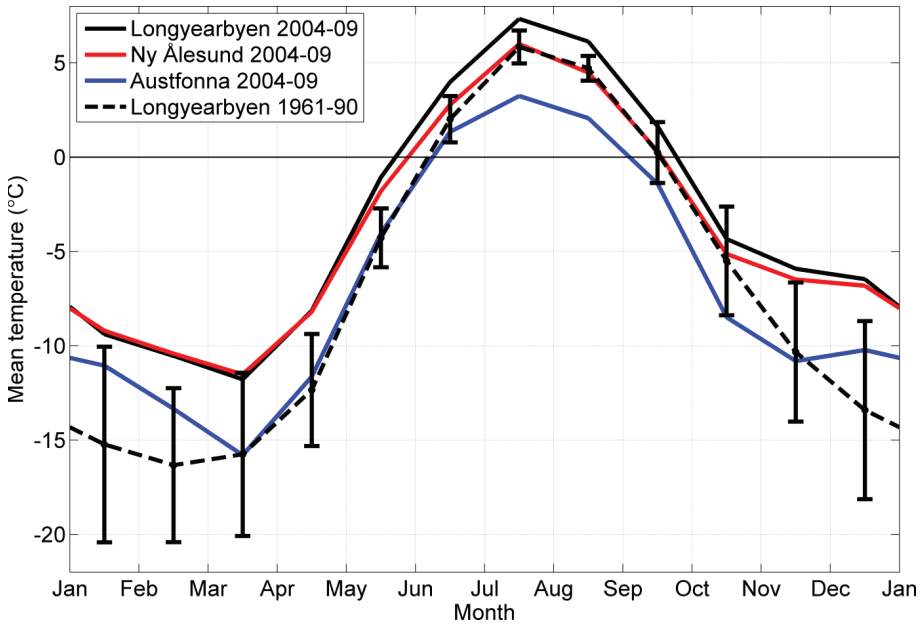

Fig. 3. Mean monthly air temperatures from Longyearbyen, Ny-Ålesund and Austfonna ice cap for the 2004-2009 time period. The meteorological reference period 1961-1990 is included for the Longyearbyen station along with one standard deviation bars to show the year-to-year variability of the monthly temperatures. Austfonna's temperatures were reduced from 340 m a.s.l. to sea level by using a constant lapse rate of -0.0044 K m^{-1} (Schuler et al., 2007). Data from the sea-level stations in Longyearbyen and Ny-Ålesund were provided by the Norwegian Meteorological Institute (met.no).

Two automatic weather stations have been operated at the Austfonna ice cap on the Nordaustlandet island, northeastern Svalbard, since 2004 (Schuler et al., 2007). Temperature data from there confirm that northeastern Svalbard has a colder climate than western Spitsbergen. The mean temperature in Longyearbyen and Ny-Ålesund during 2004-2009 was above zero for 3.5-4 months, while Austfonna only had 2.5-3 months of positive temperatures

at sea level (Fig. 3). In Longyearbyen, the 2004-2009 period was warmer than the 1961-1990 normal period for all months of the year, particularly in winter time. The temperature was at average 3.9˚ C warmer, and the above zero summer period was 0.7 months longer than normal. The recent warm years in western Spitsbergen coincide with a warming of the West Spitsbergen Current and a slight decrease in sea ice extent (Piechura and Walczowski, 2009).

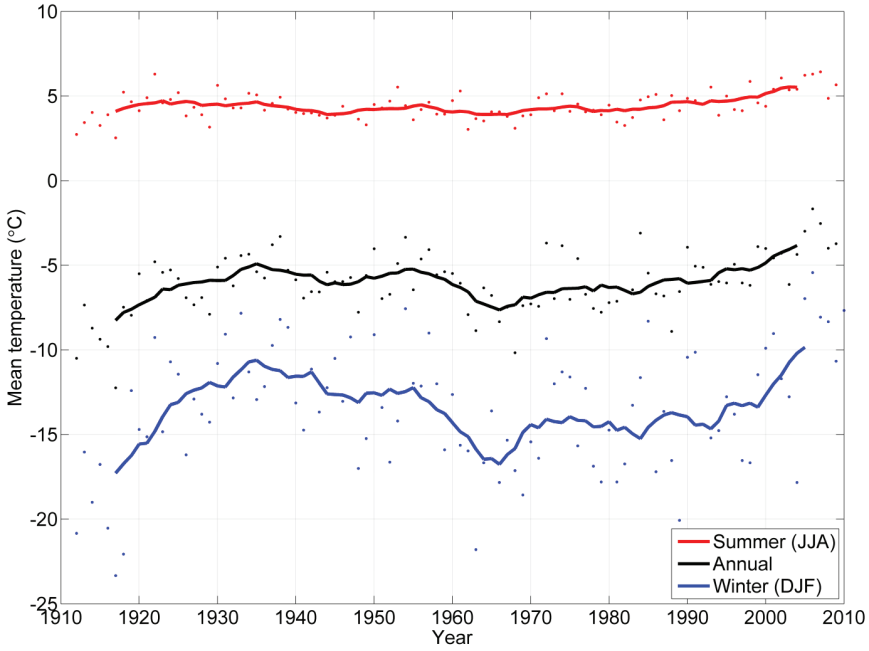

Fig. 4. Homogenized annual and seasonal mean air temperatures from Svalbard Airport, Longyearbyen (Nordli and Kohler, 2004). The summer average was calculated from June-August records, while the winter average is from December-February. The solid lines are running means over one decade. Data from the Norwegian Meteorological Institute (met.no).

2.1.2. Precipitation

Precipitation measurements in the Arctic are hampered by snow drift, icing, evaporation and wetting. Corrected observations from meteorological stations on Svalbard indicate a gradual increase in precipitation of 2-3 % per decade over the last century (Førland and Hanssen-Bauer, 2003), although there has been observed a recent decrease at the Hopen station in southeast Svalbard (Fig. 5). Svalbard generally receives less precipitation in late spring and early summer than during the rest of the year, but variations are large from year to year. There are also large local and regional variations in the amount of precipitation.

Longyearbyen in central Spitsbergen receives only about 1/3 of the precipitation of Barentsburg which is just 35 km to the west (Førland and Hanssen-Bauer, 2003). End-of-winter transects of snow depth measurements from Ground-Penetrating Radar (GPR) have revealed clear regional gradients in snow accumulation. The east coast of Spitsbergen receives over 40% more snow than the west coast, and the accumulation rate in the south is approximately twice as high as in the north (Sand et al., 2003). There is also a general increase in accumulation with increasing elevation. The average annual snow accumulation on Spitsbergen glaciers during 1997-1999 was estimated to 590 mm water equivalent (w.e.) (Sand et al., 2003) which is in line with scattered accumulation estimates from shallow ice cores spanning the 1963-1997 time period (Pinglot et al., 1999). A deep ice core from Lomonosovfonna, northeast Spitsbergen, indicates that the accumulation rate over the last 50 years was 25% higher than over the previous two hundred years (Pohjola et al., 2002a).

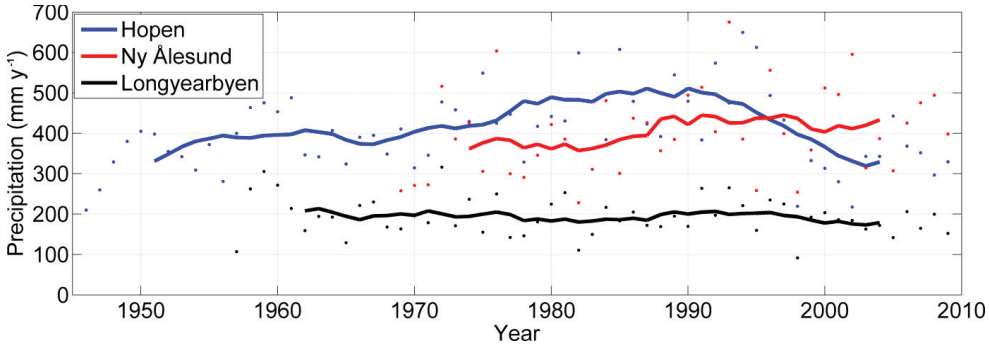

Fig. 5. Mean annual precipitation from meteorological stations in Hopen, Ny-Ålesund and Longyearbyen. The solid lines are running means over one decade. Data from the Norwegian Meteorological Institute (met.no).

2.2. Glacier characteristics

Svalbard glaciers and ice caps cover an area of 34600 km^2 (Paper IV) with a total ice volume of roughly 7000 km^3 (Hagen et al., 1993). The glaciers are of various geometric types: The alpine Spitsbergen island is dominated by extensive icefields flowing into valley glaciers divided by mountain ridges and nunataks (Fig. 1). Small cirque glaciers are also common in the more mountainous regions. The other islands, facing the Barents Sea, have less relief and mainly accommodate low-lying ice caps of which Austfonna (7800 km^2) and Vestfonna (2400 km^2) on the Nordaustlandet island are the two largest ones (Fig. 1). About

60 % of the total glaciated area on Svalbard drains into tidewater glaciers, terminating into the sea as grounded ice-tongues with a marked cliff in front (Blaszczyk et al., 2009).

2.2.1. Thermal regime

Permafrost is present in ice-free land areas on Svalbard due to a low mean annual air temperature (MAAT = -6˚ C at Svalbard Airport, 1912-2009). The permafrost thickness ranges from less than 100 m near the coasts to more than 500 m in the highlands (Liestøl, 1976; Humlum et al., 2003). The thermal regime of glaciers and ice caps is more varied and complex. In the accumulation area, the annual winter cooling reaches depths of 10-15 m (unpublished data, Austfonna), but it is partly compensated by the release of latent heat through refreezing of meltwater and rain that percolate into the snow and firn layers during summer. It is common to distinguish between super-imposed ice formed on top of last year's summer surface and other refrozen layers within the snow and firn pack. The internal heating from refreezing continues during the melting season until the temperature of the snow and firn pack is raised to the melting point (Sverdrup, 1935). In the ablation area, all snow melts during summer and runs off along the surface or in englacial channels instead of providing latent heat through refreezing. Internal heating from deformation is also decreasing towards the glacier margins due to a thinner ice cover. The lower parts of most Svalbard glaciers are therefore cold and frozen to the ground, while the upper parts can contain considerable volumes of temperate ice. Glaciers like these, with a mix of cold and temperate zones, are often denoted as sub-polar or polythermal glaciers (e.g. Paterson, 1994).

The thermal regime of Svalbard glaciers has been investigated by means of boreholes (e.g. Hodgkins, 1997; Kotlyakov et al., 2004) and radio echo-sounding from the air (e.g Dowdeswell et al., 1984; Kotlyakov and Macheret, 1987) and from the glacier surface (e.g. Hagen and Saetrang, 1991; Björnsson et al., 1996). Temperate ice has mainly been found in accumulation areas and at the bottom of glaciers that are thick enough to reach the pressure-melting point from deformational heating. Some of the small and thin glaciers with thicknesses less than 100 m are entirely cold (Hagen et al., 1993). Northeastern Svalbard glaciers have a higher fraction of cold ice than western ones (Bamber, 1987), probably due to a colder climate with a shorter melting season (Fig. 3) where the meltwater refreezing is sometimes not sufficient to reach temperate firn conditions (Schytt, 1964). The Austfonna ice cap, for example, shows few signs of temperate ice despite an ice thickness of several hundred meters (Dowdeswell et al., 1986; Zagorodnov et al., 1990).

2.2.2. Dynamics

Gravity makes glaciers flow through plastic deformation and basal sliding (e.g. Paterson, 1994). The dynamics of Svalbard glaciers is strongly dependent on the thermal regime. The deformation of ice decreases with decreasing temperature, and basal sliding normally requires a temperate layer of ice at the bed. Most smaller glaciers and ice caps are frozen to the ground around the margins (Björnsson et al., 1996), hence the movement is dominated by internal deformation with decreasing velocities towards the bed and the margins. Typical surface velocities for land-terminating glaciers are between 2 m y^{-1} in the lower ablation area and 10 m y^{-1} close to the equilibrium-line altitude (Hagen et al., 2003a). Some larger tidewater glaciers are able to maintain a steady fast-flow with a temperate sole sliding on lubricated sediments (e.g. Dowdeswell and Collin, 1990; Blaszczyk et al., 2009). The best example of such a glacier is Kronebreen in northwestern Spitsbergen which moves at velocities of 1-4 m d^{-1} (Liestøl, 1988; Kääb et al., 2005). Sediment plumes from glacier erosion can often be observed in front of these glaciers, especially during summer when surface meltwater reaches the bed. If no efficient subglacial drainage system is present, enhanced basal lubrication from surface melting can induce glacier acceleration (e.g. Zwally et al., 2002a). Summer speed-up events on daily to monthly time-scales have been observed on Eriksbreen (Etzelmuller et al., 1993b), Finsterwalderbreen (Nuttall and Hodgkins, 2005), Hansbreen (Vieli et al., 2004), Kronebreen (Kääb et al., 2005), Nordenskiöldbreen (den Ouden et al., 2010) and in Basin 3 on Austfonna (unpublished data).

Many of Svalbard's slow-moving glaciers are thickening in the upper parts and thinning in the lower parts (e.g. Hagen et al., 2005). The gradual surface steepening causes an increase in basal shear stress. At some point, the shear stress exceeds a stability threshold, triggering an episodic event of enhanced flow known as a surge. Observational data and models of glacier surges on Svalbard suggest that surge events are initiated when cold parts of the glacier bed are heated to the pressure-melting point, and basal meltwater is produced more rapidly than it can be evacuated (Fowler et al., 2001; Murray et al., 2003). The active phase of surges on Svalbard is typically 3-10 years, while the quiescent upbuilding phase lasts for 50-500 years (Dowdeswell et al., 1991). Surges occur independently of climate variations although the duration of the quiescent phase is affected by the climate (Hagen et al., 2003a). Surge-type glaciers are very common on Svalbard, and surging has been observed at all glacier scales, ranging from small cirque glaciers to large ice cap outlets (e.g. Liestol, 1969; Lefauconnier and Hagen, 1991; Hagen et al., 1993; Sund et al., 2009).

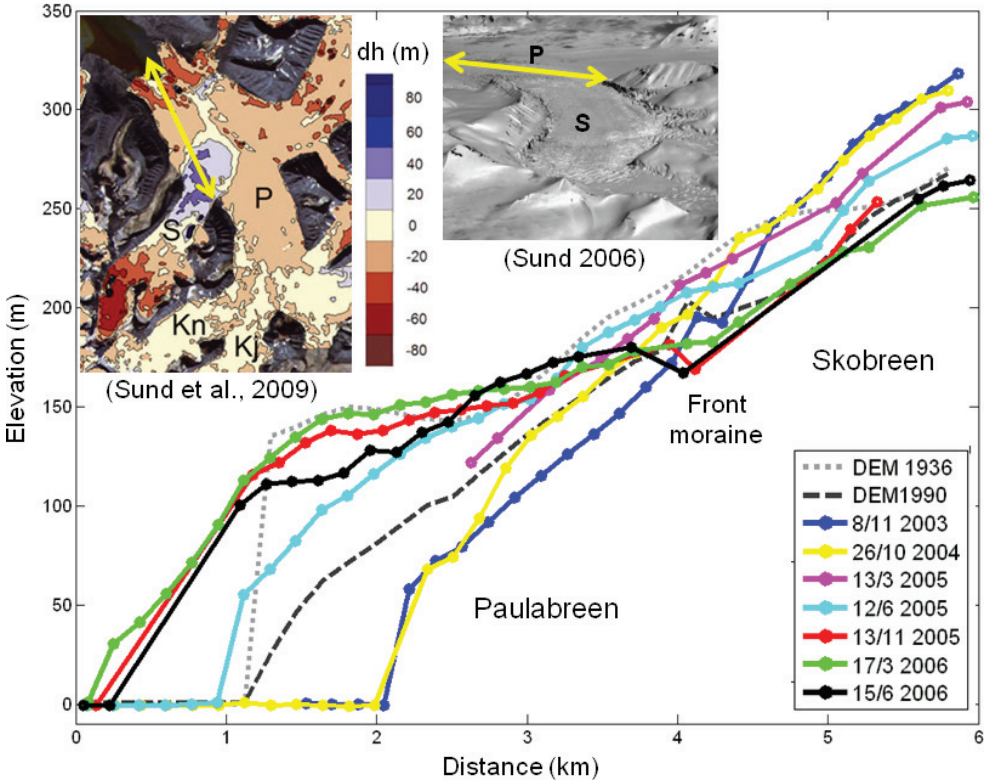

Fig. 6. The inset map and picture show the location of Skobreen (S), Paulabreen (P) and the ground-tracks of the ICESat laser altimeter (yellow arrows). Skobreen started surging sometime between 1990 and 2003, with the result of a ~50 m thinning of the upper basin and a corresponding thickening of the lower basin during the period (map from Sund et al., 2009). Around 2003, the surge front of Skobreen propagated into the lower parts of Paulabreen, causing a rapid thickening and advance of the Paulabreen glacier front as seen from repeat-track ICESat profiles (dotted lines) between 2003 and the surge termination in 2006. During this advance phase, the Skobreen glacier front dropped down by about 50 m to reach the pre-surge level as indicated by the 1990 DEM (dashed line).

The geometric changes of a glacier during a surge can be tremendous. The 30 km wide tidewater front of Bråsvellbreen, an outlet glacier from the Austfonna ice cap, was pushed ~20 km forward during a surge between 1936 and 1938 (Schytt, 1969). A more recent major surge is that of the Nathorstbreen glacier system in southern Spitsbergen which reached the glacier terminus in winter 2008/09, causing a rapid advance of at least 7 km over the course of less than one year (Sund and Eiken, 2010). An example of geometric changes due to glacier surging is shown in Fig. 6 for Skobreen/Paulabreen in southern Spitsbergen.

2.3. Surface mass balance

Surface mass balance (SMB) is the sum of surface accumulation (precipitation, wind deposition, avalanches and riming) and surface ablation (runoff of meltwater and rain, wind erosion, sublimation and evaporation) (e.g. Paterson, 1994). Glacier areas with a positive annual SMB are referred to as the accumulation area, while areas with a negative annual SMB are referred to as the ablation area. Since temperature decreases with elevation, there is typically an elevation-dependent boundary between the upper ablation area and the lower accumulation area, denoted the equilibrium-line altitude (ELA). A rise of the annual ELA typically implies a lower total glacier SMB since the ablation area has become larger and the accumulation area smaller. The ratio between accumulation area and total glacier area is called the accumulation-area ratio (AAR). The global average AAR for steady-state glaciers has been estimated to 58 % (Dyurgerov et al., 2009) which is similar to the average AAR at Austfonna between 2004 and 2008 (Paper II).

The SMB year ideally refers to the period between two successive annual minima in glacier mass, typically occurring at the end of the summer melting season. The length of this period is not necessarily 365 days since weather conditions vary from year to year. The annual maximum in glacier mass occurs in late spring or early summer before melting intensifies. The mass change from the annual minimum to the annual maximum is denoted the winter SMB, while corresponding change from the annul maximum to the annul minimum is denoted the summer SMB. The sum of the winter SMB (B_w) and the summer SMB (B_s) equals the annual SMB, often referred to as the net SMB (B_n):

$$B_n = B_w + B_s \tag{1}$$

Glacier SMBs (B_n, B_w and B_s) are usually given in gigaton (Gt) or in water equivalent volume (km^3 w.e.) where 1 km^3 w.e. = 1 Gt. Specific SMBs at one particular location (b_n, b_w and b_s) or area-averaged values over the entire glacier ($\bar{b}_n$, $\bar{b}_w$ and $\bar{b}_s$) are expressed as mass per unit area (kg m^{-2}) or water equivalent height (m w.e.) where 1 m w.e. = 1000 kg m^{-2}.

The next sections give an overview of different methods and results from previous and current SMB investigations on Svalbard. Geodetic mass balance estimates derived from geometric changes are kept aside and treated separately in Chapter 4 and Papers II-IV.

2.3.1. Seasonal and annual field measurements

Specific SMB estimates can be obtained at point locations from a combination of stake and snow pit measurements (e.g. Østrem and Brugman, 1991). A set of stakes is typically deployed along the center-line of a glacier in different elevation bands (e.g. Paper II: Fig. 1a). Stake heights are recorded at the end of the winter season and at the end of the summer season to infer glacier thickness changes relative to the stakes. The winter season data are sometimes expanded spatially by including snow thickness soundings from manual probing and/or ground-penetrating radar (Kohler et al., 1997). Each winter-season thickness-change is multiplied with the average snow pack density from snow pit measurements to derive b_w. Similarly, b_n is calculated from the annual thickness change multiplied with the average density of firn and super-imposed ice (in the accumulation area) or the density of ice (in the ablation area). The summer balance (b_s) is estimated from Eq. 1. All stake balances (b) from one particular season or year are then plotted as a function of elevation (Paper II: Fig. 5) and parameterized in a suitable way such that $b = b(h)$. Finally, the specific SMB function $b(h)$ is multiplied with the glacier hypsometry (Paper II: Fig. 4) and summed to obtain the total SMB:

$$B = \sum_{1}^{Z} b(h_Z) \cdot A_Z \tag{2}$$

where h_Z is the middle elevation of Z elevation bins (e.g. 75 m for a 50-100 m elevation bin) and A_Z is the area for each of the elevation bins (glacier hypsometry). The area-averaged specific SMB for the glacier is then $\bar{b} = B/A$. The procedure is analogous for $\bar{b}_n$, $\bar{b}_w$ and $\bar{b}_s$ although one of them can be found from the algebraic sum of the two others.

Most SMB measurements on Svalbard are done in late April / early May (winter SMB) and late August / early September (summer SMB) whenever weather conditions and logictics permit. Hence, the SMB estimates do not strictly follow the annual minima and maxima in glacier mass (stratigraphic SMB). The majority of SMB measurements have been carried out on small glaciers in western and central Spitsbergen (Hagen et al., 2003a). The longest SMB record on Svalbard is from Austre Brøggerbreen, a 5 km^2 cirque glacier close to the Ny-Ålesund settlement in northwestern Spitsbergen (Fig. 1). The 1967-2008 SMB time series show a strongly negative SMB regime which is mainly controlled by the summer SMB (Fig. 7). There are no clear temporal trends in SMB although summer temperature (Fig. 4) and winter precipitation (Fig. 5) have increased slightly over the same period. The very negative $\bar{b}_n$ at Austre Brøggerbreen is in contrast to similar measurements between 1987 and 2008 at Kongsvegen, a 105 km^2 quiescent surge-type glacier only ~15 km away. The average

$\bar{b}_n$ at Kongsvegen in this period was -0.05 m w.e. y^{-1}, while the corresponding number at Austre Brøggerbreen was -0.51 m w.e. y^{-1} (J. Kohler, pers. com.). This mismatch illustrates how difficult it can be to extrapolate local SMB estimates to entire glacier regions (Sect. 2.5).

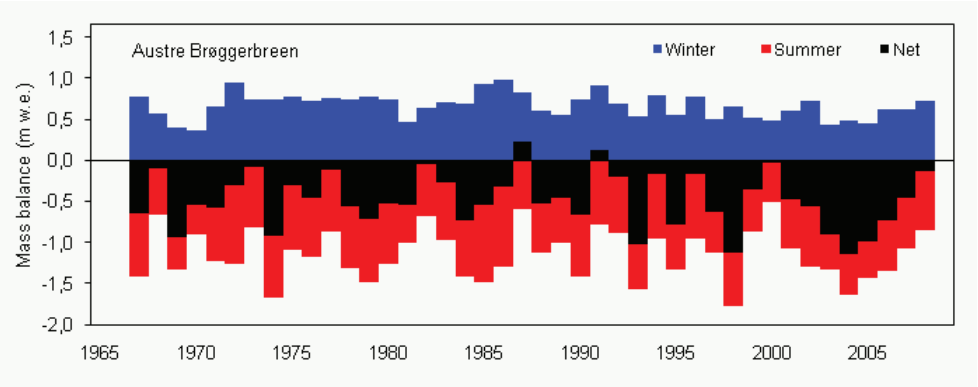

Fig. 7. Seasonal and annual surface mass balance (SMB) between 1967 and 2008 at Austre Brøggerbreen, close to Ny-Ålesund. *Courtesy of J. Kohler, Norwegian Polar Institute (NPI).*

Seasonal SMB can also be estimated from only end-of-winter field campaigns if last year's summer surface is easily detectable under the snow pack. The summer surface can be recognized as a harder and denser layer where melting has occurred. It is often overlaid by a low-density layer of depth hoar. The snow depths down to the summer surface are then subtracted from the winter stake heights to derive the end-of-summer stake heights. Firn densities for estimating b_n can be obtained from firn cores or deep pits. The rest of the SMB calculations are similar to the descriptions above. The SMB of the Austfonna ice cap has been estimated in this manner from 2004 to 2008 (Paper II: Fig. 6). The average $\bar{b}_n$ for these years was close to balance, although the annual values varied by ±0.5 m w.e. y^{-1}.

There are two major uncertainties in field-based SMB estimates for polythermal glaciers. First, one has to assume that the stake locations are representative for the rest of the glacier surface. This can sometimes be problematic due to local variations in wind deposition/erosion, solar illumination (aspect/slope) and surface roughness. Crevasse zones, for example, will collect more drifting snow during winter and have a larger surface area exposed to melting during summer. Second, SMB measurements usually do not account for internal refreezing of meltwater and rain that occurs beneath the previous summer surface. Ice cores from Austfonna indicate that meltwater percolate into 3-4 annual layers (Nagornov et al., 2005), and from an ice core at Lomonosovfonna it has been found that up to 50% of the

annual accumulation may melt and percolate into the firn, with a median of 25% (Pohjola et al., 2002b). If all meltwater in the accumulation area of Austfonna were to refreeze between 2004 and 2008, then the average $\bar{b}_n$ would rise from 0.05 m w.e. y^{-1} to 0.12 m w.e. y^{-1} (Paper II). Although it is very difficult to quantify the annual refreezing component of the SMB, attempts have been made to use percolation trays and automatic weather station data for this purpose (Koerner, 2005). Area-averaged internal accumulation rates of about 0.05 m w.e. y^{-1} (below the summer surface) have been reported for Barnes Ice Cap on Baffin Island and McCall Glacier in Alaska (Cogley and Adams, 1998).

2.3.2. Ice-core analysis

Ice cores contain a well of historical information about climate, pollution and mass balance (e.g. Isaksson et al., 2003; Nagornov et al., 2006). Specific net SMB (b_n) can be estimated from ice cores by tracking annual layers and/or detecting reference horizons from volcanic eruptions or nuclear events (e.g. Banta and McConnell, 2007; Colgan and Sharp, 2008). This is not straight forward on Svalbard since chemical deposition layers often get spread within several meters depth due to meltwater percolation (Pohjola et al., 2002b). With careful analysis, the depth-smoothed signals can yield a quasi-annual record of b_n which can be referenced to detectable horizons in the core. A three-century time series of b_n has been derived from a deep ice core on Lomonosovfonna in northeastern Spitsbergen (Pohjola et al., 2002a). The record indicates a positive shift in b_n of ~25% from the 1950s and onwards. The ice core measurements were complemented with low-frequency ground-penetrating radar (GPR) in order to expand the spatial coverage of the most obvious dating horizons. Trackable layers from nuclear fallouts in 1963 (test bombs) and 1986 (Chernobyl accident) did not reveal any significant trend in SMB from 1963-1986 to 1986-1999 (Pälli et al., 2002). The same was found by Pinglot et al. (1999) who investigated the same time spans in a series of shallow ice cores spread around in the accumulation area of several major Svalbard glaciers.

Ice core SMB records are limited to the higher accumulation areas and give no direct information about ablation below the ELA, which is the major control on SMB in Svalbard (Fig. 6; Hagen et al., 2003a). Parts of this lacking information can be inferred by expanding net SMB curves ($b_n(h)$) from the the accumulation area to lower elevations. Pinglot et. al (2001) estimated the ELA for five transects on Austfonna based on linear curves fitted to b_n estimates from 19 shallow ice cores spanning the period between 1986 and 1998/99. These b_n gradients were further expanded to the ablation area by Hagen et al. (2003b) who assumed

that the shape of the $b_n(h)$ curves would be similar to those found in other parts of Svalbard. The b_n estimates from 1986-1998/99 fit fairly well with recent $b_n(h)$ curves from annual SMB measurements in the 2004-2008 period, indicating that the average $\bar{b}_n$ of Austfonna has been close to zero in both periods (Paper II: Fig. 5).

2.3.3. Remote sensing

There have been several attempts to infer SMB from remote sensing analyses of surface characteristics. The annual ELA would be a good indicator of SMB, but it has proven to be extremely difficult to locate the ELA in satellite imagery (Winther, 1993; Engeset et al., 2002). Glacier facies at the end of summer give a good indication of recent SMB conditions, but cloud-free optical images from this short period are often not available. Radar instruments on the other hand, can see through a dry winter snow pack and thus provide an image of the end-of-summer conditions. Studies at Kongsvegen and Austfonna have shown that there is a good correspondence between backscatter zones in synthetic aperture radar (SAR) images and glacier facies mapped from surface profiles with ground-penetrating radar (Langley et al., 2008; Dunse et al., 2009). Although it is feasible to separate between regular glacier ice and super-imposed ice, it remains a challenge to identify the annual ELA since new super-imposed ice appears similar to old super-imposed ice (König et al., 2002). Statistical analyses have still shown that an annual SMB signal can be obtained from SAR imagery. König et al. (2004) used a k-means clustering technique to classify SAR images into three classes and found that the area of the uppermost class correlated well with the annual SMB of Kongsvegen over a decadal time period. The above techniques can be useful for monitoring regional variations in SMB, but they have so far only been applied to limited study areas.

Radar scatterometer images from the QuickScat satellite have been used in the Canadian Arctic to map interannual variations in the duration of the melting season (Wang et al., 2005) and in glacier facies (Wolken et al., 2009). Similar melt season studies on Svalbard show a pronounced regional and interannual variability in time of melt onset and number of melt-days per year (Sharp and Wang, 2009; Rotschky et al., In press). Melting season characteristics from temporal changes in surface properties can also be investigated by passive microwave and optical imagery (e.g. Mote et al., 1993; Hall et al., 2006). The albedo product of the Moderate Resolution Imaging Spectroradiometer (MODIS) has been used to derive annual SMB anomalies for 18 Svalbard glaciers (Greuell et al., 2007). Surface albedo controls the amount of energy available for melting in summer. It is also linked to the winter

SMB since a deep snow pack keeps the albedo high in early summer until the snow melts away in the ablation area. The correlation between estimated SMB anomalies and calculated ones from in situ measurements was as high for the annual SMB as for the summer SMB. The anomalies need to be tied to in situ measurements in order to derive absolute SMB values, but they are still useful for investigating regional and temporal variations. The results indicate that the SMB years 2000-2001 were anomalously positive, while 2002-2005 were anomalously negative, especially in the two first years (Greuell et al., 2007).

Elevation changes derived from remote sensing data can be used to obtain the overall glacier SMB if the firn/ice density and iceberg calving are known. Local specific SMBs can usually not be obtained from elevation changes unless the glacier is dynamically stagnant (Hagen et al., 2005). These issues are discussed in more detail in Chapter 4 and Papers II-IV.

2.3.4. Modelling

It has become increasingly popular to model glacier SMB from meteorological input data, both backward in time and into the future. The numerical models in use are mainly differing in the way melt is treated (e.g. Hock, 2005). *Energy balance models* sum up all energy fluxes at the surface to determine the residual energy available for snow heating (when $T_{snow} < 0^{\circ}C$) or melting (when $T_{snow} = 0^{\circ}C$). This is the most correct physical approach, but it requires good input data on shortwave and longwave radiation (incoming and outgoing) as well as turbulent fluxes close to the surface. *Temperature-index models* assume an empirical relation between temperature and melt, typically by adding all positive daily temperatures during the year and multiplying the sum with a locally adapted degree-day factor. Some temperature-index models are also accounting for local variations in incoming solar radiation due to topographic effects (Hock, 1999). Meteorological forcing data are usually obtained from local automatic weather stations (AWS), nearby meteorological stations or continuous meteorological reanalysis data. Input temperature data in distributed SMB models should be adjusted according to temperature lapse rate, while input precipitation data might need to be corrected for dominating weather system directions (Schuler et al., 2007) and orography (Schuler et al., 2008). SMB models in cold regions like Svalbard also need to incorporate internal cooling and heating, as well as meltwater refreezing in firn (Wright et al., 2007).

There have been several SMB modelling studies on Svalbard. Schuler et al. (2007) developed a distributed SMB model for the Austfonna ice cap using a temperature-index approach and an empirical index map of the spatial accumulation pattern (Taurisano et al.,

2007). The model parameters were optimized with respect to SMB measurements at stakes. The calibrated model was driven with temperature data from an automatic weather station and precipitation data from Ny-Ålesund. The results confirmed the asymmetrical spatial pattern of SMB at Austfonna, with a ~200 m lower ELA in the Southeast than in the Northwest (Paper II). Several energy-balance models have been employed to the glaciers around Ny-Ålesund where long term records of meteorology and SMB are available (Fleming et al., 1997; Wright et al., 2005; Arnold et al., 2006b). A recent study succeeded to use ERA-40 meteorological reanalysis data to model the SMB of Midtre Lovenbreen between 1958 and 2001 (Rye et al., 2009). The model was calibrated with in situ SMB data from 1968-2001. If the locally optimized parameters turn out to be representative for other Svalbard glaciers, the model can be applied to wider regions and ultimately to the entire Svalbard. Geodetic mass balance estimates (Papers II-IV) will be crucial for validating reanalysis models over larger areas.

The sensitivity of Svalbard glaciers to climate change has been investigated by simple SMB modelling. The SMB response to a hypothetical warming of +1 K has been estimated to -0.25 m y^{-1} K^{-1} (Oerlemans et al., 1998) and -0.45 m y^{-1} K^{-1} (De Woul and Hock, 2005), while the response to a 10 % increase in precipitation was estimated to < 0.10 m y^{-1} $(10\%)^{-1}$. It has been suggested that internal refreezing will slow down the SMB response to climate change (Wright et al., 2005) and that the more maritime western glaciers are more sensitive to warming than the colder and drier eastern glaciers (Fleming et al., 1997).

2.4. Calving

The mass balance of Svalbard glaciers is not only dependent on surface processes, but also iceberg calving from the extensive ice-cliff fronts that stretch out along much of Svalbard's coastline (Dowdeswell, 1989). The total mass loss due to calving (excluding Kvitøya) has been estimated to be 4 ± 1 Gt y^{-1} (Hagen et al., 2003b) and 6.7 ± 1.7 Gt y^{-1} (Blaszczyk et al., 2009) which is 10-40 % of the estimated 25 ± 5 Gt y^{-1} total runoff from glacier melting (Hagen et al., 2003a). Due to measurement constraints, it is common to separate calving mass loss (B_{calv}) into an ice-flux component at a fixed gate (B_{flux}) and a terminus fluctuation component (B_{front}) due to glacier retreat or advance:

$$B_{calv} = B_{flux} - B_{front} \tag{3}$$

where $B_{flux} \geq B_{front}$ and B_{front} is positive for an advancing glacier and negative for a retreating glacier. Parts of B_{calv} will actually be from melting at the ice-cliff front (above and

below water), but it is not common to distinguish between the two measures since it has no implication for the glacier mass balance (Dowdeswell et al., 2008).

2.4.1. Ice-flux at a fixed gate

The ice-mass flux through a fixed gate close to the terminus can be approximated by:

$$B_{flux} = v_{surf} \cdot h \cdot w \cdot \rho_{ice} \quad (4)$$

where v_{surf} is the surface velocity across the gate, h is the ice thickness, w is the width of the tidewater front and ρ_{ice} is the density of ice. Surface velocities can be found from image matching techniques, differential SAR interferometry (DInSAR) or field measurements. Ice thickness data are often sparse, but some tidewater glaciers on Svalbard have been surveyed with airborne radio-echo sounding (Dowdeswell et al., 1984; Dowdeswell et al., 1986; Kotlyakov and Macheret, 1987). The average ice thickness of tidewater fronts (h) has been estimated to be about 100 m (Hagen et al., 2003b). The total length of tidewater fronts (w) has been estimated to 1030 km (Dowdeswell, 1989) and more recently to 860 ± 15 km from recent ASTER imagery (Blaszczyk et al., 2009). Hagen et al. (2003b) combined all available glacier velocity data to estimate an average surface velocity (v_{surf}) of 20-40 m y^{-1}, yielding a total Svalbard ice flux of 3 ± 1 Gt y^{-1}. Velocities of unmeasured glaciers have also been estimated from a regression model between surface velocity and crevasse-zone length for 17 reference glaciers (Blaszczyk et al., 2009). The resulting average velocity (v_{surf}) was almost 70 m y^{-1}, yielding a total Svalbard ice flux (excluding Kvitøya) of 4.7 ± 1.4 Gt y^{-1}. An independent study of the Austfonna ice cap used DInSAR velocities to estimate an ice flux of 1.1 Gt y^{-1} through the 230 km long tidewater front (Dowdeswell et al., 2008).

2.4.2. Tidewater front fluctuations

The terminus mass change due to glacier advance or retreat can be approximated by:

$$B_{front} = v_{front} \cdot h \cdot w \cdot \rho_{ice} \quad (5)$$

where v_{front} is the rate of terminus advance (positive) or retreat (negative), and the other parameters are similar to Eq. 4 and the succeeding descriptions. Terminus fluctuations (v_{front}) can be measured from repeat-pass imagery or altimetry. Most of Svalbard's tidewater glaciers are in a phase of retreat, although there are examples of rapid advances due to

surging. The total Svalbard mass change due to terminus retreat (Q_{front}) has been estimated to -1 Gt y^{-1} (Hagen et al., 2003b) and -2.1 ± 0.8 Gt y^{-1} excluding Kvitøya (Blaszczyk et al., 2009) based on average retreat rates (v_{front}) of -10 m y^{-1} and -30 m y^{-1}, respectively. The latter retreat rate was obtained from the average v_{front} of 30 tidewater glaciers covered with repeated ASTER imagery acquired in 2000-2006. A similar retreat rate has been measured along the 100 km long tidewater front of Kvitøya (Paper IV), yielding an adjusted Q_{front} of -2.3 ± 0.8 Gt y^{-1} for the entire Svalbard. Another more detailed study of the Austfonna ice cap used repeated Landsat and ASTER imagery to estimate an average retreat rate of -40 m y^{-1} corresponding to a mass change of -1.4 ± 0.4 Gt y^{-1} (Dowdeswell et al., 2008).

2.5. Overall estimates of mass balance

There have so far only been a few attempts to calculate the overall mass balance of Svalbard glaciers. Some good time series on SMB exists (Fig. 7), but they are not necessarily representative for other glaciers. Glacier specific SMBs do not only vary because of meteorological factors, but also because of geometric considerations like size, slope, aspect and hypsometry. For example, a glacier surge will move large ice masses from high elevations to low elevations, resulting in a changed hypsometry and possibly a new SMB regime. SMB extrapolations should therefore be based on mass balance gradients ($b_n(h)$) and local hypsometries rather than glacier-specific SMB values ($\bar{b}_n$). Also, there is a clear southwest-northeast gradient in climate (Sect. 2.1) which needs to be considered if the sparsely measured eastern glaciers are going to be extrapolated from the western Spitsbergen SMB records. These issues are clearly exemplified in the three existing long-term SMB estimates for Svalbard. Dowdeswell et al. (1997) averaged glacier-specific SMB records from Spitsbergen to find an overall Svalbard SMB of -0.55 m w.e. y^{-1}. Hagen et al. (2003a) used a selection of SMB measurements to make a Svalbard-wide SMB curve ($b_n(h)$) which was integrated over the total hypsometry. Ice core SMB measurements from the accumulation area of eastern Svalbard glaciers were included, but ablation data were limited to the western glaciers. Hence, it is likely that the resulting Svalbard SMB of -0.27 m w.e. y^{-1} is somewhat biased towards the warmer western Spitsbergen climate. In order to avoid this problem, Hagen et al. (2003b) used all available SMB data to make 13 regional $b_n(h)$ curves in which lacking ablation data were extrapolated from the $b_n(h)$ gradient in the accumulation area,

assuming that the shape of the curves was similar to the other regions. This approach yielded a much less negative Svalbard SMB of -0.01 m w.e. y^{-1}.

Accounting for the iceberg calving loss (B_{calv}), the overall mass balance becomes:

$$B_{tot} = B_n - B_{calv} = B_w + B_s - (v_{surf} - v_{front}) \cdot h \cdot w \cdot \rho_{ice} \quad (6)$$

where the expanded equation follows from Eqs. 1-5. There are no floating ice shelves on Svalbard (Dowdeswell, 1989), so basal melting is negligible and not included in the mass balance equation. The various estimates of B_n and B_{calv} illustrate the large uncertainty of the overall mass balance of Svalbard glaciers. If the near zero B_n estimate from Hagen et al. (2003b) is used in combination with the B_{calv} estimate from Blaszczyk et al. (2009), then the overall mass balance becomes -7.2 ± 1.7 Gt y^{-1}, corresponding to an area-averaged mass balance of -0.21 ± 0.05 m w.e. y^{-1}. This is less negative than the long-term geodetic estimate in Paper III and more negative than the recent ICESat estimate in Paper IV. However, these data sets cover different time spans and slightly different areas, so they are not directly comparable. Geodetic estimates of Svalbard's mass balance are presented and discussed in Chapter 4 and Papers III-IV.

3. Measurements of glacier topography

Glacier topography can be mapped by image processing techniques like photogrammetry and SAR interferometry, or by profiling techniques like radar or laser altimetry. This chapter presents a methodological overview with emphasis on techniques that have been applied to Svalbard glaciers. A deeper theoretical background is provided for SAR interferometry and ICESat laser altimetry due to the importance of those techniques in Papers I-IV. Elevation change detection from repeated surveys is discussed in Chapter 4.

3.1. Photogrammetry

Photogrammetry is the practise of determining geometric properties of objects from measurements in photographic images. This section will focus on the use of aerial and satellite photogrammetry to obtain topographic maps or digital elevation models (DEM) on Svalbard. This has mainly been done using airborne stereo imagery from 1936-1990 and more recent satellite imagery from Landsat, ASTER and SPOT. The earliest mapping projects used analog or analytical photogrammetry to manually construct contour lines, while more recent work has used semi-automatic image matching techniques to make continuous DEMs.

Two overlapping images acquired from different positions or angles form a stereo image pair. Terrain objects will be distorted in the two image frames depending on the two camera positions and viewing angles, as well as ground topography. In vetrical frame images, objects that are far away from the image center get a larger radial distortion than objects closer to the image center. The difference in location of an object in two image frames is known as the stereo parallax (e.g. Mikhail et al., 2001). If the camera position and viewing angle are precisely known for the two image acquisitions, then the residual parallaxes will be due to surface topography. The camera positions and attitudes can be determined from onboard navigation systems (GNSS/INS) or from visible ground control points.

The elevation-dependent radial distortions in aerial imagery imply that single images should not be used to delineate glacier outlines and basins. This should instead be done in a stereo model or in an orthophoto where radial distortions have been corrected. The orthophoto correction is done by stretching and compressing the original image according to modeled radial distortions from a DEM. Most glacier outlines in this thesis have been obtained from the Norwegian Polar Institute (NPI, 2010a; Paper III) or been manually digitized from

orthorectified SPOT and Landsat imagery (Papers I and IV). Semi-automatic delineation of glacier outlines is also feasible, but it requires a clear spectral difference between glaciers and surrounding terrain (e.g. Andreassen et al., 2008).

There are three main limitations for the use of stereo photogrammetry on Svalbard. First, optical photogrammetry requires cloud-free conditions which are often not given on Svalbard. Second, a good image contrast is needed in order to recognize similar objects in both images. Snow and firn have a low optical contrast, so stereo image-pairs should ideally be obtained in late summer when glacier ice is exposed in the ablation area and melting features are visible in the accumulation area. Third, nunataks and ice-free ground are needed to obtain a good spatial distribution of ground control points. The latter problem can be avoided by using accurate navigation data (GNSS/INS) from the aircraft or satellite, but some sort of ground control is always desirable. In general, photogrammetry works well for Spitsbergen glaciers apart from in areas with cloud-cover or low-contrast snow. The large ice caps in the northeast, especially Austfonna, are more troublesome due to the extensive featureless firn areas and fewer possibilities for ground control.

3.1.1. Topographic maps from aerial photos

Most topographic maps and DEMs around the world are made from airborne stereo imagery. The first large-scale topographic mapping of Svalbard was done by the Norwegian Polar Institute (NPI) with oblique aerial photographing in 1936 (Nuth et al., 2007). Mapping campaigns from the 1960s and onwards have used vertical aerial imagery. The main topographic map series (S100) has been produced in scale 1:100000 with a 50 m contour interval (NPI, 2010a). A continuous DEM has also been constructed from 1990 imagery in southern Spitsbergen using a digital photogrammetric workstation. A new photogrammetric survey of Svalbard is under way (G. Melland, pers. com.), but no maps or DEMs have been published yet. An overview and accuracy assessment of the existing NPI maps and DEMs on Svalbard can be found in Nuth et al. (2007) and in Paper III.

Historical maps and images are invaluable for studies of glacier change. However, the quality of older maps is often limited by the photogrammetric processing and the availability of accurate ground control. Recent development with GNSS positioning and airborne laser scanning (Sect. 3.4.3) has made it possible to collect a large number of accurate ground-control points (outside the glaciers) which can be used to reprocess archived stereo imagery and make new DEMs with improved accuracy (James et al., 2006). This concept has been

tested at Midtre Lovenbreen by using airborne laser scanning to extract up to 50 ground-control points around the glacier (Barrand et al., 2009). A more cost-effective approach is to use satellite photogrammetric DEMs for the scaling and orientation of archival photogrammetric data sets (Miller et al., 2009).

3.1.2. ASTER stereo-imagery

ASTER (Advanced Spaceborne Thermal Emission and Reflection Radiometer) is a push-broom imaging instrument onboard the Terra satellite which was launched in 1999. It operates in 14 spectral bands and provides high resolution imagery of the Earth at resolutions between 15 m and 90 m (Yamaguchi et al., 1998). An additional backward-looking camera in the near infrared band provides along-track stereo-viewing capability together with overlapping nadir scenes (Welch et al., 1998). Cross-track stereo photogrammetry between different satellite orbits is also feasible although temporal decorrelation of the images can be a problem. ASTER DEMs are mostly generated from automated image matching techniques, with an expected vertical accuracy of 7-15 m for images with good quality and adequate ground control (Hirano et al., 2003).

The freely available ASTER Global Digital Elevation Model (GDEM), released by NASA and METI in 2009 (http://asterweb.jpl.nasa.gov/gdem.asp), is independent of any local ground control (Fujisada et al., 2005). More than 1 million cloud-filtered ASTER scenes were automatically stereo-correlated to produce multiple DEMs that were stacked and averaged in order to improve the vertical accuracy. Unlike previous semi-global mapping systems like the SRTM (Sect. 3.2.2), it provides comprehensive coverage of the polar regions (83˚S - 83˚N). A comparison with ICESat laser altimetry over Svalbard glaciers show a vertical precision of around 20 m depending on the timing and number of stacked DEMs. The GDEM is however of limited use for glacier elevation change studies since it is averaged over almost a decade. There are also some data voids present, like in the interior of Austfonna.

ASTER stereo-imagery has been widely used within glaciology (Toutin, 2008). A test study on Edgeøya, southeastern Svalbard, found that a DEM precision of about 15 m was achievable in areas with good optical contrast and ground control (Kääb, 2008). This was more than sufficient to calculate glacier volume changes with respect to a topographic map from the 1970s. Sund et al. (2009) made an ASTER DEM to derive geometric geometric changes due to a glacier surge within 1990-2003. In order to maximize optical contrast, both of these studies selected scenes from summers with strong melting and little firn.

3.1.3. SPOT5 stereo-imagery

SPOT (Satellite Pour l'Observation de la Terre) comprises a series of high-resolution optical imaging satellites. The SPOT push-broom scanners operate in panchromatic and multispectral modes at ground resolutions down to 5 m. DEMs can be generated from multitemporal panchromatic scenes using cross-track camera steering or from along-track stereo scenes obtained with the forward- and backward-looking High Resolution Stereoscopic (HRS) instrument onboard the SPOT5 satellite (Toutin, 2006). The cross-track method has been used to produce time series of glacier DEMs (Berthier et al., 2004), but its use is limited due to few image pairs with cross-track steering and due to radiometric variations between image acquisitions. Along-track stereoscopic scenes are available since the launch of SPOT5 in 2002. A thorough discussion about DEM generation from SPOT5-HRS in glacier terrain can be found in Berthier and Toutin (2008).

During the 2007-2009 International Polar Year (IPY), a project was initiated to provide freely accessible SPOT5 topographic data over polar ice masses. The SPIRIT project (SPOT5 stereoscopic survey of Polar Ice: Reference Images and Topographies) uses automatic image matching techniques and accurate orbit data to generate DEMs without any ground control points (Bouillon et al., 2006; Korona et al., 2009). About 3/4 of Svalbard is covered with SPIRIT DEMs at 40 m resolution and orthorectified source images at 5 m resolution from the summers of 2007 and 2008 (Fig. 8). The vertical precision with respect to co-registered ICESat laser altimetry profiles from February 2008 is around 5 m over most land and glacier surfaces in Spitsbergen (Paper IV). The featureless firn areas of the Vestfonna and Austfonna ice caps are much less accurate due to low optical contrast and some scattered clouds. The SPIRIT DEMs in Spitsbergen have been used to correct repeat-track ICESat altimetry profiles for the cross-track slope and to calculate new glacier hypsometries (Paper IV). There is also a large potential for elevation change studies with respect to previous photogrammetric DEMs (Nuth and Kääb, 2010). In this way, the scattered elevation change profiles in Paper III can be expanded to a semi-continuous spatial coverage which will provide more information about local glacier changes. However, the lack of ground control in SPIRIT DEMs implies a need for correcting systematic errors due to inaccuracies in the satellite positions and attitudes during image scanning. ICESat laser altimetry has proven to be an efficient tool for determining horizontal and vertical biases in the DEMs (Berthier et al., 2010; Nuth and Kääb, 2010).

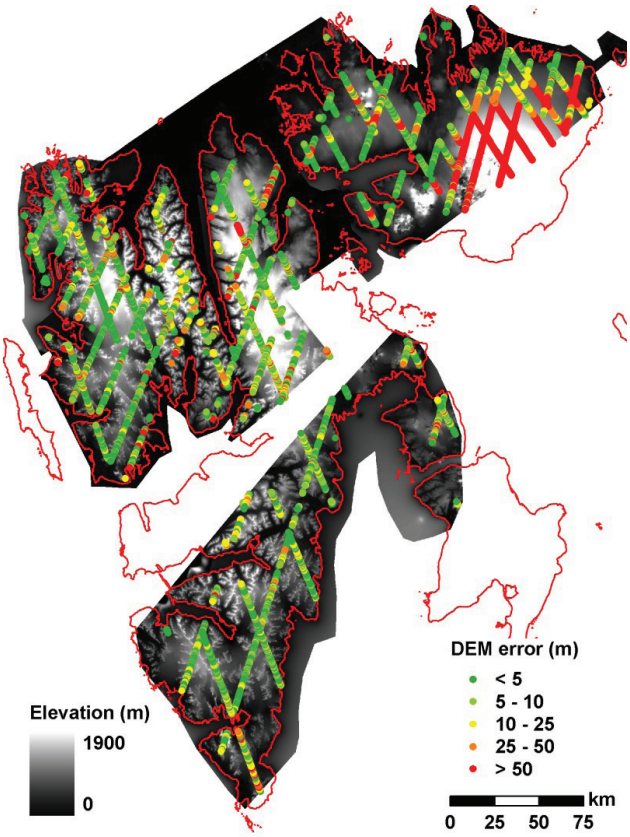

Fig. 8. A mosaic of five freely available SPOT5 DEMs at Svalbard obtained from the IPY SPIRIT project during the summers of 2007 and 2008 (Korona et al., 2009). Glacier elevation differences between the mosaiced DEM and ICESat laser altimetry profiles from February 2008 are also shown. The DEM quality is mostly good apart from some large errors in the firn areas of the Vestfonna and Austfonna ice caps on the Nordaustlandet island.

3.1.4. Shape-from-shading

Topographic information can also be derived from individual images by means of the relation between image brightness and surface slope. Since the geometry of solar illumination is constant for a given image, the radiance of a surface with homogenous reflectance will mainly depend on the solar incidence angle relative to the surface slope. Surfaces that face towards the Sun appear brighter than those that face away from it. This effect is often used visually to identify glacier drainage divides and to characterize surface roughness (e.g. Dowdeswell and McIntyre, 1987). Algorithms have also been developed to make topographic maps from the slope-to-brightness relation (Cooper, 1994). Such techniques are referred to as shape-from-shading or photoclinometry, and can also be applied to radar backscatter imagery.

In contrast to stereo-photogrammetry, shape-from-shading works best on winter images where a homogeneous snowcover ensures a stable albedo. Imagery from polar regions has typically a strong slope-to-brightness relation due to low solar elevation angles, but the slopes need to be small in order to avoid shadow areas where the relationship fails. Bingham and Rees (1999) used shape-from-shading to make a 100×100 m DEM of the Austfonna ice cap from a cloud-free Landsat scene acquired in winter 1973. Surface elevations from airborne radio echo-sounding (RES) profiles in 1983 (Dowdeswell et al., 1986) were used as tie points in the algorithm to constrain the brightness model to real elevations. The RMS accuracy of the DEM with respect to the RES tie points was ±0.8˚ for slopes and ±14 m for elevations (Bingham and Rees, 1999) which is not as good than for other Austfonna DEMs derived from SAR interferometry (Unwin and Wingham, 1997; Paper I). In conclusion, shape-from-shading is mainly an alternative when other more accurate techniques like stereo photogrammetry and SAR interferometry fail to operate due to poor optical contrast for image matching and poor coherence between repeat-pass SAR scenes, respectively.

3.2. Synthetic Aperture Radar (SAR)

Topographic mapping from optical images requires cloud-free conditions which are often not given in maritime regions like Svalbard. This is not a problem in radar imaging since microwaves penetrate the atmosphere in any weather. *Side-looking radar* antennas on airplanes or satellites transmit microwave pulses in a fan-shaped beam which illuminates a continuous swath of the Earth's surface on one side of the ground track (Fig. 9). The radar signals are scattered and reflected on the ground and return to the antenna where travel times are recorded for all echoes. These travel times are used to derive slant ranges and positions of the ground targets in the range (cross-track) direction. The range resolution (ρ_{ra}) depends on the effective chirped pulse length (τ_p), the speed of light (c) and the imaging geometry:

$$\rho_{\mathrm{ra}} = \frac{c\tau_p}{2\sin\theta} \tag{7}$$

where θ is the radar look angle (or incidence angle at the Earth surface) between the slant range and the vertical. The azimuth (along-track) resolution (ρ_{az}) is given by (Rees, 2006):

$$\rho_{az} = \frac{H\lambda}{L\cos\theta} \tag{8}$$

where H is the flight altitude above the surface, λ is the signal wavelength and L is the antenna length. The relation implies that the azimuth resolution is restricted by the antenna

length. For example, a desired azimuth resolution of 10 m for a satellite C-band radar system would require a several kilometers long antenna, which is not feasible. However, such an antenna can be synthesized by combining multiple along-track radar acquisitions into one image, known as a *synthetic aperture radar* (SAR) scene. Successful SAR processing presupposes that overlapping ground targets from multiple pulses can be resolved coherently and added together to form smaller synthetic targets. The new and improved azimuth resolution is given by the simple relation:

$$\rho_{az} = \frac{L}{2} \tag{9}$$

where L is still the physical length of the antenna. The synthetic length of the antenna varies with the slant range in such a way that the azimuth resolution becomes independent of the slant range ($H / \cos\theta$) and the signal wavelength (λ). The range resolution (Eq. 7) is however still dependent on the slant range, with better resolution for long ranges (large θ).

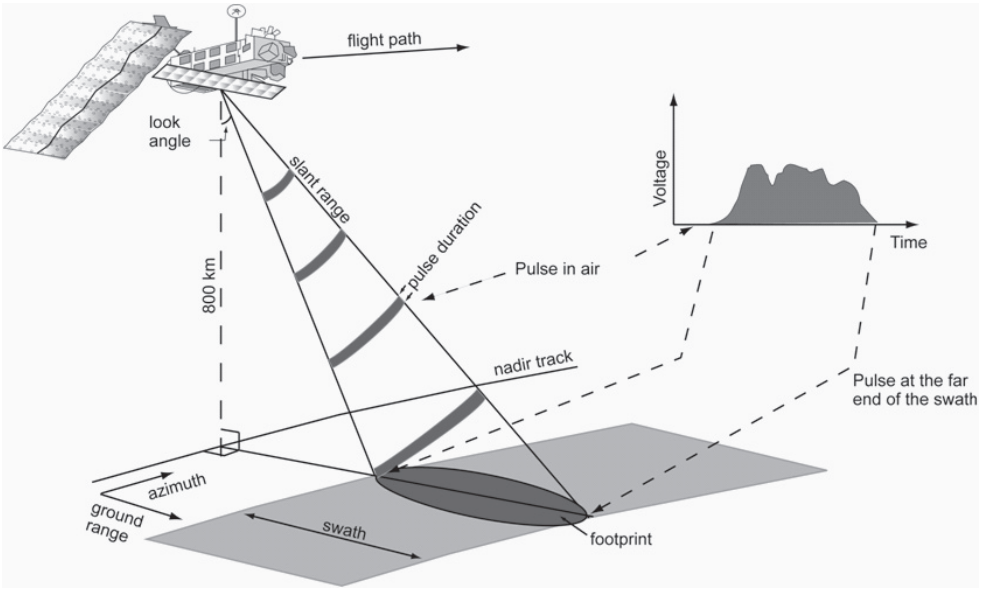

Fig. 9. Geometry and terminology of side-looking radar imaging. *Courtesy of K. Langley*.

Radar antennas record backscattered energy and phase for all return echoes. These data are stored in 2-dimensional *complex images* with real and imaginary parts. The backscatter information can be visualized as graytone *amplitude images* with bright shades for high energy returns and dark shades for low energy returns (Fig. 10). Geometric distortions

arise in SAR images due to the side-looking geometry and the range-dependent positioning of the targets. High mountains have a shorter range to the radar than surrounding terrain and are thus imaged closer to the satellite ground track than their real locations. These distortions can be corrected by means of an accurate DEM, although slope-dependent radiometric effects from foreshortening, layover and shadowing will still be present in the stretched image. *Terrain-geocoded* amplitude images can be used to delineate glacier outlines and drainage basins in the same ways as optical orthophotos. Stereoscopic *radargrammetry* from pairs of amplitude images is also possible, and DEM accuracies down to 5 m have been achieved using high resolution RADARSAT scenes in moderate relief land terrain (Toutin, 2004).

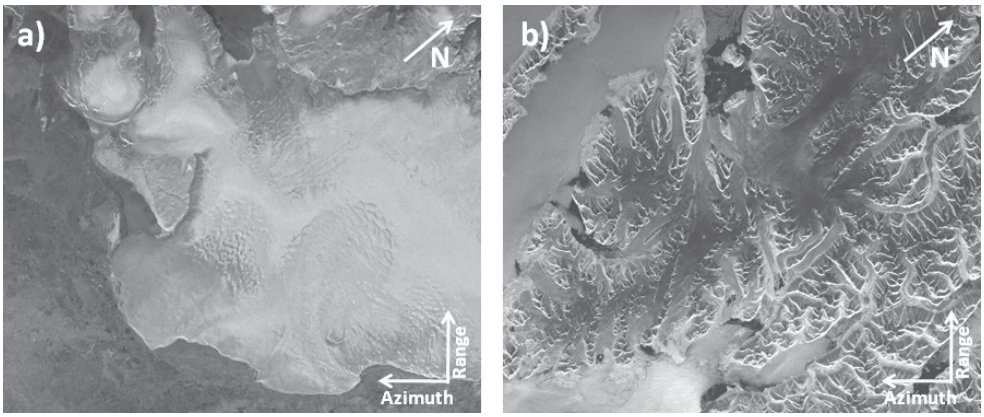

Fig. 10. Two ERS SAR amplitude images from Svalbard with very different characteristics: (a) Austfonna winter scene from 5 March 1996 with high backscatter over dry snow. (b) Northwest Spitsbergen summer scene from 17 August 2000 with low backscatter over wet snow and many geometric distortions due to mountainous terrain.

Phases contain little information by themselves since they are only recorded as fractions (0 - 2π) of the cm-scale radar wavelength. However, phase differences between two images acquired from slightly different locations (spatial baseline) and/or at different times (temporal baseline) are less ambiguous and can be used to extract information about surface topography and/or movement (Fig. 11). Such *interferograms* are formed by multiplying one complex SAR image with the complex conjugate of another image and extracting the phase information (Rosen et al., 2000). The two images must be co-registered with sub-pixel precision, typically achieved by image matching between the two amplitude images. Common ground targets need to have similar scattering properties in both images. The latter is often not the case due to *speckle* (Goodman, 1976), an image granulation that occurs from signal interference between the many scatterers that contribute to each image pixel. Speckle noise

can be reduced by spatial averaging of image cells, often referred to as *multilooking*. This improves the amplitude correlation and the phase coherence between images at the cost of a lower spatial resolution. Some degree of multilooking in the azimuth and range directions is usually beneficial for interferometric processing.

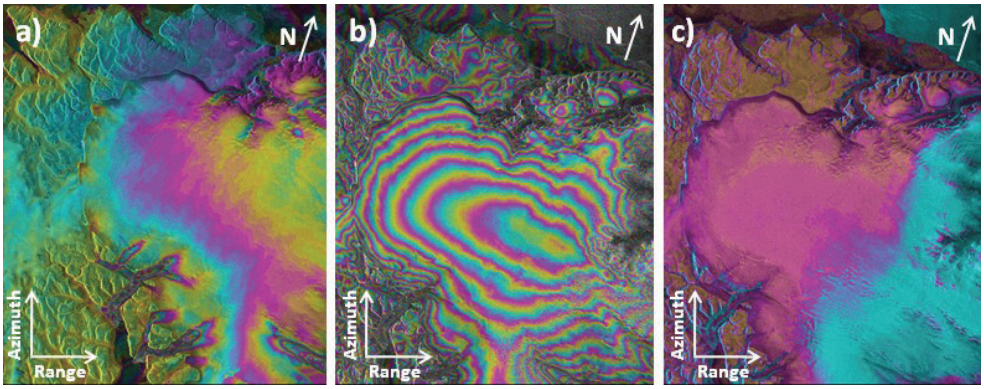

Fig. 11. SAR data from the ERS tandem period over the Devon ice cap in Arctic Canada: (a) Interferogram from 11-12 May 1996 with a short baseline ($B_\perp$ = 4 m) where most fringes are due to moving ice streams in the South and North. (b) Interferogram from 4-5 December 1995 with a long baseline ($B_\perp$ = 77 m) where most fringes are due to the ice cap topography. (c) Coherence image for interferogram (b) with brown colors representing high coherence and turquoise colors representing low coherence. The low coherence area is probably due to a winter storm from the east causing changes in the snow surface properties and consequently the backscatter. The same area in the interferogram suffers from a noisier fringe pattern.

There are several ways to obtain a pair of SAR scenes for interferometry. Most airborne systems have two antennas which are separated along or across the flight path. One of these antennas can be passive (receive only). Interferograms can thus be obtained from *single-pass* overflights, allowing maximum phase coherence and minimal phase distortions from surface movement. SAR satellites have only one antenna, so interferograms can only be formed between *repeat-pass* SAR scenes. This is often a problem over glaciers and snow-covered surfaces due to temporal phase decorrelation from precipitation, wind scouring and melting. The repeat-pass *phase coherence* is often better for radars with long wavelengths (e.g. L-band) than short wavelengths (e.g. C-band) since longer wavelengths penetrate deeper into the surface layer where the scattering mechanisms are not changing so much (Rott et al., 1993; Strozzi et al., 2008). However, short wavelength SAR like C-band is still preferential for glacier DEM generation since most signal reflections come from the uppermost 5-10 m of the snow/firn pack (Rignot et al., 2001; Langley et al., 2007).

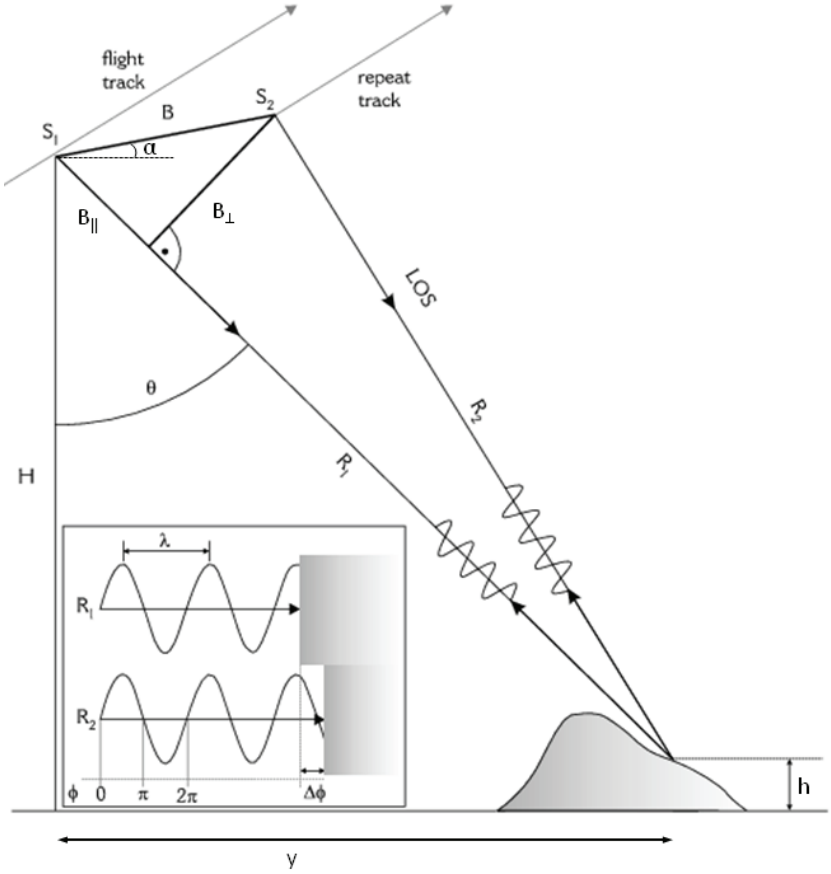

Fig. 12. Geometry of cross-track SAR interferometry *(adapted from Rott, 2009)*. The different short terms are; antenna positions (S_1, S_2), baseline components ($B, B_{\|}, B_{\perp}$), slant ranges (R_1, R_2), horizontal range (y), satellite altitude (H), terrain elevation (h), wavelength (λ) and signal phase (ϕ). The inset shows how a phase difference ($\Delta\phi$) is derived from the difference in slant range ($\Delta R = R_1 - R_2$).

An interferogram consists of modulo 2π phase differences ($\Delta\phi$) that arise from the ellipsoidal Earth ($\Delta\phi_{earth}$), surface topography ($\Delta\phi_{topo}$), surface movement ($\Delta\phi_{move}$), atmospheric disturbances ($\Delta\phi_{atm}$) and noise ($\Delta\phi_{noise}$):

$$\Delta\phi = \Delta\phi_{earth} + \Delta\phi_{topo} + \Delta\phi_{move} + \Delta\phi_{atm} \quad (10)$$

The $\Delta\phi_{atm}$ term is usually neglectable in single-pass SAR interferometry (InSAR) since the radar beams travel through the same atmosphere (Rosen et al., 2000). In spaceborne InSAR,

significant changes in the atmospheric propagation delay may occur between repeat-pass acquisitions, especially in atmospheres with a high water vapour content (Zebker et al., 1997).

The following equations are based on a simplified flat-Earth viewing geometry, although similar equations can been developed for an ellipsoidal Earth (Eldhuset et al., 2003). Assuming no $\Delta\phi_{atm}$, the remaining $\Delta\phi$ is a result of the InSAR geometry (Fig. 12) and potential line-of-sight movements (ΔR_{move}) at the ground (Kwok and Fahnestock, 1996):

$$\Delta\phi_{earth+topo+move} = \frac{4\pi}{\lambda} B \sin(\theta - \alpha) + \frac{4\pi}{\lambda} \Delta R_{move} \tag{11}$$

where $B \sin(\theta - \alpha) = B_{\parallel}$, and $4\pi/\lambda$ is the conversion factor between distance and phase if both antennas are active (i.e. $2\pi/\lambda$ for single-pass InSAR with one passive antenna). The phase sensitivity with respect to range (assuming a flat Earth) is found by substituting $\theta = \sin^{-1}(y/R_1)$ and differentiating Eq. 11 with respect to range (y):

$$\frac{\partial\phi_{earth}}{\partial y} = \frac{4\pi}{\lambda} \frac{B_{\perp}}{R_1 \cos\theta} \tag{12}$$

where $B_{\perp} = B\cos(\theta - \alpha)$. This results in a striped phase pattern in the interferogram which can be easily removed by integrating Eq. 12 over the interferogram ranges (y). In a similar way, the phase sensitivity with respect to topography is found by substituting $\theta = \cos^{-1}((H - h)/R_1)$ and differentiating with respect to elevation (h):

$$\frac{\partial\phi_{topo}}{\partial h} = \frac{4\pi}{\lambda} \frac{B_{\perp}}{R_1 \sin\theta} \tag{13}$$

The corresponding height difference for a 2π phase shift (one *fringe* in the interferogram) is:

$$\Delta h_{2\pi} = \frac{\lambda}{2} \frac{R_1 \sin\theta}{B_{\perp}} \tag{14}$$

It follows that a long perpendicular baseline ($B_{\perp}$) is beneficial for topographic mapping since it infers a dense fringe pattern (Fig. 11). However, the phase coherence decreases with an increasing $B_{\perp}$, so there is an upper limit to $B_{\perp}$ which is known as the critical baseline, e.g. ~1.1 km for the ERS satellites (Bamler and Hartl, 1998).

After removing $\Delta\phi_{earth}$, the remaining $\Delta\phi$ is due to topography ($\Delta\phi_{topo}$) and movement ($\Delta\phi_{move}$). Potential movements are usually neglected in single-pass InSAR and over stable ground, but in repeat-pass InSAR over dynamic surfaces like glaciers, $\Delta\phi_{move}$ needs to be considered. If surface movement (ΔR_{move}) is the main interest, an existing DEM can be used to remove $\Delta\phi_{topo}$ based on Eq. 13. The other way around is more difficult since there are typically no accurate external data on ΔR_{move}. Instead, $\Delta\phi_{move}$ can be removed

differentially (DInSAR) by means of another interferogram which is assumed to be influenced by the same movements. Since $\Delta\phi_{move}$ is independent of any baseline, one can subtract two interferograms ($\Delta\phi_1, \Delta\phi_2$) to obtain another one with only topographic fringes:

$$\Delta\phi_{12} = (\Delta\phi_{topo1} + \Delta\phi_{move1}) - (\Delta\phi_{topo2} + \Delta\phi_{move2}) = \Delta\phi_{topo12} \quad (15)$$

where $\Delta\phi_{move1} = \Delta\phi_{move2}$ is assumed. The topographic fringes do not cancel each other since they are dependent on $B_\perp$ (Eq. 13) which varies from interferogram to interferogram. The new fringe pattern ($\Delta\phi_{topo12}$) is thus dependent on the differential baseline $B_{\perp,12}$ in accordance with Eq. 13. The DInSAR principle can also be used the other way around by scaling one of the interferograms ($\Delta\phi_{12} = \Delta\phi_1 - k\Delta\phi_2$) such that $B_{\perp,12}$ becomes zero and consequently cancels $\Delta\phi_{topo}$ while scaled movement fringes remain, i.e. $(1-k)\Delta\phi_{move}$.

Interferogram fringes represent modulo 2π phase differences without any mathematical connection between the fringes. This ambiguity needs to be resolved through phase unwrapping, a process where integer multiples of 2π are added to $\Delta\phi$ whenever it wraps from 2π to 0 (e.g. Gens and VanGenderen, 1996). Ideally, unwrapped phase differences $\Delta\phi_{unw}$ form a continuous smooth model, but in reality, there are often errors and phase discontinuities due to steep topography, rapid movement and poor phase coherence. A range of different algorithms have been developed to make the unwrapping as continuous and correct as possible (Zebker and Lu, 1998). The two main groups of methods are *branch-cut* algorithms (Goldstein et al., 1988) and *least-squares* (LS) algorithms (Ghiglia and Romero, 1994). Branch-cut algorithms are first trying to isolate potential discontinuities in the interferograms automatically or with user interaction, and then the unwrapping is carried out along paths of integration between these "branch-cut" barriers. The idea is that all closed paths should have a zero sum of phase differences, which is not always easy to achieve. LS algorithms provide a smoother and more continuous approach where the goal is to minimize the difference between the gradients of the solution and the wrapped phases. Consequently, errors in LS unwrapping are not necessarily integer multiples of 2π like for the branch-cut method, and local errors are easily distributed to larger areas due to the least-squares concept. Unwrapping of topographic interferograms can also be aided by simulated unwrapped interferograms from existing DEMs (Eldhuset et al., 2003).

Successfully unwrapped interferograms yield consistent absolute phases that can be converted to movement or topography if there is at least one known reference point within the interferogram. If the baseline geometry is poorly resolved, it is beneficial to have a set of well

distributed reference points on the ground, e.g. from ICESat laser altimetry (Paper I), which can be used to refine the baseline parameters and recalculate the results. The final processing step is to geocode the DInSAR model into a suitable map projection. This is usually done by means of precise orbit data, ground control points or image matching with respect to a simulated interferogram or amplitude image from an external DEM.

3.2.1. Airborne SAR

There is a wide range of airborne SAR systems made for topographic mapping. Most of them are dual-antenna setups for single-pass interferometry at X- to L-band frequencies (i.e. 2-30 cm wavelengths). The horizontal resolution and vertical accuracy of the resulting DEMs can be down to a sub-meter level depending on SAR frequency, airplane positioning and terrain characteristics. Glacier DEMs with an accuracy of a few meters have been generated for a few areas in Greenland from the C-band InSAR systems TOPOSAR (Bindschadler et al., 1999) and EMISAR (Dall et al., 2001). The EMISAR system obtained unbiased surface elevations in the wet snow zone, but elevations in the percolation zone could be biased by up to 13 m due to signal penetration in dry snow and firn. An EMISAR DEM of the Vatnajökull ice cap in Iceland has been used to calculate volume change with respect an earlier photogrammetic DEM (Magnusson et al., 2005). There has so far not been any dedicated InSAR campaigns for topographic mapping on Svalbard.

3.2.2. Shuttle Radar Topography Mission

The Shuttle Radar Topography Mission (SRTM) was designed to obtain high resolution DEMs of all land surfaces between 56˚S and 60˚N (Farr et al., 2007). This was achieved with a single-pass C-band SAR interferometry system flown by Space Shuttle Endeavour over 11 days in February 2000. The active SAR antenna (transmit/receive) was placed in the shuttle, while an additional passive antenna (receive only) was installed on a 60 m mast to acquire a second set of SAR scenes needed for topographic interferometry. The C-band SAR was complemented with a narrow swath X-band SAR for quality control (Hoffmann and Walter, 2006). The absolute and relative accuracies (90% error) of the global C-band DEMs have been reported to be 5-10 m on average (Rodriguez et al., 2006), but some major data voids exist in regions with steep mountain slopes.

The freely accessible SRTM DEMs have been frequently compared with other elevation data sets to derive regional glacier volume changes (e.g. Rignot et al., 2003; Schiefer et al., 2007; Paul and Haeberli, 2008). However, there are elevation-dependent biases in SRTM which need to be corrected when calculating volume changes (Berthier et al., 2006; Paul, 2008). High latitudes regions like Svalbard are unfortunately not covered by SRTM.

3.2.3. Satellite SAR

Satellite SAR interferometry has a large potential for global topographic mapping, but so far the use has been limited by the long repeat-time of most SAR satellites, typically 20-50 days (Rott, 2009). Temporal changes of the surface properties can decorrelate the phases, especially over snow- and ice-covered areas. Therefore, most glacier DEMs from DInSAR are based on data from the short-term repeat campaigns of the European Remote Sensing (ERS) satellites in the 1990s. Interferograms are generated from the ERS-1 3-day repeat cycle in winter 1992 and 1994, or from the 1-day tandem cycle in 1995-1996 when ERS-2 was following the ERS-1 orbit at a 24-hour delay. These data have been used to generate glacier DEMs in Antarctica (e.g. Drews et al., 2009), Greenland (e.g. Joughin et al., 1996) and Svalbard (Unwin and Wingham, 1997; Eldhuset et al., 2003; Paper I). The different studies have reported DEM precisions of 5-15 m depending on the availability of ground control.

The quality and availability of satellite InSAR DEMs will most likely improve considerably with the new twin satellites TerraSAR-X and TanDEM-X which were launched in 2007 and 2010. TanDEM-X will follow closely behind TerraSAR-X in a flexible baseline configuration to obtain a global DEM with an unprecedented accuracy (Krieger et al., 2007). The almost simultaneous image acquisitions ensure a high phase coherence and limit the need for differential InSAR to remove movement fringes (Eq. 15). Due to the short wavelength of X-band SAR, the interferogram fringes will be more sensitive to topography (Eq. 13) than existing C-band (ERS, Envisat, Radarsat) and L-band (JERS and ALOS) satellite SAR systems. The signal penetration in cold snow and ice is also less of an issue for X-band SAR.

3.3. GNSS surface profiling

Surface profiling with Global Navigation Satellite Systems (GNSS) is an accurate method for in-situ measurements of glacier topography. A GNSS receiver (GPS/GLONASS) is typically mounted on a tripod on a sledge which is pulled by a snowmobile (Paper II).

Although it is feasible to derive a DEM from a dense grid of surface profiles (e.g. Palmer et al., 2009), GNSS profiles are usually only driven along the glacier center line (Eiken et al., 1997; Hagen et al., 2005; Hodgkins et al., 2007). An elevation accuracy of less than 0.1 m is achievable for dual frequency receivers with correction data from a nearby base station or with absolute post-processing using precise satellite clocks and ephemerides.

3.4. Airborne altimetry

Airborne laser and radar altimetry are popular tools for glacier mapping. Laser altimeters are used for surface profiling as well as continuous topographic mapping (e.g. Baltsavias et al., 2001), while radar altimeters, apart from SAR (Sect. 3.2.2), usually operate profile-wise at long wavelengths to allow radio-echo sounding (RES) of ice thickness in addition to surface topography (e.g. Dowdeswell and Evans, 2004). More accurate, short-wavelength radar altimetry systems like ASIRAS (Sect. 3.5.2) are also in operation, but they have so far not been applied for large scale topographic mapping. All altimetry systems rely on precise positioning of the aircraft and calculation of range vectors based on the attitude of the instrument and the time-delay of the reflected pulse. Modern airborne altimeters use GNSS and INS (Inertial Navigation System) to determine accurate instrument positions and attitudes (Zhang and Forsberg, 2007), while RES surveys prior to the 1990s had to rely on pressure altimeters and simple aircraft navigation tools (Dowdeswell et al., 1986).

3.4.1. Radio-echo sounding

Although the main purpose of airborne RES is to measure ice thickness, it is also useful for determining the surface topography in areas where traditional photogrammetry is difficult, e.g. Antarctica, Greenland and some larger Arctic ice caps (Dowdeswell and Evans, 2004). The Austfonna, Vestfonna and Kvitøyjøkulen ice caps were profiled in detail in spring 1983 (Dowdeswell et al., 1986; Bamber and Dowdeswell, 1990), and later topographic maps and DEMs have been partly derived from the RES surface elevations. The precision (or relative accuracy) of RES elevations can be determined from elevation differences at crossover points, but it is difficult to assess the absolute accuracy unless coincident measurements at the glacier surface are available. Elevation comparisons over stable ground, which are common for photogrammetric error analysis (Paper III), are of limited use since the reflective properties vary between surfaces of land, ice and snow/firn. An elevation precision

of about 10 m was found for the 1983 RES survey at Austfonna and Vestfonna based on 265 crossover points (Dowdeswell et al., 1986). However, field investigations show that elevation biases might be present in this data set due to potential local pressure anomalies that would influence the aircraft pressure altimeter readings (Paper II and Sect. 5.5.1).

3.4.2. Laser scanning

Laser sensors measure the travel time of reflected laser pulses to derive ranges to objects or surfaces. The technique is often referred to as *LIDAR* (light detection and ranging). Lasers usually operate in the near infrared part of the electromagnetic spectrum, so the signal can be scattered or absorbed by clouds. In contrast to radars with long wavelengths, laser pulses are only reflected from the top of the glacier surface. Airborne laser altimeters operate as *laser profilers* with one fixed laser beam orientation and/or as *laser scanners* with a mechanism for spreading the laser pulses in different directions, e.g. by means of an oscillating mirror (Wehr and Lohr, 1999). Laser scanning with a high density of points can be used to derive a continuous DEM. Footprint size, point density and swath width at the ground depend on the characteristics of the laser instrument as well as on flight altitude. Low altitude scanning yields a smaller footprint size and a higher point density at the cost of a narrower swath width. Accuracies better then 1 m in the horizontal and 0.1 m in the vertical can be achieved with precise GNSS/INS and well calibrated laser instruments (Krabill et al., 2002).

NASA's Airborne Topographic Mapper (ATM) is a laser scanning system which obtains accurate surface elevations within a cross-track swath of a few hundred meters. Repeated profiles have been flown over much of the Greenland ice sheet (Krabill et al., 2000) and over selected glaciers and ice caps in the Canadian Arctic (Abdalati et al., 2004) and in Svalbard (Bamber et al., 2004, 2005). Although the ATM profiles on Svalbard from 1996 and 2002 yielded some very interesting elevation change data, the density of scanning profiles was still too low to estimate volume change. Smaller laser scanning campaigns with slightly different instruments have been carried out on Austfonna in spring 2004-2007 in conjunction with CryoSat calibration work (Paper II).

Continuous laser scanning for DEM generation has been conducted to make new glacier inventories in South Tyrol, Italy (Knoll and Kerschner, 2009) and the Ötztal Alps in Austria (Abermann et al., 2009). Glacier outlines were extracted from the DEMs by means of automatic delineation algorithms. No laser scanning campaigns of similar scale have been carried out on Svalbard. Laser scanning for DEM generation has been limited to a few small

test site glaciers (Arnold et al., 2006a; Barrand et al., 2009; Miller et al., 2009). Although laser scanning is very promising for glacier monitoring, it is still an expensive technique. If the current development continues, airborne laser scanning with additional orthophoto generation might gradually take over for traditional photogrammetric mapping. Laser scanning provides more accurate elevations, and it performs equally well over snow-covered areas where photogrammetry suffers from low optical contrast (Kennett and Eiken, 1997).

3.5. Satellite altimetry

The principle of satellite altimetry is similar to airborne altimetry in the way that satellite-to-Earth ranges are obtained from the two-way travel time of radar or laser pulses. Most altimeters are *profilers* that emit pulses in the nadir direction along the satellite orbit. Radar altimeters with a range precision of a few centimeters have been profiling the Earth since the 1970s (Davis, 1992). The radar footprints of these altimeters are several kilometers in diameter, so they are mainly used to map sea surface topography and gentle sloping areas of the Greenland and Antarctic ice sheets. Since the ground tracks of polar orbiting satellites converge towards the poles, it has been possible to generate high-resolution ice sheet DEMs from multitemporal altimetry profiles (Bamber et al., 2001; Bamber et al., 2009). Elevation changes have also been estimated from crossover points between time-separated tracks (Johannessen et al., 2005; Wingham et al., 1998; Zwally et al., 1989).

On Svalbard, the elevation variation within a single radar altimetry footprint can be several tens of meters, and the return echo is a complex mixed signal from the entire footprint topography. Although it is possible to extract some useful elevation information for gentle Arctic ice caps (Rinne et al., Subm.), Svalbard glaciers are generally too steep to apply traditional satellite altimetry data. The slope issue is now largely overcome with the invention of high-resolution satellite altimeter systems like CryoSat and ICESat. They are able to measure precise surface elevations within a diameter of less than 100 m. These elevation data are thus much less sensitive to surface slope. The expected elevation accuracy of CryoSat and ICESat in gentle terrain is about 0.15 m (Wingham et al., 2006; Zwally et al., 2002b). A description of these two altimeter systems follows below.

3.5.1. CryoSat-2 radar altimetry

The first CryoSat was launched in 2005 but never got into orbit due to a failure in the launch rocket. A new satellite, CryoSat-2, was built and successfully launched in spring 2010. The primary instrument in CryoSat-2 is the SAR/Interferometric Radar Altimeter (SIRAL). It can operate in three alternating modes; one low resolution radar altimeter mode over oceans and ice sheet interiors, one general SAR mode over sea ice, and one SAR interferometric mode over glaciers, ice caps and ice sheet margins (Wingham et al., 2006). The latter mode is designed such that the cross-track angle to the earliest radar return can be precisely determined from the phase difference between the two antennas, allowing a precise positioning of the closest surface reflector in sloping terrain. The SIRAL interferometric mode can thus obtain accurate elevation profiles for most types of glaciers and ice caps. It will hopefully be an important tool for short-term mass balance monitoring on Svalbard.

Austfonna has been selected as one of the field sites of the CryoSat Calibration and Validation Experiment (CryoVEX). An airborne SIRAL simulation instrument named ASIRAS (Airborne SAR Interferometric Altimeter System) has been flown over Austfonna during spring field campaigns between 2004 and 2007. The aircraft has also been equipped with a GPS-tied laser scanner to investigate radar-laser range differences arising from the penetration of the Ku-band radar into the snow pack. Coincident field measurements of snow pack properties and densities have been carried out to indentify the radar reflection horizons along the altimeter profiles (Brandt et al., 2008). The data show that there are usually two dominant peaks in the ASIRAS backscatter; one from the air-snow interface close to the surface and one from the strong density gradient around last year's summer surface. By means of specialized radar re-tracking algorithms it is possible for ASIRAS, and maybe CryoSat, to derive both surface elevations and winter snow-pack depths (Helm et al., 2007).

3.5.2. ICESat laser altimetry

The Ice, Cloud and Land Elevation Satellite (ICESat) was the first spaceborne laser-ranging system in operation. It was launched in 2003 and has been acquiring surface elevation data over 18 observation campaigns of ~35 days until October 2009 (Table 1). The Geoscience Laser Altimeter System (GLAS) derived ranges from the two-way travel time of 1064 nm (near infrared) laser pulses (Zwally et al., 2002b). GLAS had 3 lasers that were operated one at a time in different observation campaigns. Due to an early failure of Laser 1, the continuous observation plan was reduced to three annual campaigns (two since 2006) in

Feb./Mar., May/Jun. and Oct./Nov., which each covers one 33-day sub-cycle of the nominal 91-day repeat orbit period (Schutz et al., 2005). This modification was done to lengthen the life time of the two remaining lasers and at the same time achieve a consistent coverage of repeated altimetry tracks. The 8-day orbit cycle in laser campaign 1A and parts of 2A was performed to obtain frequent repeat-passes over calibration sites at the ground.

Table 1. ICESat observation campaigns with laser/campaign identifier, days of operation, start date, end date and orbit repeat period (days). The last laser failed on Oct. 11, 2009.

Laser	Nr. of days	Start date	End date	Orbit
1A	38	2003-02-20	2003-03-29	8 d
2A	56	2003-09-24	2003-11-18	8/91 d
2B	34	2004-02-17	2004-03-21	91 d
2C	35	2004-05-18	2004-06-21	91 d
3A	37	2004-10-03	2004-11-08	91 d
3B	36	2005-02-17	2005-03-24	91 d
3C	35	2005-05-20	2005-06-23	91 d
3D	35	2005-10-21	2005-11-24	91 d
3E	34	2006-02-22	2006-03-27	91 d
3F	34	2006-05-24	2006-06-26	91 d
3G	34	2006-10-25	2006-11-27	91 d
3H	34	2007-03-12	2007-04-14	91 d
3I	35	2007-10-02	2007-11-05	91 d
3J	34	2008-02-17	2008-03-21	91 d
3K	16	2008-10-04	2008-10-19	91 d
2D	17	2008-11-25	2008-12-11	91 d
2E	34	2009-03-09	2009-04-11	91 d
2F	12	2009-09-30	2009-10-11	91 d

GLAS emits 40 laser pulses per second, resulting in an along-track footprint spacing of ~170 m at the ground (Fig. 13). The ground footprints have a varying elliptical shape with average dimensions of 52×95 m for Laser 1/2 and 47×61 m for Laser 3 (Abshire et al., 2005). In sloping terrain, the footprint size becomes even larger. The reflected photons that reach the GLAS detector are counted at a temporal resolution of 1 ns (0.15 m range) to form the return echo waveform (Fig. 14). The magnitude and shape of a return waveform vary with surface slope, roughness, snow/ice properties, type of reflection and atmospheric conditions. The noisy nature of a waveform is mitigated by fitting modeled curves to the waveforms. The satellite-to-Earth range is then calculated from the time delay between the peak of the transmitted waveform and the peak of the modeled return waveform. Over smooth glacier terrain, there is usually only one main peak in the return waveform, and a single peak

Gaussian curve is well suitable to represent the waveform. The standard parameterization in the GLA12 ice sheet product (for Greenland and Antarctica) and the GLA06 global elevation product (used in Papers I-IV) is to fit a maximum of two Gaussian curves to the waveform and use the maximum peak to determine the range. In rough terrain, multiple peaks easily occur, and several Gaussian curves might be needed to model the waveform. The terrain parameterization in the GLA14 product uses the centroid of a maximum of six Gaussians curves to determine the range. Near coincident crossover points over glacier ice on Svalbard yield an RMS error of 0.60 m for GLA06 and 0.80 m for GLA14, indicating that the ice sheet parameterization is most suitable in low-slope glacier regions like Svalbard.

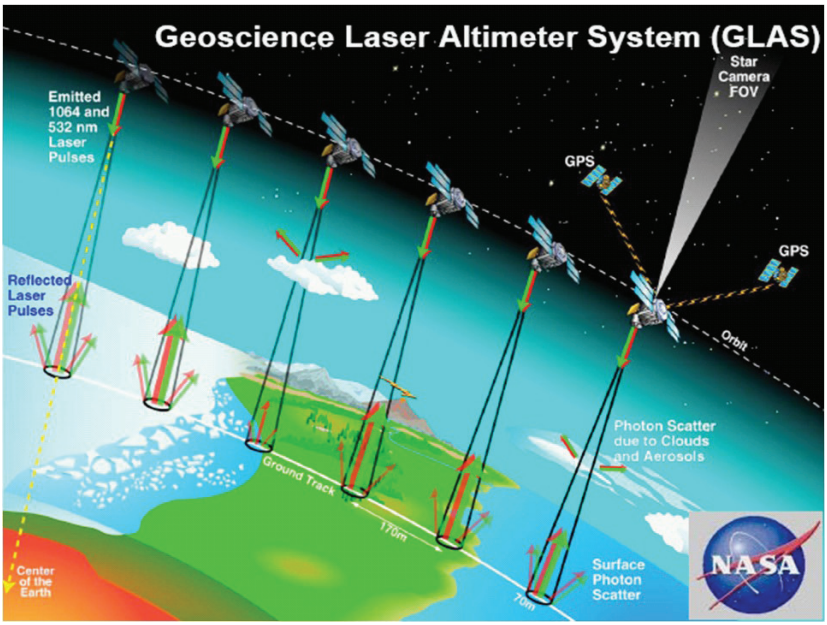

Fig. 13. A sketch of the ICESat measurement system. GPS, INS and a star camera are used to determine the satellite position and attitude. Each laser pulse illuminates a ~70 m footprint at the ground at an along-track spacing of ~170 m. The surface scattering of the signal varies with surface properties, and some pulses are scattered or absorbed by clouds and aerosols.

Surface elevations are calculated from the measured range, the off-nadir pointing angle and the height of the satellite above the ellipsoid. These quantities form the basis for the ICESat error budget (Table 2). The point-to-point precision of range measurements is extremely good in optimal conditions, but under conditions favourable to detector saturation or forward scattering, the ranging performance can degrade with several meters. Detector saturation occurs for near specular reflections where the high return energy overloads the

GLAS detector, leading to distorted waveforms that are clipped and artificially wide (Fricker et al., 2005). The Gaussian fit procedure will then be biased towards longer ranges and thus too low surface elevations. This effect has been empirically modeled to derive a saturation range correction which is provided with the newest ICESat releases (Zwally et al., 2010). The range error due to forward scattering of photons by clouds and blowing snow is more difficult to quantify (Duda et al., 2001; Mahesh et al., 2002). Forward scattering delays the signal and causes a long tail in the echo waveforms with the result of too low elevation estimates (Fig. 14c). Several studies have filtered their ICESat data for suspected cloud-affected returns based on proxy parameters such as energy, gain, reflectivity and waveform misfit (Fricker and Padman, 2006; Smith et al., 2009; Yi et al., 2005). The most used cloud-filtering parameter is detector gain. It is an instrumet setting which is automatically adjusted according to the waveform amplitudes of the previous laser echoes. The gain is set higher when the echo amplitudes become lower. Hence, it is expected that cloud-affected returns (Fig. 14c) receive a higher gain than cloud-free ones (Fig. 14a). Elevation comparisons at crossover points on Svalbard glaciers show that the elevation precision is better for low gain echoes (Fig. 15). However, gain filtering also removes a high amount of usable data. A gain threshold of 30 (Yi et al., 2005) applied to Svalbard will removed ~60 % of the data and make it impossible to do an elevation change analysis like in Paper IV. For such purposes on Svalbard, it is therefore necessary to sacrifice accuracy for a higher amount of data and a better spatial distribution.

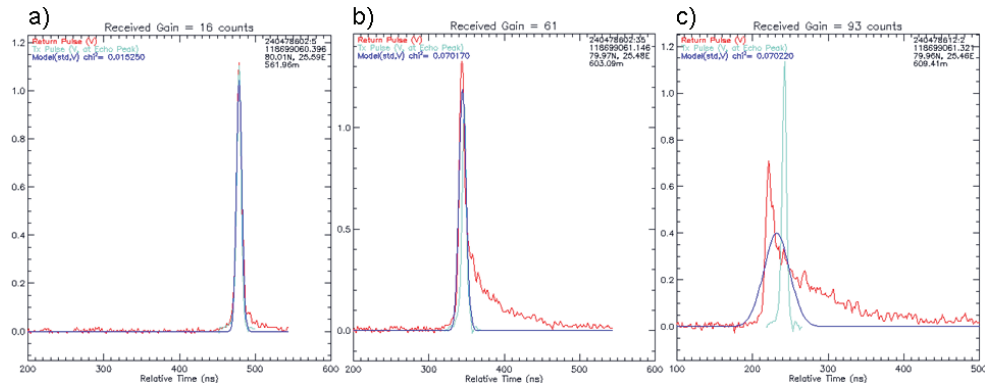

Fig. 14. Transmitted (turquoise), received (red) and modeled (blue) laser pulse waveforms for (a) a signal with no cloud scattering and a low gain, (b) a signal with moderate cloud scattering and a medium gain, and (c) a signal with heavy cloud scattering and a high gain. The three examples are from smooth and gentle glacier terrain at Austfonna, so the waveform widening from surface slope and roughness is most likely small.

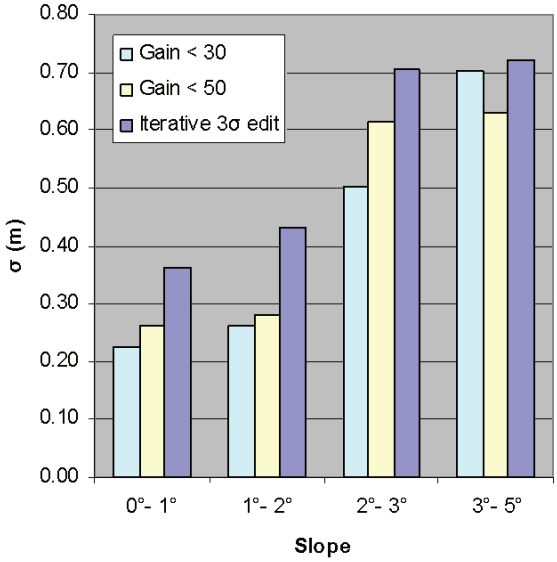

Fig. 15. ICESat precision (σ) as a function of surface slope and detector gain. The precisions were estimated from the RMS of the elevation differences at ~300 crossover points within individual observation campaigns. Outliers were removed through an iterative 3σ edit filter. The estimated precisions include a small residual error due to crossover point interpolation and temporal elevation changes within the observation campaigns (maximum 35 days).

Table 2. Single-shot error budget for ICESat elevation measurements. The table is modified from Zwally et al. (2002b) based on later observational error assessments.

Error source (elevation)	Error (m)	Reference
Range measurement precision	0.02	(Shuman et al., 2006)
Precision orbit determination (POD)	0.02	(Schutz et al., 2005)
Precision attitude determination (PAD)*	0.10	(Martin et al., 2005)
Atmospheric delay	0.02	(Zwally et al., 2002b)
Atmospheric forward scattering	0-1	(Duda et al., 2001)
Detector saturation	0-1	(Fricker et al., 2005)
Others (e.g. tides)	0.01	(Zwally et al., 2002b)
RSS (optimal conditions)	0.11	

* A laser pointing error (PAD) of 2 arcsec (Martin et al., 2005) and an assumed surface slope of 1˚ lead to a horizontal geolocation error of 6 m and an elevation error of 0.10 m.

Satellite positions and attitudes are determined from ground-based satellite laser ranging (SLR) and onboard GPS receivers, star trackers and gyroscopes. The satellite orbit is stable and accurate to within a few centimeters (Table 2). The satellite attitude, or laser pointing direction, oscillates slightly during flight and causes an error in the horizontal positioning of the ground footprint. This induces an elevation error which is proportional to

the tangent of the surface slope. A laser pointing error of 2 arcsec (Martin et al., 2005) yield an elevation error of 0.2-0.3 m for typical Svalbard glacier slopes of 2-3˚. Hence, the dominant error sources for ICESat elevations on Svalbard are laser pointing, detector saturation and forward scattering. The root-sum-squares (RSS) of single-shot elevation errors under optimal conditions is only 0.11 m (Table 2), but the errors can easily reach the meter level in high slopes and cloudy conditions. A lot of data is also lost due to signal absorption in optically thick clouds which are frequent at Svalbard (Fig. 16).

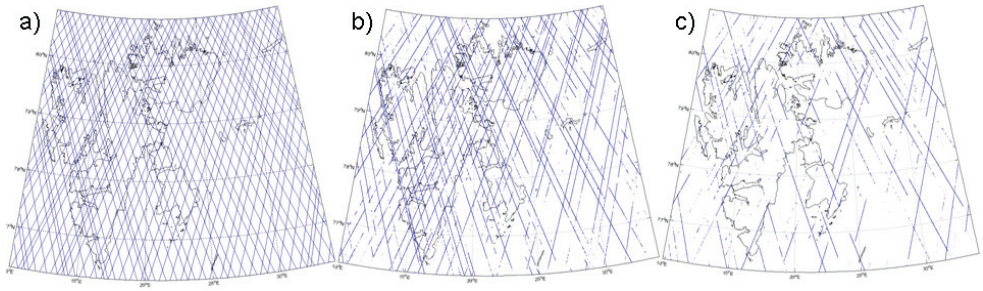

Fig. 16. Spatial coverage of ICESat tracks on Svalbard for (a) an ideal observation campaign with no cloud cover, (b) the fall 2003 campaign with little data loss due to cloud cover, and (c) the summer 2005 campaign where most data were lost in the clouds. The cross-track spacing of ICESat tracks on Svalbard is approximately 15 km.

The ICESat program will continue with ICESat-2 which is scheduled for launch in 2015 (Abdalati et al., 2010). Until then, a series of airborne laser campaigns will be conducted over high priority areas in order to fill some of the observational time gap between the two ICESat missions (Operation IceBridge: http://www.espo.nasa.gov/oib/). ICESat-2 will be of similar characteristics as ICESat-1, though with a slightly smaller footprint size (~50 m) and a slightly denser along-track sampling (~140 m). The same 91-day orbits will be repeated, allowing calculations of decadal elevation changes. Since ICESat-2 is planned to measure continuously, it will achieve a 3 times denser cross-track sampling than the current campaign mode. There are also plans on implementing a cross-track measurement capability to allow a more precise comparison of multitemporal elevation profiles that do not repeat exactly. Such a feature would have made the elevation change analysis in Paper IV much more precise.

4. Methods for elevation change and mass balance

This chapter describes how elevation change and volume change can be estimated from repeated elevation measurements. The general principles and formulas for mass balance determination from elevation changes are outlined in Sect. 4.1. Data processing techniques for calculating elevation change and volume changes follow in Sect. 4.2-4.6. These techniques include both continuous methods (DEM differencing, Sect. 4.2) and discontinuous methods where scattered elevation change data have to be spatially extrapolated in order to estimate volume change (Sect. 4.3-4.6). The sometimes problematical conversion from volume change to mass balance is discussed in Sect. 4.7. Finally, a brief overview is provided about alternative geodetic techniques for determining glacier mass balance (Sect. 4.8-4.9).

4.1. Basic relations between elevation change and mass balance

Before describing methods for determining elevation change and mass balance from geodetic data, it is useful to define the kinematic components of a measured elevation change and the relation with glacier mass balance. Let us first consider the temporal mass change of a fixed vertical ice column from the bed (B) to the surface (S) (Paterson, 1994):

$$\frac{\partial}{\partial t}\int_B^S \rho \, dh = b - \frac{\partial q}{\partial x}\rho \tag{16}$$

where t is the time, ρ is the density, b is the surface mass balance rate, and q is the ice flux along the horizontal flow line x asuming a plane strain. The temporal density distribution is usually not known and is typically assumed to be constant (Bader, 1954; Paper III). This lacking knowledge is the major weakness of mass balance estimates from elevation change measurements. If we assume a constant density similar to that of ice (ρ_{ice}), Eq. 16 becomes:

$$\frac{\partial h}{\partial t}\rho_{ice} = b - \frac{\partial q}{\partial x}\rho_{ice} \tag{17}$$

where h is the ice thickness at time t, and $\partial h/\partial t$ becomes the ice thickness change or equivalently the surface elevation change. A measured elevation change at one spot is hence a combination of surface mass balance and ice flux. If we consider horizontal (in the flow line direction) and vertical velocities at the surface (v_x and v_z), Eq. 17 can be rewritten to:

$$\frac{\partial h}{\partial t}\rho_{ice} = b + \left(v_z - v_x \frac{\partial z}{\partial x}\right)\rho_{ice} \tag{18}$$

where $\partial z/\partial x$ is the surface slope along the flow line, and $v_z - v_x \partial z/\partial x$ is the ice emergence velocity. Glacier emergence is the upward flow of ice relative to the surface at a fixed point in the long-term ablation area, while glacier submergence is the corresponding downward flow in the long-term accumulation area. The transition between submergence and emergence occurs at the long-term equilibrium-line altitude (ELA).

The overall glacier mass balance (B) is found by integrating Eq. 17 over the entire glacier area (A):

$$B = \rho_{ice} \int \frac{\partial h}{\partial t} dA \tag{19}$$

The integral term represents the glacier volume change. The ice flux term in Eq. 17 vanishes since the sum of ice fluxes over a glacier system is zero, i.e. the total submergence above the dynamic ELA is equal to the total emergence below the ELA. Hence, it is feasible to use elevation change data to estimate the overall glacier mass balance (assuming no density changes), but not the specific mass balance at one particular spot unless the ice flux is known (Eq. 17). The glacier-specific mass balance ($\bar{b}$) is found by dividing the overall mass balance (B) with the average glacier area ($\bar{A}$) over the survey period ($t_1 - t_0$):

$$\bar{b} = B/\bar{A} \tag{20}$$

where $\bar{A}$ is typically estimated from the average of the old (t_0) and new (t_1) glacier areas (Arendt et al., 2002) or assumed to be equal to the area of a reference data set of glacier outlines (Papers II-IV). If glacier outlines are only available for the first survey (t_0), then glacier area changes will influence the glacier-specific $\bar{b}$, but not the overall B (Paper III).

For land-terminating glaciers, B and $\bar{b}$ in Eqs. 19-20 are equivalent to the surface mass balance terms B_n and $\bar{b}_n$ in Sect. 2.3. For tidewater glaciers, the relation is more complicated. Eqs. 19-20 are theoretically valid for calving glaciers, with B and $\bar{b}$ equaling the total glacier mass balance including calving and terminus fluctuations. However, due to measurement constraints, it is sometimes necessary to confine the usage of Eq. 19 to the area above the minimum extent of the tidewater terminus (Papers II-IV). This is because detailed sea-bed topography is needed in order to infer ice volume changes in front of the minimum terminus extent. It is also difficult to obtain spatially representative elevation change data from this small area unless continuous measurement techniques are employed. If a separation

is made between interior mass change B_{int} (above the minimum terminus extent) and frontal mass change B_{front} due to terminus fluctuations, the total glacier mass balance B_{tot} becomes:

$$B_{tot} = B_{int} + B_{front} \tag{21}$$

where B_{front} can be found from Eq. 5. Ice-flux calving at a fixed gate (B_{flux}, Eq. 4) is included in B_{int} when the flux gate corresponds to the minimum terminus extent. Paper III uses Eq. 19 over the initial glacier area to obtain the total mass balance, but excludes ice volume changes below sea level which can not be measured with satellite altimetry. Paper II and IV use Eq. 19 to calculate the mass change above the minimum terminus extent (B_{int}) and then apply external estimates of B_{front} (Blaszczyk et al., 2009; Dowdeswell et al., 2008) to estimate the total mass balance. None of the approaches are ideal. The first one ignores ice mass changes below sea level, while the second one uses external data that cover other time spans than the elevation change data. Special terminus considerations are also needed in order to convert the mass balance estimates into sea-level equivalents, more details in Papers II-IV.

4.2. DEM differencing

DEM differencing is a technique where two DEMs acquired at different times are differenced to obtain pixel-wise elevation changes. These pixel values can be summed over the glacier area and multiplied with the ground pixel-size (R^2) to obtain the volume change:

$$\Delta V = R^2 \sum_{glacier} (H_{DEM2} - H_{DEM1}) \tag{22}$$

The main advantage of this technique is the continuous data coverage which eliminates the need for spatial extrapolation techniques like hypsometric averaging (Paper II-IV). However, there is limited availability of multitemporal DEMs, and the accuracy of photogrammetric DEMs is sometimes too coarse for short-term elevation change calculations. The applicability of DEM differencing requires that the DEMs are precisely co-registered and that the DEM elevations are unbiased. Precise DEM co-registration can be achieved with ground-control points (e.g. Kääb, 2008), by 2-dimensional relative shifting to minimize either the RMS of elevation differences (e.g. Howat et al., 2008) or the cosinusoidal dependency between aspect and elevation differences (Nuth and Kääb, 2010). These adjustments should be determined over stable land surfaces to avoid artificial adjustments due to glacier changes. It is also essential to correct for potential vertical biases between the DEMs, either in terms of a

constant shift (e.g. Nuth et al., 2007) or an elevation-dependent correction (e.g. Kääb, 2008). Horizontal and vertical co-registration can also be carried out at once by least-squares matching of the DEMs using a 3-dimensional conformal transformation (Miller et al., 2009). A more detailed discussion about these issues can be found in Nuth and Kääb (2010).

Until recently there have only been a limited amount of multitemporal DEMs available in Svalbard (Etzelmuller et al., 1993a; Fox and Nuttall, 1997). Kohler et al. (2007) differenced photogrammetric DEMs and lidar DEMs for a few selected glaciers in western Spitsbergen to derive a time series of elevation changes indicating an increased glacier thinning over the last few decades. The new era of imaging satellites with stereo capability, i.e. ASTER, SPOT and ALOS, opens up new possibilities for generating multitemporal DEMs which can be differenced against each other or against photogrammetric DEMs from archival stereo imagery (Nuth and Kääb, 2010).

4.3. Point comparisons over a DEM

Paper III compares ICESat point elevations with glacier DEMs that were interpolated from topographic contour maps. The DEM elevations were interpolated to the ICESat footprint locations using bilinear interpolation, a technique that uses linear interpolation between the four closest underlying pixels. Bilinear interpolation yields smoother elevation values than nearest neighbour interpolation which would be an alternative technique. Kohler et al. (2007) differenced airborne laser profiles from 1996/2002 with respect to a 1990 DEM in southern Spitsbergen to derive elevation changes for 1990-1996 and 1990-2002.

4.4. Crossover point comparisons

A crossover point is the location where two elevation profiles intersect each other (Paper II: Fig. 2a). Along-profile interpolation is used to estimate crossover point elevations which are then differenced. Most studies use linear interpolation between the two closest points in each profile to calculate crossover elevations (e.g. Brenner et al., 2007; Papers II-IV), but more sophisticated methods fitting least-squares curves or surfaces to a higher number of along-track points can also be used. Least-squares fitting smoothes the elevation profiles and is particularly suited for noisy profiles with a dense data sampling and a small footprint size. Curved fits will also account for the natural curvature of a smooth surface. We tested several such methods in connection with Papers II-III, but the RMS of crossover

elevation differences between near-coincident profiles did not improve significantly. Hence, we used simple two-point linear interpolation in all final calculations. Paper IV uses elevation differences at crossover points between ascending and descending ICESat tracks. Paper II analyses all kinds of crossovers between elevation profiles from ICESat, laser scanning and GNSS. And Paper III uses crossover points between ICESat and contour lines from topographic maps as an alternative method to point comparisons over a DEM (Sect. 4.3).

4.5. Repeat-track comparisons

An efficient way to determine elevation changes is through repeat measurements of pre-defined survey tracks. However, it is difficult to repeat a kinematic profile exactly. Annual GNSS profiles at Austfonna are typically repeated within a cross-track distance of less than 10 m (Paper II). This introduces a relative elevation difference of less than 0.25 m for an average Austfonna surface slope of 1.4˚. Paper II only compares GNSS points within a 5 m distance, so the slope-induced elevation error should be less than half of that. More accurate elevation change estimates could have been achieved using only crossover points, but that would have limited the spatial sampling of elevation changes.

Airborne laser scanning profiles can be repeated within a few tens of meters. This is usually sufficient to obtain overlapping ground swaths. Hence, densely spaced laser points can be compared in overlapping areas such that the slope-induced error is minimal. Abdalati et al. (2004) used a search radius of 1 m to compare elevation points from two laser campaigns in the Canadian Arctic, while Krabill et al. (2000) fitted 70 m planes to each laser scanning swath on the Greenland ice sheet and then compared the plane elevations of repeated overflights. A similar strategy was used by Thomas et al (2005) to compare 70 m laser scanning planes with ICESat altimetry footprints of approximately the same size.

Repeat-track satellite altimetry data are more difficult to compare since the profiles can be separated by up to several hundred meters. The average cross-track separation between pairs of repeat-tracks on Svalbard was 73 m after removing occasional pairs separated by more than 200 m (Paper IV). This would introduce an average relative elevation difference of 1.8 m for an average Austfonna surface slope of 1.4˚. Hence, it is necessary to correct for the cross-track slope-bias if the data are going to be used to detect short-term elevation changes. The most intuitive way to do that is to use an independent DEM to extract the cross-track topography and project one profile to the location of the other profile (Sect. 4.4.1). A more elegant approach is to use the ICESat data themselves to estimate both cross-track slope and

elevation change. This can be done by means of planes fitted to repeat-tracks (Sect. 4.4.2) or by means of triangulation of selected tracks (Sect. 4.4.3). Although such elevation comparisons are much less accurate than crossover points, they are still very useful since the spatial distribution of data is much better than for crossovers (Papers III-IV).

4.5.1. DEM projection methods

A DEM can be used directly to correct for natural topographic elevation differences between two points separated in space. Most DEMs are too coarse to capture small-scale topographic undulations which also vary with time due to wind drift loading/erosion and glacier movement. We wanted to test if DEM smoothing could improve the local relative accuracy of the DEMs on Svalbard (Paper IV). An iterative low-pass mean filter of increasing pixel size (3×3, 5×5, 7×7 etc.) was applied to each DEM until the improvement of the RMS of along-track ICESat-DEM point-pair differences was less than 5%. It was found that the optimum averaging window size for SPOT5 DEMs in Spitsbergen was about 300×300 m. Hence, it is mainly large-scale, linear topographic variations that can be removed through a DEM projection. Another study at the Greenland ice sheet used a DEM of 1×1 km resolution to correct for the dominating surface slopes around the ICESat tracks (Slobbe et al., 2008). Only overlapping footprints were compared in the analysis in order to minimize the slope-induced errors. This restriction would have been too strict on Svalbard where a lot of data are lost due to clouds. The error analyses in Papers II-IV show that it is more important to have a good spatial distribution of elevation change data than to have the best possible accuracy. The maximum cross-track separation distance for repeat-track elevation comparisons was therefore set as high as 200 m, implying a maximum DEM projection error of 1-4 m depending on glacier region (Paper IV). Due to the large error contribution from DEM projections, we applied a method which performs an initial along-track interpolation to restrict the DEM projection to the cross-track distance between two repeat-tracks (Fig. 2, Paper II). A detailed description and error analysis of the method is found in Papers II and IV.

4.5.2. Plane fitting

Ideally, it should not be necessary to rely on a DEM or other external data to compare near repeat-track satellite altimetry. A set of multitemporal repeat-tracks contain a mixed signal from local topography and elevation changes between overflights. If observations are

grouped, least-squares regression techniques can be used to estimate local surface slopes along with temporal elevation changes. Howat et al. (2008) fitted rectangular planes to segments of repeat-track ICESat data in Greenland to estimate planar surface slopes and an average elevation change rate (dh/dt) for each plane. A similar strategy has been applied in Antarctica to detect elevation changes due to subglacial water drainage (Stearns et al., 2008; Smith et al., 2009). Paper IV assigns all repeat-track ICESat points to 700 m long planes which overlap by 350 m. All data in each plane are then used in a lest-squares analysis to estimate north-slope, east-slope and dh/dt for each plane (Paper IV: Eq. 1). The regression residuals are further used to remove outliers and to estimate short-term elevation changes between the different observation campaigns (Paper IV: Eq. 2). The surface slopes are assumed to be constant for the whole ICESat period (2003-2009).

The elevation change accuracy mainly depends on the number of profiles in the plane and the underlying surface slope and roughness. The plane method yield more precise dh/dt estimates than the DEM method (0.34 m y^{-1} versus 0.48 m y^{-1}) on Svalbard, so all final results in Paper IV were processed with planes only. Although individual elevation change estimates are hardly significant, the errors get reduced with regional averaging since most error sources are of random nature. The success of the plane method implies that it can also be applied to other Arctic regions of similar characteristics where accurate DEMs are typically not available. Work is underway to do a similar analysis in the Canadian and Russian Arctic.

4.5.3. Triangulation

Another approach of using planar surfaces to compare near repeat-tracks is to generate a triangulated irregular network (TIN) between a selection of tracks, and then compare other tracks to this reference surface. Pritchard et al. (2009) fitted triangles between any 3 ICESat measurements within 300 m distance that were acquired within a similar 2-year period (Fig. 17). Potential elevation changes within the 2-year reference period were accounted for by including a temporal component in each triangle such that any location in a triangle is associated with an elevation and a time, both linearly interpolated from the three corner points of the triangle. Overlapping points from earlier or later repeat-tracks were compared directly to the TINs to derive elevation change rates (*dh/dt*) for a range of different time spans which were eventually averaged to derive overall *dh/dt* estimates along each reference track.

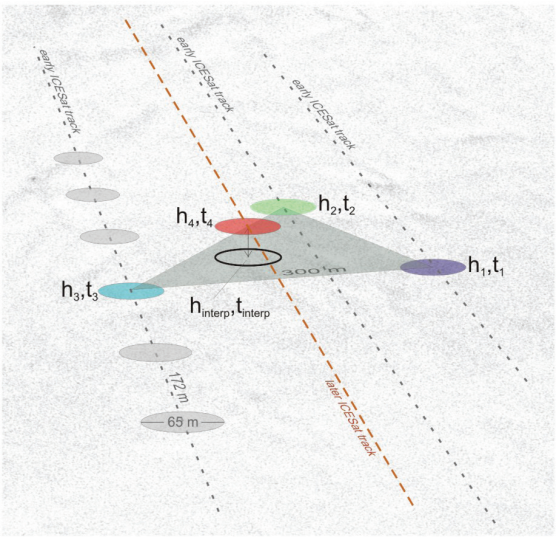

Fig. 17. Comparing an ICESat footprint elevation with a triangular surface spanned by 3 earlier near repeat-tracks (from Pritchard et al., 2009). The 3 triangle points (1-3) are used to linearly interpolate elevation (h_{interp}) and time (t_{interp}) to the same location as the later point (4). Hence, an elevation change rate is found from $dh/dt = (h_4 - h_{interp})/(t_4 - t_{interp})$.

The triangulation method has so far only been applied to Greenland and Antarctica (Pritchard et al., 2009). In regions like Svalbard where seasonal elevation changes are relatively large, each individual *dh/dt* estimate will be very dependent on the seasonality of the 4 points involved in the comparison. For example, if the 3 points spanning a triangle are from ICESat fall campaigns and the 4th point is from a later winter campaign, then the derived *dh/dt* will be positively biased due to the winter snow cover of the latest observation. However, there will be many neighbouring *dh/dt* estimates from different time spans and triangle configurations, so these kinds of errors will be considerably reduced by along-track averaging of *dh/dt*. A weighting scheme according to the length of the *dh/dt* time spans, with higher weights to long time spans, would probably also improve the results. It remains to be tested whether this method can produce *dh/dt* estimates of comparative quality and quantity to the DEM- and plane methods on Svalbard (Paper IV).

Seasonal and temporal analyses of elevation changes are more complicated for the triangulation method since each triangle surface operates in a floating time frame covering the entire period between the earliest and latest observation in the triangle. The time span of a dh/dt comparison is thus not only dependent on the measurement times, but also the location of the overlapping track with respect to the underlying triangle. Elevation change

comparisons at a campaign-to-campaign temporal resolution (Paper IV: Table 1 and Fig. 3) is therefore not possible for the triangulation method.

4.6. Extrapolation of discontinuous data

All elevation change measurements in Papers II-IV are discontinuous point data. Since the goal is to estimate glacier volume change and mass balance, unsampled glacier areas need to be considered. If there is a homogeneous spatial distribution of data, the mean elevation change can be used as an estimate of the area-averaged change which is converted to volume change by multiplying with the total glacier area. Otherwise, it is necessary to apply spatial extrapolation techniques to account for the uneven distribution of data. In the following two sections, we discuss how spatial interpolation and hypsometric averaging can be used to determine glacier volume change from discontinuous elevation change data. The conversion from volume change to mass balance is discussed in Sect. 4.12.

4.6.1. Spatial interpolation

Spatial interpolation is the procedure of estimating values at unsampled sites within an area covered by scattered observations. Here, we use the term to describe the process of interpolating a continuous surface from discontinuous data. It can for example be used to generate DEMs from contour maps (Paper II) or to generate continuous elevation change surfaces from scattered elevation change data (Fig. 18). In the latter case, volume change is estimated by summing all glacier elevation change values and multiplying them with the cell size at the ground (Eq. 22). Spatial interpolation requires a good spatial distribution of data in order to avoid interpolation artifacts. The ICESat data sets in Papers I-IV and Fig. 18 are limited to a few tens of profiles which are too sparse to obtain reliable interpolated surfaces. For that reason, it was necessary to complement the ICESat data with differential SAR interferometry in order to generate a new DEM of Austfonna (Paper I).

The choice of interpolation technique depends on the characteristics of the input data (e.g. points/contours, data density and data uncertainty) and the desired properties of the interpolated surface (e.g. accuracy and smoothness). Kääb (2008) used spline, kriging and inverse-distance-weighting (IDW) algorithms to interpolate continuous elevation change surfaces from elevation change data along contour lines on Edgeøya. He found that the three interpolation methods yielded similar volume change estimates. Nuth et al. (2007) used an

iterative finite-difference interpolation technique (Hutchinson, 1989) for the same purpose in southern Spitsbergen. This technique was also used to generate DEMs from topographic maps in Paper III. A thorough discussion about DEM generation from contour lines can be found in Wise (2000). Kääb (2008) found that it was more accurate to interpolate an elevation change surface from elevation change data along contours than to interpolate a DEM from the contours and then difference it with respect to the other DEM. Paper III acknowledges that elevation comparisons against an interpolated DEM yield a better spatial distribution of elevation change data than comparisons against contours.

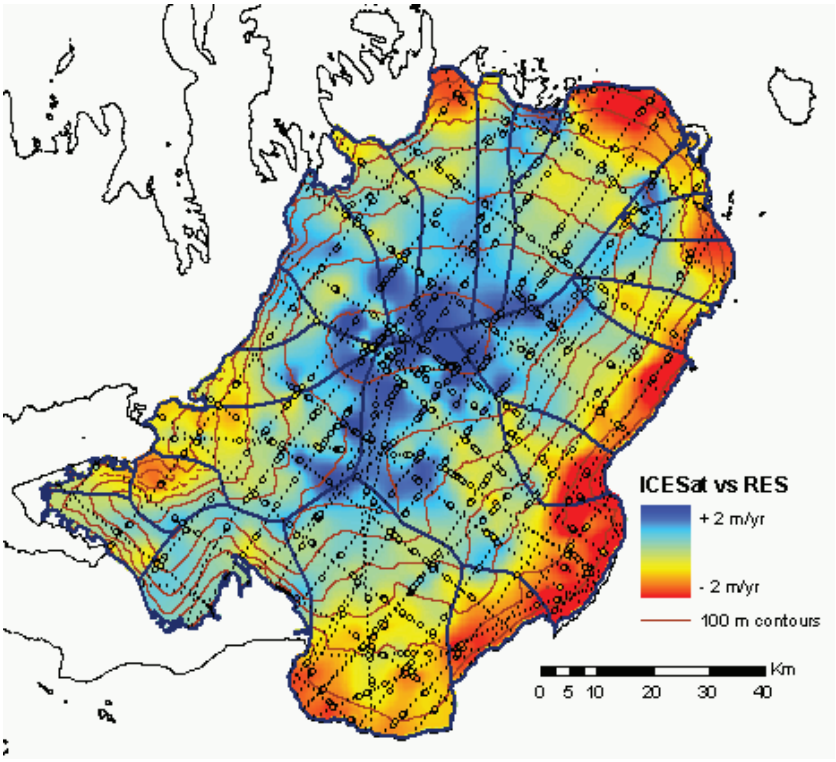

Fig. 18. Interpolated elevation change surface from calculated elevation changes at crossover points (circles) between 2003-2008 ICESat laser altimetry (not shown) and 1983 airborne radio-echo sounding (dotted lines). A minimum curvature spline was used for the spatial interpolation. Note that interpolation artifacts exist in areas with few crossover points and that the results might be biased due to pressure-altitude errors in the 1983 survey (Sect. 5.5.1).

4.6.2. Hypsometric averaging

Due to climate and dynamic factors, there is often a relation between glacier elevation changes and elevation (Papers II-IV). This trend is difficult to account for by spatial interpolation if there is not a good spatial data coverage over most elevation bands (Fig. 18). In such cases, it is better to parameterize elevation changes Δh as a function of elevation z and multiply the function $\Delta h(z)$ with the glacier hypsometry $A(z)$ over the glacier elevations to obtain estimates of volume change ΔV:

$$\Delta \mathrm{V} = \int \Delta h(z)\, A(z)\, dh \tag{23}$$

This is analogous to the hypsometric method in Eq. 2 if the parameterization is done for a fixed number of elevation bins. Paper II uses Eq. 23 over a semi-continuous hypsometry of Austfonna at a height resolution of 1 m (Paper II: Fig. 4), while Papers III-IV uses 50 m elevation bins to calculate regional volume changes. In the case of Austfonna, the choice of hypsometric resolution had no significant impact on the final volume change numbers.

Several different $\Delta h(z)$ parameterizations are in use for hypsometric averaging. The most common approach is to calculate average elevation changes within elevation bins and assume that these average changes are representative for the entire area within the corresponding elevation bin (e.g. Arendt et al., 2002). A laser scanning study in the Canadian Arctic used the median elevation change in each elevation bin since it is less sensitive to outliers (Abdalati et al., 2004). An alternative method is to fit higher order polynomial functions to the relation between elevation change Δh and elevation z:

$$\Delta h(z) = a_0 + \sum_{1}^{n} a_n z^n \tag{24}$$

where n is the order of the polynomial fit. Kääb (2008) chose the polynomial order by increasing it iteratively until the improvement of the RMS to a higher order was below a certain limit. A similar approach was followed in Paper III although subjective judgments were needed in some regions to avoid runaway tails at the edges of the data. Papers II and IV use third order polynomial fits in all regions since the r^2coefficient of determination and the RMS error of the polynomail fits were typically stablilizing after adding the third order coefficient. All these studies found that the resulting volume change would not differ much between different orders of polynomial fits and the mean/median elevation bin methods. An advantage with the polynomial method is that it is smooth and continuous over all glacier elevations, providing elevation change estimates also in elevation bins with no data.

4.7. Conversion from volume change to mass balance

Estimates of glacier volume change are obtained from DEM differencing (Eq. 22) or hypsometric averaging (Eq. 23). Volume change (ΔV) is typically converted to mass balance (B) by assuming that all changes consist of glacier ice at a density of ρ_{ice} (~900 kg m^{-3}):

$$B = \rho_{ice}\,\Delta V \tag{25}$$

This is essentially the same equation as Eq. 19. The assumption of an unchanged density distribution with time (Bader, 1954) is acceptable for long-term mass balance estimates where changes in the firn pack are small in comparison with the overall volume change. This is the case in Paper III where the estimated mass balances are average rates for time spans of 15-40 years. Although the negative mass balance regime has probably caused a decrease of the firn mass, this bias is certainly much smaller than the estimated mass loss of -9.7 ± 0.5 Gt y^{-1} which equals an area-averaged elevation change rate of -0.36 ± 0.02 m w.e. y^{-1}. All previous studies on Svalbard have also used the density of ice to convert from volume change to mass balance (Etzelmuller et al., 1993a; Bamber et al., 2005; Nuth et al., 2007; Kääb, 2008).

Over time spans of less than a decade, fluctuations in firn density and thickness can have a significant impact on the overall mass balance. Eq. 25 is still applicable in the ablation area and the super-imposed ice area (assuming snow-free conditions), but not in the firn area where the density distribution in Eq. 16 might have changed. In a changing firn pack, Eqs. 17-19 are strictly not valid since a glacier can theoretically gain or lose mass even though its volume is not changing. This issue is further complicated by the glacier emergence velocity (Eq. 18). Although the concept of converting volume change to mass balance in the firn area can fail, it is still one of few ways to get a handle on regional mass balances. Detailed data on firn column density changes are rare (Paper III: Fig. 7), so it is usually not possible to integrate density variations with depth like Eq. 16 suggests. Volume to mass conversions over short time spans must therefore rely on nonsteady-state firn-pack modelling (Reeh, 2008) or simple density assumptions based on observed firn pack changes (Papers II and IV).

An elevation change in the firn area can be due to surface mass balance, firn densification and glacier dynamics (Eq. 16). Dynamic elevation changes occur when the submergence is lower or higher than the steady-state condition. Such volume changes can be multiplied with the density of ice (Eq. 25). Annual volume changes due to anomalies in the net surface mass balance are typically consisting of firn at a density (ρ_{firn}) of 400-600 kg m^{-3}. Over multiple years there will always be some degree of densification in underlying firn

layers. Multiyear volume changes should therefore be converted with a slightly higher density than ρ_{firn} if steady-state dynamics is assumed. However, in a cold region like Svalbard a lot of meltwater refreezes within the snow/firn pack and does not contribute towards a negative mass balance. The density conversion factor for negative volume changes in high firn areas can therefore reach zero when steady-state dynamics and complete refreezing is assumed.

The main problem with the above assumptions is that it is often not possible to distinguish between dynamic elevation changes and elevation changes due to surface mass balance and firn densification. Many glaciers on Svalbard are for example dynamically thickening at the higher elevations due to low emergence velocities in the quiescent phase of a surge cycle. All these factors make it very hard to determine the best suitable density conversion factors for volume changes in the firn area. The chosen densities should be justified from observational data on the firn pack evolution. Annual glacier facies maps from satellite scatterometer images (Wolken et al., 2009) would be a useful tool for constraining the density conversion factors, but no such analysis has been done on Svalbard yet. Satellite imagery, surface mass balance measurements and ground-penetrating radar profiles show that the firn area on Svalbard expanded over the ICESat period between 2003 and 2009 (Dunse et al., 2009; Paper IV). Hence, it is likely that the total firn volume increased over these years. This would cause a positive mass balance bias if ρ_{ice} was used to convert from volume change to mass change. Based on this knowledge, several density scenarios were applied to the elevation change curves in Papers II and IV. The resulting upper and lower mass balance estimates were used as error bounds, while the mid-points of the ranges were used as the final mass balance estimates. The estimated mass balance conversion error was ±0.02 m w.e. y^{-1}. The surprisingly low error is possible because most of the changes occur below the firn area.

4.8. Mass balance fluxes from surface velocities

Glacier mass redistribution can be inferred from measurements of glacier movement. A glacier in dynamic equilibrium will have an ice flux across the equilibrium-line altitude (ELA) which is similar to the annual surface mass balance rate in the accumulation area. Surge-type glaciers in their quiescent phase have typically a lower velocity across the ELA than the balance velocity, and they are hence building up in the accumulation area. Bevan et al. (2007) used differential SAR interferometry to estimate surface velocities across the ELA at Austfonna. The ice flux across the ELA was then calculated from the velocities in combination with ice thicknesses obtained from airborne radio-echo sounding (Dowdeswell,

1986). A theoretical balance flux was estimated from the average annual surface mass balance above the ELA between 1986 and 1998/99 (Pinglot et al., 2001). The difference between the measured flux and the balance flux at the ELA yield the mass balance of the accumulation area. The results indicate that most glacier basins at Austfonna have experienced interior thickening during the last few decades. Average thickening rates of up to 0.3 m w.e. y^{-1} are consistent with elevation change data from 1996-2002 airborne laser altimetry (Bamber et al., 2004) and from 2002-2008 GNSS profiling, laser scanning and ICESat (Paper II).

Ice flux considerations can only say something about the dynamic state of a glacier. Elevation changes can be derived if the surface mass balance is known, and in the opposite case; surface mass balance can be derived if the elevation changes are known. The only ice flux that is relevant to the overall glacier mass balance is the iceberg calving flux. All other fluxes are only redistributing mass within the glacier system.

4.9. Gravity and surface deformation measurements

The gravity field at the Earth's surface varies with tides, hydrology, land uplift/ subsidence, ocean loading, atmospheric loading and changes in the cryosphere. If glacier gravity changes can be isolated from other factors, then gravimetric measurements can be used to derive glacier mass balance. Gravity is directly linked with mass, so there is no need for additional density information like for elevation changes (Eq. 16). Attempts have been made use ground-based gravimetry to measure local glacier mass changes (Breili and Rolstad, 2009). Larger scale mass changes can be measured from airborne- or spaceborne gravimetry. The Gravity Recovery and Climate Experiment (GRACE) satellite has provided monthly global spherical harmonic gravity fields since 2002. It has been used to estimate mass changes in Antarctica (e.g. Chen et al., 2009), Greenland (e.g. Wouters et al., 2008), Patagonia (Chen et al., 2007) and Alaska (Luthcke et al., 2008). The primary limitation of GRACE is that it can not provide finer spatial resolutions than a few hundred kilometers, and that it is particularly sensitive to post-glacial rebound (Velicogna and Wahr, 2006). So far, there have been no dedicated GRACE studies on Svalbard, but Wouters et al. (2008) estimated a mass change of -8.8 ± 3 Gt y^{-1} between Feb. 2003 and Jan. 2008 for a basin that covers Svalbard.

Changes in mass loading from glaciers cause deformation of underlying and surrounding land surfaces. There are both long-term deformations from post-glacial rebound and short-term deformations caused by mass redistributions and surface mass balance fluctuations. The ground uplift in the Ny-Ålesund area on Svalbard has been precisely

measured by a permanent GNSS/VLBI station and annual GNSS campaigns over a network of survey sites (Kierulf et al., 2009). The measured uplifts rates are several times larger than those predicted by post-glacial rebound models. This is probably due to present-day ice melting in the region. Ice-loading models were forced by annual surface mass balance data from surrounding glaciers to predict the additional uplift at each site. The model predictions correlated well with observations both with respect to interannual variations and spatial patterns. Hence, variations in surface deformation can be a useful proxy for regional glacier mass balance. Crustal uplift can also be measured by SAR interferometry, an approach that has been used to constrain glacier mass changes in Greenland (Liu et al., Subm.).

5. Summary of papers

This chapter provides a brief summary of the papers and some auxiliary material that was not included in the published versions. All papers are discussed at once since they relate well to each other. Summaries of individual papers can be found in the paper abstracts.

5.1. Study areas

Papers I and II concern the Austfonna ice cap (7800 km^2) which is the main target glacier for this thesis and the place where annual spring field campaigns have been carried out since 2004. Austfonna contains 30-40 % of all ice masses on Svalbard and differs from most other Svalbard glaciers and ice caps in terms of geometry, climate and dynamics. The ice cap has a simple dome-shaped geometry which feeds a number of drainage basins (Paper I: Fig. 1). Its large extent and gentle slopes make it an ideal test site for ICESat laser altimetry. Glacier velocities are typically less than 10 m y^{-1} although a few fast-flowing units exist (Dowdeswell et al., 2008; Strozzi et al., 2008). Surge advances have been reported for three of the basins prior to 1940 (Lefauconnier and Hagen, 1991). The ~230 km long tidewater fronts are in a steady phase of retreat, resulting in an annual mass loss of about 1.4 Gt y^{-1} (Dowdeswell et al., 2008). There is a pronounced accumulation gradient across Austfonna, with most snow accumulating in the southeast close to the main moisture source in the Barents Sea (e.g. Taurisano et al., 2007). The average net surface mass balance in the summit area has been estimated to 0.5 m w.e. y^{-1} from ice cores spanning 1986-1998/99 (Pinglot et al., 2001). Summit thickening rates of a similar magnitude have been observed by airborne laser scanning in 1996 and 2002 (Bamber et al., 2004).

Paper III covers all Svalbard glaciers apart from Austfonna and Kvitøya which lack accurate topographic maps from earlier times. The ICESat analysis in Paper IV includes the entire glaciated area on Svalbard (34600 km^2) although not all glaciers are covered by actual observations. The glaciers and icefields of the Spitsbergen island are generally steeper and more alpine than the gentle ice caps of the eastern islands. This is a challenge for elevation change analyses since the ICESat performance degrades in sloping terrain. Long-term surface mass balance records from western Spitsbergen indicate a negative mass balance regime since at least the mid 1960s (Hagen et al., 2003b). Comparisons of photogrammetric maps/DEMs, dating back to 1936, show substantial decreases of glacier area and volume (Nuth et al., 2007)

with enhanced thinning rates after 1990 when compared to airborne laser scannings in 1996 and 2002 (Bamber et al., 2005; Kohler et al., 2007). Overall mass balance estimates from northeastern Svalbard are largely lacking, but Hagen et al. (2003b) suggest that these glaciers and ice caps are closer to balance than the negative western glaciers. The mass loss due to a general tidewater front retreat has been estimated to 2.3 ± 0.8 Gt y^{-1} (Blaszczyk et al., 2009).

5.2. Data sets

The most detailed topographic mapping of Austfonna was done in 1983 by airborne radio-echo sounding (RES) (Dowdeswell et al., 1986). These data were a large improvement from previous incomplete photogrammetric mappings, and the RES profiles were used as tie points for remote sensing DEMs (Bingham and Rees, 1999; Unwin and Wingham, 1997). However, recent elevation measurements show that the RES-tied DEMs are systematically too low in the summit area and too high in the terminus area by up to 50 m. This was the background for constructing a new and more up-to-date DEM (Paper I). Photogrammetry is difficult to apply to Austfonna due to the large featureless firn area and the lack of ground control along the extensive tidewater fronts. Therefore, we chose to use SAR interferometry (InSAR) in combination with ICESat laser altimetry to generate a new DEM. Differential InSAR provides a continuous topographic surface with a good relative accuracy, but it lacks an absolute reference. ICESat altimetry has the opposite properties; it has a very good absolute accuracy, but the spatial coverage is limited to profiles which are separated by around 15 km (Paper I: Fig. 3). ICESat point elevations are therefore used as ground control in the interferometric DEM. Winter SAR scenes were obtained from the 1-day tandem phase of the ERS satellites in 1996. Newer SAR data have unfortunately too long repeat times to allow coherent interferometric processing over rapidly changing glacier surfaces.

The idea in Paper II was initially to calculate elevation changes between the 1983 RES data and the 2003-2009 ICESat data. However, the derived elevation changes were unexpectedly large with thickening rates of up to 2 m y^{-1} in the summit area (Fig. 18). We therefore investigated the possibility of systematic errors in the 1983 pressure altimeter readings due local pressure anomalies (Sect. 5.5.1). Pressure anomalies of up to ~3 hPa were found between the coast and the summit during the 2008 field campaign. This would translate to an elevation underestimation of 20-30 m in the summit area during the 1983 survey. In order to eliminate this potential bias, we chose to compare ice thicknesses between the 1983 RES survey and a similar 2007 RES survey instead (Paper II: Fig. 1d).

Paper III compares ICESat altimetry with topographic maps and DEMs. The topographic maps and glacier outlines were constructed by the Norwegian Polar institute on analog stereoplotters using aerial imagery from 1965, 1966, 1971 and 1990 depending on region. The maps were produced in scale 1:100 000 with a contour interval of 50 m (NPI, 2010a). A digital photogrammetric DEM from 1990 imagery was used in southern Spitsbergen. ICESat GLA06 data was at that point available for all campaigns between 2003 and 2007 in Release 28 (Table 1). The investigated time spans between the NPI maps/DEMs (1965-1990) and ICESat (2003-2007) were thus varying from region to region.

Papers II and IV both use repeat-track ICESat data to calculate elevation changes within the 2003-2008 period. A set of reference tracks is repeated in each observation campaign (Table 1), but they do not repeat exactly and a lot of data are also lost due to clouds. The average cross-track separation between pairs of repeat-track profiles on Svalbard is 73 m when removing occasional repeat-track pairs separated by more than 200 m. Paper IV only compares ICESat data, while Paper II also uses repeated GNSS surface profiles and airborne laser altimetry from within the 2002-2008 period. These data are more precise than ICESat, but their spatial distribution is limited (Paper II: Fig. 1). Both papers use glacier DEMs for cross-track slope correction and hypsometric averaging. The InSAR/ICESat DEM (Paper I) was used at Austfonna, while new SPOT5 DEMs from 2007/08 were used for most of Spitsbergen (Fig. 8). New glacier outlines were digitized from SPOT5 and Landsat imagery (NPI, 2010b), yielding a total glacier area of 34600 km^2 which is less than the 36000 km^2 area from the last glacier inventory of Svalbard (Hagen et al., 1993).

Coincident winter and summer surface mass balance estimates from in-situ measurements were included in Papers II and IV. The records are from Austfonna, Kongsvegen (northwestern Spitsbergen) and Hansbreen (southern Spitsbergen), covering the 2004-2008 mass balance years (Paper II: Figs. 5-6 and Paper IV: Fig. 3). The data from Kongsvegen and Hansbreen were externally processed, while the Austfonna results were calculated from stake and snow pit measurements in field campaigns between 2004 and 2009.

5.3. Methods

The new Austfonna DEM in Paper I was made from SAR interferometry with ground control from ICESat laser altimetry. Differential InSAR was performed in order to remove the influence from glacier movement in the interferogram. The resulting topographic interferogram was unwrapped and transformed to absolute elevations by means of ICESat.

The interferometric baseline was precisely refined using a full set of ICESat profiles as ground control points. The DEM was produced in the WGS84 datum with one version containing ellipsoidal heights and one version containing orthometric heights referenced to the EGM2008 geoid model. Existing drainage basin outlines for Austfonna were updated according to the new topography, and ice cap outlines were digitized from an orthorectified SPOT-5 2008 scene (Korona et al., 2009).

Paper III uses three methods to compare ICESat to existing topographic maps and DEMs. Method 1 compares contour elevations to overlapping ICESat footprints (~70 m diameter), while method 2 performs linear interpolation between the two closest footprints to compare elevations at the crossover point between an ICESat track and a contour line. Method 3 uses an iterative finite difference interpolation technique (Hutchinson, 1989) to generate continuous DEMs from the contour lines. All ICESat data can then be compared with the interpolated DEMs using bilinear interpolation to extract DEM elevations to the ICESat footprint center. Method 2 was found to be the most precise one, but method 3 was used in the final calculations since it provides the best spatial distribution of data. Regional volume changes were estimated by multiplying the polynomial fits (Eq. 24) in 50 m elevation bins with the corresponding glacier hypsometry (Eq. 2). The firn mass was assumed to be constant such that the density of ice could be used to convert into mass balance (Eq. 25).

Papers II and IV compare surface elevation profiles at crossover points and along repeated tracks. Along-track linear interpolation is used to compare elevations at crossover points (Paper II: Fig. 2a). Paper II compares all kinds of crossover points within and between GNSS, airborne lidar and ICESat, while Paper IV relies on ICESat data only. Repeat-track GNSS profiles are compared directly at neighbour points whenever two profiles are within 5 m of each other. Repeat-track ICESat profiles are not precisely repeated, so the cross-track slope between the profiles needs to be corrected. A DEM projection method was applied in both papers to project one profile to the location of the other profile by means of the cross-track elevation difference in the DEM (Paper II: Fig. 2b). More precise along-track interpolation can then be used to compare elevations at individual footprints. Paper IV also tested an alternative repeat-track method which uses all ICESat data in a joint analysis where surface slope and elevation change are estimated for 700 m long least-squares planes that are fitted to the data along each track (Paper IV: Fig. 4c). These methods produce elevation change estimates for many different time spans within the 2002-2008 time period. In order to derive consistent elevation change rates, we only compared data between similar seasons (i.e. winter-winter, summer-summer, fall-fall) and over time spans of minimum 2 years (Paper IV)

or 3 years (Paper II). The resulting elevation change points were then averaged within clusters with a diameter of 350 m (Paper II) and 2 km (Paper IV) to obtain representative elevation change rates for the whole observation period. Volume changes were then calculated at a regional scale using third order polynomial fits (Eq. 24) over the glacier hypsometries (Eq. 2). The firn pack on Svalbard may have changed considerably over the 2002-2008 period, so several density assumptions were tested in order to derive a range of possible mass balances.

Seasonal and annual surface mass balances for Austfonna were calculated by fitting second order polynomial curves to the specific balances of the stakes (Paper II: Fig. 5) and multiplying with the glacier basin hypsometry (Eq. 2). Average surface mass balance rates were calculated separately for the southern and northern basins, while seasonal surface mass balances were only calculated for the Eton-/Winsnesbreen basin which has been measured each year. The surface mass balance records of Kongsvegen and Hansbreen in Paper IV were externally provided. The three surface mass balance records were used to validate a seasonal time series of area-averaged ICESat elevation changes (Paper IV: Table 2 and Fig. 3).

5.4. Results

The new Austfonna DEM and glacier basin outlines from Paper I are freely accessible through the IPY GLACIODYN project. The quality of the DEM was evaluated using ICESat ground control points and independent surface profiles from GNSS and airborne laser altimetry in 2007. The relation between ICESat elevations and unwrapped phases was greatly improved after refining the DInSAR baseline with ICESat. The RMS error of the DEM is about 10 m both with respect to ICESat and independent GNSS and airborne lidar. The largest error source in the DEM is residual elevation changes between the SAR and ICESat acquisitions in 1996 and 2006-2008. This causes a elevation-dependent bias in the DEM which is non-linear and hence can not be captured in the baseline refinement (Paper I: Fig. 4).

Paper II found that repeat-track ICESat altimetry yield consistent results with more precise elevation change calculations from crossover points and repeat GNSS profiling (Paper II: Fig. 3a). In fact, the good spatial distribution of ICESat data help to reduce the extrapolation error associated with volume change calculations. The clustered elevation change rates show that Austfonna has thickened at high elevations and thinned at low elevations between 2002 and 2008. This pattern is consistent with airborne laser altimetry from 1996-2002 (Bamber et al., 2004) and ice-thickness changes between 1983 and 2007 (Paper II: Fig. 3d). There is no significant difference between surge-type basins and other

basins which are not known to have surged (Paper II: Fig. 3b). Other basins at Austfonna might also be capable of surging in the future if the current surface steepening trend continuous. Southern basins are thickening more than northern basins (Paper II: Fig. 3c), probably reflecting the southeast to northwest accumulation gradient across Austfonna (e.g. Taurisano et al., 2007). The mean mass balance for 2002-2008 is estimated to -1.3 ± 0.5 Gt y^{-1} (or -0.16 ± 0.06 m w.e. y^{-1}) when accounting for a marine retreat loss of -1.4 ± 0.4 Gt y^{-1} (Dowdeswell et al., 2008). In-situ measurements of 2004-2008 surface mass balance indicate a slightly positive balance of 0.05-0.12 m w.e. y^{-1} depending on whether refreezing below the annual layer is assumed or not in the firn area. If iceberg calving is accounted for, the estimated overall mass balance becomes slightly more negative than for the geodetic data.

Paper III shows that ICESat laser altimetry is also a valuable data set for determining elevation changes with respect to historical topographic maps and DEMs, especially if no recent DEMs are available. Reliable volume changes can be obtained at a regional scale (Paper III: Table 2), but typically not for individual glaciers since the spatial distribution of ICESat profiles is limited (Paper III: Fig. 5). The average Svalbard mass balance, excluding Austfonna and Kvitøya, for the period between 1965-1990 and 2003-2007 is estimated to -9.71 ± 0.55 Gt y^{-1} (or -0.36 ± 0.02 m w.e. y^{-1}) which corresponds to a global sea level rise of 0.026 mm y^{-1}. The most negative area-averaged mass balance was found in the Southern Spitsbergen region followed by Barents-/Edgeøya and Northwestern Spitsbergen. Vestfonna was close to balance between 1990 and 2005. Several glacier surges can be observed in the data set, characterized by high elevation thinning and low elevation thickening (Paper III: Fig. 5). Otherwise, the general trend is thinning at low elevations combined with slight thinning or thickening at high elevations (Paper III: Fig. 5).

Paper IV applies ICESat repeat-track analysis to the entire Svalbard. In addition to the DEM projection method in Paper II, we tested a least-squares technique which fits rectangular planes to the data along each track and estimates surface slope and elevation change rate for each plane. The DEM method and the plane method yield similar results (Paper IV: Fig. 5), but the plane method is slightly more precise as compared to crossover points (Paper IV: Fig. 6). The main advantage of the plane method is however that it does not require any external data to account for the cross-track slope. The results show a general pattern of low-elevation thinning combined with high-elevation balance (in the south and west) or thickening (in the northeast). Such changes are typical for slow-moving glaciers in their quiescent phase of a surge cycle. The seasonal analysis reveals that the western and southern regions have a larger mass turnover than the northeastern regions, characterized by more thickening during winter

(0.62-0.87 vs. 0.30-0.61 m) and more thinning during summer (0.87-1.09 vs. 0.40-0.55 m) (Paper IV: Table 2). The large summer thinning in the west and south is probably the main reason for the spatial gradient in mass balance from negative rates in the south/west to slightly positive rates in Northeastern Spitsbergen and at Austfonna. This pattern is consistent with Paper III although the recent change rates are significantly less negative than in the previous few decades. The average Svalbard mass balance for 2003-2008 is estimated to -4.3 ± 1.4 Gt y^{-1} (or -0.12 ± 0.04 m w.e. y^{-1}). Tidewater front fluctuations may account for an additional mass loss of 2.3 ± 0.8 Gt y^{-1} (Blaszczyk et al., 2009). The spatial and temporal trends in the area-averaged ICESat elevation changes are consistent with surface mass balance records from Kongsvegen, Hansbreen and Austfonna (Paper IV: Fig. 3).

5.5. Auxiliary material to the papers

The following subsections include some auxiliary material that is relevant to the papers although it was not included in the published versions.

5.5.1. Basic relations and assumptions for error analysis (Papers I-IV)

In error analysis it is common to separate between accuracy and precision. *Accuracy* is the closeness of a measurement to its true value. It is ideally determined by independent external measurements of the same quantity although this is not always possible. *Precision* is the repeatability of measurements and can be determined from repeated measurements of the same quantity under unchanged conditions. For example, ICESat elevation measurements have an accuracy of about 10 cm with respect to a global reference frame, while the shot-to-shot elevation precision is only a few centimeters (Table 2). This difference is because accuracy accounts for time-correlated systematic errors (e.g. satellite orbit, laser pointing and atmospheric delay), while precision only considers random measurement noise. Most repeated elevation measurements are gradually decorrelating with time, so it is not always easy to distinguish between accuracy and precision.

The *standard deviation* (s) of a normally distributed sample of measurements (x) is:

$$s = \sqrt{\frac{1}{n}\sum_{i=1}^{n}(x_i - \bar{x})^2} \tag{26}$$

where n is the number of measurements (often $n-1$ is used to account for the degrees of freedom), and $\bar{x}$ is the average value of the measurements. Sometimes, we are interested in the deviation with respect to a given or estimated value (a) rather than the measurement mean. This is the basis for the root mean square (*RMS*) error:

$$RMS = \sqrt{\frac{1}{n}\sum_{i=1}^{n}(x_i - a_i)^2} \tag{27}$$

The main difference between the two statistical measures is that RMS includes the mean bias, while standard deviation does not. Both quantities are sensitive to outlier measurements, e.g. cloud reflections in an ICESat data set. An alternative measure of the spread of a data set is the interquartile range (*IQR*). It is the range of the middle 50 % of the measurement values. The IQR is slightly higher than the standard deviation for a normally distributed sample, but it becomes lower when gross errors are present. Paper II uses the IQR for data sets that contain outliers, while Papers III and IV use a filter to remove observations that deviate by more than 3 times the standard deviation (or RMS). The filter is run iteratively until the standard deviation (or RMS) converges below a certain threshold, e.g. 5 %.

The standard deviation, RMS and IQR yield the average error of a single measurement with respect to the mean ($\bar{x}$) or a reference value (a_i). If the purpose of the measurements is to estimate the parameter $\bar{x}$ or a_i, then the error of the parameter decreases with an increasing number of measurements. The *standard error* (SE) of the estimated parameter is:

$$SE = \frac{\sigma}{\sqrt{f}} \tag{28}$$

where σ refers to the standard deviation, IQR or RMS, and f is the degrees of freedom of the parameter. The degrees of freedom equal the total number of measurements (n) minus the number of measurements needed to estimate the parameter. For example, the degrees of freedom for estimating $\bar{x}$ in Eq. 26 are $n-1$, while the degrees of freedom for a third order polynomial fit in Eq. 24 are $n-4$ (Papers II and IV).

If all measurements in Eqs. 26-28 are correlated, one obtains the precision. The accuracy is obtained if the measurements are uncorrelated. In elevation change analysis, we are mainly interested in the accuracy of a single-point elevation change and the accuracy of the overall volume change and mass balance. This requires simplified assumptions about measurement correlations. Papers II and IV estimate the accuracy of single repeat-track ICESat elevation changes by comparing them with crossover points which are assumed to be

uncorrelated. In reality, they are not perfectly uncorrelated since one of the profiles is typically shared between the repeat-tracks and the crossover point. However, the accuracy estimate also includes some residual uncertainty due to spatial and temporal variations in elevation change between the two estimates, so the estimated accuracy estimate should still be realistic. Along-track ICESat elevation changes are correlated due to the point-to-point similarity in surface topography, satellite orbit, laser pointing and atmosphere. These factors are gradually decorrelating with time, so in order to estimate accuracy, it is necessary to make assumptions about the spatial scale of autocorrelation. Paper III assumes that ICESat measurements along a profile are correlated within each 50 m elevation bin, but not between the bins. Paper IV uses an along-track ICESat correlation length of 5 km, while Paper II averages all elevation change measurements into 2 km clusters which are assumed to be uncorrelated. The degrees of freedom in Eq. 28 are then determined from the calculated number of uncorrelated observations. Although the assumptions about spatial autocorrelation are rather subjective, they still produce error estimates with a good relative consistency.

Independent errors of the same quantity can be combined as root-sum-squares (*RSS*):

$$\sigma_{RSS}{}^2 = \sqrt{\sum_{i=1}^{n} \sigma_i{}^2} \tag{29}$$

where n is the number of independent errors σ. This relation can be used to estimate the overall mass balance error from the independent error contributions of the observations, the spatial extrapolation, the density conversion and the tidewater front fluctuations (Paper II).

5.5.2. Potential systematic errors in pressure altimeter altitudes (Paper II)

An attempt was made to compare the 1983 radio-echo sounding (RES) profiles (Dowdeswell et al., 1986) with recent elevation data from GNSS surface profiles, airborne laser altimetry and ICESat laser altimetry (Fig. 18). Such an analysis requires a good knowledge about potential systematic errors in the data sets. No clear elevation bias was found in the RES data over land surfaces with respect to existing DEMs and ICESat crossovers. This is no surprise since the RES instrument was frequently calibrated over sea level during the survey and most land surfaces are at low elevations. Potential errors in the aircraft pressure altimeter due to temporal pressure variations would also be largely removed by these calibrations. However, one can not exclude the possibility of pressure altimeter

biases due to local pressure fields over the ice cap. The local pressure anomaly (Δp) with respect to a homogeneous pressure field can be calculated from the barometric formula:

$$\Delta p = p_0 \left(\frac{t_0}{t_0 - L(h_1 - h_0)} \right)^{\frac{gM}{RL}} - p_1 \tag{30}$$

where h, t and p refers to the elevation (m), temperature (K) and pressure (kPa) at two stations (0 and 1) separated in space, L is the temperature lapse rate between the two stations (K m^{-1}), g is the gravity (9.807 m s^{-2}), M is the molar mass of air (0.02897 kg mol^{-1}) and R is the universal gas constant for air (8.314 N m mol^{-1} K^{-1}). Such a pressure anomaly will introduce a barometric height error (Δh) in a temperature-corrected pressure altimeter:

$$\Delta h = h_0 - \frac{t_0}{L} \left(1 - \left(\frac{p_1}{p_0} \right)^{-\frac{RL}{gM}} \right) - h_1 \tag{31}$$

A simple field experiment was carried out in spring 2008 to test the relative stability of the air pressure at Austfonna with respect to a coastal weather station to the north of the ice cap. Air pressure and temperature were logged at both sites and used to calculate the summit pressure anomaly (Eq. 30) and the corresponding barometric height error (Eq. 31). Mean sea level pressure values from ERA-40 reanalysis data were interpolated to the same sites and used to calculate comparable barometric height errors (Fig. 19). The spatial resolution of ERA-40 is too coarse to capture local pressure fields over a few tens of kilometers, but it gives a good indication of typical horizontal pressure gradients across the ice cap. The barometric height error between the two sites for ERA-40 varies within ~15 m, while the meteorological readings show a larger variation. A positive pressure anomaly of up to 0.1-0.3 kPa was registered at the summit between April 26 and May 30, corresponding to a negative barometric height error of 10-30 m (Fig. 19). This occurred after a marked pressure increase of ~2 kPa combined with a weather transition from stormy and cloudy conditions ("camp weather") to calm and clear conditions ("work weather"). The 5-day pressure anomaly started and ended with a sharp temperature peak close to 0 ˚C at the coastal station with stable temperatures between -10 and -15 ˚C in the intermediate and subsequent period.

The weather during the RES campaign in April 23-28 1983 was characterized by high sea level pressures (102-104 kPa), low temperatures (-10 to -20 ˚C), calm winds and clear weather (ERA-40 / T. Eiken, pers. com.). Hence, it is not unlikely that a similar local pressure anomaly to spring 2008 was present at the summit during the survey. A negative elevation bias of a few tens of meters could therefore be present in the 1983 surface elevations in the summit region. This might explain the extreme elevation differences between the 1983 data

set and recent elevation measurements. Some of the elevation differences in Fig. 18 are definitively due to interior thickening and peripheral thinning, but the exact amount can not be quantified. This uncertainty was the background for comparing ice thickness changes at crossover points between RES profiles in 1983 and 2007 instead (Paper II). Ice thickness measurements are not influenced by potential pressure altitude biases since they are determined from the time delay time between the surface and bedrock echoes, assuming a signal propagation velocity of 169 m μs^{-1} for ice (Kristensen et al., 2008). Unfortunately, there are much fewer crossover points between ice thickness profiles (Paper II: Fig. 1d) than surface elevation profiles (Fig. 18), and the precision of ice thickness measurements is also lower than that of surface elevation measurements. It was therefore not justifiable to estimate volume change and mass balance for the period between 1983 and 2003-2008 in Paper II.

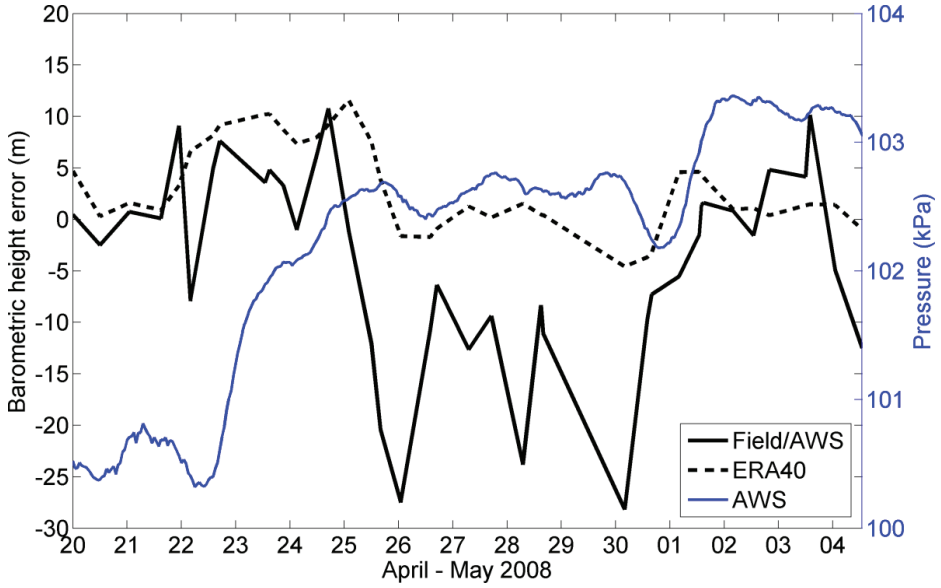

Fig. 19. Potential pressure altitude errors during the spring 2008 field campaign at Austfonna. Temperature and air pressure were logged several times a day at the summit camp while an automatic weather station (AWS) at sea level in Rijpfjorden (45 km northwest of the summit) was recording hourly temperature and air pressure (blue line). These data were then used to calculate the barometric height of the summit. The difference with respect to the true summit elevation yields the barometric height error (solid black line). A similar calculation was done using interpolated pressure values from ERA-40 reanalysis data (dotted line).

The aircraft positioning in 1983 relied on a ranging system to four ground-based transponders. Three of the transponders were precisely positioned to ±2 m using satellite Doppler geoceivers. Two geoceiver locations were re-measured with GNSS in 2008, yielding

elevation changes of +10 m close to the summit and -12.5 m at 200 m elevation in Basin 3. This corresponds to average elevation change rates of +0.4 m y^{-1} and -0.5 m y^{-1} which fit well with the rough trend between 1983 and 2007 (Paper II: Fig. 3d) and the more precise data from 1996-2002 (Bamber et al., 2004) and 2002-2008 (Paper II: Fig. 3a). The recent interior thickening is thus probably a part of a long term trend related to quiescent glacier dynamics rather than precipitation increase. The net surface mass balance in the summit area is also consistent between 1986-1998/99 (Pinglot et al., 2001) and 2004-2008 (Paper II: Fig. 5).

5.5.3. Glacier emergence velocities at Austfonna (Paper II)

Glacier submergence or emergence is the downward or upward flow of ice relative to the surface at a fixed point on a glacier. Ice submerges in the long-term accumulation area and emerges in the long-term ablation area, with the transition from submergence to emergence occurring at the long-term ELA. The emergence velocity is given by (Paterson, 1994):

$$v = v_z - v_x \frac{\partial z}{\partial x} \tag{32}$$

where v_x is the horizontal velocity in the flow line direction, v_z is the vertical velocity at the surface, and $\partial z/\partial x$ is the surface slope. The mass balance stakes at Austfonna have been measured with differential static GNSS (over at least 5 min) in each spring field campaign since 2004. These data can be used to estimate the annual movement of the stakes and hence the horizontal and vertical velocity components (v_x and v_z). The surface slope ($\partial z/\partial x$) along the movement path of a stake can be estimated from repeated GNSS profiles which follow the stake transects, although not always directly in the direction. The resulting uncertainty of GNSS-derived emergence velocities is in the order of a few decimeters, with the best results being achieved in areas low-slope areas (< 1˚) with slow horizontal velocities (< 10 m y^{-1}). Fig. 20 shows the estimated emergence velocities at stake locations on Austfonna.

Elevation changes on a glacier occur when the emergence/submergence does not counterbalance the specific surface mass balance (Eq. 18). Paper II concluded that ice emergence/submergence plays a minor role in the observed elevation changes at Austfonna since the elevation change curves are almost similar to the surface mass balance curves (Paper II: Fig. 5). Later calculations of emergence velocities from GNSS measurements at stakes show that there is actually a significant vertical ice flux component at Austfonna, even in surge-type basins like Etonbreen and Bråsvellbreen (Fig. 20). The imbalance between elevation change, surface mass balance and emergence/submergence indicates that at least

one of the data sets contain a systematic error. The emergence velocities in the firn area could be overestimated (too negative) if the stakes were sinking down in the firn from year to year. This would however cause a similar overestimation of the surface mass balance (too positive), so that the mismatch between the three components in Eq. 18 would persist. Two more likely explanations for the imbalance are internal refreezing and firn build-up.

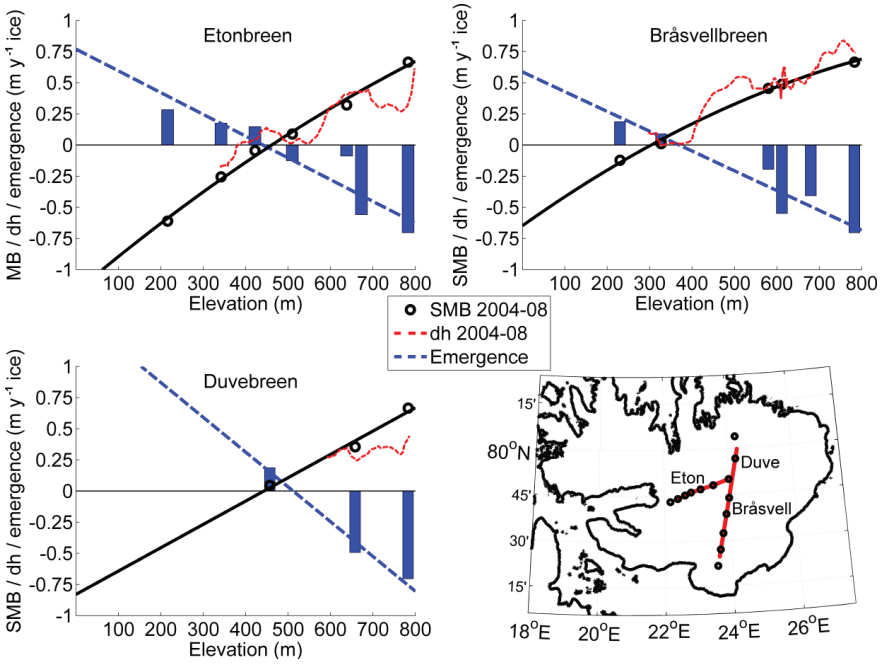

Fig. 20. Specific surface mass balance and glacier emergence velocity at stake locations along three mass balance transects on Austfonna. A straight line is fitted to the emergence velocities, while a second order polynomial curve is used for the surface mass balances. Elevation change estimates along repeated GNSS profiles are indicated in red. The locations of the stakes and profiles are shown in the lower right panel. All rates are annual averages for the 2004-2008 period in ice equivalents using the 0.9 ice/water density ratio for conversion.

Internal refreezing of meltwater and rain below the previous summer surface is common at Austfonna (e.g. Nagornov et al., 2005), but it is not accounted for in traditional surface mass balance measurements. If we assume that no meltwater drains off the firn area of Austfonna and that there is no significant summer accumulation, then the net surface mass balance in the firn area would be equal to the winter mass balance. This would rise the surface mass balance curves in Fig. 20 by 0.1-0.3 m in the firn area, resulting in a positive shift in the overall surface mass balance from 0.05 to 0.12 m w.e. y^{-1} (Paper II). Firn area expansion and

firn build-up has been observed at Austfonna between 2004 and 2008 (Dunse et al., 2009; Paper II). If we assume no firn compaction during the period, then elevation changes in the firn area should be multiplied with the firn/ice density ratio to obtain ice equivalent changes. This would lower the elevation change curves in Fig. 20 by 40-50 % in the firn area, corresponding to a negative shift in the overall mass balance from 0.04 to -0.01 m w.e. y^{-1} (Paper II). Both these assumptions about refreezing and density are extreme cases, but nevertheless they help to explain the imbalance between elevation change, surface mass balance and emergence/submergence (Fig. 20) as well as the difference between the geodetic mass balance (-1.3 Gt y^{-1}) and the mass balance from in-situ measurements plus calving (-2.1 Gt y^{-1}) (Paper II). Unfortunately it is very difficult to quantify the mass balance contribution from density changes in deeper annual firn layers.

5.5.4. Ice-cliff height and terminus fluctuations from ICESat (Papers II and IV)

Repeat-track ICESat data can also be used to estimate the height and location of tidewater glacier fronts (Fig. 21). Marine ice cliffs are recognized by a sudden jump in elevation from sea level to the glacier surface at the terminus. ICESat footprints that overlap both areas are typically lost due to the large distortion of the return echo waveform. Considering a footprint diameter of ~70 m at a spacing of 170 m, the terminus can be located to within 100 m along-track. The vertical accuracy of the ice-cliff height depends on the along-track surface slope close to the front. The ice-cliff heights will be slightly overestimated since the lowermost surface footprint can be located up to ~140 m upslope from the cliff. Assuming a 70 m distance and a slope of 3˚, the ice-cliff height will be overestimated by less than 4 m. In connection with Paper II, terminus elevation differences were measured at 26 profile-locations around Austfonna, yielding values of 14-46 m at an average of 34 m. The average ice-cliff height was estimated to 30 m after correcting for the slope bias (Paper II). Tidewater front retreat with respect to 1990-1992 glacier outlines was also estimated at the same locations (Fig. 22). The average retreat rate between 1990-1992 and 2003-2005 was about 40 m y^{-1} which is consistent with independent estimates from optical satellite imagery over the last few decades (Dowdeswell et al., 2008). The average retreat rate of the Kvitøyjøkulen ice cap was similarly estimated to ~25 m y^{-1} by comparing terminus positions from the 1983 RES survey with recent ICESat profiles (Paper IV).

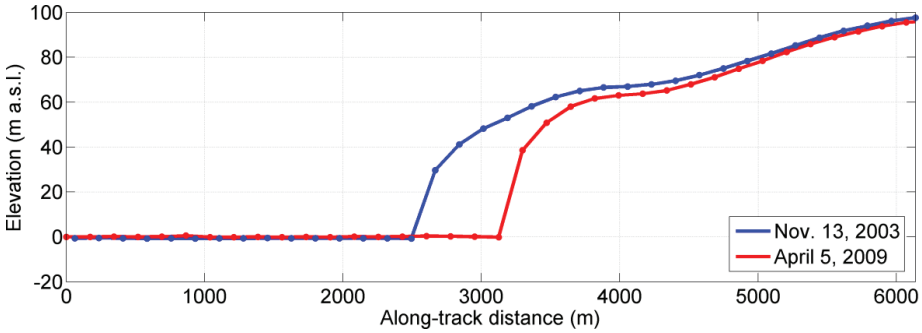

Fig. 21. An example of tidewater front retreat along two ICESat repeat-track profiles over the Bråsvellbreen outlet glacier on Austfonna. The retreat between 2003 and 2009 is about 600 m, and the ice-cliff height can be estimated to 30-40 m. The cross-track separation is 40 m.

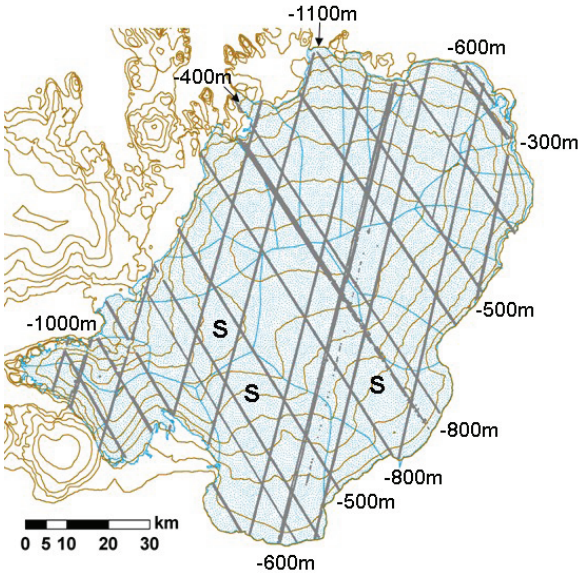

Fig. 22. Tidewater front retreat at Austfonna between aerial photos and GNSS helicopter data from 1990-1992 and ICESat altimetry from 2003-2005. The average retreat over the period was about 600 m or 40 m y^{-1}. The average ice cliff height was estimated to 30 m.

5.5.5. Additional plots and results from Paper IV

This section includes some relevant plots and results from Paper IV that were not included in the published version. Fig. 23 shows a histogram of estimated elevation change rates on Svalbard for the three ICESat elevation change methods in Paper IV. The shapes of the histograms and the mean and median of the data agree well, indicating that there are no

methodological biases in the data sets. The histograms do not follow a normal distribution, but are skewed to the left towards negative change rates. This is because strong thinning, typically found at the lowermost elevations, is more common than strong thickening. The mean values are therefore lower than the median values which are not representative for the overall glacier change. The mean values are significantly less negative than the estimated area-averaged elevation change rate of -0.12 m y^{-1} because of a spatial under-sampling of the thinning regions in the west and south where frequent cloud cover and rugged topography sometimes hinder the elevation change calculations. This underlines the importance of considering the spatial data distribution when calculating overall glacier change rates.

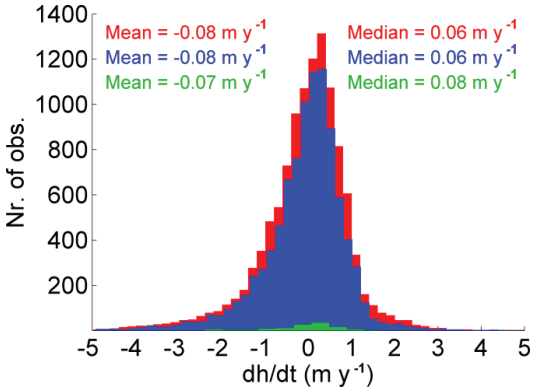

Fig. 23. Histogram of Svalbard elevation change rates from 2003 to 2008 for the crossover point method (green), the DEM projection method (red), and the plane method (blue). Mean and median elevation change rates for each method are indicated in corresponding colors.

An accurate estimate of the average elevation change rate at a plane presupposes that the tilt of the plane is correctly resolved. In Paper IV, we validated this assumption by comparing the cross-track slope of planes with the corresponding slopes of crossover points and smoothed glacier DEMs (Paper IV: Fig. 7). In a similar way, one can calculate the slope and aspect of each plane and validate them against crossover points and DEMs (Fig. 24). The RMS errors after iterative 3σ filtering were 0.41˚ for the slopes (σ_{slope}) and 14˚ for the aspects (σ_{aspect}) with mean errors close to zero. The RMS errors with respect to the smoothed DEMs were higher, probably reflecting a higher noise level in the DEMs. According to the planes, the average glacier slope on Svalbard is 2.5˚, ranging from an average of 1.4˚ at Austfonna to an average of 3.1˚ in Spitsbergen. The plane aspects can also be useful for analytical purposes. An attempt has been made to correlate elevation changes with aspects at

Vestfonna in order to see if wind-drift patterns can explain the large spatial variability in elevation change (V. Pohjola, pers. com.). Plane aspects can also be used to determine drainage divides between different glacier basins (Paper I).

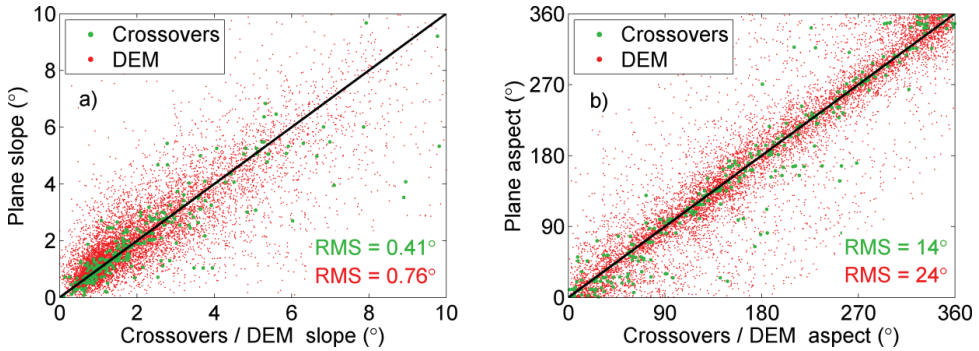

Fig. 24. Validation of the estimated slopes and aspects of planes: (a) Plane slopes compared to slopes from neighbouring crossover points and slopes calculated from the smoothed DEMs. (b) Plane aspects compared to aspects from neighbouring crossover points and aspects calculated from the smoothed DEMs. 303 crossover points were compared to the closest plane within 500 m, and the DEM slopes and aspects were extracted for all 9350 planes.

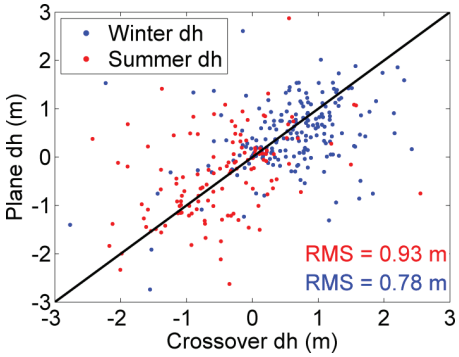

Fig. 25. Validation of seasonal elevation change estimates (dh) close to crossover point locations. 207 and 138 crossovers spanning the winter season (Oct./Nov.-Feb./Mar.) and the summer season (Feb./Mar.-Oct./Nov.) were compared to the closest seasonal dh within 500 m distance. The RMS errors yield the estimated seasonal dh accuracies (σ_{winter} and σ_{summer}) of the plane method (Paper IV: Table 2).

Winter and summer elevation changes (dh_w and dh_s) were calculated between the Oct./Nov. and Feb./Mar. observation campaigns for the five "ICESat winters" from 2003/2004 to 2007/2008 and the four "ICESat summers" from 2004 to 2008. The seasonal elevation changes were validated against crossover points spanning the same season and year

(Fig. 25). The RMS error is lower for winter elevation changes (0.78 m) than for summer elevation changes (0.93 m), probably because the magnitudes of change are generally smaller for the ~4 month ICESat winter season than the ~8 month ICESat summer season. The polynomial fits to winter and summer elevation changes are shown in Fig. 26. A general thickening occurs during the winter season with a slightly decreasing trend towards the lowermost elevations. All elevations are thinning during the ICESat summer season, especially at the lowest few hundred meters of elevation. The polynomial fits were used to calculate area-averaged seasonal elevation changes for each glacier region (Paper IV: Table 1). Although there are a few runaway tails at the edges of the elevation change curves, these potential artifacts have little influence on the area-averaged elevation changes since the associated glacier areas are very small (Fig. 26). The polynomial fits yielded consistent results with other hypsometric methods using the mean or median in each elevation bin (Sect. 4.6.2).

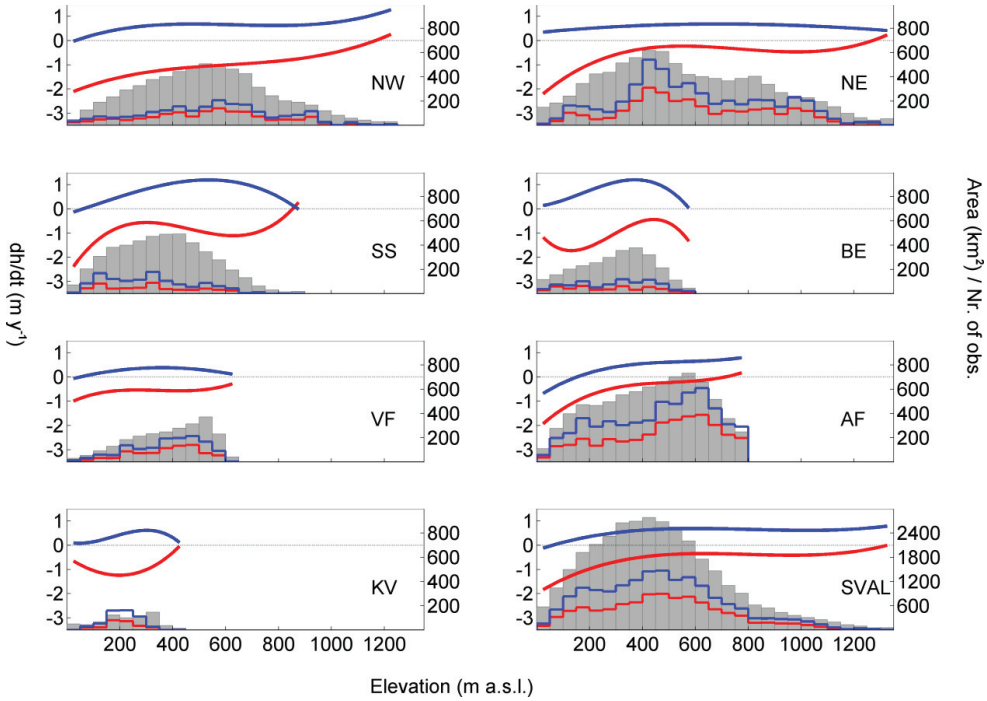

Fig. 26. Third order polynomial fits to the winter elevation changes (blue curve) and the summer elevation changes (red curve) for the 7 glacier regions and the entire Svalbard using the plane method. Winter elevation changes (dh_w) are calculated between the observation campaigns in Oct./Nov. and Feb./Mar., while summer elevation changes (dh_s) are calculated between the Feb./Mar. and Oct./Nov. campaigns. Grey bars show the glacier hypsometries as area per 50 m elevation bin in the glacier DEMs. The lowermost lines represent the number of dh estimates per elevation bin for the winter season (blue) and the summer season (red).

Table 3. Area-averaged elevation changes and volume changes using the DEM projection method rather than the plane method (Paper IV: Table 1). Regional and overall numbers are given for the 2004-2008 winter seasons $\overline{dh}_w$ (Oct./Nov.-Feb./Mar.), the 2003-2007 summer seasons $\overline{dh}_s$ (Feb./Mar.-Oct./Nov.), and the 2003-2008 average annual $\overline{dh/dt}$ and dV/dt.

Glacier region	Area (km^2)	$\overline{dh}_w$ (m)	$\overline{dh}_s$ (m)	$\overline{dh/dt}$ (m y^{-1})	dV/dt (km^3 y^{-1})
Northwestern Spitsbergen (NW)	6300	0.88 ± 0.16	-1.25 ± 0.18	-0.55 ± 0.09	-3.47 ± 0.66
Northeastern Spitsbergen (NE)	8630	0.68 ± 0.13	-0.56 ± 0.15	0.12 ± 0.07	1.04 ± 0.61
Southern Spitsbergen (SS)	4760	1.16 ± 0.24	-1.41 ± 0.31	-0.17 ± 0.15	-0.81 ± 0.72
Barentsøya and Edgeøya (BE)	2680	0.82 ± 0.24	-1.17 ± 0.36	-0.17 ± 0.11	-0.46 ± 0.30
Vestfonna ice cap (VF)	2410	0.47 ± 0.17	-0.66 ± 0.19	-0.12 ± 0.10	-0.29 ± 0.24
Austfonna ice cap (AF)	7800	0.53 ± 0.07	-0.52 ± 0.08	0.06 ± 0.04	0.47 ± 0.32
Kvitøyjøkulen ice cap (KV)	700	0.52 ± 0.36	-1.19 ± 0.40	-0.49 ± 0.15	-0.34 ± 0.11
Regions total	33280	0.74 ± 0.06	-0.87 ± 0.08	-0.12 ± 0.04	-3.86 ± 1.26
Svalbard total (SVAL)	34560	0.74 ± 0.06	-0.87 ± 0.08	-0.12 ± 0.04	-4.12 ± 1.27

All final results in Paper IV are obtained from the plane method (Paper IV, Table 1). The corresponding numbers for the DEM projection method are shown in Table 3. The overall volume change estimate is similar for both methods, and there is also a good agreement at the regional scale. A larger variation is seen in the seasonal elevation change estimates although most differences are still within the error bounds. The area-averaged seasonal errors are typically lower for the plane method than the DEM method and lower for the winter season than the summer season, which is consistent with error estimates at crossover points (Paper IV: Table 2). The magnitudes of seasonal elevation change are generally larger for the DEM method than the plane method. This is because the plane fitting minimizes the elevation residuals in a least-squares way (Paper IV: Eq. 1) and hence slightly smoothes out seasonal elevation variations. The $\overline{dh}_w$ and $\overline{dh}_s$ estimates from the DEM method are therefore more accurate than for the plane method although the higher precision of the plane data make them more suitable for interregional comparisons like in Paper IV.

6. Thesis implications

6.1. Past and current mass balance of Svalbard glaciers

Annual mass balance records of small glaciers in western Spitsbergen indicate a negative mass balance regime since at least the mid 1960s (Hagen et al., 2003b). Comparisons of photogrammetric maps/DEMs, dating back to 1936, show substantial decreases of glacier area and volume (Nuth et al., 2007; Kääb, 2008) with enhanced thinning after 1990 as compared to recent airborne lidar (Bamber et al., 2005; Kohler et al., 2007) and ICESat altimetry (Paper III). The glacier mass balance of northeastern Spitsbergen and Nordaustlandet has been more uncertain due to a lack of long term mass balance programs and few repeated geodetic observations. Regional mass balance estimates derived from DEMs and ICESat altimetry show that the specific mass balance of northeastern Svalbard is much less negative than in the southern and western parts of Svalbard (Papers II-IV). The trend is consistent with time despite large temporal variations in the magnitude of regional mass balances. A stronger summer thinning in the south and west due to higher temperatures in these regions seems to be the main reason for this spatial pattern in mass balance (Paper IV).

Until 2010, the only overall mass balance estimates of Svalbard glaciers had been obtained by extrapolating long-term surface mass balance records from in situ measurements and shallow ice cores to the entire archipelago. These estimates have varied from -0.55 m w.e. y^{-1} (Dowdeswell et al., 1997) to -0.01 m w.e. y^{-1} (Hagen et al., 2003b), mainly depending on how the limited surface mass balance data have been extrapolated to northeastern Svalbard. The elevation change data in Papers III and IV are typically too coarse to estimate the mass balance of individual glaciers, but they benefit from a relatively homogeneous spatial coverage in all regions and all elevation bands such that the spatial extrapolation error becomes acceptable. The overall mass balance of Svalbard during the 2003-2008 ICESat period is estimated to -4.3 ± 1.4 Gt y^{-1} (or -0.12 ± 0.04 m w.e. y^{-1}) when tidewater front retreat is not accounted for (Paper IV). This is only about 1/3 of the specific mass balance for the previous few decades which is estimated to -0.36 ± 0.02 m w.e. y^{-1}, excluding Austfonna and Kvitøyjøkulen (Paper III). This decrease in mass loss is surprising since there is a rising trend in temperature (Fig. 4) and no apparent change in precipitation (Fig. 5). There has however been a marked turn from very negative surface mass balances around 2003-2004 towards positive balances in 2008 (Paper II: Fig. 6, Paper IV: Fig. 3). These large annual variations make it difficult to interpret the 5-year ICESat changes in a climate perspective.

6.2. Satellite altimetry for mass balance monitoring of Arctic glaciers

Satellite radar altimetry has for long been a popular tool for measuring glacier elevation changes in the interior of the Antarctic and Greenland ice sheets. The large footprint size of these altimeters has however made it difficult to apply these measurements to the higher relief areas along the margins. The ICESat laser altimeter has a much finer resolution, and overlapping footprint elevations have been used to estimate the volume change of the entire Greenland ice sheet (Slobbe et al., 2008). Other high Arctic glaciers have an equally dense coverage of ICESat tracks, but the quantity and quality of elevation comparisons are degraded due to smaller glacier sizes and steeper slopes. The studies in Papers II and IV still show that it is feasible to obtain reasonable elevation change estimates from repeat-track ICESat data in a region like Svalbard. Reliable glacier volume changes can be estimated when the data are hypsometrically averaged within glacier regions larger than ~1000 km^2. It is also possible to derive time-series of volume change if the averaging is performed over even larger regions, e.g. the entire Svalbard (Paper IV). These volume change estimates include iceberg calving for stable tidewater fronts, but possible terminus fluctuations must be explicitly accounted for. The estimated volume changes can finally be converted to mass balance if the firn pack changes are known or assumed to be small. Field data and other remote sensing data are essential for keeping track of temporal variations of the firn pack.

Paper IV shows that the most efficient and accurate way to correct for the cross-track slope between near repeat-tracks is to use all available ICESat data in a joint analysis where surface slope and elevation change are estimated in a least-squares way for homogeneous planes that are fitted to the data along each track. The good performance of the plane method implies that it can also be applied to other Arctic regions of similar characteristics where accurate DEMs are typically not available. The next step will be to do similar calculations in the Russian Arctic and the Canadian Arctic. Together with Svalbard, these regions cover a total glacier area of ~230 000 km^2 which is about 30% of the world-wide glacier cover outside of the Greenland and Antarctic ice sheets. Altogether they might contribute significantly to current and future global sea level rise.

The ICESat program will continue with ICESat-2 which is scheduled for launch in 2015 (Abdalati et al., 2010). ICESat-2 will repeat the ICESat-1 tracks, allowing calculations of decadal elevation changes and volume changes which will be of greater value for climate interpretations than the current 5-year records. In the meantime, the newly launched Cryosat-2 radar altimeter will provide surface elevation data of comparable quality for the entire Arctic.

References

Abdalati, W., Krabill, W., Frederick, E., Manizade, S., Martin, C., Sonntag, J., Swift, R., Thomas, R., Yungel, J., and Koerner, R. 2004. Elevation changes of ice caps in the Canadian Arctic Archipelago. *Journal of Geophysical Research-Earth Surface,* 109(F4).

Abdalati, W., Zwally, H. J., Bindschadler, R., Csatho, B., Farrell, S. L., Fricker, H. A., Harding, D., Kwok, R., Lefsky, M., Markus, T., Marshak, A., Neumann, T., Palm, S., Schutz, B., Smith, B., Spinhirne, J., and Webb, C. 2010. The ICESat-2 Laser Altimetry Mission. *Proceedings of the IEEE,* 98(5), 735-751.

Abermann, J., Lambrecht, A., Fischer, A., and Kuhn, M. 2009. Quantifying changes and trends in glacier area and volume in the Austrian Otztal Alps (1969-1997-2006). *The Cryosphere,* 3(2), 205-215.

Abshire, J. B., Sun, X. L., Riris, H., Sirota, J. M., McGarry, J. F., Palm, S., Yi, D. H., and Liiva, P. 2005. Geoscience Laser Altimeter System (GLAS) on the ICESat mission: On-orbit measurement performance. *Geophysical Research Letters,* 32(21).

Andreassen, L. M., Paul, F., Kääb, A., and Hausberg, J. E. 2008. Landsat-derived glacier inventory for Jotunheimen, Norway, and deduced glacier changes since the 1930s. *The Cryosphere,* 2(2), 131-145.

Arendt, A. A., Echelmeyer, K. A., Harrison, W. D., Lingle, C. S., and Valentine, V. B. 2002. Rapid wastage of Alaska glaciers and their contribution to rising sea level. *Science,* 297(5580), 382-386.

Arnold, N. S., Rees, W. G., Devereux, B. J., and Amable, G. S. 2006a. Evaluating the potential of high-resolution airborne LiDAR data in glaciology. *International Journal of Remote Sensing,* 27(5-6), 1233-1251.

Arnold, N. S., Rees, W. G., Hodson, A. J., and Kohler, J. 2006b. Topographic controls on the surface energy balance of a high Arctic valley glacier. *Journal of Geophysical Research-Earth Surface,* 111(F2).

Bader, H. 1954. Sorge's Law of densification of snow on high polar glaciers. *Journal of Glaciology,* 2(15), 319-323.

Baltsavias, E. P., Favey, E., Bauder, A., Bosch, H., and Pateraki, M. 2001. Digital surface modelling by airborne laser scanning and digital photogrammetry for glacier monitoring. *Photogrammetric Record,* 17(98), 243-270.

Bamber, J. 1987. Internal reflecting horizons in Spitsbergen glaciers. *Annals of Glaciology,* 9, 5–10.

Bamber, J. L., and Dowdeswell, J. A. 1990. Remote-sensing studies of Kvitøyjøkulen, an ice cap on Kvitøya, North-east Svalbard. *Journal of Glaciology,* 36(122), 75-81.

Bamber, J. L., Ekholm, S., and Krabill, W. B. 2001. A new, high-resolution digital elevation model of Greenland fully validated with airborne laser altimeter data. *Journal of Geophysical Research-Solid Earth,* 106(B4), 6733-6745.

Bamber, J., Krabill, W., Raper, V., and Dowdeswell, J. 2004. Anomalous recent growth of part of a large Arctic ice cap: Austfonna, Svalbard. *Geophysical Research Letters,* 31(12).

Bamber, J. L., Krabill, W., Raper, V., Dowdeswell, J. A., and Oerlemans, J. 2005. Elevation changes measured on Svalbard glaciers and ice caps from airborne laser data. *Annals of Glaciology,* 42, 202-208.

Bamber, J. L., Gomez-Dans, J. L., and Griggs, J. A. 2009. A new 1 km digital elevation model of the Antarctic derived from combined satellite radar and laser data â€“ Part 1: Data and methods. *The Cryosphere,* 3(1), 101-111.

Bamler, R., and Hartl, P. 1998. Synthetic aperture radar interferometry. *Inverse Problems,* 14(4), R1-R54.

Banta, J. R., and McConnell, J. R. 2007. Annual accumulation over recent centuries at four sites in central Greenland. *Journal of Geophysical Research-Atmospheres,* 112(D10).

Barrand, N. E., Murray, T., James, T. D., Barr, S. L., and Mills, J. P. 2009. Optimizing photogrammetric DEMs for glacier volume change assessment using laser-scanning derived ground-control points. *Journal of Glaciology,* 55(189), 106-116.

Berthier, E., Arnaud, Y., Baratoux, D., Vincent, C., and Remy, F. 2004. Recent rapid thinning of the "Mer de Glace" glacier derived from satellite optical images. *Geophysical Research Letters,* 31(17).

Berthier, E., Arnaud, Y., Vincent, C., and Remy, F. 2006. Biases of SRTM in high-mountain areas: Implications for the monitoring of glacier volume changes. *Geophysical Research Letters,* 33(8).

Berthier, E., and Toutin, T. 2008. SPOT5-HRS digital elevation models and the monitoring of glacier elevation changes in North-West Canada and South-East Alaska. *Remote Sensing of Environment,* 112(5), 2443-2454.

Berthier, E., Schiefer, E., Clarke, G. K. C., Menounos, B., and Remy, F. 2010. Contribution of Alaskan glaciers to sea-level rise derived from satellite imagery. *Nature Geoscience,* 3(2), 92-95.

Bevan, S., Luckman, A., Murray, T., Sykes, H., and Kohler, J. 2007. Positive mass balance during the late 20th century on Austfonna, Svalbard, revealed using satellite radar interferometry. *Annals of Glaciology,* 46, 117-122.

Bindschadler, R., Fahnestock, M., and Sigmund, A. 1999. Comparison of Greenland ice sheet topography measured by TOPSAR and airborne laser altimetry. *IEEE Transactions on Geoscience and Remote Sensing,* 37(5), 2530-2535.

Bingham, A. W., and Rees, W. G. 1999. Construction of a high-resolution DEM of an Arctic ice cap using shape-from-shading. *International Journal of Remote Sensing,* 20(15-16), 3231-3242.

Björnsson, H., Gjessing, Y., Hamran, S. E., Hagen, J. O., Liestol, O., Palsson, F., and Erlingsson, B. 1996. The thermal regime of sub-polar glaciers mapped by multi-frequency radio-echo sounding. *Journal of Glaciology,* 42(140), 23-32.

Blaszczyk, M., Jania, J. A., and Hagen, J. O. 2009. Tidewater glaciers of Svalbard: Recent changes and estimates of calving fluxes. *Polish Polar Research,* 30(2), 85-142.

Bouillon, A., Bernard, M., Gigord, P., Orsoni, A., Rudowski, V., and Baudoin, A. 2006. SPOT 5 HRS geometric performances: Using block adjustment as a key issue to improve quality of DEM generation. *ISPRS Journal of Photogrammetry and Remote Sensing,* 60(3), 134-146.

Brandt, O., Hawley, R. L., Kohler, J., Hagen, J. O., Morris, E. M., Dunse, T., Scott, J. B. T., and Eiken, T. 2008. Comparison of airborne radar altimeter and ground-based Ku-band radar measurements on the ice cap Austfonna, Svalbard. *The Cryosphere Discuss.,* 2(5), 777-810.

Breili, K., and Rolstad, C. 2009. Ground-based gravimetry for measuring small spatial-scale mass changes on glaciers. *Annals of Glaciology,* 50, 141-147.

Brenner, A. C., DiMarzio, J. R., and Zwally, H. J. 2007. Precision and accuracy of satellite radar and laser altimeter data over the continental ice sheets. *IEEE Transactions on Geoscience and Remote Sensing,* 45(2), 321-331.

Chen, J. L., Wilson, C. R., Tapley, B. D., Blankenship, D. D., and Ivins, E. R. 2007. Patagonia icefield melting observed by gravity recovery and climate experiment (GRACE). *Geophysical Research Letters,* 34.

Chen, J. L., Wilson, C. R., Blankenship, D., and Tapley, B. D. 2009. Accelerated Antarctic ice loss from satellite gravity measurements. *Nature Geoscience,* 2(12), 859-862.

Cogley, J. G., and Adams, W. P. 1998. Mass balance of glaciers other than the ice sheets. *Journal of Glaciology,* 44(147), 315-325.

Colgan, W., and Sharp, M. 2008. Combined oceanic and atmospheric influences on net accumulation on Devon ice cap, nunavut, Canada. *Journal of Glaciology,* 54(184), 28-40.

Cooper, A. P. R. 1994. A simple shape-from-shading algorithm applied to images of ice-covered terrain. *IEEE Transactions on Geoscience and Remote Sensing,* 32(6), 1196-1198.

Dall, J., Madsen, S. N., Keller, K., and Forsberg, R. 2001. Topography and penetration of the Greenland ice sheet measured with airborne SAR interferometry. *Geophysical Research Letters,* 28(9), 1703-1706.

Davis, C. H. 1992. Satellite radar altimetry. *IEEE Transactions on Microwave Theory and Techniques,* 40(6), 1070-1076.

De Woul, M., and Hock, R. 2005. Static mass-balance sensitivity of Arctic glaciers and ice caps using a degree-day approach. *Annals of Glaciology,* 42, 217-224.

den Ouden, M. A. G., Reijmer, C. H., Pohjola, V., van de Wal, R. S. W., Oerlemans, J., and Boot, W. 2010. Stand-alone single-frequency GPS ice velocity observations on Nordenskiöldbreen, Svalbard. *The Cryosphere Discuss.,* 4(3), 981-1010.

Dowdeswell, J., Drewry, D., Liestøl, O., and Orheim, O. 1984. Radio echo-sounding of Spitsbergen glaciers: problems in the interpretation of layer and bottom returns. *Journal of Glaciology,* 30(104), 16-21.

Dowdeswell, J. A. 1986. Remote sensing of ice cap outlet glacier fluctuations on Nordaustlandet, Svalbard. *Polar Research,* 4(1), 25-32.

Dowdeswell, J. A., Drewry, D. J., Cooper, A. P. R., Gorman, M. R., Liestøl, O., and Orheim, O. 1986. Digital mapping of the Nordaustlandet ice caps from airborne geophysical investigations. *Annals of Glaciology,* 8, 51–58.

Dowdeswell, J. A., and McIntyre, N. F. 1987. The surface topography of large ice masses from Landsat imagery. *Journal of Glaciology,* 33(113), 16-23.

Dowdeswell, J. A. 1989. On the nature of Svalbard icebergs. *Journal of Glaciology,* 35(120), 224-234.

Dowdeswell, J. A., and Collin, R. L. 1990. Fast-flowing outlet glaciers on Svalbard ice caps. *Geology,* 18(8), 778-781.

Dowdeswell, J. A., Hamilton, G. S., and Hagen, J. O. 1991. The duration of the active phase on surge-type glaciers - Contrasts between Svalbard and other regions. *Journal of Glaciology,* 37(127), 388-400.

Dowdeswell, J. A., Hagen, J. O., Bjornsson, H., Glazovsky, A. F., Harrison, W. D., Holmlund, P., Jania, J., Koerner, R. M., Lefauconnier, B., Ommanney, C. S. L., and Thomas, R. H. 1997. The mass balance of circum-Arctic glaciers and recent climate change. *Quaternary Research,* 48(1), 1-14.

Dowdeswell, J. A., and Evans, S. 2004. Investigations of the form and flow of ice sheets and glaciers using radio-echo sounding. *Reports on Progress in Physics,* 67(10), 1821-1861.

Dowdeswell, J. A., Benham, T. J., Strozzi, T., and Hagen, J. O. 2008. Iceberg calving flux and mass balance of the Austfonna ice cap on Nordaustlandet, Svalbard. *Journal of Geophysical Research-Earth Surface,* 113(F3).

Drews, R., Rack, W., Wesche, C., and Helm, V. 2009. A spatially adjusted elevation model in Dronning Maud Land, Antarctica, based on differential SAR interferometry. *IEEE Transactions on Geoscience and Remote Sensing,* 47(8), 2501-2509.

Duda, D. P., Spinhirne, J. D., and Eloranta, E. W. 2001. Atmospheric multiple scattering effects on GLAS altimetry - Part I: Calculations of single pulse bias. *IEEE Transactions on Geoscience and Remote Sensing,* 39(1), 92-101.

Dunse, T., Schuler, T. V., Hagen, J. O., Eiken, T., Brandt, O., and Høgda, K. A. 2009. Recent fluctuations in the extent of the firn area of Austfonna, Svalbard, inferred from GPR. *Annals of Glaciology,* 50, 155-162.

Dyurgerov, M., Meier, M. F., and Bahr, D. B. 2009. A new index of glacier area change: a tool for glacier monitoring. *Journal of Glaciology,* 55(192), 710-716.

Eiken, T., Hagen, J. O., and Melvold, K. 1997. Kinematic GPS survey of geometry changes on Svalbard glaciers. *Annals of Glaciology,* 24, 157-163.

Eldhuset, K., Andersen, P. H., Hauge, S., Isaksson, E., and Weydahl, D. J. 2003. ERS tandem InSAR processing for DEM generation, glacier motion estimation and coherence analysis on Svalbard. *International Journal of Remote Sensing,* 24(7), 1415-1437.

Engeset, R. V., Kohler, J., Melvold, K., and Lunden, B. 2002. Change detection and monitoring of glacier mass balance and facies using ERS SAR winter images over Svalbard. *International Journal of Remote Sensing,* 23(10), 2023-2050.

Etzelmuller, B., Vatne, G., Odegard, R. S., and Sollid, J. L. 1993a. Mass-balance and changes of surface slope, crevasse and flow pattern of Erikbreen, northern Spitsbergen - An application of a geographical information-system (GIS). *Polar Research,* 12(2), 131-146.

Etzelmuller, B., Vatne, G., Odegard, R. S., and Sollid, J. L. 1993b. Dynamics of 2 subpolar glaciers - Erikbreen and Hannabreen, Liefdefjorden, northern Spitsbergen. *Geografiska Annaler,* 75(1-2), 41-54.

Farr, T. G., Rosen, P. A., Caro, E., Crippen, R., Duren, R., Hensley, S., Kobrick, M., Paller, M., Rodriguez, E., Roth, L., Seal, D., Shaffer, S., Shimada, J., Umland, J., Werner, M., Oskin, M., Burbank, D., and Alsdorf, D. 2007. The shuttle radar topography mission. *Reviews of Geophysics,* 45(2), 33.

Fleming, K. M., Dowdeswell, J. A., and Oerlemans, J. 1997. Modelling the mass balance of northwest Spitsbergen glaciers and responses to climate change. *Annals of Glaciology,* 24, 203-210.

Fowler, A. C., Murray, T., and Ng, F. S. L. 2001. Thermally controlled glacier surging. *Journal of Glaciology,* 47(159), 527-538.

Fox, A., and Nuttall, A. 1997. Photogrammetry as a research tool for glaciology. *The Photogrammetric Record,* 15(89), 725-737.

Fricker, H. A., Borsa, A., Minster, B., Carabajal, C., Quinn, K., and Bills, B. 2005. Assessment of ICESat performance at the Salar de Uyuni, Bolivia. *Geophysical Research Letters,* 32(21).

Fricker, H. A., and Padman, L. 2006. Ice shelf grounding zone structure from ICESat laser altimetry. *Geophysical Research Letters,* 33(15).

Fujisada, H., Bailey, G. B., Kelly, G. G., Hara, S., and Abrams, M. J. 2005. ASTER DEM performance. *IEEE Transactions on Geoscience and Remote Sensing,* 43(12), 2707-2714.

Førland, J., and Hanssen-Bauer, I. 2003. Past and future climate variations in the Norwegian Arctic: overview and novel analyses. *Polar Research,* 22(2), 113-124.

Gens, R., and VanGenderen, J. L. 1996. SAR interferometry - Issues, techniques, applications. *International Journal of Remote Sensing,* 17(10), 1803-1835.

Ghiglia, D. C., and Romero, L. A. 1994. Robust 2-dimensional weighted and unweighted phase unwrapping that uses fast transforms and iterative methods. *Journal of the Optical Society of America a-Optics Image Science and Vision,* 11(1), 107-117.

Goldstein, R. M., Zebker, H. A., and Werner, C. L. 1988. Satellite radar interferometry - Two-dimensional phase unwrapping. *Radio Science,* 23(4), 713-720.

Goodman, J. W. 1976. Some fundamental properties of speckle. *Journal of the Optical Society of America,* 66(11), 1145-1150.

Greuell, W., Kohler, J., Obleitner, F., Glowacki, P., Melvold, K., Bernsen, E., and Oerlemans, J. 2007. Assessment of interannual variations in the surface mass balance of 18 Svalbard glaciers from the Moderate Resolution Imaging Spectroradiometer/Terra albedo product. *Journal of Geophysical Research-Atmospheres,* 112(D7).

Hagen, J. O., and Saetrang, A. 1991. Radio-echo soundings of subpolar glaciers with low-frequency radar. *Polar Research,* 9(1), 99-107.

Hagen, J. O., Liestøl, O., Roland, E., and Jørgensen., T. 1993. *Glacier atlas of Svalbard and Jan Mayen*. Meddelser nr. 129. Oslo: Norwegian Polar Institute, 141 pp.

Hagen, J. O., Kohler, J., Melvold, K., and Winther, J. G. 2003a. Glaciers in Svalbard: mass balance, runoff and freshwater flux. *Polar Research,* 22(2), 145-159.

Hagen, J. O., Melvold, K., Pinglot, F., and Dowdeswell, J. A. 2003b. On the net mass balance of the glaciers and ice caps in Svalbard, Norwegian Arctic. *Arctic, Antarctic, and Alpine Research,* 35(2), 264-270.

Hagen, J. O., Eiken, T., Kohler, J., and Melvold, K. 2005. Geometry changes on Svalbard glaciers: mass-balance or dynamic response? *Annals of Glaciology,* 42, 255-261.

Hall, D. K., Williams, R. S., Casey, K. A., DiGirolamo, N. E., and Wan, Z. 2006. Satellite-derived, melt-season surface temperature of the Greenland Ice Sheet (2000-2005) and its relationship to mass balance. *Geophysical Research Letters,* 33(11).

Helm, V., Rack, W., Cullen, R., Nienow, P., Mair, D., Parry, V., and Wingham, D. J. 2007. Winter accumulation in the percolation zone of Greenland measured by airborne radar altimeter. *Geophysical Research Letters,* 34(6).

Hirano, A., Welch, R., and Lang, H. 2003. Mapping from ASTER stereo image data: DEM validation and accuracy assessment. *ISPRS Journal of Photogrammetry and Remote Sensing,* 57(5-6), 356-370.

Hock, R. 1999. A distributed temperature-index ice- and snowmelt model including potential direct solar radiation. *Journal of Glaciology,* 45(149), 101-111.

Hock, R. 2005. Glacier melt: a review of processes and their modelling. *Progress in Physical Geography,* 29(3), 362-391.

Hodgkins, R. 1997. Glacier hydrology in Svalbard, Norwegian high arctic. *Quaternary Science Reviews,* 16(9), 957-973.

Hodgkins, R., Fox, A., and Nuttall, A. M. 2007. Geometry change between 1990 and 2003 at Finsterwalderbreen, a Svalbard surge-type glacier, from GPS profiling. *Annals of Glaciology,* 46, 131-135.

Hoffmann, J., and Walter, D. 2006. How complementary are SRTM-X and -C band digital elevation models? *Photogrammetric Engineering and Remote Sensing,* 72(3), 261-268.

Howat, I. M., Smith, B. E., Joughin, I., and Scambos, T. A. 2008. Rates of southeast Greenland ice volume loss from combined ICESat and ASTER observations. *Geophysical Research Letters,* 35.

Humlum, O., Instanes, A., and Sollid, J. L. 2003. Permafrost in Svalbard: a review of research history, climatic background and engineering challenges. *Polar Research,* 22(2), 191-215.

Hutchinson, M. F. 1989. A new procedure for gridding elevation and stream line data with automatic removal of spurious pits. *Journal of Hydrology,* 106(3-4), 211-232.

Isaksson, E., Hermanson, M., Hicks, S., Igarashi, M., Kamiyama, K., Moore, J., Motoyama, H., Muir, D., Pohjola, V., Vaikmäe, R., van de Wal, R. S. W., and Watanabe, O. 2003. Ice cores from Svalbard - useful archives of past climate and pollution history. *Physics and Chemistry of the Earth,* 28, 1217-1228.

James, T. D., Murray, T., Barrand, N. E., and Barr, S. L. 2006. Extracting photogrammetric ground control from lidar DEMs for change detection. *Photogrammetric Record,* 21(116), 312-328.

Johannessen, O. M., Khvorostovsky, K., Miles, M. W., and Bobylev, L. P. 2005. Recent ice-sheet growth in the interior of Greenland. *Science,* 310(5750), 1013-1016.

Joughin, I., Winebrenner, D., Fahnestock, M., Kwok, R., and Krabill, W. 1996. Measurement of ice-sheet topography using satellite radar interferometry. *Journal of Glaciology,* 42(140), 10-22.

Kennett, M., and Eiken, T. 1997. Airborne measurement of glacier surface elevation by scanning laser altimeter. *Annals of Glaciology,* 24, 293-296.

Kierulf, H. P., Plag, H. P., and Kohler, J. 2009. Surface deformation induced by present-day ice melting in Svalbard. *Geophysical Journal International,* 179(1), 1-13.

Knoll, C., and Kerschner, H. 2009. A glacier inventory for South Tyrol, Italy, based on airborne laser-scanner data. *Annals of Glaciology,* 50(53), 46-52.

Koerner, R. M. 2005. Mass balance of glaciers in the Queen Elizabeth Islands, Nunavut, Canada. *Annals of Glaciology,* 42, 417-423.

Kohler, J., Moore, J., Kennett, M., Engeset, R. V., and Elvehoy, H. 1997. Using ground-penetrating radar to image previous years' summer surfaces for mass-balance measurements. *Annals of Glaciology,* 24, 355-360.

Kohler, J., James, T. D., Murray, T., Nuth, C., Brandt, O., Barrand, N. E., Aas, H. F., and Luckman, A. 2007. Acceleration in thinning rate on western Svalbard glaciers. *Geophysical Research Letters,* 34(18).

Korona, J., Berthier, E., Bernard, M., Remy, F., and Thouvenot, E. 2009. SPIRIT. SPOT 5 stereoscopic survey of Polar Ice: Reference Images and Topographies during the fourth International Polar Year (2007-2009). *ISPRS Journal of Photogrammetry and Remote Sensing,* 64(2), 204-212.

Kotlyakov, V. M., and Macheret, Y. Y. 1987. Radio echo-sounding of sub-polar glaciers in Svalbard: Some problems and results of Soviet studies. *Annals of Glaciology,* 9, 151-159.

Kotlyakov, V. M., Arkhipov, S. M., Henderson, K. A., and Nagornov, O. V. 2004. Deep drilling of glaciers in Eurasian Arctic as a source of paleoclimatic records. *Quaternary Science Reviews,* 23(11-13), 1371-1390.

Krabill, W., Abdalati, W., Frederick, E., Manizade, S., Martin, C., Sonntag, J., Swift, R., Thomas, R., Wright, W., and Yungel, J. 2000. Greenland ice sheet: High-elevation balance and peripheral thinning. *Science,* 289(5478), 428-430.

Krabill, W. B., Abdalati, W., Frederick, E. B., Manizade, S. S., Martin, C. F., Sonntag, J. G., Swift, R. N., Thomas, R. H., and Yungel, J. G. 2002. Aircraft laser altimetry measurement of elevation changes of the greenland ice sheet: technique and accuracy assessment. *Journal of Geodynamics,* 34(3-4), 357-376.

Krieger, G., Moreira, A., Fiedler, H., Hajnsek, I., Werner, M., Younis, M., and Zink, M. 2007. TanDEM-X: A satellite formation for high-resolution SAR interferometry. *IEEE Transactions on Geoscience and Remote Sensing,* 45(11), 3317-3341.

Kristensen, S. S., Christensen, E. L., Hanson, S., Reeh, N., Skourup, H., and Stenseng, L. 2008. *Airborne ice-sounder survey of the Austfonna Ice Cap and Kongsfjorden*

Glacier at Svalbard, May 3, 2007. Copenhagen, Denmark: Danish National Space Center, 14 pp.

Kwok, R., and Fahnestock, M. A. 1996. Ice sheet motion and topography from radar interferometry. *IEEE Transactions on Geoscience and Remote Sensing,* 34(1), 189-200.

Kääb, A., Lefauconnier, B., and Melvold, K. 2005. Flow field of Kronebreen, Svalbard, using repeated Landsat 7 and ASTER data. *Annals of Glaciology,* 42, 7-13.

Kääb, A. 2008. Glacier Volume Changes Using ASTER Satellite Stereo and ICESat GLAS Laser Altimetry. A Test Study on Edgeoya, Eastern Svalbard. *IEEE Transactions on Geoscience and Remote Sensing,* 46(10), 2823-2830.

König, M., Wadham, J., Winther, J. G., Kohler, J., and Nuttall, A. M. 2002. Detection of superimposed ice on the glaciers Kongsvegen and midre Lovenbreen, Svalbard, using SAR satellite imagery. *Annals of Glaciology,* 34, 335-342.

König, M., Winther, J. G., Kohler, J., and König, F. 2004. Two methods for firn-area and mass-balance monitoring of Svalbard glaciers with SAR satellite images. *Journal of Glaciology,* 50(168), 116-128.

Langley, K., Hamran, S. E., Hogda, K. A., Storvold, R., Brandt, O., Hagen, J. O., and Kohler, J. 2007. Use of C-band ground penetrating radar to determine backscatter sources within glaciers. *IEEE Transactions on Geoscience and Remote Sensing,* 45(5), 1236-1246.

Langley, K., Hamran, S. E., Hogda, K. A., Storvold, R., Brandt, O., Kohler, J., and Hagen, J. O. 2008. From glacier facies to SAR backscatter zones via GPR. *IEEE Transactions on Geoscience and Remote Sensing,* 46(9), 2506-2516.

Lefauconnier, B., and Hagen, J. O. 1991. *Surging and calving glaciers in Eastern Svalbard*. Meddelelser. Oslo: Norwegian Polar Institute, 130 pp.

Liestol, O. 1969. Glacier surges in west Spitsbergen. *Canadian Journal of Earth Sciences,* 6(4P2), 895-&.

Liestøl, O. 1976. *Pingos, springs and permafrost in Spitsbergen*. Årbok Norsk Polarinstitutt 1975, 7-29.

Liestøl, O. 1988. The glaciers in the Kongsfjorden area, Spitsbergen. *Norsk Geografisk Tidsskrift-Norwegian Journal of Geography,* 42(4), 231-238.

Liu, L., Wahr, J., Howat, I. M., Khan, S. A., Joughin, I., and Furuya, M. Subm. Constraining ice mass loss from Jakobshavn Isbræ (Greenland) using InSAR-measured crustal uplift. *Submitted for publication in Geophysics Journal International*.

Luthcke, S. B., Arendt, A., Rowlands, D. D., McCarthy, J. J., and Larsen, C. F. 2008. Recent glacier mass changes in the Gulf of Alaska region from GRACE mascon solutions. *Journal of Glaciology,* 54(188), 767-777.

Magnusson, E., Bjornsson, H., Dall, J., and Palsson, F. 2005. Volume changes of Vatnajokull ice cap, Iceland, due to surface mass balance, ice flow, and subglacial melting at geothermal areas. *Geophysical Research Letters,* 32(5).

Mahesh, A., Spinhirne, J. D., Duda, D. P., and Eloranta, E. W. 2002. Atmospheric multiple scattering effects on GLAS altimetry - part II: Analysis of expected errors in antarctic altitude measurements. *IEEE Transactions on Geoscience and Remote Sensing,* 40(11), 2353-2362.

Manabe, S., and Stouffer, R. J. 1980. Sensitivity of a global climate model to an increase of CO2 concentration in the atmosphere. *Journal of Geophysical Research-Oceans and Atmospheres,* 85(NC10), 5529-5554.

Martin, C. F., Thomas, R. H., Krabill, W. B., and Manizade, S. S. 2005. ICESat range and mounting bias estimation over precisely-surveyed terrain. *Geophysical Research Letters,* 32(21).

Mikhail, E. M., Bethel, J. S., and McGlone, J. C. 2001. *Introduction to modern photogrammetry*. New York: Wiley, 479 pp.

Miller, P. E., Kunz, M., Mills, J. P., King, M. A., Murray, T., James, T. D., and Marsh, S. H. 2009. Assessment of glacier volume change using ASTER-based surface matching of historical photography. *IEEE Transactions on Geoscience and Remote Sensing,* 47(7), 1971-1979.

Mote, T. L., Anderson, M. R., Kuivinen, K. C., and Rowe, C. M. 1993. Passive microwave-derived spatial and temporal variations of summer melt on the Greenland Ice Sheet. *Annals of Glaciology,* 17, 233-238.

Murray, T., Strozzi, T., Luckman, A., Jiskoot, H., and Christakos, P. 2003. Is there a single surge mechanism? Contrasts in dynamics between glacier surges in Svalbard and other regions. *Journal of Geophysical Research-Solid Earth,* 108(B5), 15.

Nagornov, O. V., Konovalov, Y. V., and Tchijov, V. 2005. Reconstruction of past temperatures for Arctic glaciers subjected to intense subsurface melting. *Annals of Glaciology,* 40, 61-66.

Nagornov, O. V., Konovalov, Y. V., and Tchijov, V. 2006. Temperature reconstruction for Arctic glaciers. *Palaeogeography Palaeoclimatology Palaeoecology,* 236(1-2), 125-134.

Nordli, Ø., and Kohler, J. 2004. *The early 20th century warming - Daily observations at Grønfjorden and Longyearbyen on Spitsbergen*. Klima. Oslo: Norwegian Meteorlogical Institute.

NPI 2010a. *Topographic map series of Svalbard (1:100 000)*. The Norwegian Polar Institute, Tromsø, Norway: http://npweb.npolar.no/english/subjects/1165397816.46 (visited Oct. 2010).

NPI 2010b. *New glacier inventory of Svalbard (work in progress)*. The Norwegian Polar Institute, Tromsø, Norway: http://npweb.npolar.no/english/subjects/1165397816.46 (visited Oct. 2010).

Nuth, C., Kohler, J., Aas, H. F., Brandt, O., and Hagen, J. O. 2007. Glacier geometry and elevation changes on Svalbard (1936-90): a baseline dataset. *Annals of Glaciology,* 46(1), 106-116.

Nuth, C., and Kääb, A. 2010. What's in an elevation difference? Accuracy and corrections of satellite elevation data sets for quantification of glacier changes. *The Cryosphere Discuss.,* 4, 2013-2077.

Nuttall, A. M., and Hodgkins, R. 2005. Temporal variations in flow velocity at Finsterwalderbreen, a Svalbard surge-type glacier. *Annals of Glaciology, Vol 42, 2005,* 42, 71-76.

Oerlemans, J., Anderson, B., Hubbard, A., Huybrechts, P., Johannesson, T., Knap, W. H., Schmeits, M., Stroeven, A. P., van de Wal, R. S. W., Wallinga, J., and Zuo, Z. 1998. Modelling the response of glaciers to climate warming. *Climate Dynamics,* 14(4), 267-274.

Palmer, S., Shepherd, A., Bjornsson, H., and Palsson, F. 2009. Ice velocity measurements of Langjokull, Iceland, from interferometric synthetic aperture radar (InSAR). *Journal of Glaciology,* 55(193), 834-838.

Paterson, W. S. B. 1994. *The physics of glaciers*. Oxford, England: Elsevier Science Ltd., 481 pp.

Paul, F. 2008. Calculation of glacier elevation changes with SRTM: is there an elevation-dependent bias? *Journal of Glaciology,* 54(188), 945-946.

Paul, F., and Haeberli, W. 2008. Spatial variability of glacier elevation changes in the Swiss Alps obtained from two digital elevation models. *Geophysical Research Letters,* 35(21), 5.

Piechura, J., and Walczowski, W. 2009. Warming of the West Spitsbergen Current and sea ice north of Svalbard. *Oceanologia,* 51(2), 147-164.

Pinglot, J. F., Pourchet, M., Lefauconnier, B., Hagen, J. O., Isaksson, E., Vaikmae, R., and Kamiyama, K. 1999. Accumulation in Svalbard glaciers deduced from ice cores with nuclear tests and Chernobyl reference layers. *Polar Research,* 18(2), 315-321.

Pinglot, J. F., Hagen, J. O., Melvold, K., Eiken, T., and Vincent, C. 2001. A mean net accumulation pattern derived from radioactive layers and radar soundings on Austfonna, Nordaustlandet, Svalbard. *Journal of Glaciology,* 47(159), 555-566.

Pohjola, V. A., Martma, T. A., Meijer, H. A. J., Moore, J. C., Isaksson, E., Vaikmae, R., and Van de Wal, R. S. W. 2002a. Reconstruction of three centuries of annual accumulation rates based on the record of stable isotopes of water from Lomonosovfonna, Svalbard. *Annals of Glaciology,* 35, 57-62.

Pohjola, V. A., Moore, J. C., Isaksson, E., Jauhiainen, T., van de Wal, R. S. W., Martma, T., Meijer, H. A. J., and Vaikmae, R. 2002b. Effect of periodic melting on geochemical and isotopic signals in an ice core from Lomonosovfonna, Svalbard. *Journal of Geophysical Research-Atmospheres,* 107(D4), 14.

Polyakov, I. V., Bekryaev, R. V., Alekseev, G. V., Bhatt, U. S., Colony, R. L., Johnson, M. A., Maskshtas, A. P., and Walsh, D. 2003. Variability and trends of air temperature and pressure in the maritime Arctic, 1875-2000. *Journal of Climate,* 16(12), 2067-2077.

Pritchard, H. D., Arthern, R. J., Vaughan, D. G., and Edwards, L. A. 2009. Extensive dynamic thinning on the margins of the Greenland and Antarctic ice sheets. *Nature,* 461(7266), 971-975.

Pälli, A., Kohler, J. C., Isaksson, E., Moore, J. C., Pinglot, J. F., Pohjola, V. A., and Samuelsson, H. 2002. Spatial and temporal variability of snow accumulation using ground-penetrating radar and ice cores on a Svalbard glacier. *Journal of Glaciology,* 48(162), 417-424.

Reeh, N. 2008. A nonsteady-state firn-densification model for the percolation zone of a glacier. *Journal of Geophysical Research-Earth Surface,* 113(F03023).

Rees, G. 2006. *Remote sensing of snow and ice*. Boca Raton, FL: CRC Press, Tylor & Francis Group, 285-667.

Rignot, E., Echelmeyer, K., and Krabill, W. 2001. Penetration depth of interferometric synthetic-aperture radar signals in snow and ice. *Geophysical Research Letters,* 28(18), 3501-3504.

Rignot, E., Rivera, A., and Casassa, G. 2003. Contribution of the Patagonia Icefields of South America to sea level rise. *Science,* 302(5644), 434-437.

Rinne, E., Shepherd, A., Muir, A., and Wingham, D. Subm. A Comparison of recent elevation change estimates of the Devon Ice Cap as measured by the ICESat and EnviSAT satellite altimeters. *Submitted for publication in IEEE TGARS*.

Rodriguez, E., Morris, C. S., and Belz, J. E. 2006. A global assessment of the SRTM performance. *Photogrammetric Engineering and Remote Sensing,* 72(3), 249-260.

Rosen, P. A., Hensley, S., Joughin, I. R., Li, F. K., Madsen, S. N., Rodriguez, E., and Goldstein, R. M. 2000. Synthetic aperture radar interferometry - Invited paper. *Proceedings of the IEEE,* 88(3), 333-382.

Rotschky, G., Schuler, T. V., Haarpaintner, J., Kohler, J., and Isaksson, E. In press. Spatio-temporal variability of snow melt on Svalbard during the period 2000-2008 derived from QuickScat/SeaWinds scatterometry. *Polar Research*.

Rott, H., Sturm, K., and Miller, H. 1993. Active and passive microwave signatures of Antarctic firn by means of field-measurements and satellite data. *Annals of Glaciology,* 17, 337-343.

Rott, H. 2009. Advances in interferometric synthetic aperture radar (InSAR) in earth system science. *Progress in Physical Geography,* 33(6), 769-791.

Rye, C. J., Arnold, N. S., Willis, I. C., and Kohler, J. 2009. Modeling the surface mass balance of a high Arctic glacier using the ERA-40 reanalysis. *Journal of Geophysical Research-Earth Surface,* 115, 18.

Sand, K., Winther, J. G., Marechal, D., Bruland, O., and Melvold, K. 2003. Regional variations of snow accumulation on Spitsbergen, Svalbard, 1997-99. *Nordic Hydrology,* 34(1-2), 17-32.

Schiefer, E., Menounos, B., and Wheate, R. 2007. Recent volume loss of British Columbian glaciers, Canada. *Geophysical Research Letters,* 34(16), 6.

Schuler, T. V., Loe, E., Taurisano, A., Eiken, T., Hagen, J. O., and Kohler, J. 2007. Calibrating a surface mass-balance model for Austfonna ice cap, Svalbard. *Annals of Glaciology,* 46(1), 241-248.

Schuler, T. V., Crochet, P., Hock, R., Jackson, M., Barstad, I., and Johannesson, T. 2008. Distribution of snow accumulation on the Svartisen ice cap, Norway, assessed by a model of orographic precipitation. *Hydrological Processes,* 22(19), 3998-4008.

Schutz, B. E., Zwally, H. J., Shuman, C. A., Hancock, D., and DiMarzio, J. P. 2005. Overview of the ICESat Mission. *Geophysical Research Letters,* 32(21), 4.

Schytt, V. 1964. Scientific Results of the Swedish Glaciological Expedition to Nordaustlandet, Spitsbergen, 1957 and 1958. *Geografiska Annaler,* 46(3), 242-281.

Schytt, V. 1969. Some comments on glacier surges in eastern Svalbard. *Canadian Journal of Earth Sciences,* 6, 867-873.

Serreze, M. C., Barrett, A. P., Stroeve, J. C., Kindig, D. N., and Holland, M. M. 2009. The emergence of surface-based Arctic amplification. *The Cryosphere,* 3(1), 11-19.

Sharp, M., and Wang, L. B. 2009. A Five-Year Record of Summer Melt on Eurasian Arctic Ice Caps. *Journal of Climate,* 22(1), 133-145.

Shuman, C. A., Zwally, H. J., Schutz, B. E., Brenner, A. C., DiMarzio, J. P., Suchdeo, V. P., and Fricker, H. A. 2006. ICESat Antarctic elevation data: Preliminary precision and accuracy assessment. *Geophysical Research Letters,* 33(7).

Slobbe, D. C., Lindenbergh, R. C., and Ditmar, P. 2008. Estimation of volume change rates of Greenland's ice sheet from ICESat data using overlapping footprints. *Remote Sensing of Environment,* 112(12), 4204-4213.

Smith, B. E., Fricker, H. A., Joughin, I. R., and Tulaczyk, S. 2009. An inventory of active subglacial lakes in Antarctica detected by ICESat (2003-2008). *Journal of Glaciology,* 55(192), 573-595.

Stearns, L. A., Smith, B. E., and Hamilton, G. S. 2008. Increased flow speed on a large East Antarctic outlet glacier caused by subglacial floods. *Nature Geoscience,* 1(12), 827-831.

Strozzi, T., Kouraev, A., Wiesmann, A., Wegmuller, U., Sharov, A., and Werner, C. 2008. Estimation of Arctic glacier motion with satellite L-band SAR data. *Remote Sensing of Environment,* 112(3), 636-645.

Sund, M., Eiken, T., Hagen, J. O., and Kääb, A. 2009. Svalbard surge dynamics derived from geometric changes. *Annals of Glaciology,* 50(52), 50-60.

Sund, M., and Eiken, T. 2010. Correspondence: Recent surges on Blomstrandbreen, Comfortlessbreen and Nathorstbreen, Svalbard. *Journal of Glaciology,* 56(195), 558-559.

Sverdrup, H. 1935. The temperature of the firn on Isachsen's Plateau and general conclusions regarding the temperature of the glaciers on West-Spitzbergen. *Geografisker Annaler,* 17, 78-80.

Taurisano, A., Schuler, T. V., Hagen, J. O., Eiken, T., Loe, E., Melvold, K., and Kohler, J. 2007. The distribution of snow accumulation across the Austfonna ice cap, Svalbard: direct measurements and modelling. *Polar Research,* 26(1), 7-13.

Thomas, R., Frederick, E., Krabill, W., Manizade, S., Martin, C., and Mason, A. 2005. Elevation changes on the Greenland ice sheet from comparison of aircraft and ICESat laser-altimeter data. *Annals of Glaciology,* 42, 77-82.

Toutin, T. 2004. RADARSAT-2 stereoscopy and polarimetry for 3D mapping. *Canadian Journal of Remote Sensing,* 30(3), 496-503.

Toutin, T. 2006. Generation of DSMs from SPOT-5 in-track HRS and across-track HRG stereo data using spatiotriangulation and autocalibration. *ISPRS Journal of Photogrammetry and Remote Sensing,* 60(3), 170-181.

Toutin, T. 2008. ASTER DEMs for geomatic and geoscientific applications: a review. *International Journal of Remote Sensing,* 29(7), 1855-1875.

Unwin, B., and Wingham, D. 1997. Topography and dynamics of Austfonna, Nordaustlandet, Svalbard, from SAR interferometry. *Papers from the International symposium on Changing glaciers.,* 24, 403-408.

Velicogna, I., and Wahr, J. 2006. Acceleration of Greenland ice mass loss in spring 2004. *Nature,* 443(7109), 329-331.

Vieli, A., Jania, J., Blatter, H., and Funk, M. 2004. Short-term velocity variations on Hansbreen, a tidewater glacier in Spitsbergen. *Journal of Glaciology,* 50(170), 389-398.

Wang, L., Sharp, M. J., Rivard, B., Marshall, S., and Burgess, D. 2005. Melt season duration on Canadian Arctic ice caps, 2000-2004. *Geophysical Research Letters,* 32(19).

Wehr, A., and Lohr, U. 1999. Airborne laser scanning - an introduction and overview. *ISPRS Journal of Photogrammetry and Remote Sensing,* 54(2-3), 68-82.

Welch, R., Jordan, T., Lang, H., and Murakami, H. 1998. ASTER as a source for topographic data in the late 1990's. *IEEE Transactions on Geoscience and Remote Sensing,* 36(4), 1282-1289.

Wingham, D. J., Ridout, A. J., Scharroo, R., Arthern, R. J., and Shum, C. K. 1998. Antarctic elevation change from 1992 to 1996. *Science,* 282(5388), 456-458.

Wingham, D. J., Francis, C. R., Baker, S., Bouzinac, C., Brockley, D., Cullen, R., de Chateau-Thierry, P., Laxon, S. W., Mallow, U., Mavrocordatos, C., Phalippou, L., Ratier, G., Rey, L., Rostan, F., Viau, P., and Wallis, D. W. 2006. CryoSat: A mission to determine the fluctuations in Earth's land and marine ice fields. *Natural Hazards and Oceanographic Processes from Satellite Data,* 37(4), 841-871.

Winther, J. 1993. Landsat TM derived and in situ summer reflectance of glaciers in Svalbard. *Polar Research,* 12(1), 37-55.

Wise, S. 2000. Assessing the quality for hydrological applications of digital elevation models derived from contours. *Hydrological Processes,* 14(11-12), 1909-1929.

Wolken, G. J., Sharp, M., and Wang, L. B. 2009. Snow and ice facies variability and ice layer formation on Canadian Arctic ice caps, 1999-2005. *Journal of Geophysical Research-Earth Surface,* 114, 14.

Wouters, B., Chambers, D., and Schrama, E. J. O. 2008. GRACE observes small-scale mass loss in Greenland. *Geophysical Research Letters,* 35.

Wright, A., Wadham, J., Siegert, M., Luckman, A., and Kohler, J. 2005. Modelling the impact of superimposed ice on the mass balance of an Arctic glacier under scenarios of future climate change. *Annals of Glaciology,* 42, 277-283.

Wright, A. P., Wadham, J. L., Siegert, M. J., Luckman, A., Kohler, J., and Nuttall, A. M. 2007. Modeling the refreezing of meltwater as superimposed ice on a high Arctic

glacier: A comparison of approaches. *Journal of Geophysical Research-Earth Surface,* 112(F4).

Yamaguchi, Y., Kahle, A. B., Tsu, H., Kawakami, T., and Pniel, M. 1998. Overview of Advanced Spaceborne Thermal Emission and Reflection Radiometer (ASTER). *IEEE Transactions on Geoscience and Remote Sensing,* 36(4), 1062-1071.

Yi, D. H., Zwally, H. J., and Sun, X. L. 2005. ICESat measurement of Greenland ice sheet surface slope and roughness. *Annals of Glaciology,* 42, 83-89.

Zagorodnov, V. S., Sinkevich, S. A., and Arkhipov, S. M. 1990. Hydrothermal regime of the ice-divide area of Austfonna, Nordaustlandet. *Data of Glaciological Studies,* 68, 133-141 (in Russian).

Zebker, H. A., Rosen, P. A., and Hensley, S. 1997. Atmospheric effects in interferometric synthetic aperture radar surface deformation and topographic maps. *Journal of Geophysical Research-Solid Earth,* 102(B4), 7547-7563.

Zebker, H. A., and Lu, Y. P. 1998. Phase unwrapping algorithms for radar interferometry: Residue-cut, least-squares, and synthesis algorithms. *Journal of the Optical Society of America a-Optics Image Science and Vision,* 15(3), 586-598.

Zhang, X. H., and Forsberg, R. 2007. Assessment of long-range kinematic GPS positioning errors by comparison with airborne laser altimetry and satellite altimetry. *Journal of Geodesy,* 81(3), 201-211.

Zwally, H. J., Brenner, A. C., Major, J. A., Bindschadler, R. A., and Marsh, J. G. 1989. Growth of the Greenland ice sheet - measurement. *Science,* 246(4937), 1587-1589.

Zwally, H. J., Abdalati, W., Herring, T., Larson, K., Saba, J., and Steffen, K. 2002a. Surface melt-induced acceleration of Greenland ice-sheet flow. *Science,* 297(5579), 218-222.

Zwally, H. J., Schutz, B., Abdalati, W., Abshire, J., Bentley, C., Brenner, A., Bufton, J., Dezio, J., Hancock, D., Harding, D., Herring, T., Minster, B., Quinn, K., Palm, S., Spinhirne, J., and Thomas, R. 2002b. ICESat's laser measurements of polar ice, atmosphere, ocean, and land. *Journal of Geodynamics,* 34(3-4), 405-445.

Zwally, H. J., Schutz, R., Bentley, C., Bufton, J., Herring, T., Minster, B., Spinhirne, J., and Thomas, R. 2010. *GLAS/ICESat L1B Global Elevation Data V031, 20 February 2003 to 11 October 2009*. Boulder, CO: National Snow and Ice Data Center. Digital media.

Østrem, G., and Brugman, M. 1991. *Glacier mass-balance measurements: A manual for field and office work*. NHRI Science Report 4. Saskatoon, Sask.: Environment Canada. National Hydrology Research Institute.

Part II

Papers

I

A new DEM of the Austfonna ice cap by combining differential SAR interferometry with ICESat laser altimetry

Geir Moholdt [a*] and Andreas Kääb [a]

[a]Department of Geosciences, University of Oslo, Box 1047 Blindern, 0316 Oslo, Norway

**Corresponding author: G. Moholdt, Tel. +47 99102900, geirmoh@geo.uio.no.*

Abstract

We present a new digital elevation model (DEM) of the Austfonna ice cap at the Svalbard archipelago, Norwegian Arctic. Previous DEMs derived from synthetic aperture radar (SAR) and optical shape-from-shading have been tied to airborne radio echo-sounding surface profiles from 1983 which contain an elevation-dependent bias of up to several tens of meters as compared to recent elevation data. The new and freely available DEM is constructed purely from spaceborne remote sensing data using differential SAR interferometry (DInSAR) in combination with ICESat laser altimetry. Interferograms were generated from pairs of SAR scenes from the 1-day repeat tandem phase of the European Remote Sensing Satellites 1/2 (ERS-1/2) in 1996. ICESat elevations from winter 2006-2008 are used as ground control points to refine the interferometric baseline. The resulting DEM is validated against the same ground control points and independent surface elevation profiles from Global Navigation Satellite Systems (GNSS) and airborne laser altimetry, yielding root mean square (RMS) errors of about 10 m in all cases. This quality is sufficient for most glaciological applications, and the new DEM will be a baseline data set for ongoing and future research at Austfonna. The technique of combining satellite DInSAR with high-resolution satellite altimetry for DEM generation might be a good alternative also in other glacier regions of similar characteristics, especially when data from TanDEM-X and CryoSat-2 become available.

Keywords: SAR, ICESat, DEM, Austfonna, ice cap, glacier

1. Introduction

Surface topography is important input data for most glaciological and remote sensing studies of glaciers and ice caps. At Austfonna, digital elevation models (DEMs) have been used to delineate glacier drainage basins (Dowdeswell, 1986), to extrapolate elevation measurements and surface mass balance (Moholdt et al., 2010a), to extract surface velocities from 2-pass SAR interferometry (Dowdeswell et al., 1999), and to model surface mass balance (Schuler et al., 2007) and glacier dynamics (Dunse et al., Subm.). Most glacier DEMs are made from airborne or spaceborne stereo photogrammetry (e.g. Nuth et al., 2007; Kääb, 2008). Large and featureless ice caps are however difficult to map accurately due to low image contrast in the firn area and low availability of ground control points. Airborne SAR interferometry (Dall et al., 2001) and laser scanning (Arnold et al., 2006) are good alternatives but typically too expensive for large-scale topographic mapping. High-resolution satellite altimeters like ICESat (Zwally et al., 2002) and CryoSat-2 (Wingham et al., 2006) provide accurate elevation profiles with a sufficient spatial sampling for DEM generation over the gentle ice sheets of Greenland and Antarctica (DiMarzio et al., 2007). In the case of Arctic glaciers and ice caps, data gaps between satellite altimetry profiles need to be filled with other elevation data. Satellite differential SAR interferometry (DInSAR) is ideal for this purpose since it provides a continuous high-resolution topographic surface that can be tied to more accurate elevation profiles from satellite altimetry (Baek et al., 2005; Drews et al., 2009). Here we present a new DEM of the Austfonna ice cap by performing DInSAR on ERS-1/2 tandem SAR imagery from 1996 with ICESat laser altimetry profiles from winter 2006-2008 as ground control points.

Austfonna (7800 km^2) is located on the Nordaustlandet island in the northeast of the Svalbard archipelago (Fig. 1). The ice cap geometry is characterized by one major ice dome which rises gently up to about 800 m a.s.l. and feeds a number of drainage basins. Apart from a few fast-flowing units, most of the ice cap is slow-moving with typical velocities less than 10 m y^{-1} (Dowdeswell et al., 1999; Strozzi et al., 2008). Glacier surges have been reported for three of the basins (Fig. 1), but not during the last 70 years (Lefauconnier and Hagen, 1991). The most detailed mapping of Austfonna was done in 1983 by airborne radio echo-sounding (RES) (Dowdeswell et al., 1986). Surface and bedrock elevations were obtained along a dense grid of altimetry profiles. It was found that 30% of the ice cap is grounded below sea level, with ice thicknesses ranging from <300 m in the marine southeast to 500 m in the interior. The RES surface elevations were used by the Norwegian Polar Institute to improve their topographic map series (NPI, 2010). Others have made DEMs of Austfonna based on differential SAR interferometry (Unwin and Wingham, 1997) and optical shape-from-shading applied to Landsat imagery (Bingham and Rees, 1999). In lack of more recent ground control points, both of

these DEMs were tied to a selection of 1983 RES data with relative accuracies of 8 m and 14 m, respectively. Recent elevation data from ICESat, airborne laser altimetry and GNSS surface profiles indicate that the RES-dependent DEMs are systematically 30-50 m too low in the summit area and 10-30 m too high close to the margins. These deviations can be partly explained by interior thickening and peripheral thinning (Bamber et al., 2004), but there might also be an elevation-dependent bias in the 1983 data related to the pressure-altitude recordings (Moholdt, 2010). The large deviation between existing DEMs and the current geometry implies a need for a new baseline DEM to be used in current and future glaciological work at Austfonna.

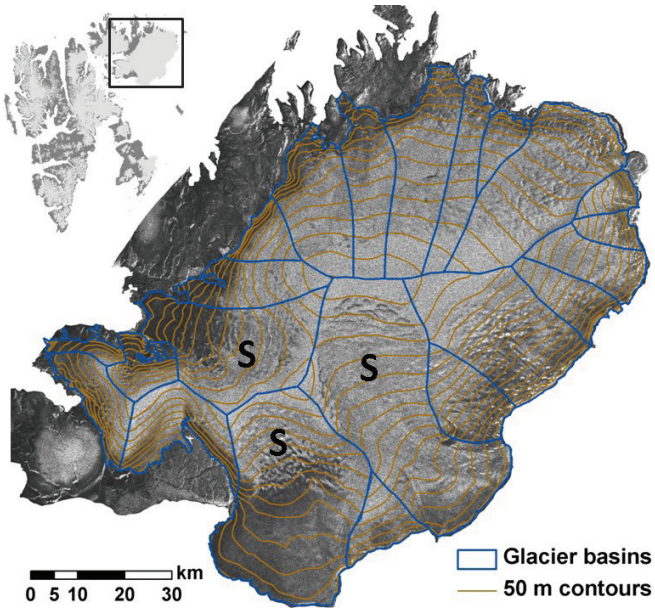

Fig. 1. Glacier topography (50 m contour interval) and drainage basins of Austfonna derived from the dInSAR/ICESat DEM. An orthorectified version of a SAR intensity image from 5 March 1996 is also shown. The inset map shows the location of Austfonna within the Svalbard archipelago. Glacier basins that are known to have surged are indicated with an *S*.

2. Data sets

Most SAR satellites have a repeat pass period of 10-50 days (Rott, 2009) which limits the phase coherence over temporally variable surfaces like glaciers. Shorter repeat-times are available for the 3-day ice phase of ERS-1 in winter 1992 and 1994, and from the tandem phase of ERS-1/2 in 1995-1996 when ERS-2 was following the ERS-1 orbit at a 24-hour delay. We selected two tandem SAR image pairs from a descending track covering the entire Austfonna with baseline configurations that are beneficial for extracting topographic phases from DInSAR (Table 1, Fig. 2). The same set of SAR

scenes have previously been used to estimate down-slope surface velocities across the ice cap (Bevan et al., 2007). Other InSAR studies at Austfonna (Unwin and Wingham, 1997; Dowdeswell et al., 1999; Strozzi et al., 2008; Dowdeswell et al., 2008) have used SAR scenes from satellite tracks where the image frames do not cover the entire ice cap. Our selection of scenes avoids the problem of mosaicing between incoherent interferograms from different satellite tracks. The SAR data were delivered by the European Space Agency (ESA) as pre-processed single-look complex (SLC) images that contain both amplitude and phase information. Adjacent SLC frames from the same satellite pass were merged together ahead of the interferometric processing to obtain scenes with full ice cap coverage. The ESA ephemerides provided with the data were replaced by precise post-processed ERS-1/2 orbits obtained from the Delft University of Technology (Scharroo and Visser, 1998).

Table 1. The three interferograms that were generated and their associated pairs of ERS-1/2 tandem SAR scenes with satellite track number, acquisition dates and baseline lengths of the parallel ($B_{||}$) and perpendicular ($B_{\perp}$) components at the interferogram center point. The third interferogram ($dInt_{A\text{-}B}$) is a differential interferogram between the two first ones (Int_A - Int_B).

Interf.	Track	Date 1	Date 2	$B_{\|\|}$	$B_{\perp}$
Int_A	223 desc.	5 Mar 1996	6 Mar 1996	78 m	178 m
Int_B	223 desc.	9 Apr 1996	10 Apr 1996	-13 m	-34 m
$dInt_{A\text{-}B}$	223 desc.	5-6 Mar 1996	9-10 Apr 1996	91 m	212 m

The Geoscience Laser Altimeter System (GLAS) onboard ICESat acquires surface elevations from ground footprints of ≈70 m diameter spaced at ≈170 m along each track (Zwally et al., 2002). Elevation accuracies of a few centimeters have been demonstrated under optimal conditions (Fricker et al., 2005), but the performance degrades over sloping terrain and under conditions favorable to atmospheric forward scattering and detector saturation (Brenner et al., 2007). An elevation precision of less than 0.5 m has been found from crossover points within individual ICESat observation campaigns (<35 days) at Austfonna (Moholdt et al., 2010a). We used the GLA06 altimetry product release 31 which is based on the ice sheet waveform parameterization (Zwally et al., 2010). Ground control points (GCPs) were selected from a subset of ICESat observations collected in the February/March observation campaign in 2006, 2007 and 2008. Priority was given to the observations with the lowest detector gain setting whenever data were available from multiple profiles along the same ICESat reference track. Gain thresholds are commonly used as cloud filters to remove observations susceptible to forward scattering (Yi et al., 2005; Brenner et al., 2007).

The boundary of the glacier DEM was determined from optical satellite imagery. New glacier outlines were manually digitized from an orthorectified SPOT-5 2008 scene (Korona et al., 2009) covering the northern and western margins of the ice cap and a Landsat 2001 scene covering the

tidewater front to the southeast (Fig. 3). The total ice cap area was calculated to 7800 km^2 which is less than previously published values (Hagen et al., 1993) but consistent with the general glacier front retreat of a few tens of meters per year over the past few decades (Dowdeswell et al., 2008).

Independent surface elevation profiles from surface GNSS and airborne laser altimetry acquired in spring 2007 were used to validate the DEM (Fig. 3). The GNSS data were obtained from a dual-frequency receiver mounted on a tripod on a sledge which was pulled by a snowmobile (Eiken et al., 1997). The measurements were differentially post-corrected against a base station at the summit. Airborne lidar data were collected in diagonal swipes within a 300 m wide ground swath (Forsberg et al., 2002). Most of the lidar profiles were overlapping with the GNSS profiles, yielding a relative elevation accuracy of a few decimeters which is more than sufficient for DEM validation purposes. The GNSS and lidar data were separately averaged within 50 m clusters to obtain a comparable resolution to the dInSAR/ICESat DEM.

3. DInSAR processing

The procedure for deriving glacier topography from differential SAR interferometry is well established (Joughin et al., 1996; Kwok and Fahnestock, 1996). The 4-pass DInSAR processing was done in the Gamma Remote Sensing software (Wegmüller and Werner, 1997) in a stepwise manner:

- Co-registration of SLC image pairs (Img_{A1} vs. Img_{A2} and Img_{B1} vs. Img_{B2}, Table 1)
- Generation of multi-look (2 × range, 10 × azimuth) complex interferograms (Int_A and Int_B)
- Calculation of baselines (B) and removal of phase trends from the curved Earth (Fig. 2 a-b)
- Co-registration of the interferograms (Int_A vs. Int_B) using their intensity images
- Topographic phase isolation by interferogram differencing ($dInt_{A-B} = Int_A - Int_B$) (Fig. 2 c)
- Adaptive filtering and phase unwrapping using the branch-cut algorithm ($dInt_{A-B} \Rightarrow dInt_{unw}$)

Image offsets for the co-registration of SLC images and interferograms were estimated to an accuracy of better than 0.1 pixels by cross-correlating the corresponding intensity images at a decreasing number of multi-looks. The flattened interferograms contain phase differences that are due to topography, movement and noise (Fig. 2 a-b). The topographic phase contribution in an interferogram increases with an increasing perpendicular baseline ($B_{\perp}$), while the phase contribution from surface movement is independent from the baseline. Hence, it is possible to remove the effect from glacier movement by differential InSAR assuming that the line-of-sight velocities are similar in both interferograms (Fig. 2c). Continuous GNSS measurements of stake positions at Austfonna in 2009-2010 indicate that the surface velocities are fairly stable during the winter season.

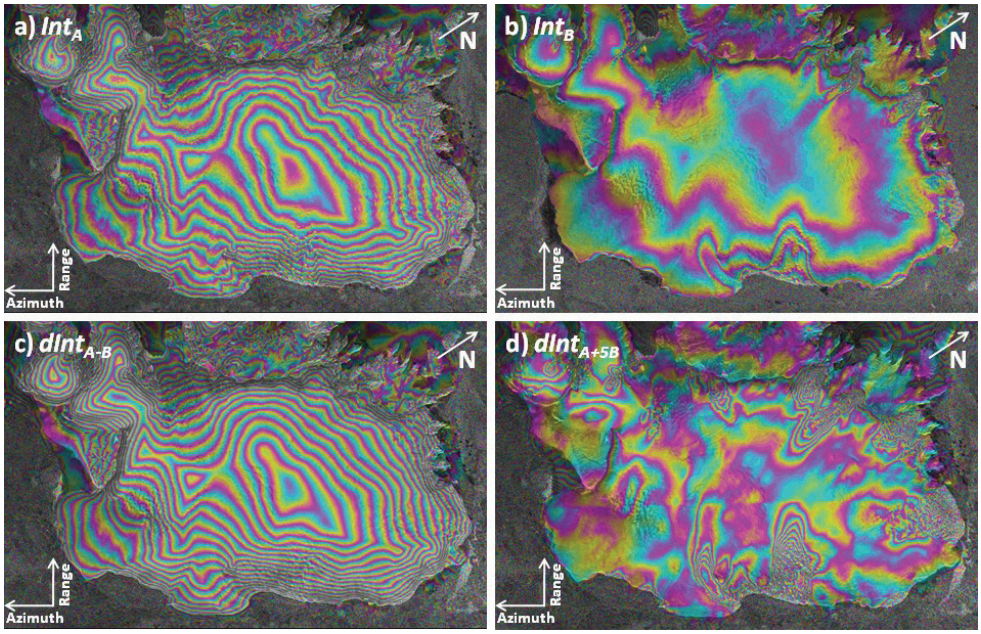

Fig. 2. Two-pass interferograms (*Int*) and smoothed combined interferograms (*dInt*): (a) Int_A from 5-6 March 1996 with dominating topographic fringes ($B_\perp = 178\ m$), (b) Int_B from 9-10 April 1996 with some visible movement fringes ($B_\perp \approx 34\ m$), (c) $dInt_{A-B}$ with topography only ($B_\perp \approx 212\ m$), and (d) $dInt_{A+5B}$ with most topography removed ($B_\perp \approx 8\ m$) and upscaled movement fringes remaining.

The most critical step in DInSAR processing is phase unwrapping. It is the process of adding the correct multiple of 2π to the interferogram fringes which are otherwise only known modulo 2 π. We used a branch-cut algorithm (Goldstein et al., 1988) which isolates potential discontinuities in the interferogram and then unwraps along paths of integration between the branch-cut barriers. The phase coherence was mostly good for both interferograms, and the gentle and smooth ice cap surface ensures a good continuity between the fringes. The resulting unwrapped interferogram ($dInt_{unw}$) defines a topographic surface of absolute phases at a combined perpendicular baseline of 212 m (Table 1), corresponding to a topographic sensitivity of about 50 m per fringe.

4. DEM generation

The unwrapped phases of the topographic interferogram ($dInt_{unw}$) were transformed into real elevations and a geocoded DEM through the following steps:

- Transformation of ICESat GCPs from UTM coordinates to SAR coordinates (range, azimuth)
- Least-squares baseline refinement using the transformed ICESat GCPs

- Phase-to-height transformation and geocoding into map geometry (UTM)
- Removal and smoothing of topographic inconsistencies (erroneous holes and cliffs)
- Resampling into a 50×50 m DEM and clipping to the glacier outlines (Fig. 1)

Precise Delft ephemerides were used to transform the ICESat GCPs from map to SAR geometry and to geocode the DEM from SAR to map geometry. We also attempted to refine the geocoding by matching one of the SAR intensity images with a simulated intensity image from an external DEM in map geometry, but that proved difficult due to the large fraction of uncorrelated surfaces over the ice cap and the ocean. The quality of the geocoding was instead evaluated by checking for correlations between aspect and elevation deviation (normalized by slope) between the geocoded DEM and ICESat (Nuth and Kääb, 2010). No significant trends were found, and the corresponding orthorectified intensity image (Fig. 1) fitted well to the coastline and glacier outlines. We did therefore not perform any further geo-referencing of the DEM. Higher order geo-referencing is precarious at Austfonna due to lacking ground reference on the southeast side of the ice cap.

Although the Delft orbits have an estimated radial RMS error of only 5 cm (Scharroo and Visser, 1998), the baseline uncertainty still have a major impact on the precision of the topographic surface of unwrapped phases. The height-equivalent RMS error of the linear fit between ICESat GCPs and unwrapped phases decreased from ≈40 m to ≈10 m after the refinement of the interferometric baseline. The refinement procedure optimizes the fit between unwrapped phases and GCP elevations by adjusting the baseline parameters in a least-squares way. Hence, the baseline is not necessarily adjusted to the exact SAR acquisition geometry of 1996, but rather to the optimal baseline configuration for fitting the DEM with the GCPs from 2006-2008. Ideally, we should have used GCPs and SAR scenes from the same time. A few airborne laser profiles are available from spring 1996 (Bamber et al., 2004), but unfortunately the spatial coverage of the GCPs was not sufficient to refine a baseline that would yield consistent elevations throughout the ice cap.

Discontinuous phases and errors in the phase unwrapping can cause data gaps and elevation jumps in the resulting DEM. All the ice cap interior was continuous and smooth, but a few smaller data voids and topographic inconsistencies were present along the margins. We suspected that pixels with a DEM-derived surface slope higher than 10° were erroneous. These pixels were classified as data voids and then filled in linearly from the surrounding pixels. Surface slopes were then calculated over again, and new error areas were identified. This process was repeated iteratively until all slopes were brought below 10°. About 1 % of the pixels were interpolated in this way, and the maximum interpolation distance was 500 m.

The main DEM was produced from GCPs with orthometric heights (above sea level) relative to the EGM2008 geoid. Since most satellite systems operate in an ellipsoidic reference systems, we also constructed a DEM with ellipsoidic heights relative to the WGS84 ellipsoid. The ICESat GCP coordinates were first transformed from the TOPEX/Poseidon ellipsoid to the WGS84 ellipsoid, and then the DEM was generated in the same way as for the orthometric DEM. The DEM validation with respect to GNSS and lidar data were done for the ellipsoidic DEM rather than transforming the data into orthometric heights. The geoid height of EGM2008 with respect to the WGS84 ellipsoid varies from 25 to 29 m across Austfonna from the east to the west.

4. DEM validation and errors

The DEM was validated against ICESat GCPs and independent surface profiles from GNSS and airborne lidar (Fig. 3 and 4). The point elevations were compared with the DEM by means of bilinear interpolation, yielding 5-6000 points of comparison for each data set. The mean bias of the DEM was close to zero for the ICESat and lidar data sets and -4 m for the GNSS data set. The standard deviations were 11 m, 10 m and 8 m respectively. The larger bias and smaller standard deviation of the GNSS comparison is probably because the GNSS profiles are spatially biased towards the higher elevations of the ice cap (Fig. 4). The most reliable error estimate is probably that of the ICESat comparison where the profiles are well distributed over the entire ice cap. The dependency between the ICESat GCPs and the DEM should have little impact since they are only used for baseline refinement without any local elevation adjustments. Hence, we would expect the same level of precision if the DEM was validated against other data of equal quality and coverage, e.g. CryoSat-2.

DEM errors can be due to low phase coherence, atmospheric disturbance, residual glacier movement, signal penetration and temporal elevation change. The baseline refinement procedure adjusts the DEM to the average elevation of the GCPs and accounts for elevation errors that vary linearly with elevation. Such elevation-dependent errors can be atmospheric disturbances and spatial variations in signal penetration and elevation change. Elevation changes between the 1996 SAR acquisitions and the 2006-2008 ICESat observations are probably on the order of ±5-10 m with thickening in the interior and thinning towards the margins (Bamber et al., 2004; Moholdt et al., 2010a). Most of this regular pattern should be incorporated in the baseline refinement, but local and non-linear elevation changes will remain in the resulting DEM. The elevation bias from the penetration of SAR signals into snow and ice will be corrected for the average penetration-depth and potential linear trends with elevation. The depth of the C-band phase center is less than a few meters in exposed ice, but it can be up to 10 m in cold and dry firn (Rignot et al., 2001). Surface

profiles with C-band ground-penetrating radar at Svalbard have shown a variation in the phase-center depth from about 1 m in the ablation area to up to 5 m in the firn area (Müller et al., Subm). The effect of small-scale errors like speckle noise has most likely been reduced by the multi-look averaging in the interferogram generation and the adaptive filtering prior to the phase unwrapping. Additional DEM smoothing by low-pass mean filtering did not improve the overall precision of the DEM nor the local slope correspondence between the DEM and pairs of neighboring ICESat observations separated by ≈170 m.

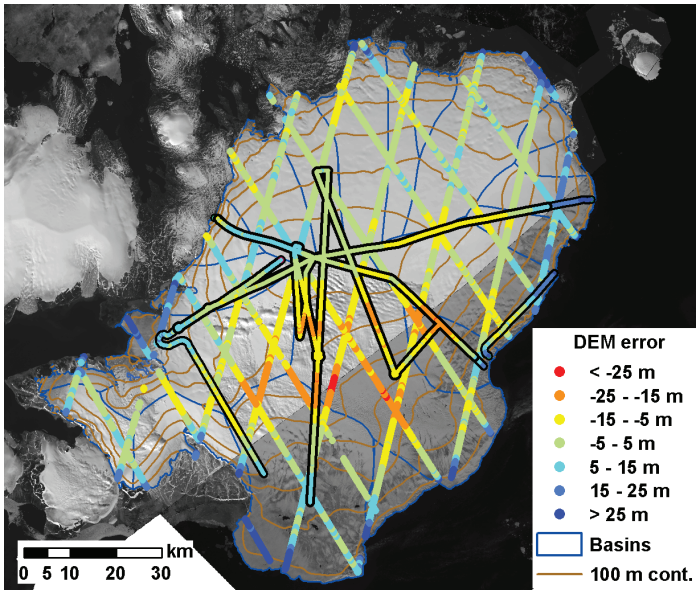

Fig. 3. Validation of the DEM with respect to ICESat GCPs from winter 2006-2008 (profiles with no outlines), GNSS surface profiles and airborne lidar (black outlines). The vertical RMS error of the DEM was 9-11 m with respect to each of the three reference data sets (Fig. 4). The underlying images are a SPOT-5 scene from 14 August 2008 and a Landsat scene from 10 July 2001 which were used to digitize new glacier outlines.

The DEM is consistently too high in the lowermost parts of the ice cap (Fig. 3 and 4). This is probably due to a strong frontal thinning of 1-3 m y^{-1} which is not compensated by the baseline refinement because the relation between elevation and elevation change has more of a curved trend than a linear trend at Austfonna (Moholdt et al., 2010a). The elevation overestimation along the margins is compensated by a slight underestimation in the interior, especially in the three known surge-type basins in the central south (Fig. 1 and 3). These quiescent basins might have been thickening faster than the other basins (Bamber et al., 2004; Bevan et al., 2007) although this was not evident between 2002 and 2008 (Moholdt et al., 2010a). The elevation-dependent bias in the

DEM can be removed by fitting a curve to the errors in Fig. 4 and correcting the DEM elevations accordingly. This would improve the precision of the DEM by about 2 m, but we chose to keep it in the original format rather than applying empirical adjustments which might not apply everywhere.

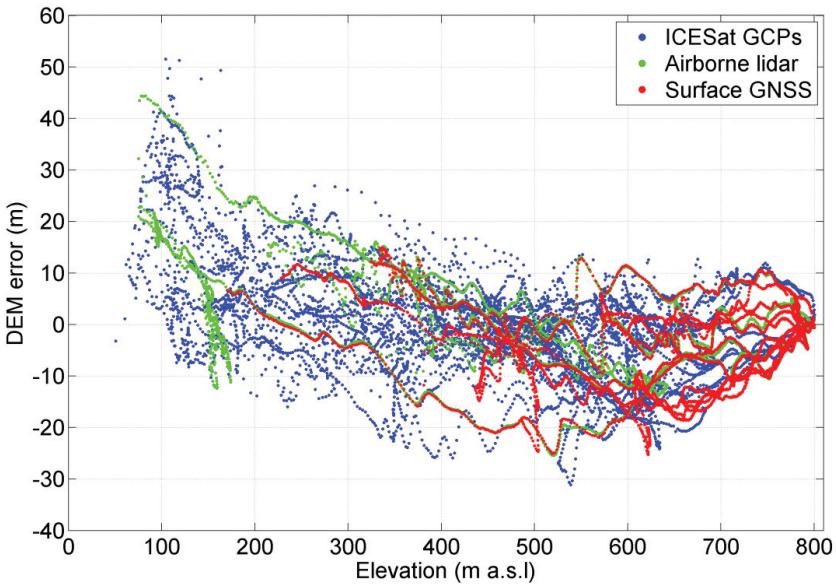

Fig. 4. Elevation differences between the DEM and the three validation data sets; ICESat GCPs, airborne lidar and surface GNSS profiles. The RMS error of the DEM with respect to the three data sets is 11 m, 10 m and 9 m, respectively. The spatial distribution of the data can be seen in Fig. 3.

DEMs can be used to derive maps of slope, aspect and topographic shading (e.g. Wilson and Gallant, 2000) which can further be used to validate the DEM. The slope precision of the DEM is estimated to about 0.3° at spatial scales of 50-200 m as compared to slopes derived from GNSS and ICESat. Compared to ICESat repeat-track planes (Moholdt et al., 2010b), the standard deviation of slopes and aspects are 0.5° and 24°, respectively. The mean slope difference was close to zero in both cases, indicating a similar degree of smoothness between the data sets. The variation in slope and aspect across Austfonna is visualized in a hillshade model in Fig. 5. The major drainage divides can be clearly identified, as well as some areas with rolling topography and phase noise.

The two previous Austfonna DEMs from DInSAR (Unwin and Wingham, 1997) and from optical shape-from-shading (Bingham and Rees, 1999) have been reported to have elevation precisions of 8 m and 14 m with respect to the 1983 RES data. The precision of the DInSAR DEM was however calculated over a small rectangular area in the interior of the ice cap where the quality of the RES

data was best. The standard deviation of the DEM increased to 42 m if all RES data were included in the comparison, but parts of this uncertainty is due to the rough RES elevations which have a precision of 17 m as calculated from 256 crossover points. Recent optical stereo DEMs from the IPY SPIRIT project (Korona et al., 2009) and the ASTER GDEM project (Fujisada et al., 2005) have a good precision in glacier areas with high image correlation, but the usage of these DEMs at Austfonna is so far limited by holes and artifacts in the summit area where the image matching has failed.

5. DEM applications

Slopes and aspects derived from a DEM are input parameters for calculating incoming solar radiation at a particular location in surface mass balance models (Hock, 1999; Schuler et al., 2007). Surface slopes are also used to calculate driving stresses in studies of glacier dynamics (Dowdeswell, 1986; Dunse et al., Subm.). Local surface slopes are essential for elevation change analysis of repeat-track satellite altimetry if a DEM is used to correct for the cross-track slope between near repeat-tracks (Slobbe et al., 2008; Moholdt et al., 2010a). The average slope of the Austfonna DEM was calculated to 1.4° which infers a relative elevation difference of 2.4 m between two parallel tracks separated by 100 m. Such cross-track elevation differences need to be corrected in order to detect elevation changes of less than a meter. The DEM has already been applied for this purpose in two studies of repeat-track ICESat elevation changes (Moholdt et al., 2010a; 2010b).

Glacier drainage basins can be determined from a DEM by assuming down-slope movement of ice. Accurate basin outlines are important for studies of glacier dynamics (Dowdeswell, 1986; Bevan et al., 2007) and surface mass balance (Moholdt et al., 2010a). DEM-derived maps of aspect, slope and topographic shading were used to update the existing basin outlines (Dowdeswell, 1986; Hagen et al., 1993) to the current geometry (Fig. 1). The basins were further adjusted according to visual ridges in the SPOT and Landsat scenes (Fig. 3) and the SAR intensity images (Fig. 1). The digitized basin outlines were finally checked against the scaled movement interferogram $dInt_{A+5B}$ (Fig. 2d) to ensure that the topographic divides were consistent with the dynamic divides. The detectable glacier flow-fields generally fitted well to the topographic basins, so no further adjustments were necessary.

Glacier hypsometry is the distribution of glacier area with elevation. Hypsometry is a major control on the glacier-wide surface mass balance, and it is often used to extrapolate elevation-dependent measurements to unsampled glacier areas. We calculated glacier areas within 100 m elevation bins for the new and old Austfonna DEM (Fig. 5). Although the lower elevations have been thinning over the past few decades (Bamber et al., 2004; Moholdt et al., 2010a), there is no

apparent change in the hypsometry at the lowermost elevations due to the simultaneous retreat of the tidewater fronts (Dowdeswell et al., 2008). At medium elevations (200-600 m), the new DEM has slightly smaller areas than the old one, which is fully compensated by a 65 % higher area in the uppermost bin (700-800 m). The maximum elevation of the new DEM is 800 m (a.s.l.) whereas it is only 760 m for the old DEM. The impact of the hypsometric difference on surface mass balance extrapolations is large locally in the summit area, but only +0.01 m w.e. y^{-1} at average when a specific balance of +0.5 m w.e. y^{-1} (Pinglot et al., 2001) in the uppermost bin is extrapolated to the remaining ice cap area. Assuming a constant climate, the long-term hypsometric trend of interior thickening combined with peripheral thinning and retreat will cause an increasingly positive specific surface mass balance until it is compensated by glacier acceleration or surging.

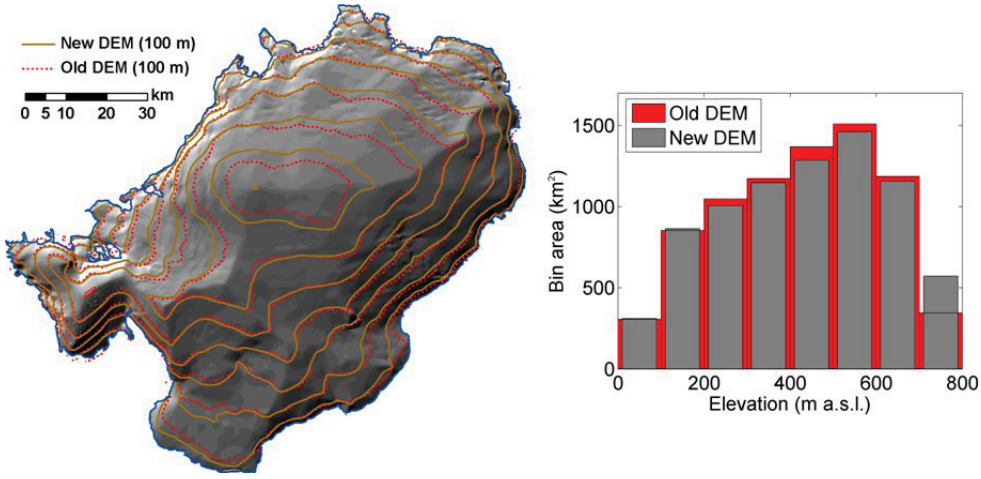

Fig. 5. A comparison of contour lines for the new and old DEM of Austfonna. The old DEM is a smoothed merge (K. Melvold, pers. com.) of the RES-tied InSAR DEM (Unwin and Wingham, 1997) and photogrammetric data from the Norwegian Polar Institute (NPI, 2010). The corresponding glacier hypsometries for 100 m elevation bins are shown to the right. The contour lines are underlain by a hillshade model of the new DEM, showing the major drainage divides of the ice cap.

6. Conclusions

We have generated a new DEM of Austfonna by performing differential SAR interferometry (DInSAR) on two pairs of ERS-1/2 tandem images from 1996. The precision of DInSAR DEMs depends mainly on the length and accuracy of the interferometric baseline. We used ICESat laser altimetry from winter 2006-2008 as ground control points to refine the baseline parameters. ICESat is ideal for this purpose since it provides accurate surface elevations at a homogeneous spatial distribution. The

baseline refinement with ICESat improved the precision of the DEM from ≈40 m to ≈10 m as compared to ICESat and independent surface profiles from GNSS and airborne lidar. The DEM has no overall bias, but there is an elevation-dependent bias with too high elevations along the margins and slightly too low elevations in the interior. This is most likely due to non-linear elevation change in the decade between the SAR and ICESat acqusitions. With the availability of coincident SAR and altimetry data from new satellite systems like TanDEM-X (Krieger et al., 2007) and CryoSat-2 (Wingham et al., 2006), it will probably be possible to generate ice cap DEMs in a similar way with significantly better accuracies than in this study.

The new Austfonna DEM has proven useful for elevation change studies where multitemporal ICESat altimetry data need to be corrected for the cross-track slope between near repeat-tracks (Moholdt et al., 2010a; 2010b). It is also well suited for delineating glacier drainage basins and calculating glacier hypsometries. The new glacier DEM and basin outlines will serve as a baseline data set for future and ongoing research on Austfonna, including surface mass balance monitoring and modelling, studies of glacier dynamics and elevation change analysis. All data presented here will be freely available through the University of Oslo and the IPY-GLACIODYN project (IPY, 2010).

Acknowledgements

This work was supported by funding to the CryoSat calibration and validation experiment (CryoVEX), the GLACIODYN project of the International Polar Year (IPY), and the ice2sea programme from the European Union 7th Framework Programme, grant number 226375, ice2sea contribution number 018. G. Moholdt was also supported through the Arktisstipend grant from the Svalbard Science Forum. We are thankful to the numerous data contributors, namely the European Space Agency proposal AOCRY.2683 (SAR data), the Delft University of Technology (ERS ephemerides), the National Snow and Ice Data Center (ICESat data), the National Space Institute at the Technical University of Denmark (lidar data), the US Geological Survey GloVis (Landsat data), the IPY-SPIRIT project (SPOT 5 stereoscopic survey of Polar Ice: Reference Images and Topographies), NASA and METI (ASTER GDEM), the Norwegian Polar Institute (topographic data) and J. Dowdeswell / T. Benham (RES data). Fieldwork at Austfonna is a joint project between the University of Oslo and NPI, and all participants are acknowledged. We also thank C. Nuth for helping out with the DEM validation. The DEM and basin outlines can be freely accessed from the IPY data server (IPY, 2010).

References

Arnold, N.S., Rees, W.G., Devereux, B.J., & Amable, G.S. (2006). Evaluating the potential of high-resolution airborne LiDAR data in glaciology. *International Journal of Remote Sensing, 27*, 1233-1251.

Baek, S., Kwoun, O.I., Braun, A., Lu, Z., & Shum, C.K. (2005). Digital elevation model of King Edward VII Peninsula, West Antarctica, from SAR interferometry and ICESat laser altimetry. *IEEE Geoscience and Remote Sensing Letters, 2*, 413-417.

Bamber, J., Krabill, W., Raper, V., & Dowdeswell, J. (2004). Anomalous recent growth of part of a large Arctic ice cap: Austfonna, Svalbard. *Geophysical Research Letters, 31*.

Bevan, S., Luckman, A., Murray, T., Sykes, H., & Kohler, J. (2007). Positive mass balance during the late 20th century on Austfonna, Svalbard, revealed using satellite radar interferometry. *Annals of Glaciology, 46*, 117-122.

Bingham, A.W., & Rees, W.G. (1999). Construction of a high-resolution DEM of an Arctic ice cap using shape-from-shading. *International Journal of Remote Sensing, 20*, 3231-3242.

Brenner, A.C., DiMarzio, J.R., & Zwally, H.J. (2007). Precision and accuracy of satellite radar and laser altimeter data over the continental ice sheets. *IEEE Transactions on Geoscience and Remote Sensing, 45*, 321-331.

Dall, J., Madsen, S.N., Keller, K., & Forsberg, R. (2001). Topography and penetration of the Greenland ice sheet measured with airborne SAR interferometry. *Geophysical Research Letters, 28*, 1703-1706.

DiMarzio, J., Brenner, A., Schutz, B., Shuman, C.A., & Zwally, H.J. (2007). *GLAS/ICESat laser altimetry digital elevation models of Greenland (1 km) and Antarctica (500 m)*. Boulder, Colorado USA: National Snow and Ice Data Center. Digital media.

Dowdeswell, J.A. (1986). Drainage-basin characteristics of Nordaustlandet ice caps, Svalbard. *Journal of Glaciology, 32*, 31-38.

Dowdeswell, J.A., Drewry, D.J., Cooper, A.P.R., Gorman, M.R., Liestøl, O., & Orheim, O. (1986). Digital mapping of the Nordaustlandet ice caps from airborne geophysical investigations. *Annals of Glaciology, 8*, 51–58.

Dowdeswell, J.A., Unwin, B., Nuttall, A.M., & Wingham, D.J. (1999). Velocity structure, flow instability and mass flux on a large Arctic ice cap from satellite radar interferometry. *Earth and Planetary Science Letters, 167*, 131-140.

Dowdeswell, J.A., Benham, T.J., Strozzi, T., & Hagen, J.O. (2008). Iceberg calving flux and mass balance of the Austfonna ice cap on Nordaustlandet, Svalbard. *Journal of Geophysical Research-Earth Surface, 113*.

Drews, R., Rack, W., Wesche, C., & Helm, V. (2009). A spatially adjusted elevation model in Dronning Maud Land, Antarctica, based on differential SAR interferometry. *IEEE Transactions on Geoscience and Remote Sensing, 47*, 2501-2509.

Dunse, T., Greve, R., Schuler, T.V., & Hagen, J.O. (Subm.). Permanent fast flow vs. cyclic surge behavior: numerical simulations of the Austfonna ice cap, Svalbard. *Journal of Glaciology*.

Eiken, T., Hagen, J.O., & Melvold, K. (1997). Kinematic GPS survey of geometry changes on Svalbard glaciers. *Annals of Glaciology, 24*, 157-163.

Forsberg, R., Keller, K., & Jacobsen, S.M. (2002). Airborne lidar measurements for cryosat validation. *IEEE International Geoscience and Remote Sensing Symposium (IGARSS 2002) and 24th Canadian Symposium on Remote Sensing* (pp. 1756-1758). Toronto, Canada.

Fricker, H.A., Borsa, A., Minster, B., Carabajal, C., Quinn, K., & Bills, B. (2005). Assessment of ICESat performance at the Salar de Uyuni, Bolivia. *Geophysical Research Letters, 32*.

Fujisada, H., Bailey, G.B., Kelly, G.G., Hara, S., & Abrams, M.J. (2005). ASTER DEM performance. *IEEE Transactions on Geoscience and Remote Sensing, 43*, 2707-2714.

Goldstein, R.M., Zebker, H.A., & Werner, C.L. (1988). Satellite radar interferometry - Two-dimensional phase unwrapping. *Radio Science, 23*, 713-720.

Hagen, J.O., Liestøl, O., Roland, E., & Jørgensen., T. (1993). *Glacier atlas of Svalbard and Jan Mayen*. Meddelser nr. 129 (141 pp.). Oslo: Norwegian Polar Institute.

Hock, R. (1999). A distributed temperature-index ice- and snowmelt model including potential direct solar radiation. *Journal of Glaciology, 45*, 101-111.

IPY (2010). *The IPY-GLACIODYN project; the dynamic response of Arctic glaciers to global warming*. The International Polar Year data center (not yet online).

Joughin, I., Winebrenner, D., Fahnestock, M., Kwok, R., & Krabill, W. (1996). Measurement of ice-sheet topography using satellite radar interferometry. *Journal of Glaciology, 42*, 10-22.

Korona, J., Berthier, E., Bernard, M., Remy, F., & Thouvenot, E. (2009). SPIRIT. SPOT 5 stereoscopic survey of Polar Ice: Reference Images and Topographies during the fourth International Polar Year (2007-2009). *ISPRS Journal of Photogrammetry and Remote Sensing, 64*, 204-212.

Krieger, G., Moreira, A., Fiedler, H., Hajnsek, I., Werner, M., Younis, M., & Zink, M. (2007). TanDEM-X: A satellite formation for high-resolution SAR interferometry. *IEEE Transactions on Geoscience and Remote Sensing, 45*, 3317-3341.

Kwok, R., & Fahnestock, M.A. (1996). Ice sheet motion and topography from radar interferometry. *IEEE Transactions on Geoscience and Remote Sensing, 34*, 189-200.

Kääb, A. (2008). Glacier Volume Changes Using ASTER Satellite Stereo and ICESat GLAS Laser Altimetry. A Test Study on Edgeoya, Eastern Svalbard. *IEEE Transactions on Geoscience and Remote Sensing, 46*, 2823-2830.

Lefauconnier, B., & Hagen, J.O. (1991). *Surging and calving glaciers in Eastern Svalbard*. Meddelelser (130 pp). Oslo: Norwegian Polar Institute.

Moholdt, G. (2010). *Elevation change and mass balance of Svalbard glaciers from geodetic data*. PhD thesis. University of Oslo, Norway.

Moholdt, G., Hagen, J.O., Eiken, T., & Schuler, T.V. (2010a). Geometric changes and mass balance of the Austfonna ice cap, Svalbard. *The Cryosphere, 4*, 21-34.

Moholdt, G., Nuth, C., Hagen, J.O., & Kohler, J. (2010b). Recent elevation changes of Svalbard glaciers derived from ICESat laser altimetry. *Remote Sensing of Environment, 114*, 2756-2767.

Müller, K., Hamran, S.E., Sinisalo, A., & Hagen, J.O. (Subm). Microwave backscatter from Arctic firn and its relation to the phase center. *Submitted to IEEE Transactions on Geoscience and Remote Sensing*.

NPI (2010). *Topographic map series of Svalbard (1:100 000)*. The Norwegian Polar Institute, Tromsø, Norway: http://npweb.npolar.no/english/subjects/1165397816.46 (visited Oct. 2010).

Nuth, C., Kohler, J., Aas, H.F., Brandt, O., & Hagen, J.O. (2007). Glacier geometry and elevation changes on Svalbard (1936-90): a baseline dataset. *Annals of Glaciology, 46*, 106-116.

Nuth, C., & Kääb, A. (2010). What's in an elevation difference? Accuracy and corrections of satellite elevation data sets for quantification of glacier changes. *The Cryosphere Discuss., 4*, 2013-2077.

Pinglot, J.F., Hagen, J.O., Melvold, K., Eiken, T., & Vincent, C. (2001). A mean net accumulation pattern derived from radioactive layers and radar soundings on Austfonna, Nordaustlandet, Svalbard. *Journal of Glaciology, 47*, 555-566.

Rignot, E., Echelmeyer, K., & Krabill, W. (2001). Penetration depth of interferometric synthetic-aperture radar signals in snow and ice. *Geophysical Research Letters, 28*, 3501-3504.

Rott, H. (2009). Advances in interferometric synthetic aperture radar (InSAR) in earth system science. *Progress in Physical Geography, 33*, 769-791.

Scharroo, R., & Visser, P. (1998). Precise orbit determination and gravity field improvement for the ERS satellites. *Journal of Geophysical Research-Oceans, 103*, 8113-8127.

Schuler, T.V., Loe, E., Taurisano, A., Eiken, T., Hagen, J.O., & Kohler, J. (2007). Calibrating a surface mass-balance model for Austfonna ice cap, Svalbard. *Annals of Glaciology, 46*, 241-248.

Slobbe, D.C., Lindenbergh, R.C., & Ditmar, P. (2008). Estimation of volume change rates of Greenland's ice sheet from ICESat data using overlapping footprints. *Remote Sensing of Environment, 112*, 4204-4213.

Strozzi, T., Kouraev, A., Wiesmann, A., Wegmuller, U., Sharov, A., & Werner, C. (2008). Estimation of Arctic glacier motion with satellite L-band SAR data. *Remote Sensing of Environment, 112*, 636-645.

Unwin, B., & Wingham, D. (1997). Topography and dynamics of Austfonna, Nordaustlandet, Svalbard, from SAR interferometry. *Annals of Glaciology, 24*, 403-408.

Wegmüller, U., & Werner, C. (1997). Gamma SAR processor and interferometry software. *3rd ERS Symposium on Space at the Service of Our Environment* (pp. 1687-1692). Florence, Italy, Mar. 14-21, 1997: European Space Agency.

Wilson, J., & Gallant, J. (2000). *Terrain analysis: principles and applications*. (479 pp.). New York, USA: John Wiley & Sons Inc.

Wingham, D.J., Francis, C.R., Baker, S., Bouzinac, C., Brockley, D., Cullen, R., de Chateau-Thierry, P., Laxon, S.W., Mallow, U., Mavrocordatos, C., Phalippou, L., Ratier, G., Rey, L., Rostan, F., Viau, P., & Wallis, D.W. (2006). CryoSat: A mission to determine the fluctuations in Earth's land and marine ice fields. *Natural Hazards and Oceanographic Processes from Satellite Data, 37*, 841-871.

Yi, D.H., Zwally, H.J., & Sun, X.L. (2005). ICESat measurement of Greenland ice sheet surface slope and roughness. *Annals of Glaciology, 42*, 83-89.

Zwally, H.J., Schutz, B., Abdalati, W., Abshire, J., Bentley, C., Brenner, A., Bufton, J., Dezio, J., Hancock, D., Harding, D., Herring, T., Minster, B., Quinn, K., Palm, S., Spinhirne, J., & Thomas, R. (2002). ICESat's laser measurements of polar ice, atmosphere, ocean, and land. *Journal of Geodynamics, 34*, 405-445.

Zwally, H.J., Schutz, R., Bentley, C., Bufton, J., Herring, T., Minster, B., Spinhirne, J., & Thomas, R. (2010). *GLAS/ICESat L1B Global Elevation Data V031, 20 February 2003 to 11 October 2009*. Boulder, CO: National Snow and Ice Data Center. Digital media.

II

The Cryosphere, 4, 21–34, 2010
www.the-cryosphere.net/4/21/2010/

The Cryosphere

Geometric changes and mass balance of the Austfonna ice cap, Svalbard

G. Moholdt, J. O. Hagen, T. Eiken, and T. V. Schuler

Department of Geosciences, University of Oslo, Box 1047 Blindern, 0316 Oslo, Norway

Received: 17 September 2009 – Published in The Cryosphere Discuss.: 13 October 2009
Revised: 29 December 2009 – Accepted: 6 January 2010 – Published: 19 January 2010

Abstract. The dynamics and mass balance regime of the Austfonna ice cap, the largest glacier on Svalbard, deviates significantly from most other glaciers in the region and is not fully understood. We have compared ICESat laser altimetry, airborne laser altimetry, GNSS surface profiles and radio echo-sounding data to estimate elevation change rates for the periods 1983–2007 and 2002–2008. The data sets indicate a pronounced interior thickening of up to $0.5\,\mathrm{m\,y^{-1}}$, at the same time as the margins are thinning at a rate of $1–3\,\mathrm{m\,y^{-1}}$. The southern basins are thickening at a higher rate than the northern basins due to a higher accumulation rate. The overall volume change in the 2002–2008 period is estimated to be $-1.3\pm0.5\,\mathrm{km^3\,w.e.\,y^{-1}}$ (or $-0.16\pm0.06\,\mathrm{m\,w.e.\,y^{-1}}$) where the entire net loss is due to a rapid retreat of the calving fronts. Since most of the marine ice loss occurs below sea level, Austfonna's current contribution to sea level change is close to zero. The geodetic results are compared to in-situ mass balance measurements which indicate that the 2004–2008 surface net mass balance has been slightly positive ($0.05\,\mathrm{m\,w.e.\,y^{-1}}$) though with large annual variations. Similarities between local net mass balances and local elevation changes indicate that most of the ice cap is slow-moving and not in dynamic equilibrium with the current climate. More knowledge is needed about century-scale dynamic processes in order to predict the future evolution of Austfonna based on climate scenarios.

1 Introduction

Glaciers and ice caps are expected to be significant contributors to sea level rise in the 21st century (e.g. Meier et al., 2007). Traditionally, regional and global mass balances have been extrapolated from a series of local mass balance estimates acquired from annual stake and snow pit measurements (e.g. Dyurgerov and Meier, 1997; Dowdeswell et al., 1997; Hagen et al., 2003b). Remote sensing techniques like photogrammetry, altimetry and synthetic aperture radar (SAR) have made it possible to expand mass balance measurements to vast and remote areas. Airborne laser altimetry has been widely used to measure elevation changes, e.g. in Alaska (Arendt et al., 2006), Arctic Canada (Abdalati et al., 2004) and Svalbard (Bamber et al., 2005). Glacier changes have also been quantified using spaceborne techniques like the Shuttle Radar Topography Mission (SRTM) (Rignot et al., 2003), the Ice, Cloud and land Elevation Satellite (ICESat) (Nuth et al., 2010) and the Gravity Recovery and Climate Experiment (GRACE) (Luthcke et al., 2008).

The Svalbard archipelago has a total glacier area of $\sim36\,000\,\mathrm{km^2}$ (Hagen et al., 2003a) which is about 7% of the worldwide glacier coverage outside of Greenland and Antarctica (Lemke et al., 2007). Several studies have shown that the mass balance of western Svalbard glaciers has been negative over the last century (e.g. Hagen et al., 2003b; Nuth et al., 2007). Kohler et al. (2007) claim that the glacier thinning rates in western Svalbard have been accelerating over the last few decades. The mass balance of eastern Svalbard glaciers is more uncertain due to a lack of long-term mass balance programs and few repeated geodetic observations. Nuth et al. (2010) compared topographic maps from 1965–1990 with recent ICESat altimetry to find that Svalbard glaciers have been thinning at an average water equivalent (w.e.) rate of $0.36\,\mathrm{m\,w.e.\,y^{-1}}$ over the last few decades. However, this study did not include Austfonna which at $\sim8000\,\mathrm{km^2}$ is the largest single ice body within the Svalbard archipelago.

There have been several separate glaciological investigations at Austfonna (e.g. Schytt, 1964; Dowdeswell and

Correspondence to: G. Moholdt
(geirmoh@geo.uio.no)

Drewry, 1989; Pinglot et al., 2001), but no continuous records of mass balance exist until 2004 when an annual mass balance program was initiated. Photogrammetric records are also sparse over Austfonna due to the large extent and featureless topography which make image analysis extremely difficult. Airborne laser altimetry from 1996 and 2002, indicated thickening of up to $0.5\,m\,y^{-1}$ in the summit area and thinning towards the margins (Bamber et al., 2004). The authors proposed that this growth was due to increased precipitation related to the loss of perennial sea ice cover in the adjacent Barents Sea. A mass build up in the accumulation area was also found by Bevan et al. (2007) who compared surface velocities derived from differential SAR interferometry (DInSAR) with calculated balance velocities across the glacier equilibrium line altitude (ELA). They suggested an underlying dynamic component to the changes since 75% of the mass gain was attributed to three basins that are expected to be in the quiescent phase of their surge cycles.

We compare several sources of altimetric observations over Austfonna to estimate elevation change rates for the periods 1983–2007 and 2002–2008. The data sets include airborne radio echo-sounding (RES) data from 1983 and 2007, GNSS (Global Navigation Satellite System) surface profiles from 2004–2008, airborne laser altimetry from 2002, 2004 and 2007, and ICESat laser altimetry from 2003–2008. We use a combination of repeat track analysis and crossover points to estimate average elevation change rates, and then we combine them in a hypsometric way to derive volume change rates. Finally, the geodetic change rates are compared to in situ mass balance measurements from 2004–2008.

2 Study site

Austfonna is a $\sim$8000 km^2 large polythermal ice cap located at 80° N on Nordaustlandet island in the northeast corner of Svalbard (Fig. 1c). The ice cap geometry is characterized by one main ice dome which rises gently up to about 800 m a.s.l. and feeds a number of drainage basins (Fig. 1a). Apart from a few fast flowing units, most of the ice cap is slow-moving with typical velocities less than $10\,m\,y^{-1}$ (Dowdeswell et al., 1999; Strozzi et al., 2008). Surge advances have been reported for three of the basins (Fig. 1a), namely Etonbreen (1938), Braasvellbreen (1937) and Basin 3 ($\sim$1873) (Lefauconnier and Hagen, 1991). About 30% of the ice cap is grounded below sea level, with ice thicknesses typically ranging from $<$300 m in the marine southeast to $\sim$500 m in the interior (Dowdeswell et al., 1986). The grounded calving fronts have a total length of 230 km and have been retreating during the last decades. Dowdeswell et al. (2008) used satellite images from between 1973 and 2001 to estimate a mean area loss rate of $11\,km^2\,y^{-1}$, of which 90% was due to marine retreat. By combining this data with terminus ice thicknesses from 1983 RES and velocities from 1996 DInSAR, they were able to estimate a total iceberg calving flux of $2.5\pm0.5\,km^3$ w.e. y^{-1}.

Meteorological conditions at Austfonna are very variable due to its location at the confluence zone between cold and dry polar air masses from the north and more humid and warm air masses from the North Atlantic current to the south. Two automatic weather stations (Fig. 1a) collecting data on Austfonna since 2004 show that the mean daily winter temperatures range from about $-30\,°C$ to $0\,°C$. The meteorological conditions during the summer season are less variable; daily temperatures usually range from $0\,°C$ to $5\,°C$ during the 1–2 months long ablation period. Most of the winter precipitation over the ice cap is originating from the Barents Sea in the southeast, resulting in a pronounced accumulation gradient with most snow in the southeast and least snow in the northwest (Schytt, 1964; Pinglot et al., 2001; Taurisano et al., 2007). This pattern is also recognized in the equilibrium line altitude (ELA) which is significantly lower in southeast than in northwest (Pinglot et al., 2001; Schuler et al., 2007). Pinglot et al. (2001) estimated an average net mass balance of $0.5\,m$ w.e. y^{-1} in the summit area for the period 1986–1998/99 by detecting the depth of the radioactive 1986 Chernobyl layer in 19 shallow ice cores (Fig. 1a). Since 2004, in-situ mass balance measurements have been carried out each spring along several transects (Fig. 1a). In addition to point measurements using mass balance stakes and snow pits, the annual snow cover has been mapped using an 800 MHz ground penetrating radar (GPR) supplemented by manual probing to the previous summer surface (Kohler et al., 1997; Taurisano et al., 2007). The annual accumulation can vary by a factor of two, but the spatial pattern remains more or less similar from year to year. Taurisano et al. (2007) used spatial multiple regression to compile an accumulation index map for the distribution of accumulation. This was further used by Schuler et al. (2007) to model the surface mass balance using a distributed temperature-index approach (Hock, 1999).

3 Data

Repeat track GNSS profiling was carried out along designated tracks each spring over a period of two weeks in late April, early May from 2004 to 2008 (Fig. 1b). A dual-frequency GNSS receiver (GPS/GLONASS) was mounted on a tripod on a sledge which was pulled by a snowmobile at a constant speed of approximately $5\,m\,s^{-1}$, resulting in one elevation measurement every $\sim$5 m at a logging interval of 1 s. The measurements were differentially post-corrected against a base station at the summit, and the elevation accuracy has proven to be better than 0.1 m (Eiken et al., 1997; Hagen et al., 2005). The pre-defined survey tracks were usually repeated within a cross-track distance of less than 10 m.

Airborne laser altimetry was conducted across Austfonna by NASA in 1996/2002 (Bamber et al., 2004), by the

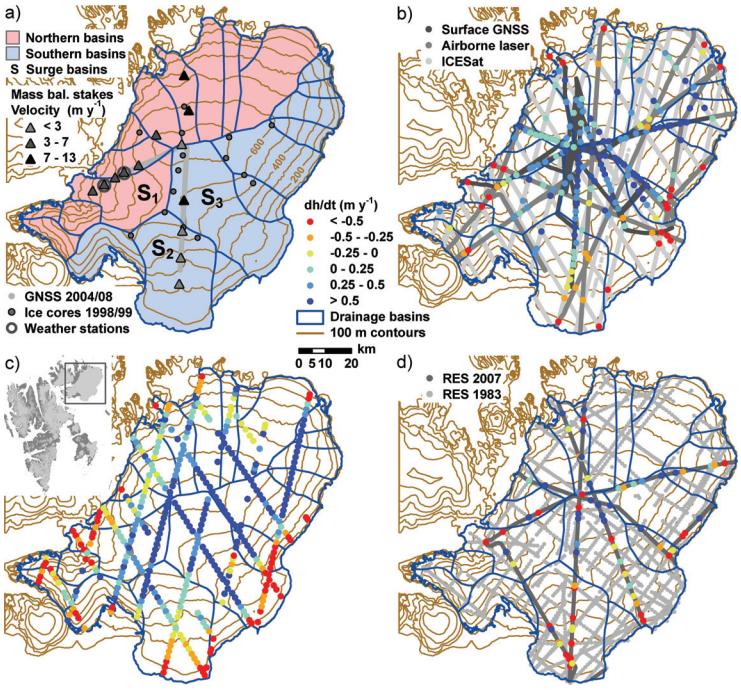

Fig. 1. **(a)** Classification of drainage basins into southern, northern and surge type regions. The basins that are known to have surged are Etonbreen (S_1), Braasvellbreen (S_2) and Basin 3 (S_3). Also shown are the locations of mass balance data used in Fig. 5: 2004–2009 mass balance stakes with average velocities, 2004/08 repeat track GNSS surface profiles, 1998/99 shallow ice cores (Pinglot et al., 2001), and 2004–2009 automatic weather stations. The other plots show estimates of elevation change rates in 2 km clusters for: **(b)** 2002–2008 crossover points (ICESat, airborne laser and GNSS) and 2004–2008 repeat track GNSS, **(c)** 2003–2008 repeat track ICESat, and **(d)** 1983–2007 RES ice thickness crossover points. The spatial coverage of the different altimetry data sets is plotted in greyscale. The inset (in c) shows the location of Austfonna within the Svalbard archipelago.

National Space Institute at the Technical University of Denmark (NSI-DTU) in 2004/07 (Forsberg et al., 2002), and by the Alfred Wegner Institute (AWI) in 2005/06. We only use the data sets from 2002, 2004 and 2007 (Table 1 and Fig. 1b), because 1996–2002 elevation differences have already been published (Bamber et al., 2004), and the AWI data sets coincide largely with simultaneous GNSS ground profiles. The individual airborne laser instruments have slightly different characteristics though all provide a dense sampling (<10 m spacing) of elevation points within a 100–300 m wide ground track. Elevation errors mainly arise from the aircraft GNSS positioning, the inertial navigation system attitude determination, and the laser ranging itself. Krabill et al. (2002) analysed crossover elevation differences and found a root-mean square (RMS) elevation accuracy better than 0.1 m for a similar instrument setup at the Greenland ice sheet.

The spaceborne Geoscience Laser Altimeter System (GLAS) onboard ICESat is designed to collect high precision surface elevations all over the globe. Since winter 2003, GLAS has been operating for three annual observation campaigns (two since 2006), each of approximately 35 days. Each laser pulse illuminates a footprint at the Earth's surface from which the return echo is used to retrieve an average surface elevation. The footprints are spaced at 172 m along-track and have a varying elliptical shape with average dimensions of 52×95 m for Laser 1 and Laser 2 (from winter 2003 to summer 2004) and 47×61 m for Laser 3 (since fall 2004) (Abshire et al., 2005). The single shot elevation accuracy was initially estimated to be 0.15 m over gentle terrain (Zwally et al., 2002), although accuracies better than 0.05 m have been achieved under optimal conditions (Fricker et al., 2005). However, the GLAS performance degrades over sloping terrain and under conditions favourable to atmospheric forward scattering and detector saturation. In cloudy regions like Svalbard, a considerable part of the data is also lost due to signal absorption in optically thick clouds. We used the GLA06 altimetry product release 28 (Zwally et al., 2008) which contains a saturation range correction that we added

Table 1. Elevation data sets with years of measurements and estimated precision for single point measurements. Also shown are the methods of elevation change calculation and the associated accuracy of single point elevation changes. ICESat data has a *dh* accuracy of 0.5 m for crossover points and 1 m for repeat track points. The accuracy of RES ice thickness changes is not assessed due to potential systematic errors related to the RES signal processing in 1983 and 2007.

Data source	Year	*h* precision	*dh* accuracy	Method
ATM laser	2002	< 0.10 m	0.5 m	Crossovers
DTU laser	2004, 2007	< 0.10 m	0.5 m	Crossovers
GNSS	2004–2008	< 0.10 m	0.5 m	Crossovers or repeat track
ICESat	2003–2008	< 0.10 m	0.5 or 1 m	Crossovers or repeat track
SRPI RES	1983	~ 22 m	NA	Ice thickness crossovers
DTU RES	2007	~ 8 m	NA	Ice thickness crossovers

to the elevations to account for the delay of the pulse centre in saturated returns (Fricker et al., 2005). We also converted ICESat data from the TOPEX/Poseidon ellipsoid to the WGS84 ellipsoid to ensure compatibility with GNSS and airborne altimetry data which refer to WGS84.

The altimetry data set with the best spatial coverage across Austfonna is from an airborne radio-echo sounding (RES) campaign carried out by the Scott Polar Research Institute (SPRI) and the Norwegian Polar Institute (NPI) in spring 1983 (Dowdeswell et al., 1986). Measurements were performed along a 5–10 km grid using a 60 MHz RES instrument (Fig. 1d) that registered both surface and bedrock returns. The positioning of the aircraft relied on a ranging system from the airplane to four ground-based transponders of which the position was accurately determined by satellite geoceivers. A more precise airplane altitude was determined from a pressure altimeter which was frequently calibrated over sea level in order to minimize errors from temporal pressure variations. However, such a calibration does not account for potential biases arising from local pressure anomalies across the ice cap. Pressure measurements in spring 2008 indicated that the air pressure at the center of the ice cap can deviate significantly ($\sim$3 hPa) from the predicted pressure based on simultaneous measurements at the coast. The pressure at the center was typically higher than expected during periods of calm and clear weather. If such conditions were ambient during the 1983 RES survey, this would have resulted in a systematic elevation underestimation of up to 20–30 m in the ice cap interior. To avoid inaccuracies in our elevation change estimates caused by this potential bias, we chose to use RES ice thickness data instead. Ice thickness was estimated from the time difference between tracked surface and bedrock echoes multiplied by the signal velocity and should thus be independent of air pressure. A few profiles of 60 MHz RES were also obtained in spring 2007 by NSI-DTU (Fig. 1d) simultaneously with the laser profiling described earlier. The aircraft position was precisely determined by three onboard GNSS receivers, and the RES ice thickness processing was done in a semi-automatic way using a surface and bottom detection software (Kristensen et al., 2008).

In order to convert volume changes into mass changes, information about the temporal evolution of the firn pack is needed. Several firn thickness and density profiles were obtained from shallow ice cores in spring 1998 and 1999 (Pinglot et al., 2001). A few $\sim$15 m shallow ice cores were also drilled in 2006 and 2007. Since 2004, the annual snow pack and glacier facies have been investigated by snow pits, probing and GPR profiling (Taurisano et al., 2007; Dunse et al., 2009). A neutron probe was used in spring 2007 to obtain four high resolution firn density profiles in connection with CryoSat-2 calibration work (Brandt et al., 2008). The bulk firn densities are typically ranging from 400 to 600 kg m^{-3} with some ice layers of higher density and a general increase of density with depth.

The geodetic change rates were also compared to point mass balance measurements acquired in annual field campaigns from 2004 to 2008. Stake and snow pit measurements have been carried out in late April/early May along several transects (Fig. 1a). Stake heights were measured down to the snow surface and down to last year's summer surface, and precise stake positions were determined by static $\sim$5 min differential GNSS surveys. The bulk density of the winter snow pack was measured annually in snow pits at stake locations, while the density of the summer snow pack was sampled in a few deeper snow/firn pits. The only stake transect that has been repeated each year is that from Etonbreen to the summit (Fig. 1a).

4 Methods

The goal of this study was to determine long-term trends of geometric change of Austfonna. However, there are only a limited number of reliable elevation data sets prior to 2002, and the spatial coverage of individual data sets is too sparse for volume change calculations. To make best use of the available elevation data, we calculated elevation change rates

(dh/dt) for all possible time intervals spanning three years or more within the 2002–2008 period. In order to avoid seasonal elevation biases in our analysis, we only compared data between similar seasons, e.g. winter to winter and fall to fall. Using average dh/dt rates from various elevation data sets and time spans allows for a robust estimation of the overall volume change and geometric change trend over the 2002–2008 period.

Elevation change rates were calculated at crossover points between two profiles (within and between GNSS, airborne laser and ICESat) and along repeated tracks (within GNSS or ICESat). Elevations at crossover points were determined by linear interpolation of the measurements between the two closest footprints within 200 m distance in each profile (Fig. 2a). The elevation differences (dh) at each crossover point were divided by the number of years ($dt \geq 3$ y) between the two surveys to obtain elevation change rates (dh/dt). Repeat track profiles in the GNSS and ICESat data sets were compared separately. Surface GNSS profiles are generally repeated within a stripe of 10–15 m width, and individual tracks cross each other frequently and randomly. Hence, we compared each GNSS point in one profile to the closest point in another profile within a radius of 5 m. This ensures a sufficiently dense sampling of dh/dt points. Furthermore, the vertical error due to cross-track slope is kept minimal since a typical Austfonna surface slope of 1° over 5 m would introduce a relative elevation bias of less than 0.10 m.

It is difficult to compare repeat track ICESat profiles due to the relatively large cross-track separation distance between repeating profiles. The average cross-track separation of 90 m at Austfonna with a 1° slope would introduce a relative elevation bias of 1.6 m. We used a new digital elevation model (DEM) of 25 m horizontal resolution to correct for elevation differences caused by the cross-track slope. The DEM was constructed from DInSAR with ground control points from ICESat altimetry. The local slopes of the DEM should not be affected by the ICESat points since they are only used to reconstruct the overall geometry of the SAR acquisitions (i.e. baseline refinement). For each pair of ICESat repeat tracks, the oldest profile was chosen as the reference profile. The second profile was projected onto the reference profile using the cross-track elevation differences in the DEM. Elevation change was then calculated at each DEM-projected point along the reference profiles by linearly interpolating neighbouring footprints along the reference profiles to the respective point locations (Fig. 2b). Repeat pass dh/dt points derived with a cross-track separation larger than 200 m or a DEM correction larger than 5 m were ignored.

The calculated dh/dt points from crossover and repeat track analysis were unevenly distributed in space and often represented change rates from different time spans and methods. In order to obtain a robust estimate of the overall elevation change trend over the 2002–2008 period, we averaged all dh/dt points within 2 km clusters for the data sets in Fig. 1b (crossover points and GNSS repeat track data) and Fig. 1c

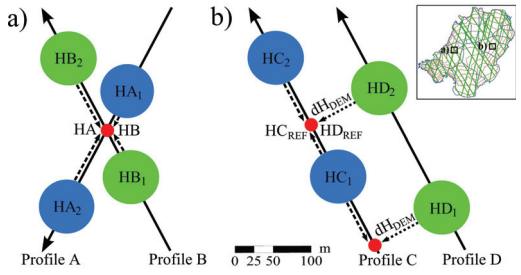

Fig. 2. The inset map shows all ICESat profiles on Austfonna and an example of two locations where elevation change can be estimated: **(a)** a crossover point where two altimetry profiles (A and B) intersect each other. Linear interpolation between the two closest footprints was used to determine the crossover point elevation for each profile (HA and HB). The difference between the two elevations (dh=HB−HA) is the estimated elevation change at the crossover point. **(b)** Repeat track ICESat observations were compared stepwise: (1) choose one profile as the reference profile (C). (2) Project each footprint from the other profile (D) perpendicularly to the reference profile (C) by means of the extracted elevation difference between the two locations in a DEM (HD_{REF}=HD_2+dH_{DEM}). (3) Estimate the elevation of the reference profile (HC_{REF}) at each DEM-projected point using linear interpolation between the two closest footprints (HC_1 and HC_2). (4) Calculate the elevation difference for each point pair along the reference profile to derive estimates of elevation change (dh=HD_{REF}−HC_{REF}).

(ICESat repeat track data). The clustered dh/dt points were then plotted as a function of elevation (Fig. 3a), and higher order polynomial functions were fitted to the data (e.g. Kääb, 2008). The r^2 coefficient of determination and the RMS error of the polynomial fits were typically stabilizing ($r^2 \sim 0.7$ and RMS$\sim$0.4 m) after adding a third order coefficient. Thus, third order polynomial fits were used to parameterize all elevation change – elevation relationships (Fig. 3).

Volume change rates dV/dt were estimated by integrating the polynomial functions over the glacier part of the DInSAR/ICESat DEM (Fig. 4). Area-averaged specific elevation change rates $\overline{(dh/dt)}$ were found by dividing dV/dt by the corresponding glacier area. We also tested discrete hypsometric approaches where volume changes are first calculated for separate elevation bins as the product between the elevation change rate and the elevation bin area, and then summed up to provide the total volume change. The elevation change rate used for one elevation bin is typically the mean (e.g. Arendt et al., 2002) or the median (e.g. Abdalati et al., 2004) of the change rates within that bin or an extracted value from a polynomial fit (Nuth et al., 2010). The $\overline{dh/dt}$ estimates from these three methods using 100 m elevation bins were all within 0.02 m w.e. y^{-1} of the continuous integration method used in this study.

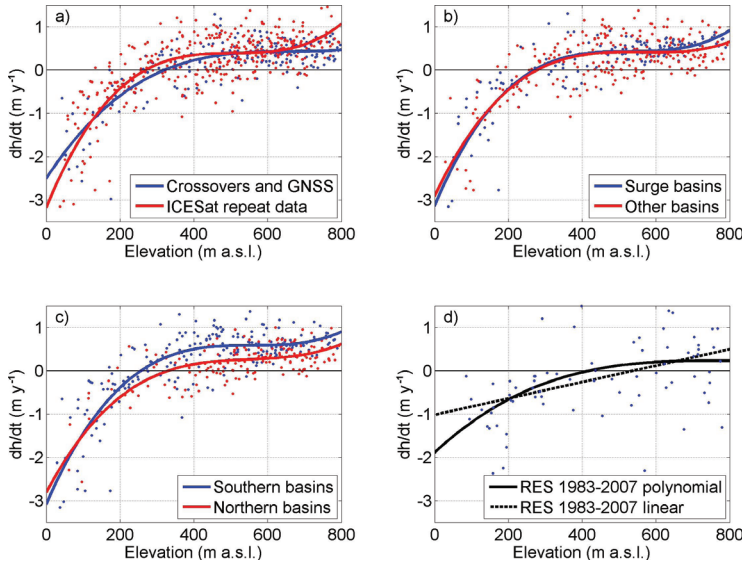

Fig. 3. (a) Elevation change rates (2 km clusters) versus elevation for the two data sets in Fig. 1b (2002–2008 crossover points and 2004–2008 repeat track GNSS) and Fig. 1c (2003–2008 repeat track ICESat). **(b)** 2002–2008 elevation change rates for surge type basins versus other basins. **(c)** 2002–2008 elevation change rates for southern basins versus northern basins. The locations of the different basins are shown in Fig. 1a. The two data sets in (a) were mixed and clustered (2 km) before forming the data sets of (b) and (c). **(d)** shows 1983–2007 elevation change rates for RES ice thickness crossover points (Fig. 1c). Solid lines show third order polynomial fits to the *dh/dt* points (a–d), while the dashed line in (d) is a linear fit.

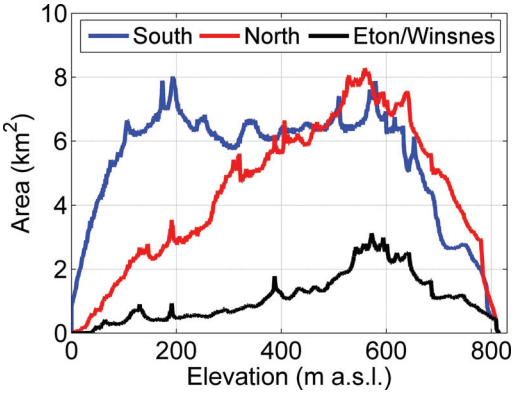

Fig. 4. Hypsometries for the southern basins, northern basins (Fig. 1a) and the Eton-/Winsnesbreen basin (Fig. 6). Glacier areas were extracted for each meter of elevation from a new DInSAR/ICESat DEM which the polynomial fits of elevation change and mass balance were integrated over to obtain volume change rates. Note the relatively large glacier areas at low elevations in the southern basins.

It is expected that the geometric changes vary regionally and from basin to basin due to the accumulation gradient across Austfonna and the surge-type characteristics of some drainage basins. Comparative *dh/dt* calculations were done for the southern basins versus the northern basins (Figs. 1a and 3c) and for surge-type basins versus basins without any reported surge history (Figs. 1a and 3b). Here, the crossover points and GNSS repeat track data (Fig. 1b) were mixed and clustered (2 km) with the ICESat repeat track data (Fig. 1c) in order to obtain a better spatial distribution of *dh/dt* points within the selected regions. The sum of the regional *dV/dt* rates was then used to estimate the total *dV/dt* and the glacier-wide $\overline{dh/dt}$.

To calculate mass balance from geodetic volume change data is complicated due to potential changes in firn thickness and density between the surveys. We considered this uncertainty by calculating a lower and an upper estimate of the area-averaged specific mass balance (b). For the upper mass balance estimate (b_{max}) we applied Sorge's Law (Bader, 1954) assuming that the firn density and thickness have not changed significantly. Hence, the volumetric changes (dV/dt) were multiplied by the density of ice (ρ_{ice}=900 kg m^{-3}) and divided by the glacier area to obtain the water equivalent b_{max}. For the lower mass balance estimate (b_{min}) we accounted for a potential build-up of firn during the 2002–

2008 period. Dunse et al. (2009) derived from GPR profiling that the firn line elevation increased slightly from 2003 to 2004 (<50 m) and then lowered over the next two years from ∼650 m to ∼550 m elevation in the northwest and from ∼600 m to 4–500 m in the southeast. Based on this, we calculated $b_{\min}$ using the density of ice (ρ_{ice}=900 kg m^{-3}) for all changes below the firn line (super-imposed ice area and ablation area) and the average density of firn (ρ_{firn}=500 kg m^{-3}) for all changes above the firn line. Average firn line elevations of 600 m and 500 m were used for the northern and the southern basins respectively. The real mass balance is expected to lie somewhere between these two extreme cases of firn density conversion. We used the average of $b_{\min}$ and $b_{\max}$ as the final estimate of water equivalent mass balance (b).

The effect of glacier retreat and advance on area-averaged $\overline{dh/dt}$ rates is usually accounted for by dividing the total volume change by the average glacier area of the measurement period (e.g. Arendt et al., 2002). However, most of Austfonna is terminating into the sea, and ice volume changes below sea level can not be measured by laser altimetry or GNSS. Elevation change measurements in the proximity of the 20–40 m high calving fronts can also vary by tens of meters over short distances due to terminus fluctuations. Therefore, we excluded all observations below 25 m a.s.l. in the polynomial fitting. Instead we applied marine loss rates from Dowdeswell et al. (2008) to consider terminus changes in the total mass balance.

The RES ice thickness data sets from 1983 and 2007 were compared by calculating the difference in ice thickness at 75 crossover points and dividing by the 24 years time span (Fig. 1d). A linear regression curve (r^2=0.20) and a third order polynomial curve (r^2=0.23) were fitted to the ice thickness change points (dh/dt) in order to reveal possible elevation change trends over the 1983–2007 period (Fig. 3d). Volume change and mass balance were not calculated from the RES measurements due to the high noise level and the possibility of systematic errors.

Surface net mass balance was estimated for each stake from the difference in stake height down to the previous summer surface between two consecutive years. The density of ice (ρ_{ice}=900 kg m^{-3}) was used to convert stake height changes into mass changes in the ablation or super-imposed ice areas, while the average density of firn (ρ_{firn}=500 kg m^{-3}) was used for all stakes in the firn areas. The estimate of ρ_{firn} was based on density measurements in the uppermost firn layer in snow/firn pits, shallow ice cores (Pinglot et al., 2001) and neutron probe profiles (Brandt et al., 2008; Dunse et al., 2009). The annual net mass balances were averaged over the 2004–2008 period. Only stake measurements that covered the entire time span were used in the analysis. We parameterized the mass balance – elevation relationship by fitting polynomial functions to the data (Fig. 5), separately for the southern and northern basins. The RMS and r^2 of the fits stabilized after adding a second order coefficient. The second order polynomial functions were then integrated over the DInSAR/ICESat DEM (Fig. 4) in order to obtain estimates of the volume change rates excluding calving. Since all stake data were referenced to previous summer surfaces, the 2004–2009 spring measurements yielded mass balance rates for the period between fall 2003 and fall 2008 (5 mass balance years).

In order to investigate the relation between local surface mass balance and elevation change, we extracted two repeat track GNSS surface profiles from 2004 and 2008 along the main mass balance transects (Fig. 1a). Along-track elevation differences were calculated and smoothed using a running mean filter over 2 km distances. The elevation changes were then converted to water equivalent rates using the density of ice (ρ_{ice}=900 kg m^{-3}) and plotted as a function of elevation along with the surface mass balance curves in Fig. 5.

Annual and seasonal mass balances were calculated for the Eton-/Winsnesbreen basin which is the only mass balance profile that has been measured each year since 2004. Winter mass balances at stakes were derived from the snow depth in the subsequent spring considering the bulk density measured in snow pits. Summer mass balances were obtained by subtracting the winter balances from the net balances. Second order polynomial functions were used to extrapolate the point observations to all elevations of the Eton-/Winsnesbreen part of the DEM (Fig. 4) and to calculate volume changes. Area-averaged specific winter, summer and net mass balances were calculated for each year from 2004 to 2008 by dividing the volume changes by the basin area (Fig. 6).

5 Error analysis

The uncertainty of an area-averaged elevation change rate ($\varepsilon_{\overline{dh/dt}}$) is equal to the standard error of the polynomial fit assuming that elevation change points are randomly spatially distributed, have no spatial autocorrelation and no systematic elevation errors:

$$\varepsilon_{\overline{dh/dt}} = \frac{\sigma_{\text{fit}}}{\sqrt{f}} \quad (1)$$

where σ_{fit} is the RMS error of the polynomial fit and f is the degrees of freedom of the polynomial fit, i.e. the number of elevation change clusters (e.g. 208 in the south and 179 in the north) minus the number of coefficients in the polynomial function (4). The GNSS profiles are slightly biased towards the higher elevations in the central parts of the ice cap, whereas the airborne laser profiles and the ICESat profiles also cover the lower elevations. Altogether, the elevation change clusters provide a good coverage over most glacier basins (Fig. 1a and b). Averaging observations within 2 km clusters ensures that potential spatial biases are minimized and that the spatial autocorrelation is low. Potential systematic elevation errors between the different observation techniques and periods are difficult to assess. A bias of 0.17 m

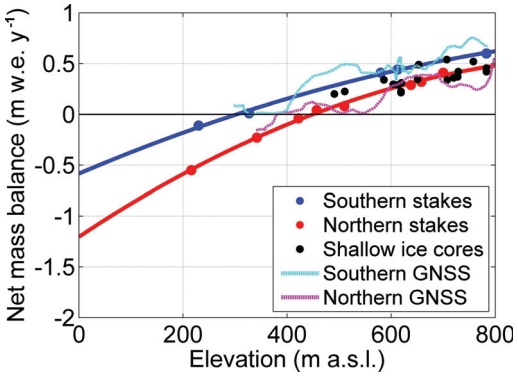

Fig. 5. The continuous lines are second order polynomials fitted to averaged point observations of annual net mass balances between fall 2003 and fall 2008 in the southern and northern basins (Fig. 1a). The area-averaged surface mass balance is 0.09 m w.e. y^{-1} for the southern basins and −0.01 m w.e. y^{-1} for the northern basins, giving an overall specific mass balance of 0.05 m w.e. y^{-1} (or 0.38 km^3 w.e. y^{-1}). The average equilibrium line altitude (ELA) is 300 m in the south and 450 m in the north which corresponds to an overall accumulation-area ratio (AAR) of 60 %. The 1986–1998/99 average net mass balances from shallow ice cores are included for comparison (Pinglot et al., 2001). The dashed lines show the average water equivalent elevation change rates between spring 2004 and spring 2008 along two repeat track GNSS profiles that follow the mass balance transects (Fig. 1a).

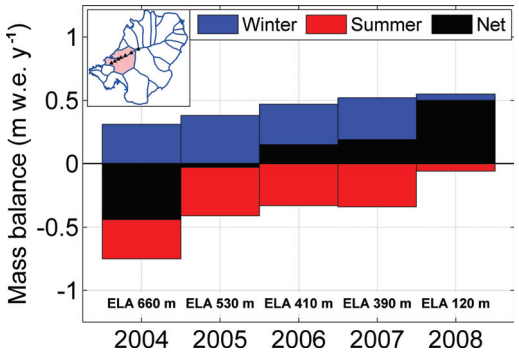

Fig. 6. Annual and seasonal surface mass balances for the Eton-/Winsnesbreen basin based on annual spring measurements. The inset map shows the basin location and the mass balance stakes that were used in the calculations. Annual ELAs are shown at the bottom. Note the rise in annual net mass balance and ELA from 2004 to 2008. The overall net mass balance of the basin is 0.02 m w.e. y^{-1} and the overall ELA is 460 m (66% AAR) over the 5 years period.

was found between two overlapping GNSS and laser profiles obtained within a few days time in 2007. In the lack of more overlapping observations, we assume that systematic elevation errors are small and mainly random due to the variety of measurement techniques and time spans involved in the analysis. Thus, the three assumptions of the standard error equation are fulfilled.

The error budget of a geodetic $\overline{dh/dt}$ calculated from a limited sample of elevation change points can be divided into an observation error and an extrapolation error (e.g. Arendt et al., 2002; Nuth et al., 2010). The error of crossover *dh/dt* points can be quantified by analysing crossovers within short time spans where no significant elevation change is expected. Within individual ICESat observation periods (dt<30 d), the interquartile range (IQR) of 113 crossover points at Austfonna was 0.46 m. Similar findings have been reported for comparable slopes in Greenland and Antarctica (Brenner et al., 2007). The airborne laser profiles have much fewer crossover points, but the precision should lie well within that of ICESat. For simplicity, we set an error estimate ($\varepsilon_{\mathrm{cross}}$) of 0.5 m for all crossover points. Errors in repeat track comparisons are mainly due to track divergence. Hagen et al. (2005) found that the precision of GNSS profiles that were measured twice during the same field campaign was better than 0.3 m even when the tracks were up to 90 m apart. However, we also accept a generous error estimate ($\varepsilon_{\mathrm{GNSS}}$) of 0.5 m for the GNSS repeat track data. The main error component in the repeat track ICESat analysis is the cross-track DEM correction. This DEM error can be estimated by comparing elevation differences between pairs of altimetric points (e.g. the elevation difference between two neighbour ICESat points in the same ground track) with the elevation differences between the corresponding point pair locations in the DEM. The relative error of the DEM ranges from ∼0.4 m (IQR) over a 50 m distance to ∼1.4 m over a 170 m distance. The additional error due to along-track interpolation should be less than the crossover point error at 0.5 m. Based on an average cross-track separation of 90 m between repeating profiles, we accept 1 m for the repeat track ICESat point error ($\varepsilon_{\mathrm{ICESat}}$). Assuming that all elevation change points within each 2 km cluster are fully correlated, the cluster error ($\varepsilon_{\mathrm{clust}}$) equals the mean of the individual point errors within that cluster:

$$\varepsilon_{\mathrm{clust}} = \frac{1}{n}\sum_{i=1}^{n}\left(\frac{\varepsilon_{\mathrm{PT}}}{dt}\right)_i \qquad (2)$$

where $\varepsilon_{\mathrm{PT}}$ represents the error of one elevation change point ($\varepsilon_{\mathrm{cross}}$, $\varepsilon_{\mathrm{GNSS}}$ or $\varepsilon_{\mathrm{ICESat}}$), dt is the time span (≥3 years), and n is the number of elevation change points within the cluster. The estimated cluster errors can be used to weight the elevation change clusters in the polynomial fitting procedure according to the expected uncertainties (e.g. $w = 1/\varepsilon^2_{\mathrm{clust}}$). In this study, the difference in $\overline{dh/dt}$ between using such a weighting scheme and using no weights at all was smaller than 0.02 m y^{-1}.

When we assume that there is no spatial autocorrelation between the clusters, it implies that the effect of cluster errors on the overall elevation change rate is reduced with an increasing number of clusters (N). The cluster errors ($\varepsilon_{\text{clust}}$) can thus be combined into an overall observation error (ε_{OBS}) related to the uncertainty of the measurements:

$$\varepsilon_{\text{OBS}} = \sqrt{1/\sum_{i=1}^{N} \frac{1}{\varepsilon_{\text{clust}_i}^2}} \quad (3)$$

The area-averaged elevation error $\varepsilon_{\overline{dh/dt}}$ is a combined result of the observation error (ε_{OBS}) and the spatial extrapolation error ε_{EXT}. Since ε_{OBS} and ε_{EXT} are independent, they will combine as root-sum-squares (RSS) to form $\varepsilon_{\overline{dh/dt}}$. Thus, the unknown extrapolation error ε_{EXT} can be estimated from:

$$\varepsilon_{\text{EXT}} = \sqrt{\varepsilon_{\overline{dh/dt}}^2 - \varepsilon_{\text{OBS}}^2} \quad (4)$$

The error introduced when converting elevation change to water equivalent mass change is more difficult to quantify due to the temporal variation in firn thickness and density. Instead, we provide a minimum (b_{min}) and a maximum (b_{max}) estimate of the mass balance. The range between these two extreme values can be used to estimate a density conversion error:

$$\varepsilon_{\rho} = \frac{1}{2}(b_{\text{max}} - b_{\text{min}}) \quad (5)$$

We also have to account for ice losses due to calving front retreat in the total estimate of Austfonna's mass balance. This adds an additional error ($\varepsilon_{\text{RETR}} = E_{\text{RETR}}/A$) in the mass balance that follows from the volumetric retreat error estimate (E_{RETR}) of Dowdeswell et al. (2008) and the glacier area (A). All the described error components can finally be combined as RSS to form the total mass balance error estimate:

$$\varepsilon_b = \sqrt{\varepsilon_{\text{OBS}}^2 + \varepsilon_{\text{EXT}}^2 + \varepsilon_{\rho}^2 + \varepsilon_{\text{RETR}}^2} \quad (6)$$

Volumetric errors (E) are easily obtained by multiplying the specific errors (ε) with the glacier area. In order to see the influence of the errors at different elevations, the computations above can be done separately for a number of elevation bins. Figure 7 shows the different error components as a function of elevation for 50 m elevation bins. The RSS of the volumetric bin errors will be equal to the overall volumetric errors if the elevation change points are randomly distributed over the ice cap.

The ice thickness comparison between 1983 and 2007 (Fig. 3d) is too coarse for a thorough error analysis. The precision of the 1983 ice thickness data is 22 m based on the IQR of 167 crossover points, while the 2007 ice thickness data have a precision of 8 m (IQR) and an accuracy of ∼1 m (mean error) as compared to overlapping low-frequency (20 MHz GPR) surface profiles from 2008. Although the random errors are fairly well known, we can not exclude the possibility of systematic errors attributed to differences in the RES signal processing between the 1983 and 2007 campaigns. The RES data sets are thus better suitable for interpretation of geometric change than for calculation of volume change.

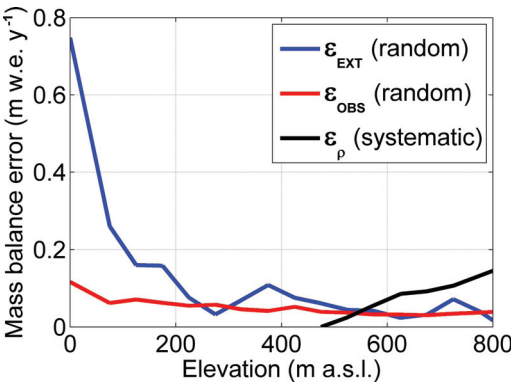

Fig. 7. Area-averaged elevation errors for 50 m elevation bins. There are three error components that vary with elevation; a spatial extrapolation error (ε_{EXT}), an observation error (ε_{OBS}), and a density conversion error (ε_{ρ}). The two first ones (ε_{EXT} and ε_{OBS}) are random errors that combine as a RSS in the overall error, while the last one (ε_{ρ}) is a systematic error that must be summed up in the error budget. The overall area-averaged error components are 0.02 m w.e. y^{-1} for ε_{EXT}, 0.01 m w.e. y^{-1} for ε_{OBS}, and 0.03 m w.e. y^{-1} for ε_{ρ}, resulting in a total RSS error of 0.04 m w.e. y^{-1} in the area-averaged geodetic mass balance. An additional error component from the marine retreat loss ($\varepsilon_{\text{RETR}}$) must be considered when assessing the total mass balance including calving front retreat (Table 2).

6 Results and discussion

Figures 1b-c and 3a-c show a pronounced interior thickening of up to 0.5 m y^{-1}, at the same time as the margins are thinning at a rate of 1–3 m y^{-1}. The 2002–2008 growth rates are consistent with those found by Bamber et al. (2004) along several laser altimetry profiles. The same elevation change pattern is also evident in the 1983–2007 comparison of ice thicknesses although the actual change rates remain uncertain due to the low accuracy of the measurements (Fig. 3d). The total ice volume change (excluding calving front retreat) is estimated to be 0.37±0.18 km^3 y^{-1} (or $\overline{dh/dt}$=0.05 m y^{-1}) for the 2002–2008 period (Table 2). When converting to water equivalent changes, the estimates range from 0.33 km^3 w.e. y^{-1} (or b_{max}=0.04 m w.e. y^{-1}) to −0.11 km^3 w.e. y^{-1} (or b_{min}=−0.01 m w.e. y^{-1}) for firn area density conversion factors between the densities of ice (ρ_{ice}=900 kg m^{-3}) and firn (ρ_{firn}=500 kg m^{-3}), respectively.

Table 2. Geodetic estimates of area-averaged elevation change rates ($\overline{dh/dt}$) and mass balances (b) between 2002 and 2008 for the southern basins, northern basins and the entire Austfonna. The total mass balance is estimated by adding the calving front retreat loss dV/dt (Dowdeswell et al., 2008) to the geodetic dV/dt and dividing by the corresponding glacier area. One standard deviation error estimates are provided for each change rate.

	Southern basins	Northern basins	Austfonna
Geodetic ($m\,y^{-1}$)	0.03±0.03	0.06±0.03	0.05±0.02
Geodetic b ($m\,w.e.\,y^{-1}$)	−0.01±0.05	0.04±0.03	0.01±0.04
Retreat dV/dt ($km^3\,w.e.\,y^{-1}$)	−1.1±0.03	−0.3±0.02	−1.4±0.4
Total mass balance ($m\,w.e.\,y^{-1}$)	−0.25±0.08	−0.04±0.06	−0.16±0.06

Mass build up in the accumulation area combined with deficits in the ablation area is typical for glaciers in a quiescent phase of their surge cycle. Bevan et al. (2007) found that the accumulation areas of surge-type basins at Austfonna were thickening at a higher rate than most other basins. Our elevation change curves for known surge-type basins versus other basins (Fig. 3b) do not indicate a clear difference in geometric change between these two glacier types at Austfonna. However, the area-averaged elevation change is slightly more negative for the three surge-type basins due to their relatively large areas at low elevations, the aftermath of previous surges. Potential differences in geometric change between individual basins are probably of smaller magnitudes than the overall change pattern which is seen across all basins. The general trend towards surface steepening suggests that other basins might also be capable of surging in the future. Lefauconnier and Hagen (1991) suggest that up to 90% of Svalbard's glaciers are surge-type, although most of them lack historic records of surges.

The southern basins are generally thickening at a faster rate than the northern basins (Fig. 3c). This is in agreement with the southeast to northwest accumulation gradient across Austfonna (Taurisano et al., 2007). The elevation change curves of the southern and northern basins are crossing the zero change line at elevations of 260 m and 330 m, respectively. This is a smaller south to north gradient than what is seen in ELA estimates from shallow ice cores (Pinglot et al., 2001) and from mass balance stakes (Fig. 5). The average ELA for the 2004–2008 period is 300 m for the southern basins and 450 m for the northern basins which agrees well with the long-term lower boundary of the super-imposed ice area mapped by Dunse et al. (2009). The southern and northern ELAs correspond to an average accumulation-area ratio (AAR) of 60%.

Elevation change curves can not be directly compared with surface mass balance curves due to glacier dynamics. However, if a glacier is stagnant or moves at very low velocities, the two curves will approach each other as was observed for Kongsvegen, a surge-type glacier in western Spitsbergen (Melvold and Hagen, 1998). Velocity fields from DInSAR (Bevan et al., 2007; Strozzi et al., 2008) and annual GNSS measurements of mass balance stake movements (Fig. 1a) show that, apart from a few fast flowing units (Dowdeswell et al., 1999), most of Austfonna is stagnant at velocities $<10\,m\,y^{-1}$. This is probably the main reason why the interior of Austfonna appears to be in a steady phase of growth. Bevan et al. (2007) found that the overall ice flux across the ELA in winter 1994/96 was only half of the mean 1986–1999 annual net mass balance above the ELA (Pinglot et al., 2001). The two elevation change curves in Fig. 5 follow the general trend of the corresponding surface mass balance curves, implying that the ice flow (Fig. 1a) is far too slow to balance out the current accumulation rate. Hence, the main pattern of elevation change at Austfonna is dominated by the surface mass balance with the ice submergence/emergence playing a secondary role.

Bamber et al. (2004) and Raper et al. (2005) linked the interior thickening between 1996 and 2002 to higher than normal precipitation rates. Figure 5 indicates that the 2004–2008 surface mass balance above 500 m elevation is similar to or slightly higher than the 1986–1998/99 mass balance from shallow ice cores (Pinglot et al., 2001). Two of the drilling sites were revisited in 2006 and 2007 to retrieve comparable ice core samplings for the 1986–2006/07 period. The results did not indicate any significant changes in the mean annual accumulation rate between the two periods 1986–1999 and 1986–2006/07. Since there is no evidence of increased precipitation over the last few decades, we interpret the observed mass build-up in the accumulation area as a natural growth that has been going on for decades and will continue in the nearest future until it is compensated by glacier acceleration or a more negative mass balance regime.

The polynomial fits to the surface mass balance point measurements (Fig. 5) were integrated over the DEM in the southern and northern basins (Fig. 4), to obtain estimates of the water equivalent volume change excluding calving. The stake data yield an overall mean annual volume change rate of $0.38\,km^3\,w.e.\,y^{-1}$ (or $0.05\,m\,w.e.\,y^{-1}$) for the 2004–2008 mass balance years. The area-averaged surface mass balance seems to be higher in the southern basins ($0.09\,m\,w.e.\,y^{-1}$) than in the northern basins ($-0.01\,m\,w.e.\,y^{-1}$). Annual and seasonal mass balances for the Eton-/Winsnesbreen basin in

the northwest are shown in Fig. 6. From 2004 to 2008, the annual net mass balance increased for each year from a very negative 2004 (-0.51 m w.e. y^{-1}) to a very positive 2008 (0.49 m w.e. y^{-1}). This remarkable trend is a combined effect of increased winter accumulation and reduced summer ablation during the 5 years of observation. The concurrent lowering of the annual ELA at Eton-/Winsnesbreen was from 660 m (18% AAR) in 2004 to 120 m (97% AAR) in 2008. This lowering of the ELA coincides with the 2003–2006 firn area expansion mapped by Dunse et al. (2009), and must have caused an overall upbuilding of firn during the 2002–2008 geodetic observation period. Still, using the density of firn (ρ_{firn}=500 kg m^{-3}) to convert elevation changes to mass changes in the firn area will probably cause an underestimation of the mass balance due to firn densification and internal refreezing over the 6 years time span (e.g. Brandt et al., 2008). In order to provide one total number for the geodetic mass balance b (excluding calving front retreat) during the 2002–2008 period (Table 2), we therefore took the average of the lower estimate b_{min} (ρ_{firn}=500 kg m^{-3}) and the upper estimate b_{max} ($\rho_{\text{firn}} = \rho_{\text{ice}}$).

For tidewater glaciers, the iceberg calving flux must be included in the total mass balance budget. Dowdeswell et al. (2008) estimated a total iceberg calving flux of 2.5±0.5 km^3 w.e. y^{-1} for Austfonna, where ∼1.1 km^3 w.e. y^{-1} was due to the ice flux at the calving fronts and ∼1.4 km^3 w.e. y^{-1} was due to calving front retreat. Our geodetic volume change rates account for ice flux calving since the elevation change curves are integrated over the entire glacier area. Marine retreat loss on the other hand is not accounted for since all geodetic measurements below 25 m elevation were excluded from the analysis due to the discrete nature of elevation changes along a retreating calving front and the inability of laser altimeters to measure ice thickness changes below sea level. With almost no geodetic volume change above the calving fronts between 2002 and 2008, the best estimate of Austfonna's total mass balance becomes almost similar to the proposed marine retreat loss, i.e. -1.3 km^3 w.e. y^{-1} (or -0.16 m w.e. y^{-1}). The stake measurements on the other hand yield a total mass balance of -2.1 km^3 w.e. y^{-1} (or -0.26 m w.e. y^{-1}) when the total iceberg calving flux (-2.5 km^3 w.e. y^{-1}) is subtracted from the surface mass balance estimate (0.38 km^3 w.e. y^{-1}). Before applying calving flux data from Dowdeswell et al. (2008), we have to assume that the marine retreat rates and the velocity fields of the ice cap have not changed significantly between the 1990s and the 2002–2008 period. Annual static GNSS surveys of mass balance stakes between 2004 and 2008 yield average surface velocities of 0.5–13 m y^{-1} (Fig. 1a) with little temporal variation. And repeat pass ICESat observations across the calving fronts do not indicate any substantial changes in the retreat rates. However, we can not exclude the possibility of a changed calving flux since we lack recent data on terminus ice thickness and velocity. The 0.9 km^3 w.e. y^{-1} difference between the total mass balance of the geodetic method and the in-situ method indicate that the ice flux calving rate is currently lower than what Dowdeswell et al. (2008) estimated. The discrepancy can also be related to the extrapolation of point measurements to the entire glacier area, or to the slightly different time spans involved, or to the uncertainty of the density conversion factors.

The westerly location of most mass balance stakes could lead to a bias in the overall in-situ estimates towards lower surface mass balances due to less winter accumulation and a relatively higher firn line which exposes more ice to melting at a low albedo during the summer. Also, the surface mass balance at stakes will be underestimated if meltwater or rain percolate through the last summer surface and refreeze in lower firn layers (Paterson, 1994). Brandt et al. (2008) found ice layers in the firn with thicknesses ranging from a few millimeters to more than 0.5 m, indicating substantial internal refreezing. Shallow ice core samples from the summit areas approach the density of ice already at 3–6 m depths, with no apparent change of firn thicknesses between 1999 (Pinglot et al., 2001) and 2007 (Brandt et al., 2008). Analysis of a deep ice core from 1987 indicated that 60–80% of the uppermost 50 m of ice was formed through refreezing (Zagorodnov and Arkhipov, 1990). Zagorodnov et al. (1990) also noted the presence of sub-surface water pockets that form in depressions during years of warm summers when the amount of meltwater exceeds the amount which can refreeze. Surface undulations at a scale of a few kilometers, which are commonly seen on Austfonna, are probably preventing the efficiency of meltwater drainage in the firn area. If we assume that all meltwater in the firn area is retained within the firn pack (as refrozen ice or water pockets) and that there is no significant summer accumulation, then the net mass balance at stakes in the firn area will be equal to the winter mass balance. Applied to the stake measurements at Austfonna, this would raise the specific surface mass balance from 0.05 m w.e. y^{-1} to 0.12 m w.e. y^{-1}. The most realistic surface mass balance will probably lie somewhere between these two extreme cases.

Our close to zero geodetic mass balance estimate of Austfonna is similar to the 1990–2005 geodetic mass balance estimate of the adjacent Vestfonna ice cap (Nuth et al., 2010). If marine retreat loss is included in the mass budget, Austfonna becomes more negative than Vestfonna where the calving fronts only span 44 km (Blaszczyk et al., 2009). In any case, the recent mass balance of the ice caps on Nordaustlandet is much less negative than the long-term trends of most Spitsbergen glaciers which have been thinning considerably over the last decades (e.g. Kohler et al., 2007; Nuth et al., 2010). The current change rates at Austfonna could in theory differ considerably from the long-term decadal trends due to the short time span of this study and the large variability in annual net mass balances (Fig. 6). However, the good correspondence between the mean net mass balance in the summit area during 1986–1998/99 (Pinglot et al., 2001) and 2004–

2008 (Fig. 5) as well as between the elevation changes during 1996–2002 (Bamber et al., 2004) and 2002–2008 (Fig. 1) indicates that the most recent mass balance conditions are also representative for the last few decades.

Austfonna's present contribution to sea level change is difficult to quantify due to the uncertain distinction between marine ice losses above and below sea level. If we assume an average ice thickness of 120 m at the calving fronts (derived from 1983 RES data) and an average ice cliff height of 30 m above sea level (derived from ICESat altimetry), then the contribution from terminus retreat or advance to sea level change will be ∼17% of the water equivalent ice volume change at the terminus. Thus, Austfonna's $1.4\,km^3$ w.e. y^{-1} terminus retreat loss will only displace $0.2\,km^3$ w.e. y^{-1} of seawater which is almost balanced by the $0.1\,km^3$ w.e. y^{-1} volume gain above the calving fronts. Austfonna's negligible contribution to sea level rise is in sharp contrast to the rest of Svalbard's glaciers which have contributed with $9.5\pm1\,km^3$ w.e. y^{-1} over the last few decades (Nuth et al., 2010).

7 Conclusions and outlook

Austfonna has experienced high elevation thickening, low elevation thinning and calving front retreat between 2002 and 2008. This geometric change pattern has also been observed recently for several glacier basins in Alaska (Arendt et al., 2008), Greenland (Wouters et al., 2008) and the Antarctic Peninsula (Pritchard et al., 2009). The 2002–2008 results at Austfonna correspond well to the elevation changes derived from 1996–2002 airborne laser altimetry (Bamber et al., 2004). Here, we show that the elevation changes are mainly driven by the surface mass balance with the response of surface thickening at high elevations and thinning at low elevations. This is a typical pattern for surge-type glaciers in their quiescent phase of a surge cycle (e.g. Hagen et al., 2005). The interior thickening rate of up to $0.5\,m\,y^{-1}$ is higher than what is seen on quiescent phase surge-type glaciers in Spitsbergen over the last few decades (Nuth et al., 2010). The general trend of surface steepening at Austfonna may ultimately lead to surge activity in some of the drainage basins.

The mean mass balance of Austfonna in the 2002–2008 period is estimated to be $-1.3\pm0.5\,km^3$ w.e. y^{-1} (or -0.16 ± 0.06 m w.e.) when taking into account the marine retreat loss of $1.4\pm0.4\,km^3$ w.e. y^{-1} from Dowdeswell et al. (2008). It remains uncertain how representative these numbers are for the longer term mass balance of Austfonna. However, shallow ice cores and in-situ mass balance measurements do not indicate any significant changes in the mean surface mass balance in the summit area since the 1986–1998/99 period (Pinglot et al., 2001). The 2002–2008 elevation change pattern is also recognized in the 1983–2007 RES ice thickness data, although the accuracy of the RES data is too low for mass balance calculations. Since there is a lack of high quality geodetic data prior to 1996, further questions on the decadal evolution of the mass balance of the ice cap need to be addressed by means of other methods like e.g. mass balance models utilizing meteorological reanalysis data.

This study underlines that Austfonna in many ways needs to be treated separately from most other glaciers and ice caps in Svalbard when assessing the overall mass budget of the archipelago. While the surface mass balance seems to be close to zero at present, the rapid retreat of the extensive calving fronts is still causing a significantly negative total mass balance. The widespread geometric changes imply that Austfonna is not in dynamic balance with its current climate. Geometric adjustments of drainage basins through glacier acceleration or surge activity are likely to occur on a century time scale. Such potential mass redistributions will also largely influence the mass balance regime of the ice cap, i.e. a more negative mass balance after a surge due to the expanded area at low elevations. Austfonna might therefore be out of phase with the surface mass balance regimes of many other glaciers and ice caps on Svalbard due to differences in their past dynamics. Numerical modelling of Austfonna's dynamics and mass balance will be a key to gain more insight into the importance of these processes in the longer term mass balance evolution of the ice cap.

Acknowledgements. The fieldwork at Austfonna is a joint project between the University of Oslo and the Norwegian Polar Institute (NPI). Funding was mainly provided from the CryoSat calibration and validation experiment (CryoVEX) coordinated by the European Space Agency, the International Polar Year project GLACIODYN; the dynamic response of Arctic glaciers to global warming, and the ice2sea project, funded by the European Commission's 7th Framework Programme through grant number 226375. G. Moholdt was also supported through the Arkisstipend grant from the Svalbard Science Forum (SSF). The authors are thankful to all participants in the annual field campaigns, and to the contributors of high quality altimetric data, namely J. Dowdeswell and T. Benham (1983 RES data), J. Bamber (2002 ATM LIDAR data), NSI-DTU (2004/07 LIDAR and 2007 RES data) and the National Snow and Ice Data Center (ICESat data). Furthermore, we acknowledge C. Nuth, T. Dunse, I. Koch, M. Pelto, L. Copland and an anonymous reviewer for useful comments and contributions to the paper manuscript.

Edited by: I. M. Howat

References

Abdalati, W., Krabill, W., Frederick, E., Manizade, S., Martin, C., Sonntag, J., Swift, R., Thomas, R., Yungel, J., and Koerner, R.: Elevation changes of ice caps in the Canadian Arctic Archipelago, J. Geophys. Res.-Earth Surface, 109, F04007, doi:10.1029/2003JF000045, 2004.

Abshire, J. B., Sun, X. L., Riris, H., Sirota, J. M., McGarry, J. F., Palm, S., Yi, D. H., and Liiva, P.: Geoscience Laser

Altimeter System (GLAS) on the ICESat mission: On-orbit measurement performance, Geophys. Res. Lett., 32, L21S02, doi:10.1029/2005GL024028, 2005.

Arendt, A. A., Echelmeyer, K. A., Harrison, W. D., Lingle, C. S., and Valentine, V. B.: Rapid wastage of Alaska glaciers and their contribution to rising sea level, Science, 297, 382–386, doi:10.1126/science.1072497, 2002.

Arendt, A., Echelmeyer, K., Harrison, W., Lingle, C., Zirnheld, S., Valentine, V., Ritchie, B., and Druckenmiller, M.: Updated estimates of glacier volume changes in the western Chugach Mountains, Alaska, and a comparison of regional extrapolation methods, J. Geophys. Res.-Earth Surface, 111, F03019, doi:10.1029/2005JF000436, 2006.

Arendt, A., Luthcke, S. B., Larsen, C. F., Abdalati, W., Krabill, W., and Beedle, M. J.: Validation of high-resolution GRACE mascon estimates of glacier mass changes in the St Elias Mountains, Alaska, USA, using aircraft laser altimetry, J. Glaciol., 54, 778–787, 2008.

Bader, H.: Sorge's Law of densification of snow on high polar glaciers, J. Glaciol., 2, 319–323, 1954.

Bamber, J., Krabill, W., Raper, V., and Dowdeswell, J.: Anomalous recent growth of part of a large Arctic ice cap: Austfonna, Svalbard, Geophys. Res. Lett., 31, L12402, doi:10.1029/2004GL019667, 2004.

Bamber, J. L., Krabill, W., Raper, V., Dowdeswell, J. A., and Oerlemans, J.: Elevation changes measured on Svalbard glaciers and ice caps from airborne laser data, Ann. Glaciol., 42, 202–208, 2005.

Bevan, S., Luckman, A., Murray, T., Sykes, H., and Kohler, J.: Positive mass balance during the late 20th century on Austfonna, Svalbard, revealed using satellite radar interferometry, Ann. Glaciol., 46, 117–122, 2007.

Blaszczyk, M., Jania, J. A., and Hagen, J. O.: Tidewater glaciers of Svalbard: Recent changes and estimates of calving fluxes, Pol. Polar Res., 30, 85–142, 2009.

Brandt, O., Hawley, R. L., Kohler, J., Hagen, J. O., Morris, E. M., Dunse, T., Scott, J. B. T., and Eiken, T.: Comparison of airborne radar altimeter and ground-based Ku-band radar measurements on the ice cap Austfonna, Svalbard, The Cryosphere Discuss., 2, 777–810, 2008, http://www.the-cryosphere.net/2/777/2008/.

Brenner, A. C., DiMarzio, J. R., and Zwally, H. J.: Precision and accuracy of satellite radar and laser altimeter data over the continental ice sheets, IEEE T. Geosci. Remote, 45, 321–331, 2007.

Dowdeswell, J. A., Drewry, D. J., Cooper, A. P. R., Gorman, M. R., Liestøl, O., and Orheim, O.: Digital mapping of the Nordaustlandet ice caps from airborne geophysical investigations, Ann. Glaciol., 8, 51–58, 1986.

Dowdeswell, J. A. and Drewry, D. J.: The dynamics of Austfonna, Nordaustlandet, Svalbard: surface velocities, mass balance, and subglacial melt water, Ann. Glaciol., 12, 37–45, 1989.

Dowdeswell, J. A., Hagen, J. O., Bjornsson, H., Glazovsky, A. F., Harrison, W. D., Holmlund, P., Jania, J., Koerner, R. M., Lefauconnier, B., Ommanney, C. S. L., and Thomas, R. H.: The mass balance of circum-Arctic glaciers and recent climate change, Quaternary Res., 48, 1–14, 1997.

Dowdeswell, J. A., Unwin, B., Nuttall, A. M., and Wingham, D. J.: Velocity structure, flow instability and mass flux on a large Arctic ice cap from satellite radar interferometry, Earth Planet. Sc. Lett., 167, 131–140, 1999.

Dowdeswell, J. A., Benham, T. J., Strozzi, T., and Hagen, J. O.: Iceberg calving flux and mass balance of the Austfonna ice cap on Nordaustlandet, Svalbard, J. Geophys. Res.-Earth Surface, 113, F03022, doi:10.1029/2007JF000905, 2008.

Dunse, T., Schuler, T. V., Hagen, J. O., Eiken, T., Brandt, O., and Høgda, K. A.: Recent fluctuations in the extent of the firn area of Austfonna, Svalbard, inferred from GPR, Ann. Glaciol., 50, 155–162, 2009.

Dyurgerov, M. B., and Meier, M. F.: Mass balance of mountain and subpolar glaciers: A new global assessment for 1961–1990, Arctic Alpine Res., 29, 379–391, 1997.

Eiken, T., Hagen, J. O., and Melvold, K.: Kinematic GPS survey of geometry changes on Svalbard glaciers, Ann. Glaciol., 24, 157–163, 1997.

Forsberg, R., Keller, K., and Jacobsen, S. M.: Airborne lidar measurements for cryosat validation, in: Proceedings - Remote Sensing: Integrating Our View of the Planet, IEEE International Geoscience and Remote Sensing Symposium (IGARSS 2002) and 24th Canadian Symposium on Remote Sensing, Toronto, Canada, 2002, 1756–1758, 2002.

Fricker, H. A., Borsa, A., Minster, B., Carabajal, C., Quinn, K., and Bills, B.: Assessment of ICESat performance at the Salar de Uyuni, Bolivia, Geophys. Res. Lett., 32, L21S06, doi:10.1029/2005GL023423, 2005.

Hagen, J. O., Kohler, J., Melvold, K., and Winther, J. G.: Glaciers in Svalbard: mass balance, runoff and freshwater flux, Polar Res., 22, 145–159, 2003a.

Hagen, J. O., Melvold, K., Pinglot, F., and Dowdeswell, J. A.: On the net mass balance of the glaciers and ice caps in Svalbard, Norwegian Arctic, Arctic, Antarctic, and Alpine Research, 35, 264–270, 2003b.

Hagen, J. O., Eiken, T., Kohler, J., and Melvold, K.: Geometry changes on Svalbard glaciers: mass-balance or dynamic response?, Ann. Glaciol., 42, 255–261, 2005.

Hock, R.: A distributed temperature-index ice- and snowmelt model including potential direct solar radiation, J. Glaciol., 45, 101–111, 1999.

Kohler, J., Moore, J., Kennett, M., Engeset, R. V., and Elvehoy, H.: Using ground-penetrating radar to image previous years' summer surfaces for mass-balance measurements, Ann. Glaciol., 24, 355–360, 1997.

Kohler, J., James, T. D., Murray, T., Nuth, C., Brandt, O., Barrand, N. E., Aas, H. F., and Luckman, A.: Acceleration in thinning rate on western Svalbard glaciers, Geophys. Res. Lett., 34, L18502, doi:10.1029/2007GL030681, 2007.

Krabill, W. B., Abdalati, W., Frederick, E. B., Manizade, S. S., Martin, C. F., Sonntag, J. G., Swift, R. N., Thomas, R. H., and Yungel, J. G.: Aircraft laser altimetry measurement of elevation changes of the greenland ice sheet: technique and accuracy assessment, J. Geodyn., 34, 357–376, 2002.

Kristensen, S. S., Christensen, E. L., Hanson, S., Reeh, N., Skourup, H., and Stenseng, L.: Airborne ice-sounder survey of the Austfonna Ice Cap and Kongsfjorden Glacier at Svalbard, 3 May, 2007, Final Report, Danish National Space Center, Copenhagen, Denmark, 14 pp., 2008.

Kääb, A.: Glacier Volume Changes Using ASTER Satellite Stereo and ICESat GLAS Laser Altimetry. A Test Study on Edgeoya, Eastern Svalbard, IEEE T. Geosci. Remote, 46, 2823–2830,

doi:10.1109/tgrs.2008.2000627, 2008.

Lefauconnier, B. and Hagen, J. O.: Surging and calving glaciers in Eastern Svalbard, Meddelelser 116, Norwegian Polar Institute, Oslo, 130 pp., 1991.

Lemke, P., Ren, J., Alley, R. B., Allison, I., Carrasco, J., Flato, G., Fujii, Y., Kaser, G., Mote, P., Thomas, R. H., and Zhang, T.: Observations: Changes in Snow, Ice and Frozen Ground, in: Climate Change 2007: The Physical Science Basis. Contribution of Working Group I to the Fourth Assessment Report of the Intergovernmental Panel on Climate Change, edited by: Solomon, S., Qin, D., Manning, M., Chen, Z., Marquis, M., Averyt, K. B., Tignor, M., and Miller, H. L., Cambridge University Press, Cambridge, England, 337–383, 2007.

Luthcke, S. B., Arendt, A., Rowlands, D. D., McCarthy, J. J., and Larsen, C. F.: Recent glacier mass changes in the Gulf of Alaska region from GRACE mascon solutions, J. Glaciol., 54, 767–777, 2008.

Meier, M. F., Dyurgerov, M. B., Rick, U. K., O'Neel, S., Pfeffer, W. T., Anderson, R. S., Anderson, S. P., and Glazovsky, A. F.: Glaciers dominate Eustatic sea-level rise in the 21st century, Science, 317, 1064–1067, doi:10.1126/science.1143906, 2007.

Melvold, K. and Hagen, J. O.: Evolution of a surge-type glacier in its quiescent phase: Kongsvegen, Spitsbergen, 1964-95, J. Glaciol., 44, 394–404, 1998.

Nuth, C., Kohler, J., Aas, H. F., Brandt, O., and Hagen, J. O.: Glacier geometry and elevation changes on Svalbard (1936-90): a baseline dataset, Ann. Glaciol., 46, 106–116, 2007.

Nuth, C., Moholdt, G., Kohler, J., and Hagen, J. O.: Geometric changes of Svalbard glaciers and contribution to sea-level rise, J. Geophys. Res., doi:10.1029/2008JF001223, in press, 2010.

Paterson, W. S. B.: The physics of glaciers, 3rd ed., edited by: Butterworth-Heinemann, Elsevier Science Ltd., Oxford, England, 1994.

Pinglot, J. F., Hagen, J. O., Melvold, K., Eiken, T., and Vincent, C.: A mean net accumulation pattern derived from radioactive layers and radar soundings on Austfonna, Nordaustlandet, Svalbard, J. Glaciol., 47, 555–566, 2001.

Pritchard, H. D., Arthern, R. J., Vaughan, D. G., and Edwards, L. A.: Extensive dynamic thinning on the margins of the Greenland and Antarctic ice sheets, Nature, 461, 971–975, doi:10.1038/nature08471, 2009.

Raper, V., Bamber, J., and Krabill, W.: Interpretation of the anomalous growth of Austfonna, Svalbard, a large Arctic ice cap, Ann. Glaciol., 42, 373–379, 2005.

Rignot, E., Rivera, A., and Casassa, G.: Contribution of the Patagonia Icefields of South America to sea level rise, Science, 302, 434–437, 2003.

Schuler, T. V., Loe, E., Taurisano, A., Eiken, T., Hagen, J. O., and Kohler, J.: Calibrating a surface mass-balance model for Austfonna ice cap, Svalbard, Ann. Glaciol., 46, 241–248, 2007.

Schytt, V.: Scientific Results of the Swedish Glaciological Expedition to Nordaustlandet, Spitsbergen, 1957 and 1958, Geogr. Ann. A, 46, 242–281, 1964.

Strozzi, T., Kouraev, A., Wiesmann, A., Wegmuller, U., Sharov, A., and Werner, C.: Estimation of Arctic glacier motion with satellite L-band SAR data, Remote Sens. Environ., 112, 636–645, doi:10.1016/j.rse.2007.06.007, 2008.

Taurisano, A., Schuler, T. V., Hagen, J. O., Eiken, T., Loe, E., Melvold, K., and Kohler, J.: The distribution of snow accumulation across the Austfonna ice cap, Svalbard: direct measurements and modelling, Polar Res., 26, 7–13, 2007.

Wouters, B., Chambers, D., and Schrama, E. J. O.: GRACE observes small-scale mass loss in Greenland, Geophys. Res. Lett., 35, L20501, doi:10.1029/2008GL034816, 2008.

Zagorodnov, V. S. and Arkhipov, S. M.: Studies of structure, composition and temperature regime of sheet glaciers of Svalbard and Severnaya Zemlya: methods and outcomes, Bulletin of Glacier Research, 8, 19–21, 1990 (in Russian).

Zagorodnov, V. S., Sinkevich, S. A., and Arkhipov, S. M.: Hydrothermal regime of the ice-divide area of Austfonna, Nordaustlandet, Data of Glaciological Studies, 68, 133–141, 1990 (in Russian).

Zwally, H. J., Schutz, B., Abdalati, W., Abshire, J., Bentley, C., Brenner, A., Bufton, J., Dezio, J., Hancock, D., Harding, D., Herring, T., Minster, B., Quinn, K., Palm, S., Spinhirne, J., and Thomas, R.: ICESat's laser measurements of polar ice, atmosphere, ocean, and land, J. Geodyn., 34, 405–445, 2002.

Zwally, H. J., Schutz, R., Bentley, C., Bufton, J., Herring, T., Minster, B., Spinhirne, J., and Thomas, R.: GLAS/ICESat L1B Global Elevation Data V028, 20 February 2003 to 21 March 2008, Boulder, CO: National Snow and Ice Data Center, Digital media, 2008.

III

JOURNAL OF GEOPHYSICAL RESEARCH, VOL. 115, F01008, doi:10.1029/2008JF001223, 2010

Svalbard glacier elevation changes and contribution to sea level rise

Christopher Nuth,[1] Geir Moholdt,[1] Jack Kohler,[2] Jon Ove Hagen,[1] and Andreas Kääb[1]

Received 16 December 2008; revised 28 September 2009; accepted 16 October 2009; published 2 March 2010.

[1] We compare satellite altimetry from the Ice, Cloud, and Land Elevation Satellite (ICESat, 2003–2007) to older topographic maps and digital elevation models (1965–1990) to calculate long-term elevation changes of glaciers on the Svalbard Archipelago. Results indicate significant thinning at most glacier fronts with either slight thinning or thickening in the accumulation areas, except for glaciers that surged which show thickening in the ablation area and thinning in the accumulation areas. The most negative geodetic balances occur in the south and on glaciers that have surged, while the least negative balances occur in the northeast and on glaciers in the quiescent phase of a surge cycle. Geodetic balances are related to latitude and to the dynamical behavior of the glacier. The average volume change rate over the past 40 years for Svalbard, excluding Austfonna and Kvitøya is estimated to be -9.71 ± 0.55 km^3 yr^{-1} or -0.36 ± 0.02 m yr^{-1} w. equivalent, for an annual contribution to global sea level rise of 0.026 mm yr^{-1} sea level equivalent.

Citation: Nuth, C., G. Moholdt, J. Kohler, J. O. Hagen, and A. Kääb (2010), Svalbard glacier elevation changes and contribution to sea level rise, *J. Geophys. Res.*, *115*, F01008, doi:10.1029/2008JF001223.

1. Introduction

[2] The most recent IPCC assessment estimates that glaciers and ice caps outside Greenland and Antarctica contain between 15 and 37 cm of sea level equivalent (SLE) [*Lemke et al.*, 2007]. Even though this is small compared to the >60 m SLE of Antarctica and Greenland, it is the smaller glaciers and ice caps that are expected to be the greatest contributors to near-future sea level rise [*Meier et al.*, 2007]. Recent studies estimate that their contribution to sea level rise has been accelerating from about 0.35–0.40 mm yr^{-1} SLE for the period 1960–1990 to about 0.8–1.0 mm yr^{-1} SLE for 2001–2004 [*Kaser et al.*, 2006], about one third of the total observed global sea level rise. It is therefore important to quantify glacier volume changes for the various glaciated regions in the world, both to estimate glacial sea level contribution and to link such contributions to regional climatic changes. In this paper we estimate the contribution of Svalbard glaciers to sea level rise.

[3] Various methods exist to estimate regional volume changes of ice masses around the world. Traditional glacier mass balance measurements are typically extrapolated to estimate regional mass balances [*Dowdeswell et al.*, 1997; *Dyurgerov and Meier*, 1997; *Haeberli et al.*, 2007; *Hagen et al.*, 2003a, 2003b]. Using mass balance data, the contribution of Svalbard glaciers to sea level rise has been estimated previously to be 0.01 mm yr^{-1} SLE [*Hagen et al.*, 2003b], 0.038 mm yr^{-1} SLE [*Hagen et al.*, 2003a], and 0.056 mm yr^{-1} SLE [*Dowdeswell et al.*, 1997]. The differences in these estimates arise from the procedures used to extrapolate traditional mass balance measurements over unmeasured areas. *Hagen et al.* [2003a] derive a single relation between mass balance and elevation, which is then integrated over the entire archipelago, whereas *Hagen et al.* [2003b] integrate 13 regional mass balance curves over the archipelago. *Dowdeswell et al.* [1997] use an averaged net mass balance estimated from three glaciers to integrate over the glacier area. The large variation in previous SLE estimates of Svalbard exemplifies the uncertainty in extrapolations of traditional mass balance measurements in a region where climatic spatial variability is significant.

[4] Remote sensing provides an independent approach for mass balance estimation through measurements of elevation changes using for example photogrammetry [*Cox and March*, 2004; *Krimmel*, 1999] or altimetry [*Arendt et al.*, 2002; *Howat et al.*, 2008; *Zwally et al.*, 2005]. Airborne laser altimetry conducted over Svalbard in 1996 and 2002 along ~1000 km of profiles was too spatially limited to allow integration of the elevation changes into volume changes; however, the data suggest that eastern parts of Svalbard may be closer to mass balance equilibrium than the western and southern regions [*Bamber et al.*, 2004; *Bamber et al.*, 2005]. Long-term volume changes estimated from maps made by a variety of methods over smaller glaciers and ice fields indicate increases in the rate of loss within the last 15 years [*Kohler et al.*, 2007; *Kääb*, 2008; *Nuth*, 2007].

[5] Satellite measurements can provide accurate estimates of recent volume and mass changes. In this paper we use the NASA Geoscience Laser Altimetry System (GLAS) instruments aboard the Ice, Cloud, and Land Elevation Satellite (ICESat) [*Schutz et al.*, 2005]. The period of ICESat observations (2003–2007) is relatively short, and it is not always possible to distinguish snowfall and mass balance

[1]Department of Geosciences, University of Oslo, Oslo, Norway.
[2]Norwegian Polar Institute, Polarmiljøsenteret, Tromsø, Norway.

0148-0227/10/2008JF001223$09.00

Table 1. Data Sources, Time of Acquisition, Bias From Stable Terrain, and Estimated Errors for Each Region[a]

Region	DEM Year	ICESat Years	Bias (m)	RMSE (m)	DEM Error (m)	ICESat Error (m)	Ablation Error (m yr^{-1})	ELA Error (m yr^{-1})	Firn Error (m yr^{-1})
NW	1965	2003–2007	−0.4	16	9	1	0.23	0.45	0.68
NE	1966	2003–2007	1.8	12	9	1	0.23	0.46	0.70
EI	1971	2003–2007	0	10	9	1	0.27	0.53	0.80
SS	1990	2003–2007	1.8	3	2	1	0.15	0.30	0.45
VF	1990	2003–2007	2.7	10	9	1	0.60	1.21	1.81

[a]See equation (2) for error definitions. Individual point errors are defined for the ablation area, for the area around the ELA and the firn area.

variability from true climatic signals using the satellite data alone. Longer-term comparisons, important for determining present-day anomalies, must rely on comparing the modern satellite data to older topographic data.

[6] Problems encountered with the GLAS lasers forced a greatly curtailed measurement program, both spatially and temporally. There is nevertheless sufficient data over the entire Svalbard archipelago in a 4 year period (2003–2007) to allow comparison of ICESat elevations with older photogrammetric maps and digital elevation models (DEMs) from 1965 to 1990. This comparison is used to generate a long-term estimate of glacier volume change of various regions and subregions for the entire archipelago except Austfonna and Kvitøya.

2. Geographic Setting

[7] Svalbard is an Arctic archipelago (~78°N to ~15°E) situated north of Norway between Greenland and Novaya Zemlya. The islands lie between the Fram Strait and the Barents Sea, which are at the outer reaches of the North Atlantic warm water current [*Loeng*, 1991]. Therefore, Svalbard experiences a relatively warm and variable climate as compared to other regions at the same latitude. To the north lies the Arctic Ocean where winter sea ice cover limits moisture supply. To the south is a region where cyclones gain strength as storms move northward [*Tsukernik et al.*, 2007]. These geographical and meteorological conditions make the climate of Svalbard not only extremely variable (spatially and temporally), but also sensitive to deviations in both the heat transport from the south and to the sea ice conditions to the north [*Isaksson et al.*, 2005].

[8] The archipelago comprises four major islands. Some 60% of the landmasses, or about 36,000 km^2, are covered by glaciers [*Hagen et al.*, 1993]. The glaciers are generally polythermal [*Björnsson et al.*, 1996; *Hamran et al.*, 1996; *Jania et al.*, 2005; *Palli et al.*, 2003], and many of them are surge type [*Hamilton and Dowdeswell*, 1996; *Jiskoot et al.*, 2000; *Murray et al.*, 2003b; *Sund et al.*, 2009]. Typical Svalbard glaciers are characterized by low velocities (<10 m yr^{-1}) [*Hagen et al.*, 2003b] with glacier beds often frozen to the underlying permafrost [*Björnsson et al.*, 1996]. The largest island, Spitsbergen, has a landscape dominated by steep, rugged mountains containing ~22,000 km^2 of glaciers. Barentsøya and Edgeøya, two islands off the eastern coast of Spitsbergen, are dominated by plateau-type terrain [*Hisdal*, 1985] containing ~2800 km^2 of low-altitude ice caps. The island of Nordaustlandet, northeast of Spitsbergen, is mainly covered by the Vestfonna (~2450 km^2) and Austfonna (~8000 km^2) ice caps, the two largest single ice bodies within Svalbard. Climate conditions are spatially variable; the relatively continental central region [*Humlum*, 2002; *Winther et al.*, 1998] receives 40% less precipitation than the east and south while the north experiences about half the accumulation of the south [*Sand et al.*, 2003].

[9] In this study, we divide Svalbard into five major regions; South Spitsbergen (SS), Northeast Spitsbergen (NE), Northwest Spitsbergen (NW), the Eastern Islands (EI), and Vestfonna (VF). This division derives partly from natural climatic conditions and partly from the temporal distribution of the available DEMs. In addition, subregions are defined within each region which are based upon drainage basins and the availability of spatially representative ICESat profiles. Throughout this study, two-letter abbreviations are used within the text to identify the five large regions. Three-letter codes are abbreviations for the defined subregions in the maps and tables though full names are used in the text.

3. Data

[10] Digitized 1:100,000 scale topographic maps made from vertical aerial photographs taken between 1965 and 1990 at scales between 1:15,000 and 1:50,000 (the Norwegian Polar Institute (NPI) S100 Series Topographic maps of Svalbard) form the base data that are compared to ICESat. In NE, NW, EI, and VF contour maps were constructed by NPI on analog stereoplotters using 1965, 1966, 1971, and 1990 imagery, respectively. The DEM for SS was constructed by NPI using the digital photogrammetry software package SOCET SET®, from 1:50,000 scale vertical photographs taken in 1990. The grid spacing is 20 m. Table 1 lists the regions and time intervals from which elevation changes are calculated. Austfonna and Kvitøya ice caps are not included in this analysis because the available topographic maps are of too low accuracy due to limited ground control available and due to the large low-contrast zones in the firn and snow areas which render photogrammetric elevation-parallax measurement very inaccurate or impossible. The 2002–2008 volume change of Austfonna has been estimated in a separate study [*Moholdt et al.*, 2009].

[11] ICESat contains a laser altimeter system (GLAS) that has been acquiring data since 2003. GLAS retrieves average surface elevations within ~70 m diameter footprints every ~170 m along track. The single shot elevation accuracy is reported to be ~15 cm over flat terrain [*Zwally et al.*, 2002], although accuracies better than 5 cm have been achieved under optimal conditions [*Fricker et al.*, 2005]. However, some data are lost to cloud cover, and ICESat performance degrades over sloping terrain and under conditions of pronounced atmospheric forward scattering and detector saturation. When the GLAS laser is transmitting pulses with high

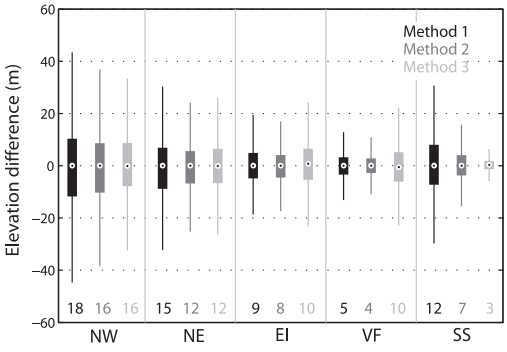

Figure 1. Box plots of the elevation differences between topographic DEMs and ICESat elevations on nonglacier terrain for the three methods outlined in section 4.1 for each region. The central point is the median, the box edges are the 25th and 75th quantile of the data, and the edges of the whiskers contain 99.3% of the data. The numbers at the bottoms of the box plots are the RMSE values of the elevation differences.

energies (i.e., during the early stages of an instrument's life) toward flat ice terrain, higher than normal echo-return energies cause detector saturation (i.e., pulse distortion) [*Abshire et al.*, 2005]. A saturation range correction [*Fricker et al.*, 2005] available since ICESat Release 28 has been added to the elevations to account for the delay of the pulse center in saturated returns. In this study, we use the GLA06 product between 2003 and 2007 from ICESat data release 428 available from the National Snow and Ice Data Center (NSIDC [*Zwally et al.*, 2008]).

4. Methods

4.1. Intersections Between ICESat Points and DEMs

[12] The satellite data, digital topographic maps, and photogrammetric DEMs are first established in the same horizontal and vertical datum and projection. The early NPI maps are referenced to the European Datum 1950 (ED50) while the 1990 DEMs are referenced to the World Geodetic System of 1984 (WGS84). A seven-parameter transformation between the UTM projections in both datums is used to convert the early maps from ED50 to WGS84. Elevation conversions are not required since the topographic maps, and photogrammetric DEMs are referenced to mean sea level using NPI mean sea level reference markers positioned around Svalbard. ICESat elevations, on the other hand, are first converted from TOPEX/Poseidon to WGS84 ellipsoid heights, and then converted to orthometric heights by subtracting the EGM96 model of geoid heights in the mean tide system. A horizontal transformation between WGS84 and TOPEX/Poseidon was not necessary since the displacements are only a few centimeters.

[13] There are various ways to produce elevation changes between ICESat profiles and contour maps. *Kääb* [2008], for example, averages eight different methods of comparison between contours, a stereo satellite-derived DEM and ICESat profiles to estimate volume changes on Edgeøya, eastern Svalbard. For region SS, a photogrammetric raster DEM is the original data product such that elevation changes are simply calculated as differences between the ICESat point elevations and the bilinear interpolation of the underlying DEM at the locations of the ICESat footprint center.

[14] For NW, NE, EI, and VF, 50 m contours were digitized by NPI from the original map foils. Three methods for calculating the vertical differences between the contours and the ICESat-derived elevations are implemented:

[15] 1. Use only ICESat points where the waveform footprint directly overlays a contour. The elevation difference is then, without any interpolation, directly calculated between the ICESat point elevation and the contour elevation included in the footprint. This method results in a small number of differences but avoids interpolation artifacts.

[16] 2. Interpolate the intersection between two successive ICESat points and a contour between them. This method results in a larger number of differences but assumes a linear slope between two successive ICESat points, i.e., over 170 m across the contours.

[17] 3. Interpolate a DEM (50 m grid spacing) from the contours using an iterative finite difference interpolation technique [*Hutchinson*, 1989], and subtract the DEM from the ICESat points as described above for the SS region. This method results in the largest number of differences but involves DEM-interpolation artifacts, in particular where contour lines are scarce due to low slopes.

[18] As a first measure to assess the characteristics and uncertainties of these three methods, elevation differences on nonglacier terrain, assumed to be stable, are analyzed for each region (Figure 1). The sample size of the three methods within each region is normalized to ensure proper inter-method comparison. The regional sizes are 4250 (NW), 2671 (NE), 1261 (EI), 954 (VF), and 5904 (SS) points. In all regions, method 1 results in a larger root-mean-square error (RMSE) than method 2 because elevation errors on steep slopes increase with distance between the ICESat center point and the contour. At 35 m distance, the radius of an ICESat footprint, the potential elevation error is 5 m for a 10° slope and up to 30 m for a 40° slope. The RMSE difference between methods 1 and 2 is greatest in NW, NE, and SS, where topography is dominated by jagged mountains with steep flanks rather than the plateau-type terrain characteristic as found for EI and VF. The RMSE for method 3 is significantly greater than for methods 1 and 2 in EI and VF. DEM interpolators are less accurate on terrain with large roughness (e.g., cliffs and plateau edges) and where distances between contours are large (relatively flat terrain, e.g., plateaus and strand flats). Both these topographic characteristics are predominant in EI and VF. The RMSE from method 3 is similar to that of method 2 in NW and NE since the DEM interpolation is as accurate as a linear interpolation between ICESat points in the more alpine mountainous terrain, with its dense contours and evenly steep slopes. The RMSE for method 3 in region SS is exceptionally small because the underlying raster DEM was directly measured using digital photogrammetry and did not have to be interpolated from contours.

[19] Method 2 is considered the most precise of the three methods for comparing ICESat to contours, especially over large flat surfaces. However, the distribution of ICESat-

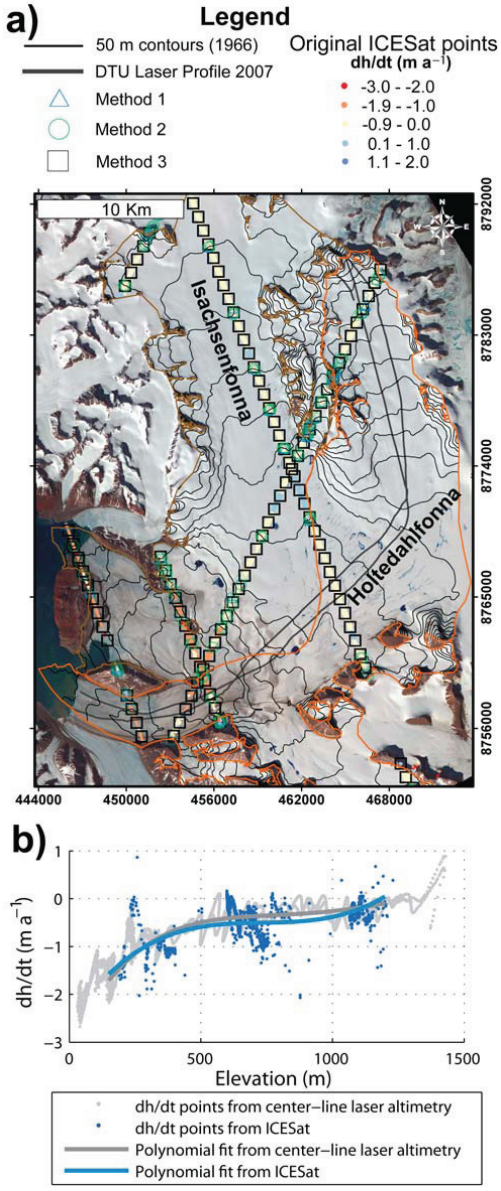

Figure 2. (a) Holtedahlfonna (orange basin outline) and Isachsenfonna (brown basin) in NW. Location of ICESat points are shown with *dh*/*dt* values indicated by color and method used by symbol. Black lines show the 2007 centerline airborne laser altimetry profile (The National Space Institute at the Technical University of Denmark). Background is an ASTER image from 12 July 2002. (b) Holtedahlfonna *dh*/*dt* points measured from ICESat and from the centerline laser altimetry along with their corresponding polynomial relationships with elevation.

contour intersections is limited in areas where profiles are transverse to the glacier centerline (for example, Figure 2a). Also, DEM interpolation of slope surfaces with limited topographic roughness, such as glaciers, introduces smaller errors than, for example, mountainous terrain outside these glaciers. Therefore, both methods 2 and 3 are implemented at the regional scale, whereas only method 3 is implemented at the subregional scale because the enhanced spatial distribution and number of elevation differences provide enough information to estimate volume change.

[20] Vertical uncertainty of the DEMs is estimated by the RMSE between ICESat elevations and the DEMs over stable terrain, assuming that the ICESat data have no error (method 3). The RMSE is largest in NW and smallest in SS (Figure 1). Accuracy of contours in the firn area may be poorer due to low optical contrast and fewer control points for the photogrammetric compilation. However, glaciers and ice caps have smoother slopes than nonglacier areas, reducing vertical errors caused by horizontal distortions and DEM interpolation.

4.2. Estimation of Elevation Change and Volume Change

[21] ICESat surface point elevations (h_1) are differenced to the underlying DEM pixels (h_0) using bilinear interpolation producing elevation changes: $dh = h_1 - h_0$. Because the ICESat points are acquired in multiple years (2003–2007), the elevation change points are divided by their respective time interval to produce point elevation change rates (dh/dt). Some outliers are present due to noisy ICESat points from atmospheric contamination, erroneous DEM elevations, or from extreme changes due to glacier surges. Outliers are removed regionally with an iterative 3σ filter within 50 m elevation bins until the improvement of the resulting standard deviation (σ) is less than 2% [*Brenner et al.*, 2007]. Because of variable cloud cover, some repeat track profiles are measured more often than others, biasing the spatial distribution of points toward those tracks that contain the most cloud-free profiles. Therefore, neighboring elevation differences within a 500 m radius are averaged to create one point for every kilometer along track. The original population of 92,811 elevation change points is reduced to 5631 points through this block smoothing.

[22] To regionalize thickness changes, relations describing the variation of dh/dt with elevation are created by fitting higher-order polynomial curves: $dh_z/dt = f(h_0)$. Higher-order polynomial fitting is less influenced by noise and outliers than averaging per elevation bin, while preserving the general trend of the elevation changes, especially at lower altitudes where thickness changes approach zero due to glacier retreat and debris-covered tongues [*Arendt et al.*, 2006; *Kääb*, 2008]. Moreover, continuous curves allow us to estimate average thickness changes also at elevation intervals where little or no data are available due to the spatial distribution of ICESat profiles. The order of the polynomials is generally increased until the RMSE converges but also requires some subjective judgment as lower-order fits can experience relatively low RMSE while still producing runaway tails at the edges of the data. At the regional scale, sixth-order polynomials were used while second- to sixth-order were used at the subregional scale. Glacier hypsometries (area-altitude distribution) for each

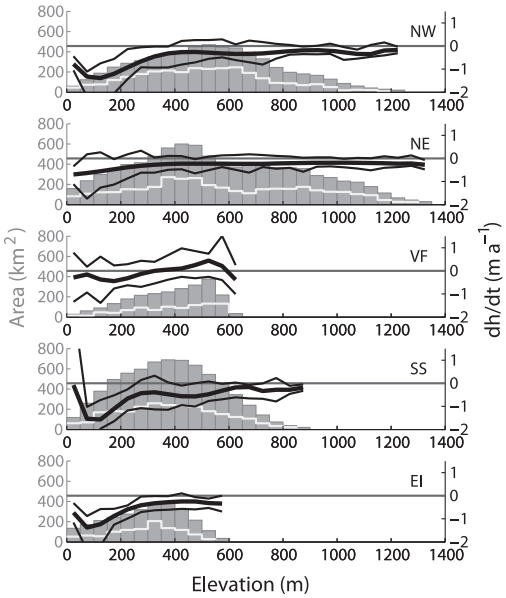

Figure 3. Area/altitude distributions of the five regions (gray, scale to the left) and the chosen polynomial fit to dh/dt by elevation (black bold line, scale to the right). The lighter black lines are one standard deviation of the original data points from the median to show the spread of the data. The lighter gray line is the number of smoothed ICESat points (see section 4.2, 5631 points for the entire study area) within each elevation bin multiplied by two for scaling purposes. The number of points thus corresponds to the y axis on the left divided by two.

region are created from the DEMs by summing the glaciated areas into 50 m elevation bins. The volume change rate (dV_{ice}/dt) is

$$\frac{dV}{dt} = \sum_{1}^{Z} \left(\frac{dh_Z}{dt} * A_Z \right), \quad (1)$$

where dh_z/dt is the elevation change curve and A is the area at each elevation bin, Z. The dh_z/dt curves and hypsometries for the five regions are shown in Figure 3.

[23] At the regional scale, a sufficient spatial distribution of dh/dt points allows robust estimates of dV_{ice}/dt. We combine these five regional estimates to calculate the total contribution of Svalbard glaciers to sea level rise. At the subregional scale, it can be more difficult to obtain a spatially representative dh/dt distribution. Approximately 33% of the glaciated area in this study did not have a suitable spatial distribution to estimate subregional volume changes. Some glaciers have only a few ICESat profiles resulting in large data gaps at some elevation bins. In cases where these data gaps are greater than 3–4 elevation bins, a straight line is used to interpolate dh/dt between higher and lower ICESat profiles. In cases where the data distribution was still too sparse, adjacent glaciers are combined to produce better dh/dt relationships. As an alternative to using polynomial elevation change curves to generate volume change rates, we could also have used the mean [*Nuth et al.*, 2007] or median [*Abdalati et al.*, 2004] dh/dt for each elevation bin. The differences in estimated volume changes between using mean, median, or polynomial fits are typically 4%–7%.

[24] We assume that all volume changes are of glacier ice [*Bader*, 1954] and multiply dV_{ice}/dt by 0.917 (the density of ice) to obtain water equivalent volume change rates (dV_{water}/dt). This assumption is valid in the ablation areas, but is more uncertain in the accumulation areas, where firn thickness or density may increase or decrease. Dividing dV_{water}/dt by the average of new and old glacier areas [*Arendt et al.*, 2002] provides geodetic mass balance rates ($\dot{b}$ in m yr^{-1}). Updated glacier areas are not yet available for the ICESat epoch, and thus we divide by the older glacier area (1966, 1971, or 1990 depending on the region) which slightly underestimates geodetic mass balances due to glacier retreat. Thickness changes (dh/dt) are given in meters of ice equivalent (m ice), while volume changes and geodetic mass balances are provided in meters of water equivalent (m w. equivalent).

4.3. Errors

[25] ICESat elevations are accurate to better than 1 m [*Brenner et al.*, 2007]. Our analysis of 237 crossover points within individual ICESat observation periods (<30 days) over Svalbard glaciers yielded a standard deviation of the elevation differences of 0.6 m, for slopes <15°. Therefore, the greatest sources of error within our estimates derive from the photogrammetrically derived topographic maps and DEMs. Errors in these products typically result from low radiometric contrast in the images, and lack of availability and quality of ground control points. To estimate single point accuracies of the DEMs relative to ICESat, we use the population of elevation differences over nonglaciated surfaces (see section 4.1) with slopes similar to those of glaciers (<15°). The population sizes for the stable terrain data sets range from 6500 points in NW to 11,826 points in SS, all distributed along the ICESat tracks. The regional ICESat-DEM differences approximate Gaussian distributions with mean differences ranging from −0.4 to 2.7 m (Table 1). We attribute these biases to ground uplift (0.10–0.24 m within our measurement periods [*Sato et al.*, 2006]), to snow cover in the ICESat observation periods (maximum 1 m), and to deviations between the EGM96 geoid model and the mean sea level references used in NPI maps (maximum 1 m). Individual vertical biases are removed from their respective regions.

[26] Individual point elevation change uncertainties (E_{PT}) are estimated by the root sum squares (RSS) of the uncertainties of each data set (Table 1). Image contrast in glacier firn areas is typically low, leading to a problem known as "floating contours" [*Arendt et al.*, 2002]. This effect has previously been accounted for by assigning accumulation area contours a vertical uncertainty of two to three times that of an ablation area contour [*Adalgeirsdottir et al.*, 1998; *Arendt et al.*, 2006; *Nolan et al.*, 2005]. We use a stepwise assignment of accuracies to the different surface types by assuming that the lowermost one-third of the elevation bins for each region and subregion corresponds to the ablation

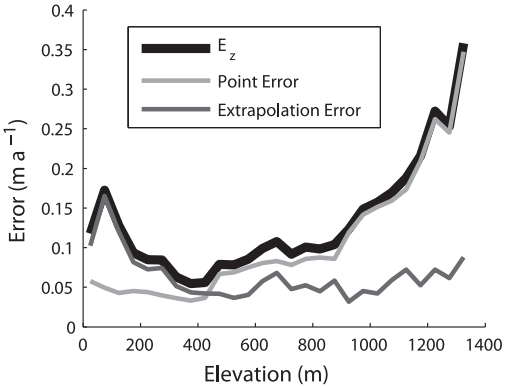

Figure 4. The estimated standard point (E_{PT}), extrapolation (E_{EXT}), and combined errors (E_Z) here exemplified for region NE. E_{PT} increases with elevation because higher elevations have poorer image contrast, and thus less accurate contour elevations from photogrammetry. E_{EXT} increases toward lower elevations because the spatial variability of *dh*/*dt* is larger because of differential ablation.

zone, the middle one-third to the zone around the equilibrium line altitude (ELA), and the upper one-third to the accumulation zone. Individual point elevation change uncertainties are then estimated by

$$E_{PT(z)} = c(z)\sqrt{\sigma^2_{DEM} + \sigma^2_{ICESat}}, \quad (2)$$

where z is the respective elevation bin, σ_{DEM} is the standard deviation of terrain differences on slopes less than 15° (Table 1), σ_{ICESat} is conservatively assigned to 1 m, and c is 1, 2, or 3 for the ablation, ELA, and accumulation zones, respectively. The middle one-third of elevations for each region (Figure 3) corresponds to a rough ELA map of Svalbard [*Hagen et al.*, 2003b]. The simplicity of this parameterization for c does not warrant a precise ELA location because anything above the lowest one-third elevation bins receives an uncertainty at least double the estimated elevation errors in the ablation area. Moreover, the resulting errors for each zone in Table 1 are provided as average annual rates to emphasize the reduction of error by having a longer time span between measurements.

[27] An additional error source arises from extrapolation (E_{EXT}) of a limited number of *dh*/*dt* points to the entire glaciated surface. E_{EXT} represents the uncertainty about the mean elevation change rate, estimated by the spatial variability of thickness changes rates [*Arendt et al.*, 2006; *Thomas et al.*, 2008]. We use the standard deviation of glacial *dh*/*dt* within each 50 m elevation bin as an approximation for the extrapolation error. At the subregional scale, elevation bins that have too few measurements (less than 5 *dh*/*dt* points) are set to twice the regional mean E_{EXT} within corresponding elevation bins.

[28] Errors in volume changes and geodetic mass balances are estimated as the combination of the two error components in each elevation bin; (1) the point elevation error (E_{PTz}), and (2) extrapolation error (E_{EXT}). Elevation changes are averaged by elevation, thus errors are reduced by the square root of the number of independent measurements within each elevation bin. Both E_{PTz} and E_{EXT} are random so that the combined errors are summed by RSS to produce the total elevation change error at each elevation bin (z):

$$E_z = \sqrt{\left(\frac{E_{PTz}}{\sqrt{N_z}}\right)^2 + \left(\frac{E_{EXTz}}{\sqrt{N_z}}\right)^2}. \quad (3)$$

When full spatial coverage is available, N may be represented by the number of pixels or measurements, assuming there is no spatial autocorrelation [*Etzelmüller*, 2000]. Conservatively, we account for spatial autocorrelation and the varying distribution of ICESat profiles over subregions and regions by defining N as the number of independent ICESat profiles within each elevation bin, rather than the number of actual data points. Thus, profiles containing more than one point within an elevation bin are, for error assessment purposes, reduced to one measurement. In our study, the total number of ICESat footprints on glaciers (92,811) is reduced by smoothing to 5631 points (see section 4.2) whereas N for the entire study area becomes 2482. Figure 4 shows an example of the elevation dependency of the error types. The standard point errors are largest at higher elevations where poor radiometric contrast makes photogrammetry difficult while the extrapolation errors are largest at the lowest elevations where spatial variability of elevation changes is greatest due to glacier retreat and differential ablation (clean ice versus dirty ice).

[29] Volume change errors (E_{VOL}) are then estimated by the RSS of the elevation errors (E_Z) multiplied by the area (A_Z) assuming that the errors are independent between the elevation bins (Z):

$$E_{VOL} = \sqrt{\sum_1^Z (E_Z * A_Z)^2}. \quad (4)$$

Uncertainties in the glacier outlines of the DEMs are an additional source of error. We expect this error to be small at the spatial scale of our volume change estimates, and therefore do not account for it. Updated glacier outlines are not available for the ICESat epoch, so while total volume change estimates are correct, geodetic mass balances are slightly underestimated due to the prevalent glacier retreat on Svalbard during the study period [*Hagen et al.*, 2003b]. Errors from seasonal differences between the end of summer DEMs and the multiseasonal ICESat acquisitions (in February/March, May/June, and September/October) are not more than 1 m or $\sim 0.02–0.13$ m yr^{-1} over the decadal measurement period. However, after accounting for the mean ICESat-DEM bias, the seasonal acquisition of ICESat introduces errors in both directions due to snow depths in acquisitions before July/August (photographic acquisitions for the topographic maps and DEMs) and additional melt that occurs after July/August thus becoming a part of our random point error. Last, the 4 year time span of ICESat

smoothes out mass balance anomalies during the 2003–2007 period.

5. Results

5.1. Thickness Changes

[30] Average annual elevation change rates (*dh*/*dt*) over Svalbard are shown in Figure 5. The mean observed *dh*/*dt* for Svalbard (excluding Austfonna and Kvitøya) is -0.40 m yr^{-1} with 95% of the data ranging between -1.65 and $+0.85$ m yr^{-1}. Frontal thinning is observed nearly everywhere except for those glaciers that have surged in the observation period. Regionally, the most negative average annual frontal thinning rates occur on SS, NW, and EI, respectively, while NE and VF have the lowest average annual frontal thinning rates (Figure 3). At higher elevations, glaciers experience only slight vertical changes, with both thinning and thickening found. Regionally, only VF experiences an average annual thickening at higher elevations while NW, NE, EI, and SS experience thinning varying between -0.15 and -0.30 m yr^{-1}. Extreme *dh*/*dt* occurs where the calving fronts of marine terminating glaciers changed their position or on glaciers that have surged. For example, the minimum and maximum change rates for the entire study area (-4.92 and $+8.21$ m yr^{-1}) are found on two glaciers that have surged recently: Perseibreen which surged in 2000 [*Dowdeswell and Benham*, 2003] and Fridtjovbreen, which surged in the mid-1990s [*Murray et al.*, 2003a].

[31] Northwest Spitsbergen (NW) glaciers experience widespread frontal thinning of -1 to -2 m yr^{-1}. The largest frontal thinning occurs on Borebreen and in Trollheimen Land. Some glaciers in NW are thinning throughout their accumulation areas (e.g., Isachsenfonna and Holtedahlfonna) while others experience significant increases at higher elevations (e.g., Kongsvegen, Borebreen, Holmströmbreen, Morabreen, and Orsabreen). On Kongsvegen, the thickening of $\sim$0.5 m yr^{-1} at upper elevations and thinning of -1 m yr^{-1} at lower elevations correspond well to previous measurements between 1991 and 2001 [*Hagen et al.*, 2005] but is less than that measured between 1966 and 1996 [*Melvold and Hagen*, 1998], +1 and -2.5 m yr^{-1} at upper and lower elevations, respectively. The surge on Abrahamsenbreen in 1978 [*Hagen et al.*, 1993] resulted in +80 m vertical increases at the tongue and -40 to -80 m decrease in the reservoir, while the surge of Osbornebreen in 1987 [*Rolstad et al.*, 1997] is seen as +50 m frontal increases and -20 m decreases at higher elevations. The larger elevation changes measured using 1966 and 1990 maps [*Rolstad et al.*, 1997] result because the latter map was made more or less at the termination of the surge, and the glacier has been rebuilding since 1990.

[32] Frontal thinning rates in NE are more moderate than in NW, ranging between -1.5 and 0 m yr^{-1}, with the most negative rates occurring at the calving fronts draining Lomonosovfonna, Kongsfonna, and Negribreen. Large thinning rates (-1.5 to -0.5 m yr^{-1}) also occur in the upper elevations of Tunabreen and Hinlopenbreen due to recent surges. Thickening of +0.5 to +1 m yr^{-1} is observed at the higher elevations of Negribreen from 1966 to $\sim$2005, slightly larger than the *dh*/*dt* measurements of +0.2 to +0.5 m yr^{-1} between 1996 and 2002 from airborne laser scanning [*Bamber et al.*, 2005]. The upper elevations of Kongsfonna and Balderfonna ice caps have thinned by -0.2 to -0.3 m yr^{-1}. Åsgardfonna ice cap is generally thinning (-0.1 to -0.3 m yr^{-1}) at higher elevations although slight thickening is observed toward the northeast. Similar patterns and magnitudes of elevation change rates were observed at high elevations ($\pm$0.10 m yr^{-1}) between 1996 and 2002 [*Bamber et al.*, 2005]. Ursafonna has thinned across the top of the ice cap (-0.1 to -0.3 m yr^{-1}) although +60 to +80 m frontal increases occur at the confluence between Chydeniusbreen and Polarisbreen. No surges have previously been recorded for these glaciers. On Oslobreen, the southern outlet glacier of Ursafonna, mid-elevation thickening of +0.3 to +0.5 m yr^{-1} is apparent both between 1966 and 2005 (this study) and from 1996 to 2002 [*Bamber et al.*, 2005].

[33] Frontal thinning of glaciers on the EI is most similar to that of NW, ranging between -0.3 and -2.0 m yr^{-1}. The largest frontal thinning occurs on Edgeøyjøkulen and Digerfonna. Elevation changes of Digerfonna are similar to those reported by *Kääb* [2008] who use the same data as in this study as well as a DEM from ASTER satellite stereo imagery. Slight thickening is observed at the higher elevations of Barentsøyjøkulen and Edgeøyjøkulen (+0.2 m yr^{-1}), where many of the outlets are suggested to be surge type [*Dowdeswell and Bamber*, 1995]. Storskavelen, a small ice cap northwest of Edgeøyjøkulen, experiences moderate thinning (0–1 m yr^{-1}) across the entire surface.

[34] Vestfonna (VF) contains the largest *dh*/*dt* variation out of all the regions, and is the only region in which significant thickening is observed. On the south side, Aldousbreen, Frazerbreen, and Idunbreen experience frontal thinning (up to -1 m yr^{-1}) and upper elevation thickening (up to +1 m yr^{-1}). Gimlebreen in the southwest has thinned over the entire surface. Bodleybreen surged in the late 1970s [*Dowdeswell and Collin*, 1990]. Since 1990, the upper glacier has thinned dramatically (-1 to -2 m yr^{-1}) implying another surge may have occurred or is occurring. Franklinbreen has thickened, greatest at lower elevations, consistent with a post-1990 advance reported by *Sneed* [2007]. To the north, both Maudbreen and Sabinebreen experience slight frontal thinning and high-elevation thickening. Rijpbreen has advanced since 1990, with mid-elevation thinning and high-elevation thickening. In general, the greatest thickening of the Vestfonna ice cap occurs along the northern ridge. Note however that point elevation errors on VF are estimated to be as much as $\pm$0.6 m yr^{-1} at lower elevations (see section 4.3), such that most of the *dh*/*dt* values are not statistically significant.

[35] In SS, frontal thinning ranges from -0.3 to -3.0 m yr^{-1}. High-elevation *dh*/*dt* values range from -1.0 to +0.5 m yr^{-1}; however, most of SS is thinning at rates of -0.1 to -0.3 m yr^{-1}. On Sørkapp, all *dh*/*dt* are negative, with frontal thinning rates up to -2.5 m yr^{-1}. In Wedel Jarlsberg Land, all glaciers have thinned. Thinning rates on the middle elevations of Rechecherbreen (1990–2005) from -0.5 to -1.0 m yr^{-1} are similar to those measured between 1996 and 2002 [*Bamber et al.*, 2005]. Zawadskibreen, Polakkbreen, and Vestre Torrellbreen experienced high-elevation thinning and mid-elevation thickening due to surges in an early stage [*Sund et al.*, 2009]. In Heerland, many glaciers have thinned, with the exception of glaciers

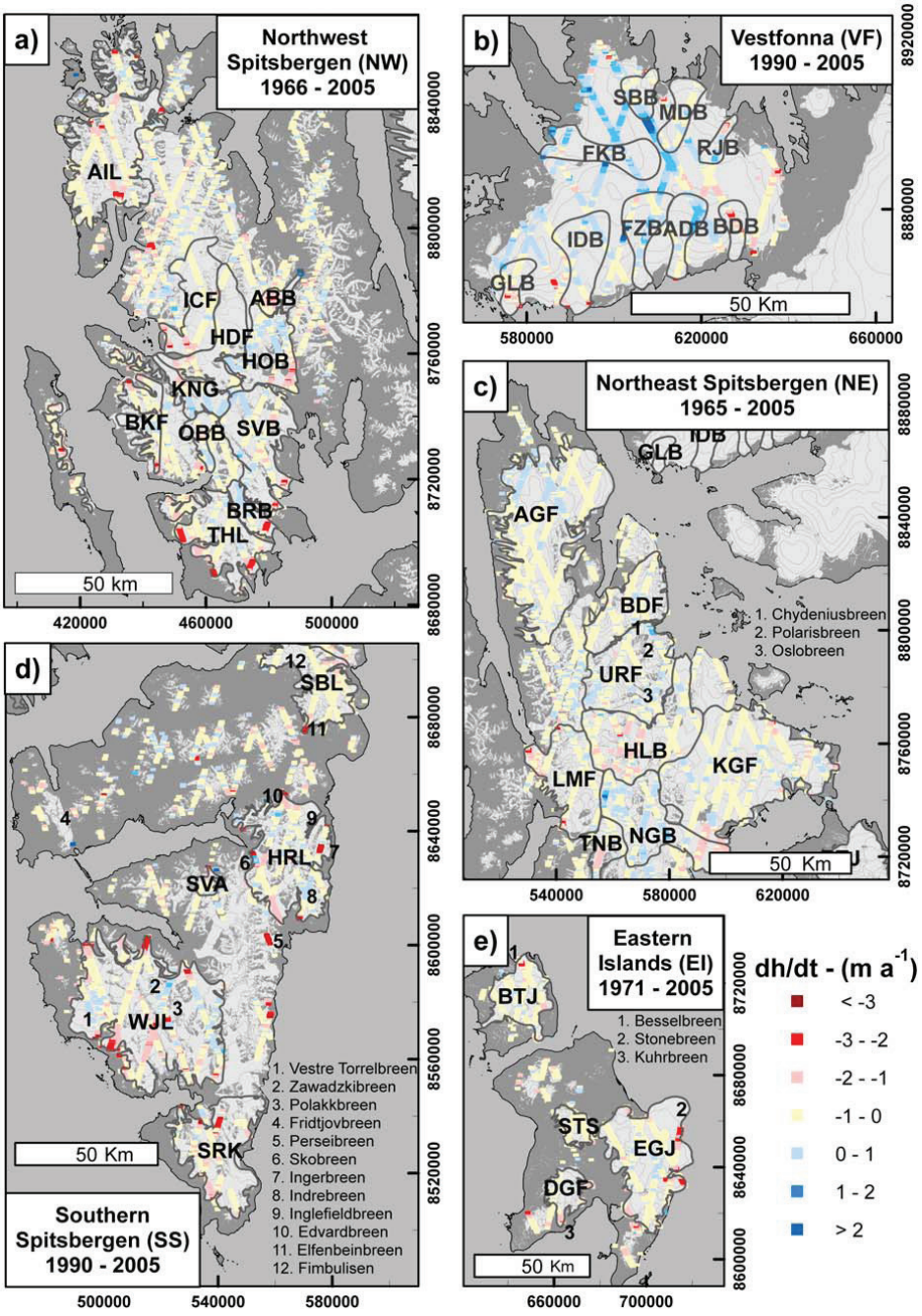
a)
Northwest Spitsbergen (NW) 1966 - 2005
AIL
ICF
ABB
HDF
HOB
KNG
BKF
OBB
SVB
BRE
THL
50 km
420000
460000
500000
8840000
8800000
8760000
8720000
8680000
b)
Vestfonna (VF) 1990 - 2005
SBB
MDB
FKB
RJB
IDB
FZB
ADB
BDB
GLB
50 Km
580000
620000
660000
8920000
8880000
c)
Northeast Spitsbergen (NE) 1965 - 2005
IDB
GLB
AGF
BDF
1
2
URF
3
1. Chydeniusbreen
2. Polarisbreen
3. Oslobreen
HLB
KGF
LMF
TNB
NGB
50 Km
540000
580000
620000
8880000
8840000
8800000
8760000
8720000
d)
12
SBL
11
10
9
4
6
HRL
7
SVA
8
5
2
1
3
WJL
1. Vestre Torrelbreen
2. Zawadzkibreen
3. Polakkbreen
4. Fridtjovbreen
5. Perseibreen
6. Skobreen
7. Ingerbreen
8. Indrebreen
9. Inglefieldbreen
10. Edvardbreen
11. Elfenbeinbreen
12. Fimbulisen
SRK
50 Km
Southern Spitsbergen (SS) 1990 - 2005
500000
540000
580000
8680000
8640000
8600000
8560000
8520000
e)
Eastern Islands (EI) 1971 - 2005
1
BTJ
1. Besselbreen
2. Stonebreen
3. Kuhrbreen
2
STS
EGJ
DGF
3
50 Km
660000
700000
8720000
8680000
8640000
8600000
dh/dt - (m a-1)
< -3
-3 - -2
-2 - -1
-1 - 0
0 - 1
1 - 2
> 2

Figure 5

that surged recently (e.g., Skobreen, Perseibreen, and Ingerbreen), and glaciers that are potentially in a quiescent phase of a surge cycle (e.g., Indrebreen, Inglefieldbreen, and Edvardbreen), which experience mid- and high-elevation increases. Glaciers in South Sabine Land have thinned at all elevations, with values ranging from -2.7 m yr^{-1} at the front of Elfenbeinbreen to -0.1 m yr^{-1} at high elevations of Fimbulisen.

5.2. Volume Changes and Geodetic Mass Balances

[36] The average volume change rate for 27,000 km^2 glaciers on Svalbard is -9.71 ± 0.53 km^3 yr^{-1} w equivalent, the equivalent to a geodetic balance of -0.36 ± 0.02 m yr^{-1} (Table 2). The most negative regional geodetic mass balance occurs in SS. However, SS is estimated over a shorter and more recent time interval (1990–2005), compared to the other regions. We note that the mass balance for the latter period is almost twice as negative as its 1936–1990 geodetic balance estimate [*Nuth et al.*, 2007], consistent with *Kohler et al.*'s. [2007] conclusion. Northeast Spitsbergen has the least negative balance of -0.25 ± 0.02 m yr^{-1} while VF is the only region with a positive geodetic balance ($+0.05 \pm 0.17$ m yr^{-1}) though not significantly different from zero. Austfonna, not included in this study, has experienced interior thickening [*Bamber et al.*, 2004] concurrent with extensive marginal thinning and retreating. *Dowdeswell et al.* [2008] suggest a volume change rate between -2.5 and -4.5 km^3 yr^{-1}, although recent altimetric measurements for the period 2002–2008 indicate total losses on the order of -1.3 km^3 yr^{-1} [*Moholdt et al.*, 2009].

[37] Table 2 provides a list of the regions and subregions with their associated volume changes, geodetic mass balances, and error estimates. The spatial variability of the subregional geodetic balances can be seen in Figure 6. As with the regional estimates, the most negative geodetic balances occur in the south and along the western and eastern coasts. Moderately negative geodetic balances occur toward NE while the subregions of Vestfonna show the most positive balances though the largest errors. Our estimate for Digerfonna in EI of -0.49 m yr^{-1} is similar to *Kääb* [2008], who estimated -0.5 m yr^{-1} by comparing the same NPI map data to a 2002 DEM generated from ASTER stereo imagery. In NW, the most negative balances occur on the surged glaciers of Abrahamsenbreen and Osbornebreen, and in subregions such as Trollheimen Land and Albert I Land that are thinning at most elevation bins. The least negative balances occur on those glaciers suspected to be in a quiescent phase of a surge cycle that experience thickening such as Kongsvegen, Borebreen, and Holmströmbreen. Similarly in NE, the most negative balances occur on the surged glaciers Hinlopenbreen and Tunabreen, and on Lomonosovfonna which is drained by two large tidewater glaciers. The least negative geodetic mass balance occurs on Negribreen which shows significant high-elevation thickening. In SS and EI, the most negative balances occur in the south while VF is the only region that shows a mix of positive and negative balances.

[38] *Hagen et al.* [2003a, 2003b] provide an overview of the in situ mass balance measurements available around Svalbard. The time periods for such measurements vary; however, they are the only available measurements from which to compare. In NW, Midre Lovénbreen and Austre Brøggerbreen are among the longest arctic mass balance measurement series [*Hagen and Liestøl*, 1990]. Their mean annual net balances of -0.38 and -0.48 m yr^{-1} are similar to our subregional estimate for Brøgger-halvøya and Prins Karls Forland of -0.43 m yr^{-1}. There is a discrepancy on Kongsvegen, however, where our estimate of -0.23 m yr^{-1} is significantly more negative than the published in situ mass balance estimate of 0.00 to $+0.04$ m yr^{-1} [*Hagen et al.*, 2003a, 2003b], or including the most recent years, -0.06 m yr^{-1}. Kongsvegen mass balance measurements start from 1987, representing about 20 years of data; this is only about half of our measurement period, roughly 40 years. In SS, mean net balances on Hansbreen (-0.52 m yr^{-1}) and Finsterwalderbreen (-0.51 m yr^{-1}) are less negative than our subregional estimate for Wedel Jarlsberg Land (-0.65 m yr^{-1}), which probably relates to spatial and temporal differences between the measurements. However, they correspond well to the regional SS estimate of -0.55 m yr^{-1}, which also includes glaciers such as Longyearbreen, Vøringbreen, Austre, and Vestre Grønnfjordbreane. In situ measurements on the latter glaciers show balances of -0.55, -0.64 -0.46, and -0.63 m yr^{-1}, respectively [*Jania and Hagen*, 1996].

6. Discussion

6.1. Elevation Change Estimation Methods

[39] Section 3.1 outlined three methods to derive elevation changes between ICESat and contour lines. On nonglacier terrain, method 2 proved to be the most accurate, especially in plateau-type terrain of EI and VF. Method 2, however, requires that the ICESat profiles cross contour lines. The distribution of such intersections on glacier tongues is limited in Spitsbergen, where glaciers tend to flow through steep valleys (see Figure 2a for an example). The opposite is true for the rest of Svalbard because the perimeter of lower-elevation contours on ice caps is largest. Method 3 introduces errors between contour lines, in places where the distance between contours is large. On the other hand, method 3 increases the number and spatial distribution of elevation change points. In using a "hypsometric" approach to estimate volume changes, we assume that the sampling distribution is representative for each elevation bin. The undersampling of method 2 at the lowest elevations has a larger impact on the volume loss of retreating glaciers than the uncertainty of the interpolation at higher elevations. Geodetic balances calculated by method 2 are 10% less

Figure 5. Annual elevation change rates (dh/dt) in (a) NW, (b) VF, (c) NE, (d) SS, and (e) EI obtained by comparing ICESat profiles from 2003 to 2007 to older DEMs from 1965 to 1990. The maps are projected in WGS84-UTM33X. Two-letter abbreviations represent the five larger regions, three-letter codes are the smaller subregions (Table 2). Numbers refer to glaciers mentioned in the text without individual estimates of volume changes and geodetic mass balances. Note that elevation changes in the subregion Brøgger-halvøya/Prins Karls Forland (BKF) within NW is from 1990 to 2005.

Table 2. Regional and Subregional Areas, Volume Changes, and Geodetic Mass Balances in Water Equivalent Along With Error Estimates[a]

Regions and Subregions[b]	Abbreviation	Area (km^2)	Volume Change ($km^3\ yr^{-1}$)	Net Mass Balance ($m\ yr^{-1}$)
Northwest Spitsbergen	NW	6027	−2.46 ± 0.15	−0.41 ± 0.02
Abrahamsenbreen[c]	ABB	76	−0.05 ± 0.01	−0.67 ± 0.14
Albert I Land[d]	AIL	931	−0.53 ± 0.06	−0.57 ± 0.07
Borebreen[e]	BRB	117	−0.03 ± 0.02	−0.22 ± 0.15
Holtedahlfonna/Kronebreen[d]	HDF	370	−0.18 ± 0.05	−0.49 ± 0.13
Holmström-/Mora-/Orsa-breenene[e]	HOB	331	−0.08 ± 0.03	−0.24 ± 0.10
Isachsenfonna/Kongsbreen[d]	ICF	408	−0.18 ± 0.05	−0.43 ± 0.13
Kongsvegen/Sidevegen[c]	KNG	180	−0.04 ± 0.03	−0.23 ± 0.14
Osbornebreen[c]	OBB	101	−0.05 ± 0.02	−0.47 ± 0.17
Svea-/Wahleen-/Sefstrom breenene[e]	SVB	523	−0.19 ± 0.05	−0.36 ± 0.10
Trollheimen[d]	THL	474	−0.29 ± 0.04	−0.60 ± 0.09
Northeast Spitsbergen	NE	8636	−2.19 ± 0.18	−0.25 ± 0.02
Asgardfonna/Vallhallfonna[d]	AGF	1613	−0.31 ± 0.09	−0.19 ± 0.06
Balderfonna[e]	BDF	491	−0.11 ± 0.04	−0.23 ± 0.08
Hinlopenbreen[c]	HLB	860	−0.50 ± 0.06	−0.58 ± 0.07
Kongsfonna/Hachstetterbreen[d]	KGF	1650	−0.51 ± 0.10	−0.31 ± 0.06
The Lomonosovfonna basin[d]	LMF	602	−0.21 ± 0.06	−0.35 ± 0.09
Negribreen[e]	NGB	711	−0.03 ± 0.05	−0.05 ± 0.07
Tunabreen[c]	TNB	174	−0.06 ± 0.02	−0.35 ± 0.14
Ursafonna/Chydeniusbreen/Oslobreen[f]	URF	703	−0.08 ± 0.05	−0.11 ± 0.07
Southern Spitsbergen	SS	6934	−3.79 ± 0.18	−0.55 ± 0.03
Brøgger-halvøya and Prins Karls Forland[d]	BKF	375	−0.16 ± 0.03	−0.43 ± 0.09
Heerland[f]	HRL	838	−0.36 ± 0.07	−0.43 ± 0.09
Sabine Land[d]	SBL	473	−0.26 ± 0.05	−0.55 ± 0.11
Sørkapp[d]	SRK	750	−0.61 ± 0.08	−0.82 ± 0.10
Svalbreen[d]	SVA	53	−0.02 ± 0.01	−0.38 ± 0.14
Wedel Jarlsberg Land[f]	WJL	1743	−1.14 ± 0.14	−0.65 ± 0.08
The Eastern Islands	EI	2799	−1.39 ± 0.14	−0.50 ± 0.05
Barentsjøkulen[d]	BTJ	566	−0.24 ± 0.06	−0.42 ± 0.11
Digerfonna[d]	DGF	264	−0.13 ± 0.06	−0.49 ± 0.21
Edgeøyjøkulen[d]	EGJ	1373	−0.79 ± 0.15	−0.58 ± 0.11
Storskavlen[d]	STS	184	−0.08 ± 0.04	−0.42 ± 0.21
Vestfonna	VF	2408	0.12 ± 0.35	0.05 ± 0.15
Aldousbreen[d]	ADB	107	0.04 ± 0.06	0.33 ± 0.52
Bodleybreen[c]	BDB	59	−0.04 ± 0.04	−0.76 ± 0.63
Franklinbreen[e]	FKB	167	0.06 ± 0.12	0.37 ± 0.72
Frazerbreen[d]	FZB	134	0.03 ± 0.07	0.24 ± 0.56
Gimlebreen[d]	GLB	61	−0.04 ± 0.03	−0.70 ± 0.45
Idunbreen[d]	IDB	188	−0.05 ± 0.09	−0.29 ± 0.46
Maudbreen[d]	MDB	92	−0.01 ± 0.05	−0.07 ± 0.52
Rijpbreen[e]	RJB	39	0.00 ± 0.03	0.07 ± 0.89
Sabinebreen[d]	SBB	64	0.01 ± 0.04	0.11 ± 0.57
Region total		26,804	−9.71 ± 0.48	−0.36 ± 0.02

[a]Abbreviations correspond with those in Figures 5 and 6. Glacier names correspond to those published by *Hagen et al.* [1993]. Subregions with multiple names indicate either that the glacier has two names, one for the upper area and one for the tongue, or that glaciers were combined to form one subregion. Footnotes c–f represent a classification of surge/quiescent/normal glaciers. Note, however, that the classification is not strict, and some glaciers may be surge-type though not inferred here to be so (the same for glaciers in a quiescent phase). Also, some subregions classified as normal glaciers may contain surge-type glaciers (i.e., Barentsøyjøkulen) and other subregions may contain a mix of surge/nonsurge glaciers (i.e., Wedel Jarlsberg Land) and are identified as such.
[b]For each group, the region is listed first, followed by the subregions.
[c]Surge glaciers.
[d]Normal glaciers.
[e]Quiescent phase glaciers.
[f]Subregions containing a surge glacier.

negative than method 3 in NW and SS (Table 3) because glacier tongues in these regions experience the greatest thinning rates and are situated in glacier valleys with few intersections between ICESat profiles and contours. The methods differ only slightly in NE because of the smaller frontal thinning rates (Figure 3). On EI, the geodetic balances calculated from the two methods are similar, while the difference on Vestfonna is hardly significant.

[40] At the subregional scale, the distribution of elevation change points has a much larger impact on the estimates.

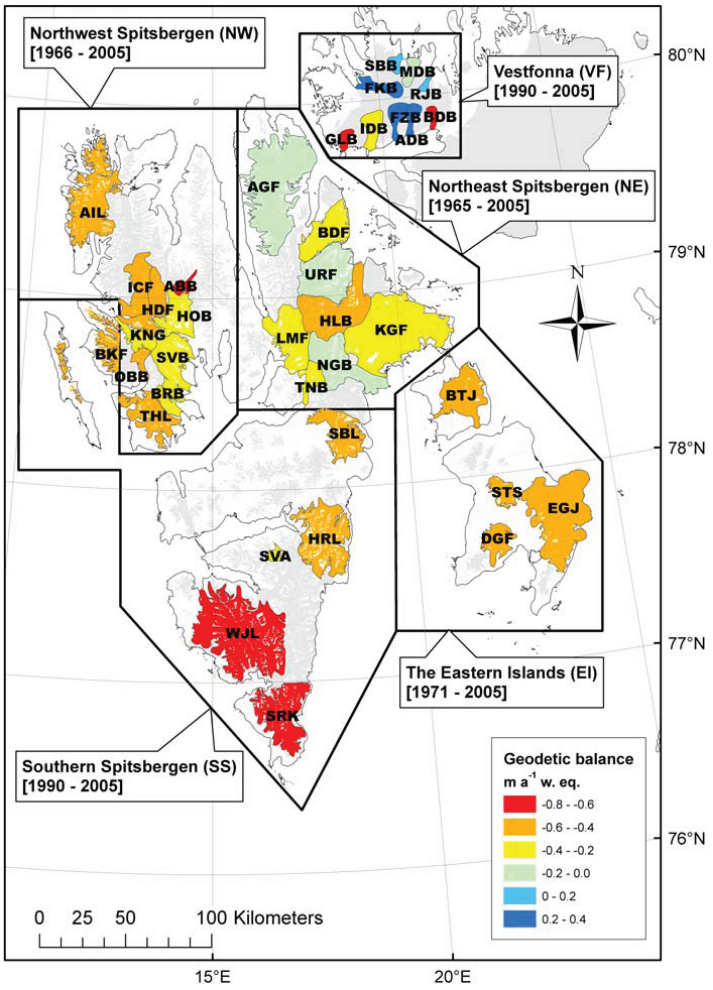

Figure 6. Estimated geodetic mass balances (w. equivalent) from subregional basins that contained a sufficient distribution of ICESat profiles. The gray areas in the background are glaciers that are not estimated individually (~33% of the total glaciated area), but are included in the total estimate for Svalbard. The exception is Austfonna which lies to the east of Vestfonna, and is not included within this study.

Table 3. Regional Geodetic Mass Balance Estimates in Water Equivalent as Estimated From Using the Three Methods Described in Section 4.1[a]

	Method 1		Method 2		Method 3	
Region	*n*	Geodetic Balance	*n*	Geodetic Balance	*n*	Geodetic Balance
NW	6706	−0.37	13509	−0.36	49536	−0.41
NE	5416	−0.26	10303	−0.26	55519	−0.25
EI	1851	−0.49	4024	−0.49	33752	−0.50
VF	1372	−0.03	2659	0.00	28706	0.05
SS	8198	−0.60	10287	−0.49	45315	−0.55

[a]Also shown is the number of original ICESat elevation change points (*n*) resulting from each of the three methods. The variation between the methods provides a reliability assessment based on different geodetic methods to compare the ICESat points to contours.

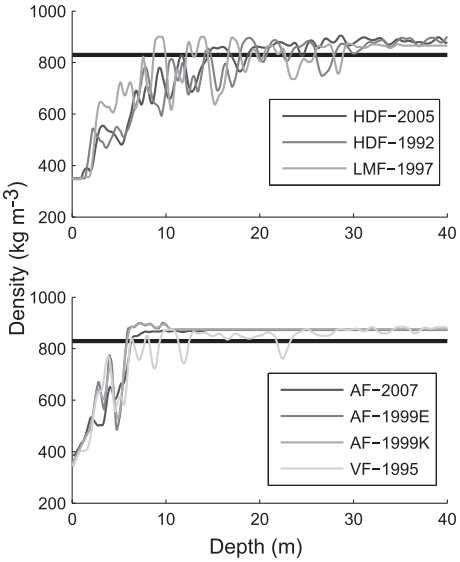

Figure 7. Firn densities profiles from the highest elevations on various glaciers in NE, NW, VF, and AF. (top) Profiles from Lomonosovfonna (LMF), 1997 [*Pohjola et al.*, 2002b]; Holtedahlfonna (HDF), 1992 [*Uchida et al.*, 1993], and 2005 [*Sjögren et al.*, 2007]. Firn-ice transition is between 15 and 19 m. (bottom) Profiles from Vestfonna (VF), 1995 [*Watanabe et al.*, 2001]; Austfonna, 1999 [*Pinglot et al.*, 2001], and 2007 [*Brandt et al.*, 2008; *Dunse et al.*, 2009]. Firn-ice transition in Nordaustlandet ranges between 7 and 10 m. Density curves on Holtedahlfonna and Austfonna are similar despite 15 and 7 year time difference, respectively, suggesting no significant changes in the firn thickness.

Errors in volume changes and geodetic mass balances are therefore considerably larger for the subregions than for the regions (Table 2). The sensitivity of the polynomial fitting to these limited data sets is tested on Holtedahlfonna, where airborne laser altimetry on the centerline was acquired in 2007 by the National Space Institute at the Technical University of Denmark (Figure 2). No formal error estimate has been made on the latter data, but airborne laser altimetry typically achieves accuracies on the order of no more than a few tens of centimeters. The centerline profiles are compared to the DEM via method 3 and a polynomial is fit following the same procedures as in section 4.3. Despite only five transverse ICESat tracks across the glacier, the *dh*/*dt* curve from ICESat is similar to that produced by the centerline profile (Figure 2b). The geodetic balance calculated from the centerline laser altimetry is -0.40 m yr^{-1}, ~20% less than our estimate of -0.49 ± 0.13 m yr^{-1} but within the error estimate.

[41] Overall, the regionalization of multitemporal thickness change rates from ICESat to map comparisons provides relatively robust estimates of volume changes and geodetic mass balances as measurements from extreme mass balance years will be smoothed out in the overall change rates due to the many different time spans involved. In addition, the multiseasonal acquisition of ICESat (February/March, May/June, and September/October) introduces a quasi-random error (see section 4.3) that limits the need for seasonal elevation adjustments, typically important in areas of high melt [*Andreassen et al.*, 2002; *Cox and March*, 2004]. The ICESat point profiles are distributed in many orientations over many glaciers rather than being concentrated along the centerlines of selected glaciers, as in other altimetric studies [*Abdalati et al.*, 2004; *Arendt et al.*, 2006, 2002; *Bamber et al.*, 2005; *Echelmeyer et al.*, 1996]. Unfavorable track configurations make it more difficult to estimate geodetic mass balances from ICESat on individual glaciers, but on a regional scale the estimate benefits from containing a greater spatial distribution of points. In addition, the location of ICESat tracks relative to the glaciers is random in regional estimates, reducing the risk of systematic errors from measurement positions.

6.2. Geodetic Balance Uncertainties

[42] The geodetic mass balance on a glacier is estimated by dividing the total volume change by the average of the old and new areas [*Arendt et al.*, 2002], and should be equivalent to the mass balance measured in situ [*Elsberg et al.*, 2001; *Krimmel*, 1999]. Since updated glacier masks for the ICESat epoch are not available, we underestimate geodetic balances because most of the glaciers are retreating. Glacier areas in SS retreated by ~0.3% per year between 1936 and 1990 [*Nuth et al.*, 2007]. This rate is used to coarsely predict the glacier area during the ICESat epoch. Re-calculation of geodetic balances using the new predicted area results in an average difference of ~5% which we take to represent the expected underestimation of our estimates. However, the final geodetic balance estimates in Table 2 do not consider area changes.

[43] The calculation of a water equivalent geodetic mass balance and sea level contribution assumes that elevation changes are the result of changes in ice thickness rather than variations in firn thickness. It is difficult to test this assumption because firn thickness varies in time and space. Long-term records (i.e., ice cores) exist only at single points at specific times. On Holtedahlfonna in NW and Lomonosovfonna in NE, the firn thickness was measured to be ~20–30 m [*Kameda et al.*, 1993; *Pohjola et al.*, 2002b; *Sjögren et al.*, 2007]. On Åsgardfonna, Vestfonna, and Austfonna, the firn thickness was measured to be only 6–10 m [*Brandt et al.*, 2008; *Dunse et al.*, 2009; *Pinglot et al.*, 2001; *Uchida et al.*, 1993; *Watanabe et al.*, 2001]. Deep firn density curves are lacking in SS and EI. The available density curves (Figure 7) show that the depths to the firn-ice transition on Holtedahlfonna and Austfonna have not changed significantly within the 15 and 8 year time intervals, respectively.

[44] Alternatively, one can apply an exponential density function (for example, $\rho(z) = 0.9 - k(z)^a$) where k and a are tuning parameters, and z is the elevation bin. The function is forced such that the lowest elevations receive a water equivalent conversion of 0.917 where higher elevations gradually receive a lower conversion factor approaching 0.55. Re-calculation of volume changes results in a 3%–7% difference in estimates. It is likely that thinning glaciers will lose some firn as the ELAs rise. This would cause an

overestimation in the geodetic mass balances since the density of firn is lower (~550 kg m^{-3}) than that of ice (917 kg m^{-3}). Setting the water equivalent conversion to that of firn in the middle one-third of elevation bins results in a maximum volume change overestimation of 15%–20%. However, in reality the loss of firn around the ELA will only be a small fraction of this. These tests exemplify that the exact water equivalent conversion will have an effect on the final water equivalent volume change but only to a small degree because at least 50%–60% of the volume changes occur in the lowest one-third of the elevation bins, that is, on ice rather than firn.

[45] In Svalbard, all marine terminating glaciers are grounded [*Hagen et al.*, 2003b] while our elevation change measurements provide thickness change rates for ice above sea level. Therefore, thinning rates of marine terminating glaciers are underestimated within the retreat areas due to ice loss below sea level. This unaccounted mass loss is important to consider when interpreting volume changes and geodetic mass balances of tidewater glaciers at a subregion scale. *Dowdeswell et al.* [2008] found that the ice loss from ice-marginal retreat at Austfonna is as much as 1.4 km^3 yr^{-1} based on ice thickness data and retreat rates from optical imagery. *Hagen et al.* [2003b] assumed an average retreat rate of 10 m yr^{-1} and an average ice thickness of 100 m along the ~1000 km long calving front of Svalbard glaciers to estimate a marine retreat loss of 1 km^3 yr^{-1} for the entire archipelago. The underestimation in our volume change estimates should be well below this value since we exclude Austfonna and account for marine ice losses above sea level. Applying the same assumptions to the ~30 km calving fronts of Vestfonna results in a marine retreat loss on the order of 0.03 km^3 yr^{-1}, which is within our error estimates.

[46] When we convert the total Svalbard volume change into SLEs, the marine retreat of grounded glaciers has only a minimal effect since the ice masses below sea level are already displacing seawater. In fact, since the density of ice is less than water, ice mass loss below sea level slightly decreases Svalbard's contribution to sea level. Nonetheless, we choose not to account for this effect due to the lack of information about ice thicknesses and retreat rates of tidewater glaciers.

6.3. Interpretation of Elevation Changes

[47] In general, three geometric patterns of elevation changes are observed on Svalbard. The most predominant pattern is recognized by large frontal thinning with slight thinning at higher elevations (above the ELA). The second pattern is characterized by large frontal thinning and high-elevation thickening. The third pattern is seen on glaciers that surged, a frontal thickening and high-elevation thinning. Variations to these patterns may occur when surges are still in progress at the time of the second elevation data acquisition (for example, see *Sund et al.* [2009]). At the lowest elevations, thickness changes are the result of ice melting and changes in ice flux. At higher elevations, Svalbard glaciers are generally thinning at rates from −0.1 to −1 m yr^{-1}. In Svalbard, the end of the Little Ice Age (LIA) occurred around the 1920s [*Nordli and Kohler*, 2004] corresponding with the onset of glacier retreat and negative mass balances [*Hagen et al.*, 1993]. Thinning above the ELA may then be explained by a decrease in the thickness of the firn column which is not the case for Holtedahlfonna (Figure 7). An alternate hypothesis may be that ice submergence velocities are larger than accumulation inputs implying a delayed or prolonged response of the dynamic system to past mass balance conditions.

[48] Some glaciers experience significant elevation increases at higher elevations. Since accumulation is dependent on atmospheric circulation and orographic effects, one would expect thickening from precipitation increases to occur regionally. Also, if accumulation is increasing, elevation increases may result from a time lag between increased mass input and the densification processes (i.e., compaction) that convert firn to ice. However, this time lag is probably shorter than the time between measurements. It is plausible that some elevation increases may be due to local precipitation increases (i.e., Asgårdfonna and Vestfonna), though previous ice core research in other parts of Svalbard does not show any significant increases in accumulation rates since 1950 [*Pinglot et al.*, 1999, *Pohjola et al.*, 2002a]. Assuming that firn density profiles remain unchanged, elevation increases above the ELA probably result from a reduced downward flux of ice that is not in balance with the present climate, most likely attributed to surge-type glaciers in quiescent phase.

[49] It remains difficult to interpret geometric changes of glaciers because a change in elevation is the result of both the mass balance and the dynamical flux [*Paterson*, 1994]. *Melvold and Hagen* [1998] and *Hagen et al.* [2005] show that geometric changes on Kongsvegen, a surge-type glacier in quiescent phase, are equivalent to the mass balance because dynamics are stagnant after the surge in 1948. *Pinglot et al.* [1999] measured the mean accumulation rates from numerous ice cores around Svalbard through radioactivity measurements and dating by nuclear tests in 1963 and the Chernobyl accident in 1986. Their analysis of two ice cores on Kongsvegen results in mean net accumulation rates of +0.53 to +0.62 m yr^{-1} from ~1963 to 1991 which compares well to our dh/dt measurements of ~+0.5 m yr^{-1}. On Holtedahlfonna, two ice cores resulted in accumulation rate estimates between +0.47 and +0.57 m yr^{-1} [*Pinglot et al.*, 1999] where our dh/dt at the highest elevations show decreases of −0.25 m yr^{-1}. This implies a submergence ice flux of ~−0.75 m yr^{-1}, which although quite large is not unlikely considering that Kronebreen, one of the fastest glaciers in Svalbard, drains Holtedahlfonna. Both Holtedahlfonna and Kongsvegen are situated within the same region, yet dh/dt measurements show completely different signals. Caution should be used when interpreting elevation changes, especially in a climatic context, as dynamic effects can be a major factor.

[50] A geodetic mass balance is a volume change rate normalized by the hypsometry and is thus a combination of the longer-term mass balance conditions as well as the dynamical conditions which lead to ice emergence or submergence and possibly calving. In the case of Kongsvegen above, the volume change and geodetic mass balance are solely related to the surface mass balance of the glacier since the dynamical component is essentially zero. Geodetic mass balances on surging glaciers require some care in interpreting since the changes reflect the presurge mass balance history, the ice volume lost into the sea through

surging, and a postsurge mass balance history. Within this data set, the geodetic balances of surged glaciers tend to be more negative than glaciers that have not surged. A good example is that of Hinlopenbreen and Negribreen in the NE region. They are adjacent basins that have surged and are building up to a new surge, respectively. The last surge of Negribreen in 1935/1936 is reported to be one of the largest known surges in Svalbard [*Hagen et al.*, 1993]. The geodetic balance of Hinlopenbreen is the most negative in the NE region, partly reflecting the removal of $\sim$2 km^3 of ice by the 1973 surge [*Liestøl*, 1973] although this is not enough to completely explain the enhanced long-term volume loss. Negribreen has the least negative geodetic balance within NE due to an extensive thickening in the accumulation area that almost balances the large thinning rates on the tongue. Down-glacier transport of ice through surging should certainly lead to an immediate change in the mass balance regime by increasing the effective ablation zone, and conversely, decreasing the accumulation zone. Furthermore, crevassing increases the surface area of the ablation zone significantly, potentially also increasing melt [*Muskett et al.*, 2003].

[51] Previous work has suggested that latitude, after accounting for elevation, can explain up to 59% of elevation change variation on Svalbard [*Bamber et al.*, 2005]. In our data sets, elevation can significantly explain $\sim$30%–70% of the variation of individual dh/dt points within each region and subregion. We further test whether the volume change after normalizing by area (i.e., geodetic balance) has any spatial trends. A multiple linear regression applied to the subregional geodetic balances (population size = 37) against latitude and longitude determined that only latitude was significant in explaining 32% of the variation (α = 0.01). Removing surging (n = 5) and quiescent phase glaciers (n = 7) from the data set (population size = 25) increases the explained variance to 46% (α = 0.01). Analysis of variance (ANOVA) tests show that surged glaciers (as classified in Table 2) are more negative than quiescent-phase glaciers (α = 0.02). Variations in geodetic balances can partly be explained by latitude with southern glaciers more negative than northern glaciers and partly by the dynamical situation with surged glaciers more negative than those in a quiescent phase.

7. Conclusions

[52] Until now, ICESat has mainly been applied to ice sheet terrain in Antarctica and Greenland. Here, ICESat laser altimetry proved to be a highly valuable data set for estimating the regional-scale glacier volume changes for smaller glaciers and ice caps at high latitudes and with mountainous topography. The precision of ICESat elevations provides good ground control on DEM generation from satellite imagery [*Berthier and Toutin*, 2008; *Korona et al.*, 2009] but also for determining the uncertainty of older topographic maps. ICESat's applicability for smaller glaciers in mountainous regions is limited because the spatial distribution of tracks does not necessarily lie along the glacier centerlines, as would be the case with airborne laser altimetric profiles. However, the spatial distribution of ICESat tracks in Svalbard is sufficient over larger regions to estimate dh/dt variation with elevation, assuming dh/dt contains normal distributions within elevation bins. The annual average volume change estimates are relatively robust due to the long time span (15–39 years) and to the large number of measurements that 4 years of ICESat tracks provide. Errors associated with such estimates are smaller at the regional scale than at the subregional scale, mainly because of the sampling distribution. Overall, ICESat has proved to be a valuable tool to measure glacier elevation and volume changes in the Svalbard archipelago.

[53] Surface elevation changes on Svalbard glaciers vary largest with elevation, before latitude. In general, glaciers are thinning at lower elevations except on glaciers which have recently surged, where thickening is observed. At higher elevations, three change patterns are present. On some glaciers slight thinning (<-0.5 m yr^{-1}) occurs in the uppermost areas which may reflect a delayed dynamic adjustment to past mass balance conditions. On other glaciers, upper altitudes are thickening, which we generally attribute to build up in the quiescent phase, as the thickening tends to occur on glaciers that have surged in the past (i.e., Negribreen and Kongsvegen), and at a subregional scale rather than at a regional scale (i.e., Borebreen and Indrebreen). Last, some glaciers experience large thinning (>-1 m yr^{-1}) at the upper altitudes (i.e., Hinlopenbreen, Ingerbreen, and Polakkbreen) implying surge activity between the measurements.

[54] Geodetic balances are a measure of the long-term total glacier change, and thus reflect general climatic influences as well as local dynamic effects, mainly in surge-type glaciers. Surged glaciers have a more negative geodetic balance than neighboring glaciers that have not surged. Glaciers that seem to be in a quiescent phase of a surge-cycle have less negative geodetic balances than other glaciers. Ignoring surge-type glaciers, 46% of the geodetic mass balance variation can be explained by latitude. Spatially, the most negative geodetic balances occur in SS followed by the coastal regions of NW, Edgeøya, and Barentsøya. The glaciers in NE show moderate losses while Vestfonna is observed to be close to zero mass balance due to a moderate interior thickening that balances frontal thinning.

[55] In summary, the total volume change for Svalbard glaciers (excluding Austfonna and Kvitøya ice caps) over the past 15–40 years is -9.71 ± 0.53 km^3 yr^{-1} or -0.36 ± 0.02 m yr^{-1} w. equivalent. This corresponds to a global sea level rise of about +0.026 mm yr^{-1} SLE, a value which lies between two previous estimates (+0.01 and +0.038 mm yr^{-1} SLE) of Svalbard's contribution to sea level rise over the past 40 years [*Hagen et al.*, 2003a, 2003b]. Our estimate is about half of the SLE contribution as estimated by *Dowdeswell et al.* [1997], and about 85% of the SLE contribution from the estimated volume changes published by *Dyurgerov and Meier* [2005]. Gravity observations from the Gravity Recovery and Climate Experiment (GRACE) satellite mission between 2003 and 2007 indicate mass losses of 8.8 Gtons yr^{-1} [*Wouters et al.*, 2008] which is similar to our 9.71 Gton yr^{-1} estimate despite the different time periods of the studies. Globally, the Svalbard contribution to sea level rise is about 4% of the total contribution from smaller glaciers and ice caps, which roughly corresponds to the area ratio between Svalbard glaciers and the sum of global glaciers and ice caps [*Kaser et al.*, 2006]. The

average annual volume loss from Svalbard is about twice the 1952–2001 loss rates in the Russian Arctic [*Glazovsky and Macheret*, 2006; *Meier et al.*, 2007] and about 40% of the 1995–2000 loss rates in the Canadian Arctic [*Abdalati et al.*, 2004]. When glacier area is considered, the Svalbard geodetic mass balance is the most negative in the Arctic, twice as negative as the Canadian Arctic, and almost four times as negative as the Russian Arctic. Lower latitude glacier regions such as Alaska [*Arendt et al.*, 2006], Iceland [*Björnsson and Pálsson*, 2008], and Patagonia [*Rignot et al.*, 2003] are losing ice at a faster rate than Svalbard.

[56] **Acknowledgments.** We would like to thank the Associate Editor, Gordon Hamilton, whose comments and suggestions considerably improved the content and presentation of this article. We would also like to thank Hester Jiskoot and two anonymous reviewers for their thorough and constructive comments. This research was supported by the IPY-GLACIODYN project (176076) funded by the Norwegian Research Council (NFR). We would like to acknowledge the Norwegian Polar Institute Mapping Department for providing the maps and DEMs, and NASA and NSIDC for providing the ICESat data, which is a remarkably accurate data set. The National Space Institute at the Technical University of Denmark provided the 2007 airborne laser altimetry profile over Holtedahlfonna. We wish to thank Elisabeth Isaksson and Veijo Pohjola for providing firn density curves. We would also like to thank Thomas Vikhamar Schuler for improving this manuscript and providing valuable insight and discussion on the validity of "Sorge's law."

References

Abdalati, W., et al. (2004), Elevation changes of ice caps in the Canadian Arctic Archipelago, *J. Geophys. Res.*, *109*, F04007, doi:10.1029/2003JF000045.

Abshire, J. B., X. Sun, H. Riris, J. M. Sirota, J. F. McGarry, S. Palm, D. Yi, and P. Liiva (2005), Geoscience Laser Altimeter System (GLAS) on the ICESat mission: On-orbit measurement performance, *Geophys. Res. Lett.*, *32*, L21S02, doi:10.1029/2005GL024028.

Adalgeirsdottir, G., K. A. Echelmeyer, and W. D. Harrison (1998), Elevation and volume changes on the Harding Icefield, Alaska, *J. Glaciol.*, *44*(148), 570–582.

Andreassen, L. M., H. Elvehoy, and B. Kjollmoen (2002), Using aerial photography to study glacier changes in Norway, *Ann. Glaciol.*, *34*, 343–348, doi:10.3189/172756402781817626.

Arendt, A. A., K. A. Echelmeyer, W. D. Harrison, C. S. Lingle, and V. B. Valentine (2002), Rapid wastage of Alaska glaciers and their contribution to rising sea level, *Science*, *297*(5580), 382–386, doi:10.1126/science.1072497.

Arendt, A., et al. (2006), Updated estimates of glacier volume changes in the western Chugach Mountains, Alaska, and a comparison of regional extrapolation methods, *J. Geophys. Res.*, *111*, F03019, doi:10.1029/2005JF000436.

Bader, H. (1954), Sorge's Law of densification of snow on high polar glaciers, *J. Glaciol.*, *2*(15), 319–323.

Bamber, J., W. Krabill, V. Raper, and J. Dowdeswell (2004), Anomalous recent growth of part of a large Arctic ice cap: Austfonna, Svalbard, *Geophys. Res. Lett.*, *31*, L12402, doi:10.1029/2004GL019667.

Bamber, J. L., W. Krabill, V. Raper, J. A. Dowdeswell, and J. Oerlemans (2005), Elevation changes measured on Svalbard glaciers and ice caps from airborne laser data, *Ann. Glaciol.*, *42*, 202–208, doi:10.3189/172756405781813131.

Berthier, E., and T. Toutin (2008), SPOT5-HRS digital elevation models and the monitoring of glacier elevation changes in North-West Canada and South-East Alaska, *Remote Sens. Environ.*, *112*(5), 2443–2454, doi:10.1016/j.rse.2007.11.004.

Björnsson, H., and F. Pálsson (2008), Icelandic glaciers, *Joekull*, *58*, 365–386.

Björnsson, H., Y. Gjessing, S. E. Hamran, J. O. Hagen, O. Liestøl, F. Palsson, and B. Erlingsson (1996), The thermal regime of sub-polar glaciers mapped by multi-frequency radio-echo sounding, *J. Glaciol.*, *42*(140), 23–32.

Brandt, O., et al. (2008), Comparison of airborne radar altimeter and ground-based Ku-band radar measurements on the ice cap Austfonna, Svalbard, *Cryosphere Discuss.*, *2*(5), 777–810.

Brenner, A. C., J. R. DiMarzio, and H. J. Zwally (2007), Precision and accuracy of satellite radar and laser altimeter data over the continental ice sheets, *IEEE Trans. Geosci. Remote Sens.*, *45*(2), 321–331, doi:10.1109/TGRS.2006.887172.

Cox, L. H., and R. S. March (2004), Comparison of geodetic and glaciological mass-balance techniques, Gulkana Glacier, Alaska, USA, *J. Glaciol.*, *50*(170), 363–370, doi:10.3189/172756504781829855.

Dowdeswell, J., and J. Bamber (1995), On the glaciology of Edgeøya and Barentsøya, Svalbard, *Polar Res.*, *14*(2), 105–122, doi:10.1111/j.1751-8369.1995.tb00684.x.

Dowdeswell, J. A., and T. J. Benham (2003), A surge of Perseibreen, Svalbard, examined using aerial photography and ASTER high resolution satellite imagery, *Polar Res.*, *22*(2), 373–383, doi:10.1111/j.1751-8369.2003.tb00118.x.

Dowdeswell, J. A., and R. L. Collin (1990), Fast-flowing outlet glaciers on Svalbard ice caps, *Geology*, *18*(8), 778–781, doi:10.1130/0091-7613(1990)018<0778:FFOGOS>2.3.CO;2.

Dowdeswell, J. A., et al. (1997), The mass balance of circum-Arctic glaciers and recent climate change, *Quat. Res.*, *48*(1), 1–14, doi:10.1006/qres.1997.1900.

Dowdeswell, J. A., T. J. Benham, T. Strozzi, and J. O. Hagen (2008), Iceberg calving flux and mass balance of the Austfonna ice cap on Nordaustlandet, Svalbard, *J. Geophys. Res.*, *113*, F03022, doi:10.1029/2007JF000905.

Dunse, T., T. V. Schuler, J. O. Hagen, T. Eiken, O. Brandt, and K. A. Høgda (2009), Recent fluctuations in the extent of the firn area of Austfonna, Svalbard, inferred from GPR, *Ann. Glaciol.*, *50*, 155–162.

Dyurgerov, M. B., and M. F. Meier (1997), Mass balance of mountain and subpolar glaciers: A new global assessment for 1961–1990, *Arct. Antarct. Alp. Res.*, *29*(4), 379–391, doi:10.2307/1551986.

Dyurgerov, M. B., and M. F. Meier (2005), *Glaciers and the Changing Earth System: A 2004 Snapshot*, 117 pp., Inst. of Arct. and Alp. Res., Univ. of Colo. at Boulder, Boulder.

Echelmeyer, K. A., et al. (1996), Airborne surface profiling of glaciers: A case-study in Alaska, *J. Glaciol.*, *42*(142), 538–547.

Elsberg, D. H., W. D. Harrison, K. A. Echelmeyer, and R. M. Krimmel (2001), Quantifying the effects of climate and surface change on glacier mass balance, *J. Glaciol.*, *47*(159), 649–658, doi:10.3189/172756501781831783.

Etzelmüller, B. (2000), On the quantification of surface changes using grid-based digital elevation models (DEMs), *Trans. GIS*, *4*(2), 129–143, doi:10.1111/1467-9671.00043.

Fricker, H. A., A. Borsa, B. Minster, C. Carabajal, K. Quinn, and B. Bills (2005), Assessment of ICESat performance at the Salar de Uyuni, Bolivia, *Geophys. Res. Lett.*, *32*, L21S06, doi:10.1029/2005GL023423.

Glazovsky, A. F., and Y. Y. Macheret (2006), Fluctuations of glaciers in the second half of 20th century caused by climate change, in *Glaciation in North and Central Eurasia at Present Time*, edited by V. M. Kotlyakov, pp. 397–402, Russ. Acad. of Sci., Moscow.

Haeberli, W., M. Zemp, and M. Hoelzle (Eds.) (2007), Glacier mass balance, *Bull. 9*, World Glacier Monit. Serv., Zurich, Switzerland.

Hagen, J. O., and O. Liestøl (1990), Long-term glacier mass-balance investigations in Svalbard, 1950–1988, *Ann. Glaciol.*, *14*, 102–106.

Hagen, J. O., O. Liestøl, E. Roland, and T. Jørgensen (1993), Glacier atlas of Svalbard and Jan Mayen, *Meddelelse 129*, Norw. Polar Inst., Oslo.

Hagen, J. O., J. Kohler, K. Melvold, and J. G. Winther (2003a), Glaciers in Svalbard: Mass balance, runoff and freshwater flux, *Polar Res.*, *22*(2), 145–159, doi:10.1111/j.1751-8369.2003.tb00104.x.

Hagen, J. O., K. Melvold, F. Pinglot, and J. A. Dowdeswell (2003b), On the net mass balance of the glaciers and ice caps in Svalbard, Norwegian Arctic, *Arct. Antarct. Alp. Res.*, *35*(2), 264–270, doi:10.1657/1523-0430(2003)035[0264:OTNMBO]2.0.CO;2.

Hagen, J. O., T. Eiken, J. Kohler, and K. Melvold (2005), Geometry changes on Svalbard glaciers: Mass-balance or dynamic response?, *Ann. Glaciol.*, *42*, 255–261, doi:10.3189/172756405781812763.

Hamilton, G., and J. Dowdeswell (1996), Controls on glacier surging in Svalbard, *J. Glaciol.*, *42*(140), 157–168.

Hamran, S. E., E. Aarholt, J. O. Hagen, and P. Mo (1996), Estimation of relative water content in a sub-polar glacier using surface-penetration radar, *J. Glaciol.*, *42*(142), 533–537.

Hisdal, V. (1985), *Geography of Svalbard*, Norw. Polar Inst., Oslo.

Howat, I. M., B. E. Smith, I. Joughin, and T. A. Scambos (2008), Rates of southeast Greenland ice volume loss from combined ICESat and ASTER observations, *Geophys. Res. Lett.*, *35*, L17505, doi:10.1029/2008GL034496.

Humlum, O. (2002), Modelling late 20th-century precipitation in Nordenskiøld Land, Svalbard, by geomorphic means, *Norw. J. Geogr.*, *56*(2), 96–103, doi:10.1080/00291950260056413.

Hutchinson, M. F. (1989), A new procedure for gridding elevation and stream line data with automatic removal of spurious pits, *J. Hydrol.*, *106*(3–4), 211–232, doi:10.1016/0022-1694(89)90073-5.

Isaksson, E., et al. (2005), Two ice-core delta O-18 records from Svalbard illustrating climate and sea-ice variability over the last 400 years, *Holocene*, *15*(4), 501–509, doi:10.1191/0959683605hl820rp.

Jania, J., and J. O. Hagen (Eds.) (1996), Mass balance of arctic glaciers, *Rep. 5*, 62 pp., Int. Arct. Sci. Comm., Potsdam, Germany.

Jania, J., et al. (2005), Temporal changes in the radiophysical properties of a polythermal glacier in Spitsbergen, *Ann. Glaciol.*, *42*, 125–134, doi:10.3189/172756405781812754.

Jiskoot, H., T. Murray, and P. Boyle (2000), Controls on the distribution of surge-type glaciers in Svalbard, *J. Glaciol.*, *46*(154), 412–422, doi:10.3189/172756500781833115.

Kääb, A. (2008), Glacier volume changes using ASTER satellite stereo and ICESat GLAS laser altimetry. A test study on Edgeøya, eastern Svalbard, *IEEE Int. Geosci. Remote Sens.*, *46*(10), 2823–2830, doi:10.1109/TGRS.2008.2000627.

Kameda, T., S. Takahashi, K. Goto-Azuma, S. Kohshima, O. Watanabe, and J. O. Hagen (1993), First report of ice core analyses and borehole temperatures on the highest icefield on western Spitsbergen in 1992, *Bull. Glacier Res.*, *11*, 51–61.

Kaser, G., J. G. Cogley, M. B. Dyurgerov, M. F. Meier, and A. Ohmura (2006), Mass balance of glaciers and ice caps: Consensus estimates for 1961–2004, *Geophys. Res. Lett.*, *33*, L19501, doi:10.1029/2006GL027511.

Kohler, J., et al. (2007), Acceleration in thinning rate on western Svalbard glaciers, *Geophys. Res. Lett.*, *34*, L18502, doi:10.1029/2007GL030681.

Korona, J., E. Berthier, M. Bernard, F. Rémy, and E. Thouvenot (2009), SPIRIT. SPOT 5 stereoscopic survey of Polar Ice: Reference images and topographies during the fourth international polar year (2007–2009), *ISPRS J. Photogramm. Remote Sens.*, *64*(2), 204–212, doi:10.1016/j.isprsjprs.2008.10.005.

Krimmel, R. M. (1999), Analysis of difference between direct and geodetic mass balance measurements at South Cascade Glacier, Washington, *Geogr. Ann., Ser. A Phys. Geogr.*, *81*(4), 653–658.

Lemke, P., et al. (2007), Observations: Changes in snow, ice and frozen ground, in *Climate Change 2007: The Physical Science Basis—Contribution of Working Group I to the Fourth Assessment Report of the Intergovernmental Panel on Climate Change*, edited by S. Solomon et al., pp. 356–360, Cambridge Univ. Press, Cambridge, U. K.

Liestøl, O. (1973), Glaciological work in 1971, in *Norsk Polarinstitutt Årbok*, pp. 31–35, Norw. Polar Inst., Oslo.

Loeng, H. (1991), Features of the physical oceanographic conditions of the Barents Sea, *Polar Res.*, *10*(1), 5–18, doi:10.1111/j.1751-8369.1991.tb00630.x.

Meier, M. F., et al. (2007), Glaciers dominate Eustatic sea-level rise in the 21st century, *Science*, *317*(5841), 1064–1067, doi:10.1126/science.1143906.

Melvold, K., and J. O. Hagen (1998), Evolution of a surge-type glacier in its quiescent phase: Kongsvegen, Spitsbergen, 1964–95, *J. Glaciol.*, *44*(147), 394–404.

Moholdt, G., J. O. Hagen, T. Eiken, and T. V. Schuler (2009), Geometric changes and mass balance of the Austfonna ice cap, Svalbard, *Cryosphere*, *4*, 21–34.

Murray, T., A. Luckman, T. Strozzi, and A. M. Nuttall (2003a), The initiation of glacier surging at Fridtjovbreen, Svalbard, *Ann. Glaciol.*, *36*, 110–116, doi:10.3189/172756403781816275.

Murray, T., T. Strozzi, A. Luckman, H. Jiskoot, and P. Christakos (2003b), Is there a single surge mechanism? Contrasts in dynamics between glacier surges in Svalbard and other regions, *J. Geophys. Res.*, *108*(B5), 2237, doi:10.1029/2002JB001906.

Muskett, R. R., C. S. Lingle, W. V. Tangborn, and B. T. Rabus (2003), Multi-decadal elevation changes on Bagley Ice Valley and Malaspina Glacier, Alaska, *Geophys. Res. Lett.*, *30*(16), 1857, doi:10.1029/2003GL017707.

Nolan, M., A. Arendt, B. Rabus, and L. Hinzman (2005), Volume change of McCall Glacier, Arctic Alaska, USA, 1956–2003, *Ann. Glaciol.*, *42*, 409–416, doi:10.3189/172756405781812943.

Nordli, Ø., and J. Kohler (2004), *The Early 20th Century Warming—Daily Observations at Grønfjorden and Longyearbyen on Spitsbergen*, Norw. Meteorol. Inst., Oslo.

Nuth, C. (2007), Geodetic mass balance of Svalbard glaciers: 1936–2004, M.S. thesis, 94 pp., Univ. of Oslo, Oslo.

Nuth, C., J. Kohler, H. F. Aas, O. Brandt, and J. O. Hagen (2007), Glacier geometry and elevation changes on Svalbard (1936–90), A baseline dataset, *Ann. Glaciol.*, *46*, 106–116, doi:10.3189/172756407782871440.

Palli, A., J. C. Moore, and C. Rolstad (2003), Firn-ice transition-zone features of four polythermal glaciers in Svalbard seen by ground-penetrating radar, *Ann. Glaciol.*, *37*, 298–304, doi:10.3189/172756403781816059.

Paterson, W. S. B. (1994), *The Physics of Glaciers*, Elsevier, New York.

Pinglot, J. F., J. O. Hagen, K. Melvold, T. Eiken, and C. Vincent (2001), A mean net accumulation pattern derived from radioactive layers and radar soundings on Austfonna, Nordaustlandet, Svalbard, *J. Glaciol.*, *47*(159), 555–566, doi:10.3189/172756501781831800.

Pinglot, J. F., M. Pourchet, B. Lefauconnier, J. O. Hagen, E. Isaksson, R. Vaikmae, and K. Kamiyama (1999), Accumulation in Svalbard glaciers deduced from ice cores with nuclear tests and Chernobyl reference layers, *Polar Res.*, *18*(2), 315–321, doi:10.1111/j.1751-8369.1999.tb00309.x.

Pohjola, V. A., T. A. Martma, H. A. J. Meijer, J. C. Moore, E. Isaksson, R. Vaikmae, and R. S. W. Van de Wal (2002a), Reconstruction of three centuries of annual accumulation rates based on the record of stable isotopes of water from Lomonosovfonna, Svalbard, *Ann. Glaciol.*, *35*, 57–62, doi:10.3189/172756402781816753.

Pohjola, V. A., et al. (2002b), Effect of periodic melting on geochemical and isotopic signals in an ice core from Lomonosovfonna, Svalbard, *J. Geophys. Res.*, *107*(D4), 4036, doi:10.1029/2000JD000149.

Rignot, E., A. Rivera, and G. Casassa (2003), Contribution of the Patagonia Icefields of South America to sea level rise, *Science*, *302*(5644), 434–437, doi:10.1126/science.1087393.

Rolstad, C. A. J., J. O. Hagen, and B. Lunden (1997), Visible and near-infrared digital images for determination of ice velocities and surface elevation during a surge on Osbornebreen, a tidewater glacier in Svalbard, *Ann. Glaciol.*, *24*, 255–261.

Sand, K., J. G. Winther, D. Marechal, O. Bruland, and K. Melvold (2003), Regional variations of snow accumulation on Spitsbergen, Svalbard, 1997–99, *Nord. Hydrol.*, *34*(1–2), 17–32.

Sato, T., et al. (2006), A geophysical interpretation of the secular displacement and gravity rates observed at Ny-Alesund, Svalbard in the Arctic: effects of post-glacial rebound and present-day ice melting, *Geophys. J. Int.*, *165*(3), 729–743, doi:10.1111/j.1365-246X.2006.02992.x.

Schutz, B. E., H. J. Zwally, C. A. Shuman, D. Hancock, and J. P. DiMarzio (2005), Overview of the ICESat Mission, *Geophys. Res. Lett.*, *32*, L21S01, doi:10.1029/2005GL024009.

Sjögren, B., O. Brandt, C. Nuth, E. Isaksson, V. Pohjola, J. Kohler, and R. S. W. Van De Wal (2007), Instruments and methods: Determination of firn density in ice cores using image analysis, *J. Glaciol.*, *53*(182), 413–419, doi:10.3189/002214307783258369.

Sneed, W. (2007), Satellite remote sensing of Arctic Glacier: Climate interactions, M.S. thesis, 83 pp., Univ. of Maine, Orono.

Sund, M., T. Eiken, J. O. Hagen, and A. Kääb (2009), Svalbard surge dynamics derived from geometric changes, *Ann. Glaciol.*, *50*, 50–60, doi:10.3189/172756409789624265.

Thomas, R., C. Davis, E. Frederick, W. Krabill, Y. H. Li, S. Manizade, and C. Martin (2008), A comparison of Greenland ice-sheet volume changes derived from altimetry measurements, *J. Glaciol.*, *52*(185), 203–212, doi:10.3189/002214308784886225.

Tsukernik, M., D. N. Kindig, and M. C. Serreze (2007), Characteristics of winter cyclone activity in the northern North Atlantic: Insights from observations and regional modeling, *J. Geophys. Res.*, *112*, D03101, doi:10.1029/2006JD007184.

Uchida, T., et al. (1993), Ice core analyses and borehole temperature measurements at the drilling site on Asgardfonna, Svalbard, in 1993, *Mem. Natl. Inst. Polar Res.*, *51*, 377–386.

Watanabe, O., et al. (2001), Studies on climatic and environmental changes during the last few hundred years using ice cores from various sites in Nordaustlandet, Svalbard, *Mem. Natl. Inst. Polar Res.*, *54*, 227–242.

Winther, J. G., O. Bruland, K. Sand, A. Killingtveit, and D. Marechal (1998), Snow accumulation distribution on Spitsbergen, Svalbard, in 1997, *Polar Res.*, *17*(2), 155–164, doi:10.1111/j.1751-8369.1998.tb00269.x.

Wouters, B., D. Chambers, and E. J. O. Schrama (2008), GRACE observes small-scale mass loss in Greenland, *Geophys. Res. Lett.*, *35*, L20501, doi:10.1029/2008GL034816.

Zwally, H. J., et al. (2002), ICESat's laser measurements of polar ice, atmosphere, ocean, and land, *J. Geodyn.*, *34*(3–4), 405–445, doi:10.1016/S0264-3707(02)00042-X.

Zwally, H. J., et al. (2005), Mass changes of the Greenland and Antarctic ice sheets and shelves and contributions to sea-level rise: 1992–2002, *J. Glaciol.*, *51*(175), 509–527, doi:10.3189/172756505781829007.

Zwally, H. J., et al. (2008), GLAS/ICESat L1B global elevation data V028, February 2003 to November 2007, http://nsidc.org/data/icesat/index.html, Natl. Snow and Ice Data Cent., Boulder, Colo.

J. O. Hagen, A. Kääb, G. Moholdt, and C. Nuth, Department of Geosciences, University of Oslo, PO Box 1047, Blindern, N-0316 Oslo, Norway. (christopher.nuth@geo.uio.no)

J. Kohler, Norwegian Polar Institute, Polarmiljøsenteret, N-9296 Tromsø, Norway.

IV